Real Aperture Synthetically Organised Radar

Ewan McCutcheon

February 2004

A thesis submitted to the University of Bristol in accordance with the requirements of the degree of Doctor of Philosophy in the Faculty of Engineering, Department of Electrical and Electronic Engineering.

Abstract

The broad objective of this research was to develop a fully functional ground penetrating radar (GPR) demonstrator system capable of detecting buried anti-personnel and anti-tank landmines when installed on a moving vehicle. The demonstrator system implements a novel Real Aperture Synthetically Organised Radar (RASOR) technique that uses a two dimensional antenna array and post-reception synthetic-focusing in order to image a three dimensional space under the array.

State-of-the-art GPR systems for landmine detection are limited by resolution, operation in highly cluttered environments, classification performance, penetration depth and operating speed. This thesis describes the author's contribution to the above research in the following areas:

- Analysis and modelling of the RASOR system concepts including an assessment of the operating environment such as soil types, target types, clutter limits, noise limits and de-correlating effects in order to postulate and analyse suitable array configurations, mounting arrangements and processing algorithms.
- Derivation, implementation and experimentation with new algorithms to deal with the problem of surface reflections, volume clutter reduction and classification.
- Definition of system parameters such as operating frequency, power and array size and configuration in order to deal with the operational environment based on modelling and early experimentation.
- System design including the design of RF and digital circuits and control software and the implementation of processing algorithms for a real time system.

Using the developed demonstrator system, measurements were obtained on real targets under various soil conditions and at a variety of test sites. Results are presented and discussed which show RASOR's ability to detect mines in challenging cluttered environments.

Dedication and Acknowledgements

Firstly I wish to acknowledge and give thanks to Prof. Ralph Benjamin for his original and deep insight into this research, and for his valuable encouragement and advice.

Thanks to Dr. Geoff Hilton and Dr. Ian Craddock for the technical advice and practical support they have provided, and to Prof. Joe McGeehan for kindly giving me the opportunity to research at the University of Bristol in the Centre for Communications Research. I am particularly grateful to Geoff for reading through this thesis in great detail and providing many helpful suggestions.

DERA Malvern (now Qinetiq) funded the major part of the research program associated with this work and I wish to acknowledge their assistance and thank, in particular, Dr. Graeme Crisp for his helpful guidance and practical advice on mine detection and radar.

I am grateful to Dr. Rajagopal Nilavalan for his collaboration and for our discussions that often provided new insights. I would also like to recognise the contribution that Stuart Litobarski and Martin Hellen made to some of the data gathering and circuit construction.

The fieldwork would not have been possible without the assistance of the following organisations and their staff; RACAL Defence Electronics at Wells in particular Malcolm White and Dudley Bird; ERA in Leatherhead; DERA Chertsey; and the University of Bristol Agricultural College at Long Ashton. I must also salute all the Bobs, Robs, Johns and Richards in the University engineering workshops who rose to all the challenges they were set with great good humour and failed not once.

I thank my family and friends for their support, sympathy and all those cups of tea, and particularly thank Peter for his enthusiastic and valuable assistance.

Lastly, and above all, I wish to acknowledge the love, patience, encouragement, understanding and motivation given by my wife, Amanda. I dedicate this work to her.

AUTHOR'S DECLARATION

I declare that the work in this dissertation was carried out in accordance with the Regulations of the University of Bristol. The work is original except where indicated by special reference in the text and no part of the dissertation has been submitted for any other degree.

Any views expressed in the dissertation are those of the author and in no way represent those of the University of Bristol.

The dissertation has not been presented to any other University for examination either in the United Kingdom or overseas.

SIGNED: E. McCabe DATE: 10/1/05

Contents

List of Figures iv
List of Tables xiii
List of Principal Symbols xiv
List of Abbreviations xv
List of Publications xvi
1 Introduction 1
1.1 The Aim of the Thesis 3
1.2 Thesis Structure 5
References 6
2 The Landmine Problem 9
2.1 Brief History of Landmines 9
2.2 Modern Landmines 10
2.3 Detection Techniques 12
2.3.1 Signal Detection Theory 14
2.3.2 Alternative Detection Approaches 16
2.3.3 Metal Detectors 16
2.3.4 Biological Sensors and Systems 18
2.3.5 Electro/Optical Sensors 18
2.3.6 Computed Tomography 19
2.3.7 Electrical Impedance Tomography 20
2.3.8 X-ray Backscatter 21
2.3.9 Acoustics/Seismic Methods 22
2.3.10 Nuclear Quadrupole Resonance 23
2.3.11 Ground Penetrating Radar 24
2.3.12 Sensor Data Fusion 25
2.4 Conclusions 26
References 27
3 Ground Penetrating Radar 32
3.1 GPR Overview 32
3.1.1 Antennas 34
3.1.2 Pulse types 35
3.1.3 Data acquisition 37
3.1.4 Signal processing 38
3.2 System Designs for Target Detection 41
3.2.1 Polarisation Discrimination 41
3.2.2 Target Resonance 43
3.2.3 Microwave Holography and Synthetic Aperture Techniques 43
3.2.4 Spot Focusing 45
3.3 Introducing RASOR 46
3.3.1 System Concept 47
3.3.2 Proposed Design 50
3.3.3 Operational Scenario 52
3.4 Conclusions 53
References 53
4 Analysis of Real Aperture Synthetically Organised Radar 57
4.1 Fundamentals 57

4.1.1 Principles of Electromagnetic Propagation 57
4.1.2 Propagation in Dielectric Materials 60
4.1.3 Dielectric Properties of Soil 62
4.1.4 Dielectric Measurements 63
4.1.5 Propagation at Dielectric Boundaries 65
4.2 Loss Mechanisms 66
4.3 RASOR Performance Analysis 72
4.3.1 Methods of Analysis 72
4.3.2 Modelling of System Impulse Response 76
4.3.3 Lateral Resolution 80
4.3.4 Vertical Resolution 81
4.3.5 Surface Macroscale Features 82
4.4 RASOR Focusing Optimisation and Weighting 85
4.4.1 Surface Scattering 86
4.4.2 Surface Clutter Processing Options 88
4.4.3 Soil Inhomogeneities 91
4.5 Conclusions 98
References 98
5 Demonstrator System Design 102
5.1 Hardware Development 103
5.1.1 Antenna Design Alternatives 103
5.1.2 Bowtie Antenna Design 105
5.1.3 Antenna Array 108
5.1.4 Switching Network 111
5.1.5 Pulse Generator 122
5.1.6 Digitisation 124
5.2 Algorithmic implementation 125
5.2.1 A-Scan Signal Processing 126
5.2.2 RASOR Coherent Focusing 128
5.3 Real Time RASOR 130
5.3.1 Data Collection 130
5.4 Conclusions 132
References 132
6 Experimental Results 135
6.1 Summary of Test Sites 135
6.2 Summary of Test Targets 136
6.3 Indoor Sandbox Experiments 137
6.3.1 Experimental Facility 137
6.3.2 Test Results 138
6.4 Quarry experiments 143
6.4.1 Trial Site 143
6.4.2 Quarry Trial Results (1st Campaign) 145
6.4.3 Quarry Trial Results (2nd Campaign) 148
6.5 Long Ashton 150
6.5.1 Trial Site 150
6.5.2 Trial Results 151
6.6 DERA Chertsey 152
6.6.1 Trial Site 152
6.6.2 Trial Results 153
6.7 ERA 157

6.7.1 Trial Site 157
6.7.2 Trial Results 161
6.8 Conclusions 164
References 164
7 Conclusions, Other Applications and Future Work 165
7.1 Specific contribution of this Dissertation 165
7.2 Suggestions for further research 166
7.3 Other applications 166
7.3.1 Archaeology 167
7.3.2 Security 167
7.3.3 Manufacturing 167
7.3.4 Medical 167
Reference 167

List of Figures

Figure 2-1 Examples of modern landmines (a) VS-50, (b) TMA-4, (c) TM-57, (d) PPM-2, (e) PMA-3, (f) M16A2 (reproduced from [7]) 11

Figure 2-2 Prodding Technique (reproduced from [11]) 12

Figure 2-3 Prodding in rough terrain (reproduced from [12]) 13

Figure 2-4 Mechanical flail for land mine detonation (reproduced from [11]) 13

Figure 2-5 Sensor response probability density functions an ROC curves (a) Probability distributions for noise and noise plus signal (b) threshold detection level added, (c) ROC curve for (b) with threshold point indicated (d) family of ROC curves 14

Figure 2-6 Block diagram of Electromagnetic Induction system 17

Figure 2-7 Transmission and detection of an induced magnetic field 17

Figure 2-8 Block diagram of an Electrical Impedance Tomography System 20

Figure 2-9 Block diagram of X-ray backscatter system 22

Figure 2-10 Block diagram of a Nuclear Quadrupole Resonance system 24

Figure 3-1 Generic Ground Penetrating Radar system 32

Figure 3-2 Basic block diagram of a FM-CW radar 36

Figure 3-3 A-scan co-ordinate system 39

Figure 3-4 Typical A-scan waveform 39

Figure 3-5 B-scan co-ordinate system 40

Figure 3-6 Representation of a B-scan plot 40

Figure 3-7 C-scan co-ordinate system 41

Figure 3-8 C-scan image (from RASOR) 41

Figure 3-9 Holographic imaging geometry 44

Figure 3-10 Spot Focusing 46

Figure 3-11 RASOR schematic in one dimension 47

Figure 3-12 Example of time alignment and focusing (a) received signals, (b) time aligned signals, (c) focused signal 49

Figure 3-13: Array and stack of three scanned planes. 51

Figure 3-14 Vehicle mounted Array 52

Figure 4-1 Plane wave propagation 57

Figure 4-2 Near field wave propagation 59

Figure 4-3 The ground probe 63

Figure 4-4 Dielectric measurement set-up 64

Figure 4-5 Variation of signal strength at 1GHz with displacement 64

Figure 4-6 Transmit path spreading loss 70

Figure 4-7 Received path spreading loss 71

Figure 4-8 FDTD model of 8-element linear array 73

Figure 4-9 Lateral focusing through target location. 73

Figure 4-10 Vertical focusing through the target location. 74

Figure 4-11 Example point spread function in one dimension (a) linear amplitude (b) log amplitude 75

Figure 4-12 Example point spread function in two dimensions (a) linear amplitude (b) log amplitude 75

Figure 4-13 Inflection point between air and ground 77

Figure 4-14 Propagation paths from an array to a focusing cell after refraction at the air-soil interface 78

Figure 4-15 Inflected paths 79

Figure 4-16 Horizontal scan through a point scatterer at depth of 300mm for (a) soil permittivity ε_r=3, (b) soil permittivity ε_r=10, (c) soil permittivity ε_r=40 81

Figure 4-17 Vertical scan through a point scatterer at depth of 300mm for (a) soil permittivity ε_r=3, (b) soil permittivity ε_r=10, (c) soil permittivity ε_r=40 82

Figure 4-18 Six modelled surfaces (a) sloping surface in x direction, (b) sloping surface in x and y direction, (c) convex surface, (d) concave surface, (e) lightly undulated, (f) heavily undulated 83

Figure 4-19 Target identification with sloping surface - horizontal slice at depth of 300mm 84

Figure 4-20 Two Elements with no common main beam surface clutter 89

Figure 4-21 Shell of common delay (a) plan view, (b) side elevation 92

Figure 4-22 3D view of shell of common delay 92

Figure 4-23 Common Delay Clutter Locus: (a) side elevation, (b) plan view 93

Figure 4-24 Common delay attenuation variation with varying antenna spacing and ε'=3, ε"=0.1 at depths of (a) 0.2m and λ spacing, (b) 0.2m and 6λ spacing, (c) 0.4m and λ spacing, (d) 0.2m and 6λ spacing, (e) 0.6m and λ spacing, (f) 0.2m and 6λ spacing, ...94

Figure 4-25 Common delay petal shaped clutter area and antennas 95

Figure 4-26 Focal quality weighting function 96

Figure 4-27 Pebbles blocking part of coverage solid angle 97

Figure 5-1 The automated experimental system 103

Figure 5-2 Bowtie element with microstrip feed 106

Figure 5-3 Radiation pattern of the bowtie element at 0.800 GHz co-polar=solid blue, cross-polar=dashed red (a) E Plane (b) H Plane 107

Figure 5-4 Radiation pattern of the bowtie element at 1.2GHz co-polar=solid blue, cross-polar=dashed red (a) E Plane (b) H Plane, blue indicates co-polar, red dash indicates cross-polar 107

Figure 5-5 Input response of bow-tie element 107

Figure 5-6 Four element antenna sub-array (a) projection view (b) plan view.....108

Figure 5-7 Frequency response and mutual couping of four element subarray, (a) return loss of the transmit element, (b) mutual coupling between A and B, (c) mutual coupling between A and C, (d) mutual coupling between A and D 109

Figure 5-8 Radiation pattern of element B in the 2x2 array (a) E plane radiation pattern, (b) H plane radiation pattern. 110

Figure 5-9 Plan view of full RASOR demonstrator array containing twenty-eight bow-tie elements 110

Figure 5-10: Part of the RASOR demonstrator bow-tie antenna array 111

Figure 5-11 Array backplane showing the switching network 112

Figure 5-12 Example switching schematic for a twenty eight element array 113

Figure 5-13 RF switching block diagram 114

Figure 5-14 Column switch schematic 114

Figure 5-15 Column switch circuit diagram layout 115

Figure 5-16 Row switch schematic 116

Figure 5-17 Row switch circuit diagram layout 116

Figure 5-18 RF switch boxes (a) seven way row switch (b) four way column switches 117

Figure 5-19 Array digital switching control box circuit 118

Figure 5-20 Array digital switching control box in situ (with associated cabling) 118

Figure 5-21 Example CPLD digital control logic 119

Figure 5-22 RASOR Switching scheme 120

Figure 5-23 Alternative RASOR Switching Scheme 122

Figure 5-24 Pulse generation circuit 123

Figure 5-25 Example transmit pulse 124

Figure 5-26 Algorithmic Implementation 125

Figure 5-27 Example A scan plot 126

Figure 5-28 FIR bandpass filter (a) Unfiltered averaged A scan signals, (b) Filter kernel - 200 point windowed-sinc with blackman shading, (c) Example filtered and unfiltered signal frequencies along with filter frequency response, (d) Example time domain signal before and after filtering 127

Figure 5-29 Focusing schematic 129

Figure 5-30 Three scan focusing frame 130

Figure 5-31 Data collection timing diagram 131

Figure 6-1 Targets used in experiments 136

Figure 6-2 Indoor experimental facility (a) sand-box dimensions (b) under construction, (c) early antenna array (d) data collection 137

Figure 6-3 Two 10cm^2 metal plates positioned on surface at x=0.3m, y=0.3m and at depth of 0.3m at x=0.8m,y=0.5m with different surface cancellation methods, (a), (c), (e), (g) are horizontal slices at the surface, (b), (d), (f), (g) are horizontal slices at 0.3m depth, (a) and (b) with no average background subtraction, (c) and (d) with median average background subtraction, (e) and (f) with adaptive windowing, (g) and (h) with post processed background subtraction 139

Figure 6-4 Focused background data set used in Figure 6-3 (g) and (h) where (a) shows a horizontal scan at the surface and (b) shows a scan at a depth of 0.3m 140

Figure 6-5 Horizontal plot at surface with median background subtraction showing APM and metal sphere flush buried at x=0.8m, y=0.5m and x=0.2m, y=0.2m respectively and metal sphere buried at x=1.4m, y=0.8m (a) amplitude profile through metal sphere, (b) amplitude profile through APM, (c) amplitude profile through ATM 142

Figure 6-6 Horizontal slice at 0.3m depth through a large APM buried at 0.3m depth, x=1.1m and y=0.6m. 128 pebble objects are present to simulate clutter.....143

Figure 6-7 Protective awning showing raised area of crushed rock 144

Figure 6-8 Inside awning, showing the array backplane, supports, processing/control PC and Infinium sampling oscilloscope 144

Figure 6-9 Close-up of PC showing current set of processed data. 145

Figure 6-10 Vertical scan through a 100mm^2 metal plate buried below the centre of the array at a depth of 0.2m and another 100mm^2 metal plate located on the surface. 146

Figure 6-11 CK APM simulant buried near the centre of the array at a depth of 0.1m and a metal sphere buried at a depth of 0.1m towards the edge of the array (a) horizontal scan at 0.1m (b) vertical scan under the centre of array. 147

Figure 6-12 Vertical scan showing a repeat of the experiment shown in Figure 6-11 after an elapsed time of thirteen days.....148

Figure 6-13 Horizontal scan: Metal sphere on surface at centre.....148

Figure 6-14 Large Colin King APM simulant on surface below centre of array (a) horizontal scan (b) vertical scan 149

Figure 6-15 Large Colin King flush with surface at centre array (a) horizontal scan (b) vertical scan.....149

Figure 6-16 Vertical slice through a TMA-4 buried at a depth of 0.5m. 150

Figure 6-17 Long Ashton experimental set-up 150

Figure 6-18 Inside the tent at Long Ashton 151

Figure 6-19 Metal sphere buried close to the surface at x=0.3 y=0.1 (a) horizontal scan at surface (b) vertical scan through 0.1m.....151

Figure 6-20 Large Colin King APM at depth of 0.1mm x=0.1 y=-0.3 (a) horizontal scan at depth of 0.1m (b) vertical scan at y=-0.3.....152

Figure 6-21 Experimental set-up at DERA Chertsey.....153

Figure 6-22 BLU-61/A/B bomblet (x=-0.3, y=0.2) and PMA-3 (x=-0.1, y=-0.1) buried in London Clay with vegetation with top flush with surface (a) picture of flush buried targets, (b) horizontal scan at -0.05m depth (c) vertical scan through y=-0.15m.....154

Figure 6-23 PMA-3 APM (x=0.05m, y=-0.1m) and VS-50 APM (x=0.4m, y=-0.15m) on surface of loam with vegetation at (a) picture showing target locations (b) horizontal scan at -0.05m depth (c) vertical scan through y=-0.1m.....155

Figure 6-24 TM-57 ATM buried in loam with no vegetation with top flush with surface at x=-0.2m, y=-0.2m (a) horizontal scan at -0.05m depth (b) vertical scan through y=-0.15m.....156

Figure 6-25 TMA-4 ATM buried in loam with no vegetation with top flush with surface at x=0.05m, y=-0.2m (a) horizontal scan at -0.05m depth (b) vertical scan through y=-0.15m.....156

Figure 6-26 PMA-3 buried in vegetation covered loam with top flush with surface at x=0.05m, y=-0.1m (a) horizontal scan at -0.05m depth (b) vertical scan through y=-0.1m.....157

Figure 6-27 Picture of ERA Trial plots.....158

Figure 6-28 Mounting frame.....159

Figure 6-29 ERA trial Set-up.....160

Figure 6-30 Zone 2 map - DTP-MOT.....162

Figure 6-31 Zone 4 results - Ballast.....163

List of Tables

Table 2-1 Dimensions [7] for those mines shown in Figure 2-1 11

Table 4-1 Dielectric properties of example soil types at 1.5GHz 63

Table 4-2 Summary of system degradation for different surface types 85

Table 6-1 Dimensions and contents of ERA soil plots 158

List of Principal Symbols

E	Electric Field Intensity
H	Magnetic Field Intensity
ε_o	Permittivity of free space
ε_r	Relative permittivity
μ_o	Permeability of free space
μ_r	Relative permeability
$\tan \delta$	Loss tangent
σ	Conductivity
λ	Wavelength
ω	Angular frequency
η	intrinsic impedance
r	Reflection
σ^o	Target Radar Cross Section
f	Frequency
w	Weighting factor
s	Signal
t	Time

List of Abbreviations

ADC	Analogue to Digital Converter
AM	Amplitude Modulation
APM	Anti-Personnel Mines
ATM	Anti-tank Mines
CPLD	Complex Programmable Logic Devices
CW	Continuous Wave
EMI	Electromagnetic Induction
FAR	False Alarm Rate
FM	Frequency Modulation
FM-CW	Frequency Modulated Continuous Wave
GPR	Ground Penetrating Radar
JTAG	Joint Test Action Group
NQR	Nuclear Quadrupole Resonance
PD	Probability of Detection
PFA	Probability of False Alarm
PRF	Pulse Repetition Frequency
PSF	Point Spread Function
RADAR	Radio Detection and Ranging
RASOR	Real Aperture Synthetically Organised Radar
RCS	Radar Cross Section
RF	Radio Frequency
ROC	Receiver Operator Characteristic
SAR	Synthetic Aperture Radar
SCR	Signal to Clutter Ratio
SLAR	Side Looking Radar
SNR	Signal to Noise Ratio
SONAR	Sound Navigation and Ranging
SPR	Surface Penetrating Radar
UHF	Ultra High Frequency
VHF	Very High Frequency

List of Publications

R. Benjamin, I. J. Craddock, G. S. Hilton, S. Litobarski, E. McCutcheon, R. Nilavalan, . 'Microwave Detection of Buried Mines using Non-Contact, Synthetic Near-Field Focusing', *IEE Proceedings of Radar, Sonar and Navigation*, Vol.148 No.4, pp233-240, Aug 2001

I.J.Craddock, E.McCutcheon, R.Benjamin, G.Crisp, 'Demonstration of the detection of buried mines with Real Aperture Radar', *Subsurface Sensing Technology and Application*, Vol.2 No.3, pp273-283, July 2001

R.Benjamin, G.Hilton, S.Litobarski, E.McCutcheon, R.Nilavalan, 'Post-Detection Synthetic Near Field Focusing in Radar or Sonar', *Electronics Letters*, Vol.35 No.8, pp664-666, 1999

R.Benjamin, G.Hilton, S.Litobarski, R.Nilavalan, E.McCutcheon, 'Synthetically-Focused Surface-Penetrating Radar for Operation from a Moving Vehicle', *Proceedings of the Second International Conference on Detection of Abandoned Land Mines*, IEE, pp60-63, Edinburg, UK, October 1998

R.Benjamin, I.J.Craddock, E.McCutcheon, R.Nilavalan, 'Through-Wall Imaging using Real-Aperture Radar', *Proc. USRI General Assembley*, Aug 2002

1 Introduction

The possibility of harnessing technology to allow us to observe objects that are hidden from the human eye has interested engineers and scientists from the earliest times. From telescopes to X-ray machines, humans have wanted to see further or to see what is hidden. It is known that animals such as scorpions, bats and whales use sound waves to navigate and detect prey and there is some evidence to suggest that migratory birds use a form of magnetic detection to reach their breeding grounds. Humans lack these direct abilities, but they do possess endeavour, reasoning and ingenuity. With these it has been possible to develop a wide range of detection technology using phenomena such as infrared, sound waves, alpha waves, seismic waves and, the subject of this thesis, electromagnetic waves in what has come to be known as Radar (Radio Navigation and Ranging) [1].

The first use of electromagnetic waves for detecting metal objects is attributed to Christian Hülsmeyer [2] who in 1904 lodged a German patent for a 'telemobiloskop' that could detect ships at a few hundred meters. The principle motivation for Radar development through the earlier twentieth century was for military air defence [3]. Its first large-scale practical application came in the UK's Chain Home system which, during the Battle of Britain in 1940, provided crucial early warning of incoming long range heavy bombers [4]. A major technical advance around this time was the development of the high power cavity magnetron [5] which allowed Radar to move up from VHF frequencies (100 to 200MHz) into the microwave region (>1GHz). At these frequencies antennas can be made much smaller and this opened up a wide range of new applications.

Since World War II technology improvements and innovations have meant that Radar systems continue to play an important role in both military and commercial environments. The major advances since the war can been summarised [6] as:

- the universal replacement of the magnetron with the more stable high-power Klystron amplifier,
- the use of Doppler Frequency Shift principles for moving target detection, terrain mapping and weather observation,
- the introduction of digital techniques which have significantly enhanced the scope and breadth of radar functionality that can be realised.

Today there is now a very wide range of different radar applications and many possibilities seem to exist for future developments. One area that still has unexplored potential and scope for improvement is in the use of Radar to accurately detect buried underground objects. This application is usually termed Ground Penetrating Radar (GPR) or Surface Penetrating Radar (SPR) and this thesis will examine a novel GPR approach suitable for, but by no means limited to, detecting buried anti-personnel and anti-tank landmines.

An early description of the use of electromagnetic waves to detect buried objects is given in a German patent lodged in 1911 by Lowy [7]. This describes how antennas could be placed at the surface of soil and, by emitting a continuous wave (CW), the reflections would indicate the depth of a buried interface. Later in 1926 Hülsenbank [8] proposed a pulsed technique to detect buried features and the use of radar for mapping through geologic materials was first carried out by Stern in 1930 [9].

Little further advancement was made for around 30 years [10] until renewed interest in subsurface imaging in geophysics and for lunar expeditions resulted in the development of custom devices for specific investigations and also in the availability of the first commercial analogue GPR systems [11]. Applications at this time focused on measuring ice thickness [12] [13] [14], mapping bedrock structures [15] [16], the probing of rock formations, desert sand, salt and coal deposits [17] [18] [19] and the detection of utilities [20].

Since the 1970s the range of applications has steadily increased [21] and the introduction of digital techniques, as with conventional Radar, has increased the potential by enabling more complex processing opportunities combined with smaller and/or lighter physical designs. Examples of more recent applications of SPR include:

- target specific detectors such as in mine detection [22], utilities detection [23] [24] and medical tumour scanning [25],
- non-invasive examinations of buildings [26] and roads [27] including concrete structure examination [28],
- remote sensing of terrestrial [29] and extra-terrestrial [30] terrain sub-structure.

- security applications [31]

1.1 The Aim of the Thesis

An area of much research interest is in the detection and clearance of unexploded ordinance, particularly buried anti-personnel mine (APM) and anti-tank mines (ATM). Abandoned landmines are a significant humanitarian problem today with millions thought to have been deployed world-wide [32] and continuing to be deployed at a rate faster than they are cleared. Typically 50-150mm in diameter and sometimes with very low metal content, these devices are difficult to find and methods of improved detection and clearance are required [33].

This thesis describes the development, analysis and experimental results obtained from a novel GPR developed for detecting buried land mines. The proposed system has a vehicle-mounted two-dimensional antenna array suspended over the ground and uses synthetic time domain focusing. The aim of the research was to develop the concept from theoretical principles into a demonstrator system capable of detecting buried landmines of different types and in different soil conditions.

Many GPR systems are designed to operate with antennas in contact with the ground in order to minimise the air-ground interface reflections, but one of the great advantages of GPR, compared with some other sensors, is its ability to operate in non-contact mode. In brief this is possible because the relative *electrical* contrast between air and soil tends to be very much less than, for example, the relative *acoustic* contrast experienced in seismic surveying. Non-contact operation means that GPR surveying and sensing is often most convenient and for some applications, such as landmine detection, it is considered essential. However, there are non-trivial difficulties with non-contact operation particularly when the target is very close to the surface, as is usually the case with landmines, due to the large surface reflection.

Remote sensing radars traditionally use side-looking radar (SLAR) and these can be separated into two types, real aperture radar and synthetic aperture radar [34]. Real aperture radar uses a single large antenna usually mounted on a satellite or aircraft. Electromagnetic pulses are transmitted at right angles to the flight direction and downward towards the earth where they are reflected back in many directions including

the antenna direction. The time at which these scattered reflections arrive back at the antenna determines the distance to the scattering object on the ground. The bandwidth determines the resolution in the direction of flight, or range resolution, and the aperture length determines the resolution in the direction parallel to the flight direction, generally termed cross-range or azimuth resolution. Synthetic aperture radar, developed as an improvement to real aperture radar, utilises the Doppler spread of an echo signal to synthesise a much larger aperture and greatly improve the azimuth resolution of SLAR [35]. A single antenna is moved to a series of positions, usually by vehicle motion, to achieve this large aperture and the slight speed difference between two points on the ground in the azimuth direction relative to the antenna provides the required Doppler shift.

The technique of synthesising an aperture has been extended to other sensing devices such as synthetic aperture sonar and particularly in ultrasonics where it has been very successful in medical imaging. Here though the Doppler spread is not used, indeed it is usually assumed that the target is stationary relative to the synthesised array during any data gathering period. Short wideband pulses are transmitted and received from a number of transducer positions and in effect a real aperture is synthetically organised. A range of methods have been developed for ultrasonics such as synthetic aperture focusing technique (SAFT) [36], multi-element synthetic aperture focusing (M-SAF) [37] and synthetic receive aperture (SRA) [38].

The ideas developed in this thesis take some of the ultrasonic focusing principles and apply them back into the radar domain, and was originally proposed by Benjamin [39]. A two dimensional real aperture antenna array sequentially transmits and receives from pairs of antennas and uses post-reception near-field time-domain focusing to image a three dimensional space in front of the array. The technique has been christened Real Aperture Synthetically Organised Radar (RASOR). Professor Benjamin and the University of Bristol successfully registered a patent for the idea [40] and the UK Defence Evaluation and Research Agency (DERA) funded a research program to work up the concept into a demonstrator system.

This thesis describes the author's key contribution to that research program, which can be broadly summarised as follows:

- Analysis and modelling of the GPR system concepts including an assessment of the operating environment such as soil types, target types, clutter limits, noise limits and de-correlating effects in order to postulate suitable array configurations, mounting arrangements and processing algorithms.
- Derivation, implementation and experimentation with new algorithms to deal with the problem of surface reflections and other clutter effects.
- Definition of system parameters such as operating frequency, power and array size and configuration in order to deal with the operational environment based on modelling and early experimentation.
- System design including the design of RF and digital circuits and control software and the implementation of processing algorithms for a real time system.
- Devising, organising and conducting experiments to verify analytical studies and assessment of the measurement results.

1.2 Thesis Structure

The thesis is comprised of seven chapters and is structured as follows:

Chapter 2 looks at the main application for this system, namely land mine detection. It provides an overview of the land-mine problem and describes current and proposed methods for their detection and disposal. The challenges of the target detection problem are introduced and Radar sub-surfacing probing is contrasted with other detection techniques.

Chapter 3 describes the hardware and processing that make up a generic GPR system and describes alternative implementations. A brief introduction to RASOR is given with an outline of the theoretical concepts highlighting their advantages in comparison with other ground penetrating radar techniques.

Chapter 4 is an important part of the thesis. It develops the RASOR system concept more rigorously using analytical modelling and early concept proving experiments in a controlled environment. Novel solutions are introduced for the reduction of clutter, arguably the most challenging aspect of ground penetrating radar.

Chapter 5 describes how the system characteristics and design trade-offs described in chapter 4 were applied in the construction of a demonstrator system. This covers antenna design and FDTD modelling, antenna array design, pulse generation, digitisation, data acquisition and algorithm implementation. Possible mounting arrangements are also considered.

Chapter 6 presents the results from experiments carried out in an indoor test facility and at a range of outdoor test sites and discusses the findings.

Chapter 7 provides a closing discussion and draws conclusions from the work. Other applications to which the RASOR technique is suited are introduced such as medical imaging, security applications, archaeological surveying and production line screening. Further developments are suggested that could be addressed as part of continuing research.

References

[1] M.Skolnik, 'Radar Handbook', McGraw-Hill, New York, 1990.

[2] C.Hülsmeyer, 1904, German Patent Number 165546

[3] S.S.Swords, 'Technical history of the beginnings of radar', Peter Peregrinus, London, 1986

[4] H.E.Guerlac, 'Radar in World War II', Tomash, American Institute of Physics, 1987

[5] R.Budari, 'The invention that changed the world', Simon & Schuster, 1996

[6] M.Skolnik, 'Opportunities in Radar - 2002', Electronics & Communications Journal, pp 263-272, December 2002.

[7] H.Lowy, 1911. German Patent Number 254517

[8] Hülsenbenk, 1926. German Patent Number 489434

[9] W.Stern, 'Principles, methods and results of electrodynamic thickness measurement of glacier ice', Zeitschrift fur Gletscherkunde, Vol. 18 No. 24., 1930

[10] D.J.Daniels, 'Surface Penetrating Radar', IEE, 1996, Chapter 1

[11] R.M.Lerner, 'Ground Radar System', United States patent #3831173.

[12] B.O.Steenson, 'Radar methods for the exploration of glaciers', PhD thesis, California Institute of Technology, Pasadena, California, 1951

[13] S.Evans, 'Radio techniques for the measurement of ice thickness', Polar Record, Vol. 11, pp 406-410, 1963

[14] C.R.Bentley, J.W.Clough, K.C.Jezek, S.Shabtaie, 'Ice thickness patterns and the dynamics of the Ross Ice Shelf, Antarctica', J.Glaciology, Vol. 24, pp 287-294, 1979.

[15] J.C.Cook, 'Radar exploration through rock in advance of mining', Transactions of AIME, Society of Mining Engineers, Vol. 254, pp 140-146, 1973.

[16] J.C.Cook, 'Radar transparencies of mine and tunnel rocks', Geophys.,Vol. 40, pp8 65-885, 1975.

[17] R.R.Unterberger, 'Radar and Sonar probing of salt', 5th international symposium on Salt, Hamburg, Northern Ohio Geological Society, USA, pp 423-437, 1978.

[18] P.K.Kadaba, 'Penetration of 1GHz to 1.5GHz electromagnetic waves into the earth surface for remoting sensing applications', Proc. Of IEEE SE region 3 conference, pp 48-50, 1976.

[19] J.C.Cook, 'Borehole-radar exploration through rock in a coal seam', Geophys., 42, pp1254-1257, 1977.

[20] R.M.Morey, 'Detection of subsurface cavities by ground penetrating radar', Highway Geological Symposium, 27, pp 28-30, 1976.

[21] D.J.Daniels, 'Surface Penetrating Radar', IEE, 1996, Chapter 7.

[22] S.Abrahamson, B.Brusmark, G.Gaunard, H.C.Strifors, 'Target identification by means of impulse radar in SADJADI', Proc.SPIE, Vol. 1471, pp130-141, 1991

[23] R.Caldecott, M.Poirier, D.Scofea, D.E.Svoboda, A.J.Terzuoli, 'Underground mapping of utility lines using impulse radar', IEE Proc. F. Communications, Radar and Signal Processing, Vol 135, pp 343-361, 1988.

[24] N.Osumi, K.Ueno, 'Detection of buried plant', IEE Proc. F. Communications, Radar and Signal Processing, Vol 135, pp 330-342, 1988

[25] E.J.Bond, 'Microwave imaging via space-time beamforming for early detection of breast cancer', IEEE Trans. Ant. Prop.,Vol. 51 No. 8, pp 1690-1705, Aug 2003.

[26] R.C.de Vekey, 'Non-destructive test methods for masonry structures', Proceesings of the 8th IBMAC conference, Vol. 3, 1673, 1988

[27] R.C.Ransome, J.T.Kunz, 'Non destructive detection of voids beneath pavement', Publ. Works, 52-54, 1986

[28] M.R.Shaw, et al, 'A large diameter transmission line for the measurement of the relative permittivity of construction materials', Br. J. Non-Dest. Test., Vol. 35 No.12, 696-704, 1993

[29] G.G.Schaber, et al, 'Shuttle imaging radar: physical controls on signal penetration and subsurface scattering in the Eastern Sahara', IEEE Trans. GE-24, 4, pp603-623, 1986

[30] Y.Barbin, 'MARS 96 GPR program', J. Appl. Geophys., 33, pp27-37, 1995

[31] E.F.Greneker, 'Radar sensing of heartbeat and respiration at a distance with security applications', Proc SPIE: Radar Sensor Technology II, Vol 2066, pp22-27, April 1997

[32]US Department of State, 'Hidden Killers: The Global Landmine Crisis', Report to US Congress, 1994.

[33] P.M.Blagden, 'The changing scene of mine clearance', 2nd International conference on the detection of abandoned land mines, Edinburgh, UK, October 1998, pp19-22.

[34] F.W.Ulaby, et al, 'Microwave Remote Sensing: from theory to applications', Artech House, 1986

[35] G.W.Stimson, 'Introduction to Airborne Radar', Sci-tech Publishing, New Jersey, 1998

[36] K.Mayer, R.Marklein, K.J.Langenberg, T.Kreutter, 'Three-dimensional imaging system based on Fourier transform synthetic aperture focusing technique', Ultrasonics, Vol. 28, pp 241-255, July 1990.

[37] M.Karaman, P.Li, M.O'Donnell, 'Synthetic aperture imaging for small scale systems', IEEE Trans. Ultrason. Ferroelec. Freq. Contr., 42, pp 429-442, 1995.

[38] G.E.Trahey, L.F.Nock, P.D.Freiburger, D.C.Kaelber 'A system for high resolution ultrasonic breast imaging', Proceedings of the Annual Conference on Engineering in Medicine and Biology, Vol. 13 No.1, pp133-135, 1991

[39] R.Benjamin, 'Near-field spot-focused microwave sensing for the detection of buried land-mines', IEE/EUREL Conference on the Detection of Buried Land-Mines, Edinburgh, UK, pp133-137, October 1996

[40] R.Benjamin: 'Post-Reception Focusing In Remote Detection Systems', US patent 5,920,285, 6/7/99.

2 The Landmine Problem

It has been estimated that over 100,000,000 landmines have been laid in over 60 countries - and new ones are still being laid faster than old ones are cleared [1]. There remains some controversy around this estimate [2], but it can not be denied that landmines present a large humanitarian problem in the world today. These devices litter the world's conflict areas often rendering agricultural land unusable for local civilian populations who can ill afford to lose it. Roughly every twenty minutes one person somewhere in the world is killed or injured by a landmine [3].

2.1 Brief History of Landmines

Modern landmines are explosive devices, but their history can be traced back to non-explosive predecessors such as spikes and stakes used by armies as far back as 2,500 years ago [4]. The earliest explosive landmines appear to have first been developed around 1530 in Sicily and were known as *fougasses*. These were in effect underground cannon that could shower rocks and debris on the enemy. Detonation was achieved by lighting a powder trail and consequently they tended to be unreliable due to the effects of rain, wind and moisture.

Pressure-detonated mines were first described in 1726 by H. Frieherr von Dlemming, but did not become regularly used in warfare until the latter part of the 19th century when electrical initiation provided improved reliability and instant firing. The Americans were the first nation to use landmines operationally particularly in the American Civil War. Indeed in 1960 five landmines were recovered almost one hundred years after they were laid and deemed to be still of some danger demonstrating the ability of these devices to remain lethal long after the conflict has ceased.

By the 20th century landmine warfare was used by most armies, but only began to appear on a large scale in 1918 as a weapon against armoured tanks commonly known as Anti-Tank (AT) mines. By the time of the Second World War Anti-Personnel (AP) mines were developed primarily to prevent enemy soldiers from removing AT mines. A number of technical innovations were introduced during this period including the introduction of non-metallic mines, e.g. bakelite or wood, which were difficult to detect using metal detectors [5].

Their use at this time was still generally well controlled and aimed in the main at achieving military objectives. However, there remain areas of Europe and North Africa in particular where Second World War mines still claim the land. Since World War II landmine proliferation has run out of control [6] and it is estimated that 400 million mines have been laid since 1939 with 65 million laid in the last 20 years [4].

2.2 Modern Landmines

There are hundreds of designs of AT and AP mines in existence employing a range of deployment and detonation techniques and constructed from a variety of materials. They can generally be classified as "blast" or "fragmentation" [5]. Blast mines are buried at shallow depths and are triggered by pressure from a person or vehicle. Their casings can be made from plastic, wood or sheet metal. Fragmentation mines disseminate fragments radially outwards and can be lethal up to as much as 100 metres. They are mounted on stakes or trees although some are buried and propelled out of the ground before exploding. They are almost always made from steel. Figure 2-1 shows pictures of some typical devices commonly found in modern conflict zones [7]. Their dimensions are summarised in Table 2-1.

The VS-50 shown in Figure 2-1 (a) is a scatterable AP mine containing 42grams of RDX explosive and consists of a plastic body and predominately plastic detonator. Its metallic content is very low, approximately 0.86 grams of non-magnetic metal [7][8].

The TMA-4 (Figure 2-1 b) and TM-57 (Figure 2-1 c) are examples of AT mines. The TMA-4 is of plastic construction with 3 Bakelite detonators (the yellow towers) and contains 5.5kg of TNT. The TM-57 is constructed from thin sheet metal containing 7kg of TNT [7][8].

PPM-2 (Figure 2-1 d) and PMA-3 (Figure 2-1 e) are AP blast mines. The PPM-2 has a plastic casing with a metal detonation mechanism and a 110grams TNT payload. The PMA-3 is again plastic with rubber seals and contains 35gr of TNT. It has a very low metallic content. The M16A2 (Figure 2-1 f) is an example of a fragmentation AP type mine with a cast iron body containing the main charge of 590grams. When operated it is

propelled out of the ground detonating at 1.2m above it with a casualty radius of 30m [7][8].

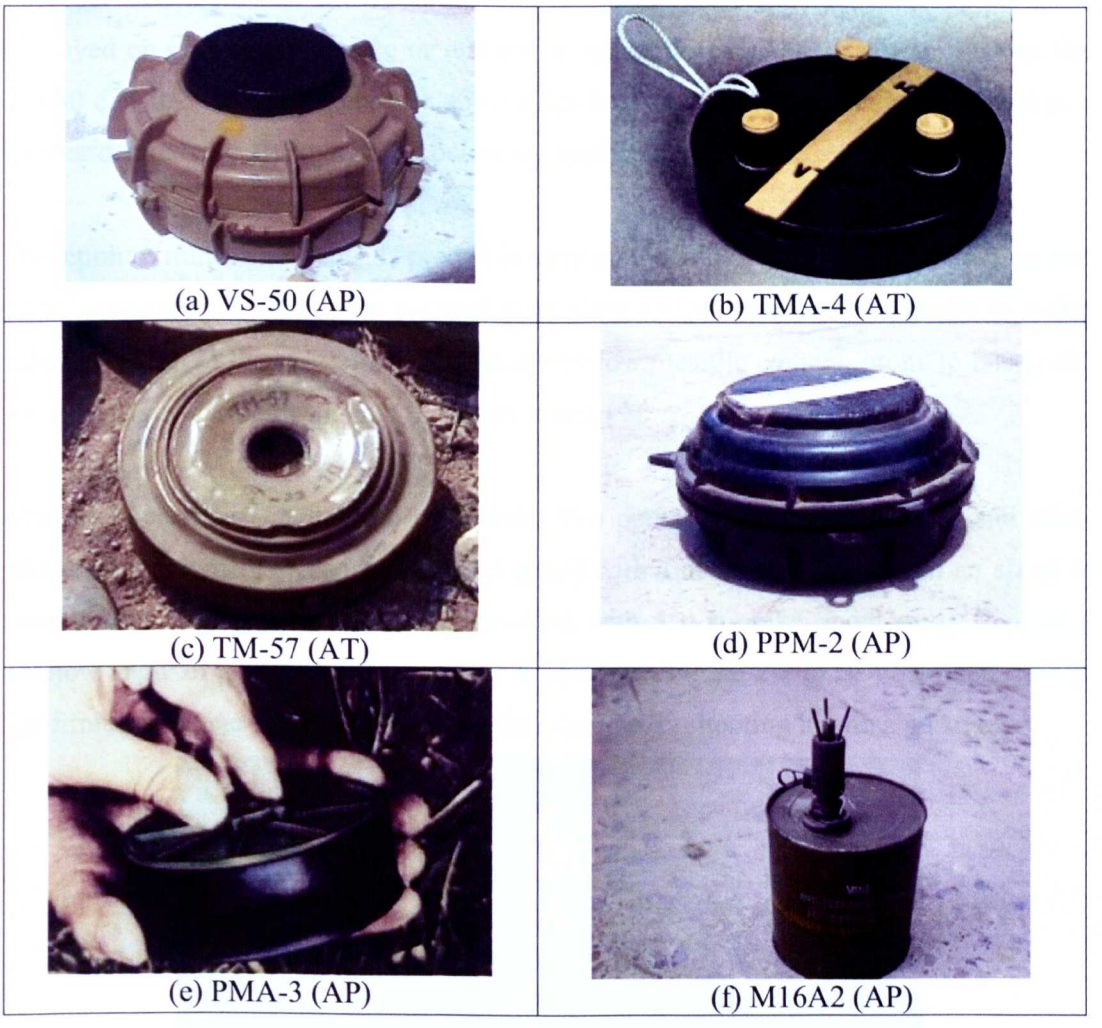

(a) VS-50 (AP)

(b) TMA-4 (AT)

(c) TM-57 (AT)

(d) PPM-2 (AP)

(e) PMA-3 (AP)

(f) M16A2 (AP)

Figure 2-1 Examples of modern landmines (a) VS-50, (b) TMA-4, (c) TM-57, (d) PPM-2, (e) PMA-3, (f) M16A2 (reproduced from [7])

Mine Type	Height	Diameter
VS-50	45mm	90mm
TMA-4	65mm	208mm
TM-57	100mm.	300mm
PPM-2	63mm	125mm
PMA-3	36mm	103mm
M16A2	203mm	103mm

Table 2-1 Dimensions [7] for those mines shown in Figure 2-1

2.3 Detection Techniques

Most AP mines are laid either manually or scattered from helicopters and are normally deployed on the ground surface or just below typically 0 to 200mm. Some, such as the VS-50 can also be laid underwater up to a depth of 1m. AT mines can be deployed to a greater depth, typically up to 0.5m below the surface.

Detection of mines still depends predominantly on a combination of manual probing and metal detectors. The former is painstakingly slow and the latter can be prone to either false alarm, or, in the case of mines with a very low metallic content, prone to false safe, i.e. mistakenly declaring an area free from mines [9].

The usual clearance method is as follows. The operative wearing a helmet and other protective equipment sweeps the ground ahead with a metal detector. When an alarm is sounded the ground ahead is gently prodded with a thin spike about every 2cm at a shallow angle of around 30 degrees [10] as shown in Figure 2-2 [11]. When detection is confirmed the mine is detonated in-situ, for example by shooting it with a gun.

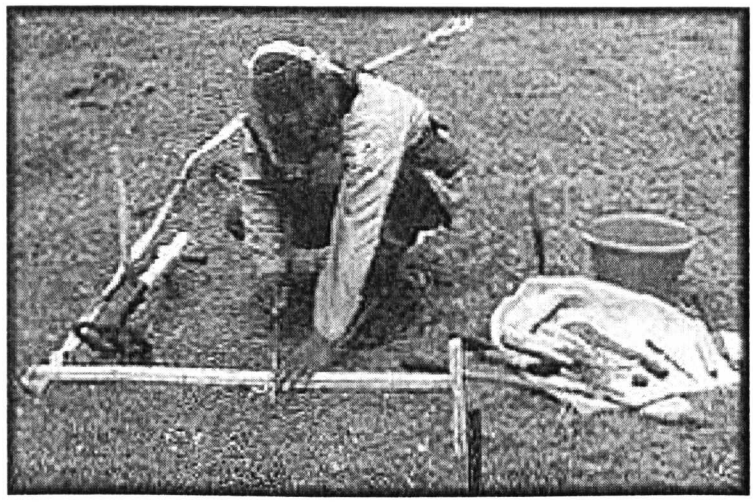

Figure 2-2 Prodding Technique (reproduced from [11])

In certain rough terrain conditions, such as that shown in Figure 2-3 below, deployment of more sophisticated detection equipment is extremely difficult and in these circumstances prodding is virtually the only viable *ground based* detection and neutralisation technique [12]. Obviously, this is an extremely hazardous process both for the operators and their colleagues. Sometimes the mine will have turned on its side causing the prodder to hit the pressure plate rather that the side resulting in accidental

detonation. The operator fatigues quickly in this stressful situation. This is exacerbated by the necessary but cumbersome helmet and protective clothing.

Figure 2-3 Prodding in rough terrain (reproduced from [12])

Often modified armoured vehicles are used to clear areas by deliberately detonating mines prior to prodding. This brute force method requires no sensors, only a driver with nerves of steel. Chains, flails and ploughs have all been used. A flail example is shown in Figure 2-4. This method is not suited to rough terrain and any mines that are missed are afterwards more difficult to detect because of the scattering of exploded ordinance and ground churning that has taken place. It is generally used for quick clearance for military access.

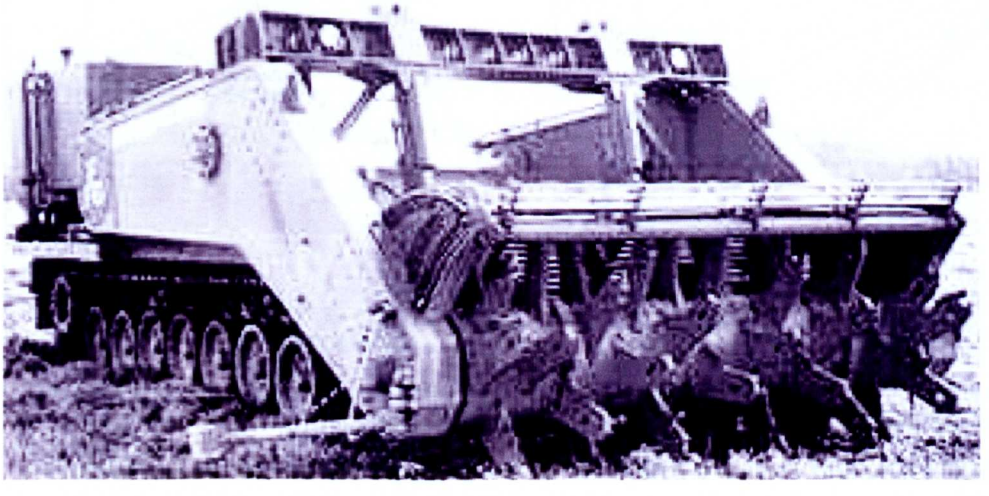

Figure 2-4 Mechanical flail for land mine detonation (reproduced from [11])

Although these techniques are the standard clearance methods they do not guarantee an exhaustive clearance, i.e. a high probability of detection (PD). The remainder of this

chapter describes a number of alternative detection techniques that have been proposed for improving the rate of clearance, whilst either maintaining the PD or decreasing the probability of false alarm (PFA) or, ideally, both.

2.3.1 Signal Detection Theory

It is usual in detection theory to quantify the balance between PD and PFA in a Receiver Operating Characteristics (ROC) curve [13] [14]. ROC curves are plotted with either the PFA or False Alarm Rate (FAR) along the horizontal axis and the PD along the vertical axis. Calculation of PFA requires the an assessment of how many false alarms could of occurred, which in practice can be difficult. It is more practical in empirical studies to measure FAR because it expresses the number of false alarms per unit area or unit time.

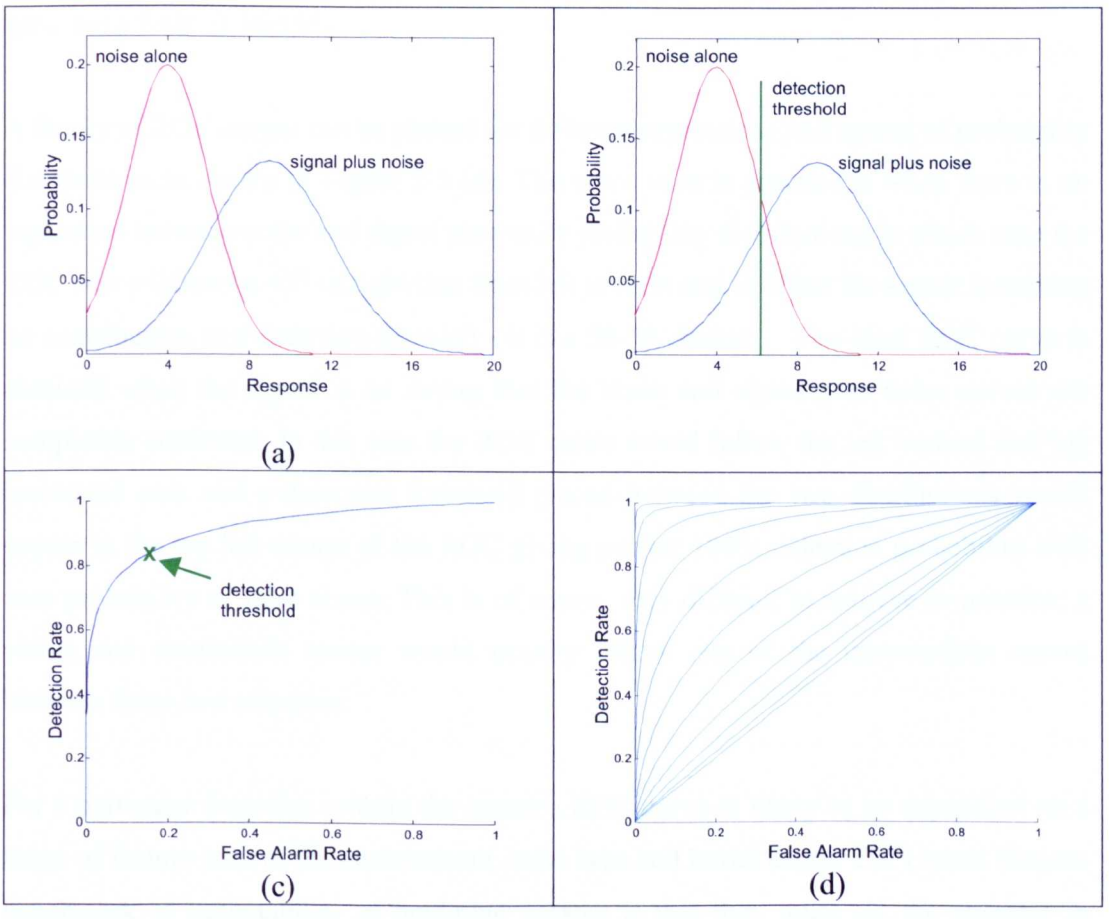

Figure 2-5 Sensor response probability density functions an ROC curves (a) Probability distributions for noise and noise plus signal (b) threshold detection level added, (c) ROC curve for (b) with threshold point indicated (d) family of ROC curves

For example, Figure 2-5 (a) shows two hypothetical probability density functions both with a Gaussian distribution, but with different mean and standard deviation. The red

solid curve gives the observed system response for trials containing noise only, i.e. with no targets present. The blue dashed curve gives the system response for trials containing signal plus noise, i.e. with a target present. If a vertical threshold line were drawn on the plot at an arbitrary point on the response axis as shown in Figure 2-5 (b), the area under the noise only curve that lies above this threshold would give the probability of false alarm. The area under the signal plus noise curve that lies above this threshold would give the probability of correct detection. Repeating this for all possible threshold values gives the ROC curve shown in Figure 2-5 (c). For given noise and noise plus signal distributions, a threshold can then be selected that most closely meets the required PD and FAR by judging at what point it appears on the ROC curve. The threshold shown in Figure 2-5 (b) is marked as a cross on the ROC curve in Figure 2-5 (c) giving a PD of 80-85% and a FAR of 10-15%.

A family of ROC curves can be plotted for different separations and spread of probability distributions as shown in Figure 2-5 (d). The worst case in practice is when there is no separation between noise and signal plus noise probability distributions in which case the ROC curve follows a 45° straight line from left to right and in effect the sensor is making no contribution to a detection decision - it is a 50-50 choice. The ideal ROC curve is obtained when the signal is so strong that the noise and signal plus noise curves are completely separated. In this case the ROC curve would follow the left vertical and top horizontal axis and a detection threshold placed between the two distributions would appear in the top left corner of the ROC giving perfect 100% detection probability with zero probability of false alarm. This is of course very difficult to achieve in practice; a viable and worthwhile sensor would usually follow one of the intermediate curves between these two extremes.

For a particular detection criteria the sensor's ROC curve is likely to be dependent on a range of factors such as the environment, mine type and burial depth. The United Nations benchmark of acceptability of landmine sensors is that they must aid the operator in achieving a 99.6% to 99.9% PD [15] whilst reducing FAR. Currently FAR results have been known to rise as high as 1000:1, i.e. 99.9% chance of a false alarm [16] making overall clearance rates very slow. Achievable improvements in this rate are difficult to quantify due to the lack of large-scale measurements with alternative technologies and any result will have a strong dependence upon the terrain and type of mine being

detected. However it is considered unlikely that order of magnitude improvements in false alarm rates will be achievable in the short term. It has been estimated that an improvement of 50% in FAR rates could improve clearance rates by between 30-60% [17].

2.3.2 Alternative Detection Approaches

Approaches to detection techniques can be broadly categorised into three general areas:

- Localised detection
- Vehicle mounted detection
- Wide area detection

Local detection covers hand held devices, such as metal detectors and other on-ground detection such as sniffer dogs. Vehicle mounted detection covers classes of sensors that, either through necessity or convenience, require some stand-off distance from the ground. These detectors are suited to detecting and marking landmines for military reconnaissance and to detect the leading edge of mine fields [18]. Wide area detection implies a stand-off capability, for example mounted on satellites, aircraft or dirigibles, that is capable of rapidly surveying large areas of land.

Some technology such as GPR can be adapted to suit all three types of approach whereas others are limited or best suited to maybe one or two of the categories. The remainder of this chapter describes the alternative detection technologies that have been proposed and discusses their relative merits.

2.3.3 Metal Detectors

As has already been mentioned metal detectors - also known as electromagnetic induction detectors (EMI) - already form part of the de-miners basic tool kit. The technology is very mature and consists of a transmit oscillator, search coil, a receiver amplifier and a discriminator [19]. A basic block diagram is shown in Figure 2-6.

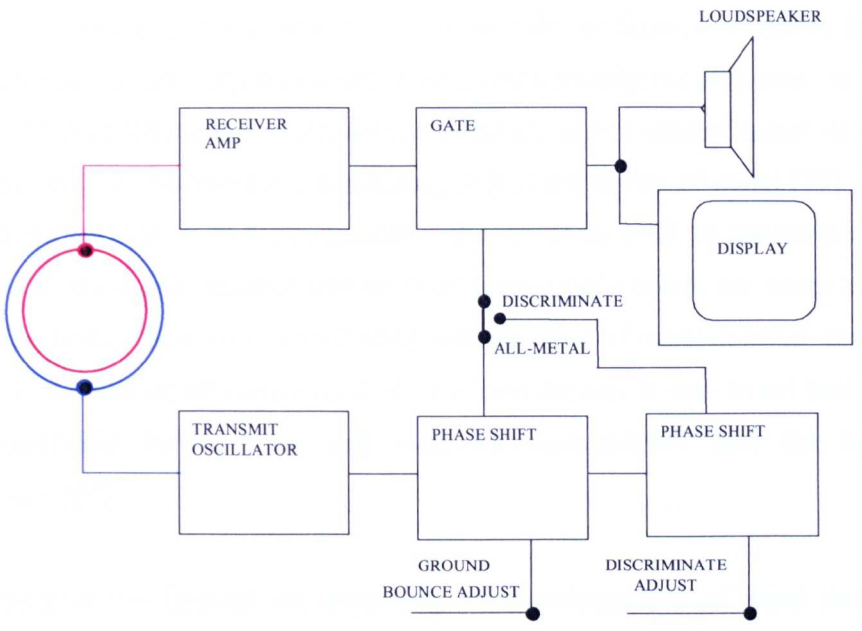

Figure 2-6 Block diagram of Electromagnetic Induction system

Eddy currents in the metal target by the transmit coil cause a secondary magnetic field to be set-up, which is then detected by the receive coil as shown in Figure 2-7. When the induced level crosses a pre-set threshold level, an alarm is generated. The frequency range employed is usually limited to a few tens of KHz [19].

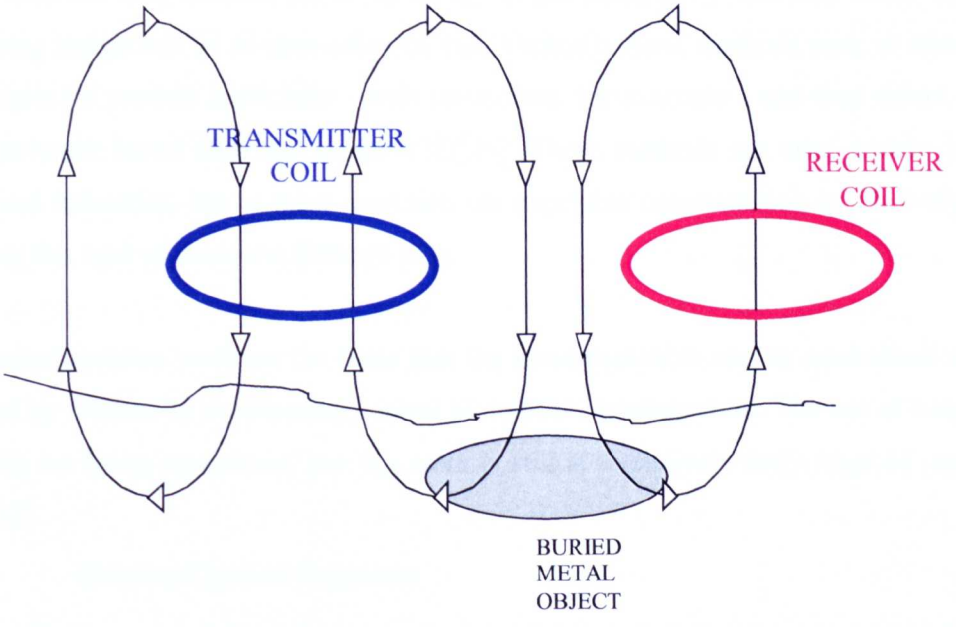

Figure 2-7 Transmission and detection of an induced magnetic field

The basic problem of metal detectors is their inability to distinguish mines from other metal debris such as cartridge cases, drinks cans and naturally metallic rock. In theory all mines can be detected since they all contain *some* metal and modern metal detectors are sufficiently sensitive to landmines containing only a few grams of metal [20]. However, increasing the sensitivity to have maximum PD increases FAR to unacceptable levels. Often, de-mining teams uncover 100 to 1000 inert metal objects for every mine [21]. Probabilities of detection vary considerably with the type of metal detector, location and soil type. In a study of 29 commercial off the shelf sensors it was found that there is a strong correlation between the soil magnetic susceptibility and the operational performances [22].

Recent attention has focused on improving the discrimination of metal detectors by measuring how the eddy currents evolve over time to ascertain the magnetic 'polarisability' of the target [23] [24], but the state of the art is still very immature [25].

2.3.4 Biological Sensors and Systems

Dogs and even pigs can be trained to detect the presence of explosives inside the mine since they have a keen sense of smell, far more sensitive than humans [26]. However, animals tend to tire quickly, their reliability is low and the location accuracy is relatively poor; they can also detonate mines in the act of searching [27]. Artificial odour sensors are being researched as an alternative to this. Typically these methods seek to stimulate the explosive particle artificially - with ultrasound, for example - and then detect them with polymer based chemical sensor [28][29]. These methods are used widely in the chemical industries, but in mine detection the expolsive concentration is relatively low making this type of detection difficult [30].

Biological systems work on the basis that the mine explosive can be neutralised in the ground by artificially accelerating natural biological decomposition. The use of bees and bacteria are being researched, but this work is still at a relatively early stage of research [31][32].

2.3.5 Electro/Optical Sensors

Electro/Optic sensors is the name given to devices which detect electromagnetic radiation in the infra-red and hyperspectral bands. Detection techniques can be summarised as passive thermal, active thermal, passive non-thermal and active non-thermal [33].

Thermal detection seeks to exploit the fact that buried mines will generally have different thermal properties than the surrounding ground thus they retain or dissipate heat at a different rate. This can be induced either passively [34], relying on solar warming, or actively through the use of high power microwave [35] or optical sources [36]. Thermal sensors measure the resulting infra-red radiation and seek to distinguish the mines from the soil.

The soil variation can come from the mine itself or the soil disturbance from the act of burying the mine. Hyperspectral techniques seek to detect this soil disturbance either passively [37], again relying on the solar heating, or actively using Lasers [38].

These techniques are very prone to error in unstable weather conditions and rely on a local knowledge of the soil properties for calibration. Even in good weather conditions it is only usually practical just after dusk or before sunrise - due to the rate of solar heat gain/heat loss and solar interference with the equipment - and is only useful for wide area detection, i.e. at large stand-off distances to detect dangerous areas, but not individual mines [33]. However, in this case local information about the ground structure may not be available. A further disadvantage for the active types is that a relatively long exposure time (of around 12 minutes) is required before measurements can be taken [36] and this, combined with a need for a very high source level, is potentially harmful to humans.

2.3.6 Computed Tomography

Computed tomography, where the word *tomography* means "a picture in a plane", is used in a number of forms for applications such as optical inverse scattering [39], medical imaging [40] and geophysics [41]. Generally this method uses an array scanning system, in the case of geophysics typically a manually scanned pair of transducers.

The basic idea is that a propagation model is assumed to solve the inverse problem on the acquired data in order to find the position and shape of scattering sources in the search space. In practice it assumed that the received data consists of a convolution of the transmitted wave and the object distribution in the subspace with the Greens function for a homogenous background [42].

The diffraction tomography method usually assumes a loss-less medium and ideal point sources and scatterers and also usually assumes a resolution that is much smaller than the objects that are being detected. Unfortunately none of these can be guaranteed for landmine detection in soil.

2.3.7 Electrical Impedance Tomography

This method uses low level electrical currents to characterise the conductivity of the ground. A block diagram of the basic system is shown in Figure 2-8.

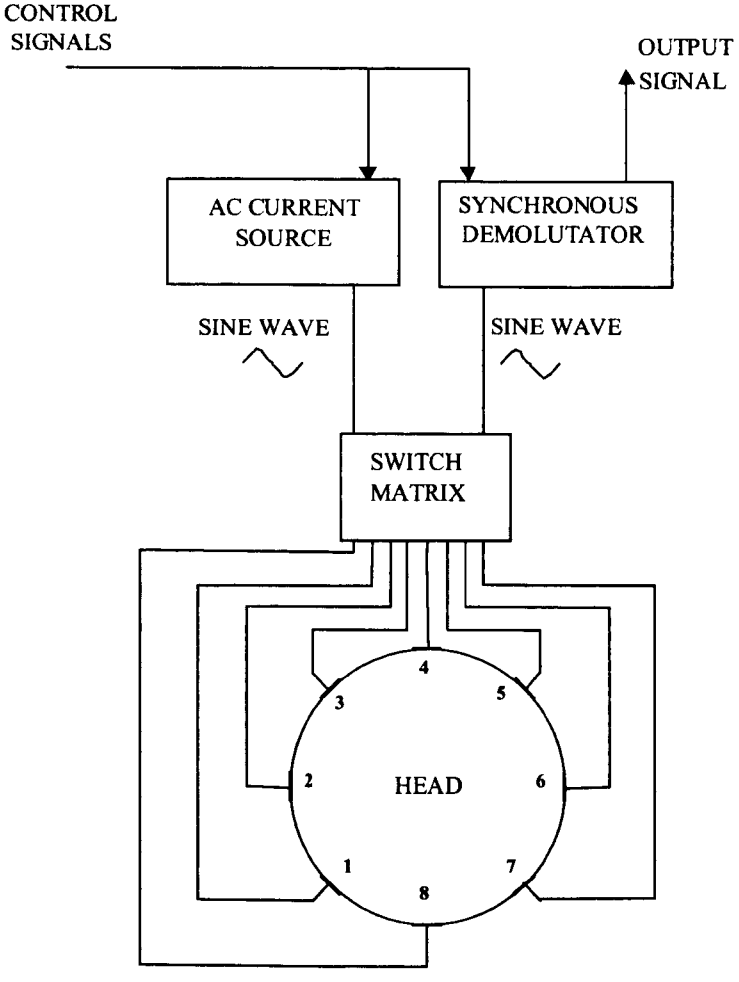

Figure 2-8 Block diagram of an Electrical Impedance Tomography System

An array of electrodes are placed into or on the ground, stimulated in pairs and the data is post-processed to produce a conductivity image [43] [44]. A metal or non-metallic mine will disturb the conductivity distribution in the ground. Typically the current level is around 1ma and the frequency is around 1KHz [45].

The major drawback of this technique is that it needs to be in contact with the ground and thus risks detonating mines. It is also not useful for very dry ground, is sensitive to electrical noise and ineffective for detecting deeply buried mines [46].

2.3.8 X-ray Backscatter

X-ray backscatter, also known as Compton Backscatter Imaging (CBI), is similar to conventional X-ray medical radiography except that, rather than detecting photons that have passed through an object, the photons that are backscattered are detected [47]. For land-mine detection transmission operation is impractical unless a radioactive source could be somehow buried under the mined area, but this raises many environmental concerns [48].

The conventional CBI approach is to selectively detect only those photons that have scattered from one object utilising a collimated source and an uncollimated detector. An example system utilising an electron-scanning beam is depicted in Figure 2-9.

This method has been shown to produce good results in landmine detection, but only in highly idealised circumstances such as a perfectly flat planar surface with homogenous dielectric properties [49]. In addition the penetration depth is relatively poor, being limited at around 5cm, and the imaging acquisition time is prohibitive for practical de-mining [50].

An alternative approach called Lateral Migration Radiography has been recently proposed [51] that utilises large area scintillating detectors of both the collimated and uncollimated type which allows the source strength and the imaging time to be decreased whilst increasing the detection depth to 10 cm. Development and experimentation with this system is continuing with the aim of incorporating it into a vehicle-mounted system.

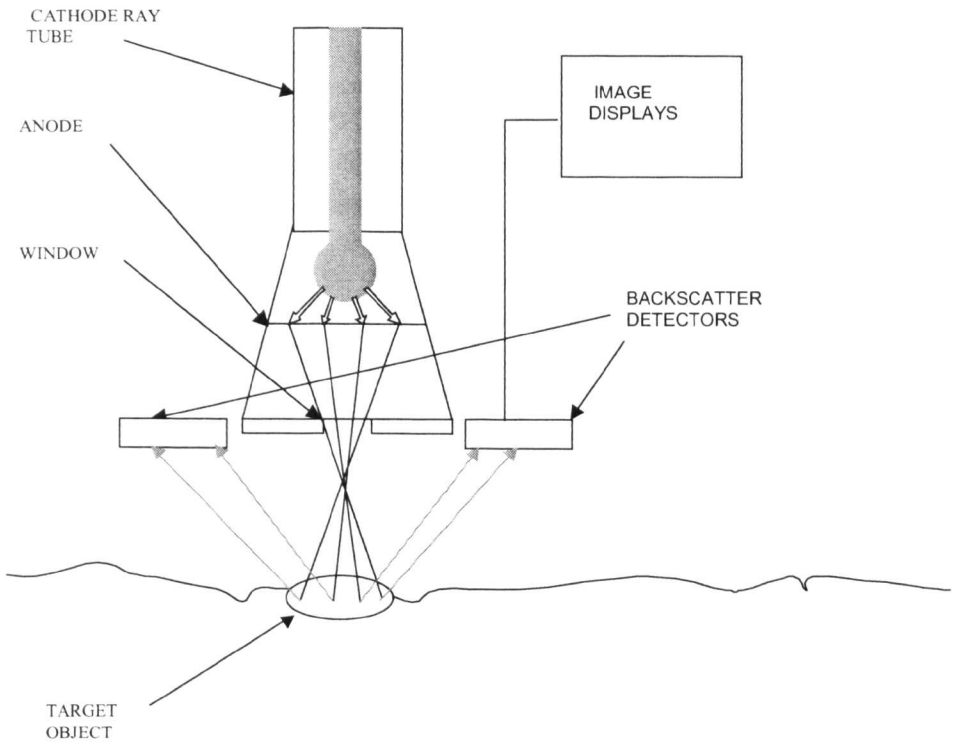

Figure 2-9 Block diagram of X-ray backscatter system

2.3.9 Acoustics/Seismic Methods

This is a mechanical approach that effectively vibrates mines with sound or seismic waves and detects the results with laser Doppler or Ultrasonic vibrometers [52]. The method relies on a high-vibration contrast between porous soils and non-porous land mines which does not exist to the same extent with rocks, roots and other man-made objects including metal and concrete. The key is that when the mine soil interface is radiated with a dual frequency sound wave, a difference frequency is generated due to the non-linear interaction between mine and soil [53]. This difference frequency is detected and the direct incident reflection (from the air soil interface for example) can be ignored, thus in theory a zero false alarm rate could be achieved [54]. The proposed system would probably be airborne and utilise an off-the-shelf loudspeaker for the transmitting source.

The technique is however limited in depth to around 30cm and is severely limited in dense vegetation [54]. However, unlike most other proposed technologies discussed in the preceding and succeeding sections this technique does not exploit electromagnetic properties and therefore it offers advantages when used in conjunction with an 'optimal' electromagnetic sensor such as GPR. Weather and dampness do not limit it and, unlike electromagnetic techniques, it can detect effectively in extremely wet terrain such as swamps and paddy fields [55] (a significant landmine problem exists in the paddy fields of Cambodia [56]).

2.3.10 Nuclear Quadrupole Resonance

Nuclear Quadrupole Resonance (NQR) is similar to magnetic resonance screening (MRI) used extensively in medical scanning [57][58][59]. MRI uses a magnetic field to align the nuclei of the material under test and detects the weak magnetic field that is emitted when the stimulus is removed and the nuclei relax. Analogously in NQR a particular sequence of radio frequency (RF) pulses at a specially selected frequency causes the nuclei of the explosive to resonate and a coil can detect the induced electrical potential. A block diagram of a basic NQR system for landmine detection is shown in Figure 2-10. It operates in close proximity to the ground and so is firmly a hand held or local detection device.

This technique is particularly attractive because it is noise limited, unlike GPR which tends to be clutter limited (as will be shown in sections 4.3.2 and 4.4.1 of Chapter 4) [60]. In other words, NQR is looking for a unique target signature that is not 'accidentally' present in other surrounding objects, therefore it is not limited by spurious returns from other objects (clutter), but by its ability to deal with purely random interference (noise). Very importantly it can, in theory, achieve a near perfect (zero) False Alarm Rate for certain explosives such as RDX and tetryl [60].

Although the process is a little slow it works well in detecting RDX explosive, but unfortunately most landmines are constructed with TNT whose nuclear properties take longer to align and even then produce only very weak electrical potentials. If the explosive mine is encased in metal the RF signals will not penetrate the casing and the process fails. Furthermore the noise limit is a problem, due to radio frequency interference (RFI), from, for example AM transmissions [60].

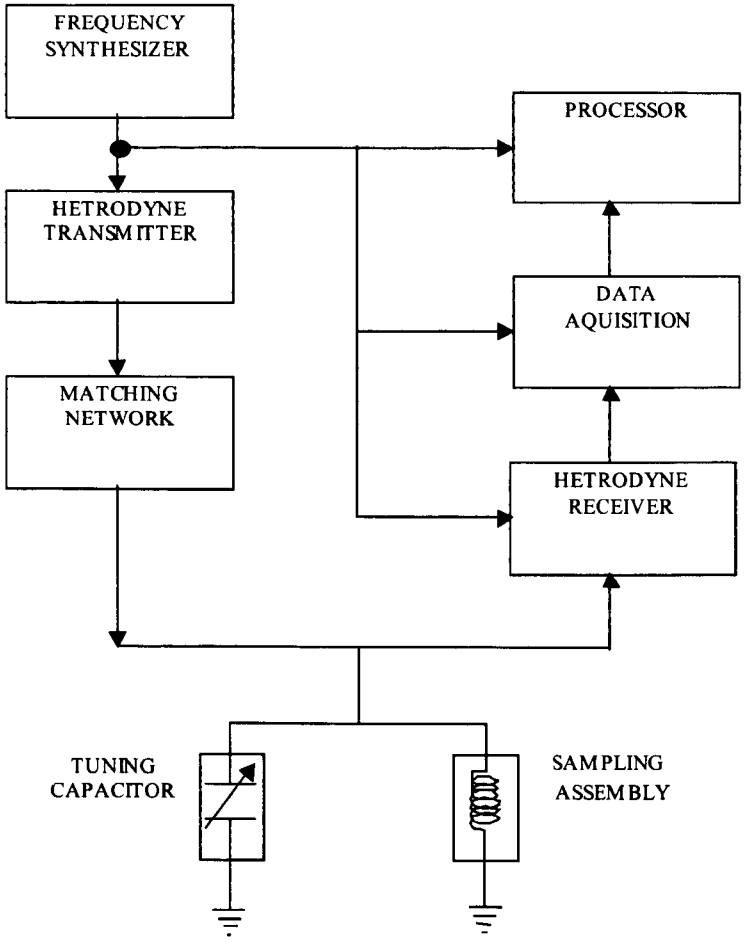

Figure 2-10 Block diagram of a Nuclear Quadrupole Resonance system

2.3.11 Ground Penetrating Radar

GPR consists of either a single antenna or an antenna array that emits a short or swept frequency electromagnetic (EM) pulse and measures reflections caused by dielectric discontinuities in the ground [61]. The resolution achievable is proportional to the wavelength employed. The shorter the wavelength, the greater the resolution, however the trade-off is that at higher frequencies the penetration depth decreases. This will be explained further in Chapter 4.

In-contact operation of GPR avoids ground reflection and refraction. However, even if the ground were sufficiently smooth and clear to permit in-contact operation, there would be a very high risk of setting off trigger devices. Most proposed GPR systems for landmine detection therefore operate at a stand-off distance from the ground.

GPR has several advantages over other mine detection technologies. Because it detects dielectric discontinuities it can succeed, where metal detectors fail, in detecting a wide range of mine cases such as those listed in Table 2-1. The wavelength required for penetration to mine detection depth happens to be similar or less than the typical landmine dimensions, i.e. 5 to 30cm. The technology design is flexible to different operating scenarios. For example, it can operate in a lightweight hand-held device, on a vehicle or in remote wide area reconnaissance and in all these situations, because transmission, propagation and receipt of EM pulses is very fast it can search very quickly compared to other techniques. Nonetheless GPR faces significant operational difficulties, the main ones being the problem of clutter and classification.

Volume clutter caused by natural ground inhomogeneities, such as roots and rocks, and surface clutter due to the air/ground interface tends to interfere or mask the wanted signal in GPR. These will be examined and quantified more fully in the following two chapters along with possible solutions to these problems offered by and developed for the RASOR system.

Classification is defined here as the task of automatically determining the type of detection that has been made. Four levels of sophistication could be envisaged:

1. Something has been detected.
2. Something man-made has been detected.
3. A mine has been detected.
4. A PMA3 anti-personnel mine has been detected.

Classification performance is a challenge for most of the sensors highlighted above and almost all are at level 1 [62]. However, a number of promising signal processing and system design options will also be described which offer the potential for overcoming these difficulties.

2.3.12 Sensor Data Fusion

Fusion methods are generally categorised as decision level, feature level or data level [63]. The majority of work to date in mine detection fusion has utilised decision level fusion whereby each individual sensor in the suite provides a detection decision from

which an overall decision is made. Data and feature level decision techniques are less mature. The state-of-the-art in fusion is typically that of individually designed sensor systems that have been combined onto a single platform, such as the HSTAMIDS hand-held system under development for the US army that utilises a GPR detector and an EMI detector.

It is generally accepted that a successful mine detection and classification system will utilise sensor data fusion from a variety of detection methods. It is likely that the optimal landmine detector will in fact fuse together the data a variety of sensors to reach a detection decision [9][64]. A system is envisaged that combines the fast search speeds of GPR (section 2.3.11) and Metal Detectors (section 2.3.3) and calls on the strong classification performance of NQR (section 2.3.10) when a possible detection has been made. This could be enhanced perhaps with an Acoustic sensor (section 2.3.9) for those situations where electromagnetic detection is impossible. A solution would offer the holy grail of land mine detection or indeed of any detection system; a fast search speed with a perfect ROC curve. However, there remains scope for improving the GPR state-of-the-art system, so that GPR may become the senior partner in this sensor partnership in terms of detection ability and perhaps even classification.

2.4 Conclusions

This chapter has briefly outlined the problems associated with landmines and their detection. Current humanitarian de-mining techniques give slow clearance rates and an improvement in detection technology could make a significant difference. In the military, improvements in detection and location techniques would also have great operational advantage.

New technologies for improving detection and classification have been described and it is concluded that GPR has significant advantages over other techniques in terms of search rate, resolution and flexibility and also its ability to detect modern landmines with very low metallic content. The outstanding problems with the GPR approach that need to be improved are its ability to operate in cluttered environments, to adapt to the different types of environments and to enhance classification performance.

References

[1] US Department of State, 'Hidden Killers: The Global Landmine Crisis', Report to US Congress, 1994.

[2] I.Bottiglero, ' 120 Million Landmines Deployed Worldwide: Fact or Fiction?', Pen & Sword Books, London, 2000

[3] S.J.Jeffrey, 'Antipersonnel Mines, Who are the victims?", J. of Acc. And Emerg. Med., Vol.13 No.5, pp343-346, 1996

[4] Mike Croll, 'History of Landmines', Pen and Sword Books, 1998

[5] J.G.Ackenhusen, et al. 'Detection of Mines and Minefields', Ann Arbor, Veridian Systems Division, 2001

[6] J.D.Nicoud, 'Mine clearance: Not only a problem for the military anymore', Proc. ISMCR '96, Brussels, May 1996, pp6-10

[7] Norwegian Peoples Aid - Mine action in Angola, Landmine Database http://www.angola.npaid.org/photo_gallery.htm, Last accessed: 10 August 2003

[8] Canadian National Defence Mine/Countermine Information Centre, http://ndmin-cidnm.forces.gc.ca/index.asp?lang=e, Last Accessed: 10 February 2004

[9] P.Horowitz, et al, 'New Technological Approaches to Humanitarian Demining', Mclean, JSR-92-115, 1996

[10] P. Jefferson, 'An overview of demining, including mine detection equipment' the Halo Trust symposium on Anti-Personnel Mines, pp 125-132, April 1993

[11] Association for research of innovative techniques in humanitarian mine clearance, http://www.artid.org/us/current_techniques.htm, Last Accessed: 21 February 2004

[12] Afghanistan Mine Clearance, www.mech.uwa.edu.au/dimining/countries/afghan/minefields-afghan2.htm, Last Accessed: 10 October 2004

[13] W.W.Peterson, T.G. Birdsall, W.C. Fox, 'The theory of signal detectability', Trans IRE, PGIT-4, 171-212, 1954

[14] C.W.Helstrom, 'Statistical theory of Signal Detection', 2nd edition, Pergamon Press, 1968

[15] B.S.G. Janzen, 'Improving the technology for humanitarian demining', Proc. EUREL Conference on the Detection of Hidden Land Mines, Edinburgh, UK, pp.11-15 Oct 1996

[16] K.Eblagh, 'Practical problems in demining and their solutions', Proc. EUREL Conference on the Detection of Hidden Land Mines, Edinburgh, UK, pp.11-15 Oct 1996

[17] J.Treveylan, 'Technology and the Landmine Problem: Practical Aspects of Mine Clearance Operations", in 'Detection of Explosives and Landmines: Methods and Filed Experience, H.Schubert, A.Kuznetsov, Kluwer 2002.

[18] D.Kerner, et al, 'Anti-Personnel Landmine (APL) Detection Technology Survey and Assessment', US Department of Defense Technical Report, DNA-96-G-0061, March 1999

[19] Y.Das, et al., 'Final report of the International Pilot Project on Technology Co-operation (IPPTC) for the evaluation of Metal/Mine Detectors', EUR 19719 EN, June 2001

[20] L.S.Riggs, et al., ' Identification of metallic mines using low frequency magnetic fields', Proc. SPIE, Vol.3392 1998

[21] M.Hewish, R.Pengelley, 'Treading a fine line: Mine detection and clearance', Jane's International Defense Review, Vol.30 No.11,1997

[22] Y.Das, J.T.Dean, et al. 'International Pilot Project for Technology Co-operation Final Report: A Multinational Technical Evaluation of Performance of Commercial Off the Shelf Metal Detectors in the Context of Humanitarian Demining', Ispra, Italy: European Commission Joint Research Centre, 2001

[23] C.E.Baum, 'Low-frequency near-field magnetic scattering from highly, but not perfectly, conducting bodies', Detection and identification of visually obscured objects, Taylor and Francis, 1999, Chapter 6

[24] T.Bell, B.Barrow, J.Miller, D.Keiswetter, 'Time and frequency domain electromagnetic signatures of unexploded ordinance', Subsurface Sensing Technologies and Applications, Vo.2 No.3, 2001, pp155-177

[25] L.S.Rigg, 'Electromagnetic Induction (Paper II)', Alternatives for Landmine Detection, RAND Science and Technology Institute, 2003, Appendix B

[26] H.Bach, 'Canine-Assisted Detection' , Alternatives for Landmine detection, RAND Science and Technology Institute, 2003, Appendix T

[27] I.McLean, 'Designer Dogs: Improving the quality of mine detection dogs', Geneva International Centre for Humanitarian Demining, 2001

[28] W.J.Buttner, et al., 'In-situ detection of Trinitrotoluene and other nitrated explosives in soils', Analytica Chemica Acta, No.341, pp63-71, 1997

[29] J.C.Cumming, et al., 'Using novel fluorescent polymers as sensory materials for above ground sensing of chemical signature compounds emanating from buried landmines', IEE Trns. Geosc. Rem. Sens., Vol.39 No.6, pp1119-1128, 2001

[30] C.Larsson, S.Abrahamsson, et al., 'Radar, multipsectral and biosensor techniques for mine detection', Symposium on Anti-Personnel Mines, ICRC, Geneva, April 1993, pp179-202

[31] P.J.Rodacy, 'The training and development of honeybees to detect explosives and other agents of harm', Proc. SPIE AeroSense CBS work, April 2002

[32] R.Fischer, 'UXO and mine detection using laser induced fluorescence imagery and genetically engineered microbes', Army AL&T, pp10-12, July-Aug 2000,

[33] B.A.Baertlein, 'Infrared/Hyperspectral methods (paper I)', Alternatives for Landmine Detection, RAND Science and Technology Institute, 2003, Appendix C

[34] B.A.Baertlein, A.H.Gunatilaka, 'Optmizing fusion architecture for limited training data', Detection and Remediation Technologies for Mines and Mine Like Targets V, Proc SPIE, pp804-815, 2000

[35] C.A.DiMarzio, C.M.Rappaport, L.Wen, 'Microwave enhanced infrared thermography', Detection and Remediation Technologies for Mines and Mine Like Targets III, Proc SPIE, pp1103-1110, 1998

[36] J.Storm, B.Haugsted, 'Detection of buried landmines facilitated by actively provoked IR signatures', Detection and Remediation Technologies for Mines and Mine Like Targets IV, Proc SPIE, pp167-172, 1999

[37] A.P.Bowman, E.M.Winter, A.D.Stocker, P.G.Lucey, 'Hyperspectral infra-red techniques for buried landmine detection', 2nd International Conference on the Detection of Abandoned Landmines, pp129-133, 1998

[38] B.Johnson, et al., 'A compact active hyperspectral imaging system for the detection of concealed targets', Detection and Remediation Technologies for Mines and Mine Like Targets IV, Proc SPIE, pp144-153, 1999

[39] M.H.Maleki, A.J.Devaney, 'Phase-retrieval and intensity-only reconstruction algorithms for optical diffraction tomography', J. Opt. Soc. Am., No.15, pp48-58, 1993

[40] A.J.Devaney, 'Inverse source and scattering problems in ultrasonic', IEEE Trans. Sonics Ultrasonics, SU-30, pp355-364, 1983

[41] A.J.Devaney, 'Geophysical diffraction tomography', IEEE Trans, Geoscm Rem. Sens., GE-22, pp3-13, 1984

[42] R.W.Deming, A.J.Devaney, 'Diffraction tomography for multi-monostatic ground penetrating radar imaging', Inverse Problems, 13, pp29-45, 1997

[43] A.Wexler, B.Fry, M.R.Neuman, 'Impedance-computed tomography algorithm and system', Applied Optics, 24, pp3985-3992, Dec 1985

[44] M.H.Loke, 'Electrical imaging surveys for environmental and engineering studies', Practical guide to 2D and 3D surveys, Technical Note for Advanced Geoscience, Inc, USA

[45] P.Church, 'Electrical Impedance Tomography', Alternatives for Landmine Detection, RAND Science and Technology Institute, 2003, Appendix I

[46] P.Church, 'Performance assessment of an electrical impedance tomography detector for mine-like objects', Detection and Remediation Technologies for Mines and Mine Like Targets VI, Proc SPIE, pp895-905, 1999

[47] E.Odeblad, A.Norhagen, 'Electron density in a localized volume by Compton scattering', Act Radiologica, No.45, pp161-167, 1956

[48] L.Grodzins, 'X-ray backscatter (Paper I)', Alternatives for Landmine Detection, RAND Science and Technology Institute, 2003, Appendix L

[49] F.Roder, R.Van Konyenburg, 'Theory and application of x-ray and gamma ray backscatter to land mine detection', US Mobility Equipment Research and Development Centre, Report 2134, 1975

[50] G.J.Lockwood, et al., 'Field tests of x-ray backscatter mine detection', 2nd International Conference on the Detection of Abandoned Landmines, pp60-33, 1998

[51] Z.Su, A.Jacobs, E.Dugan, J.Howley, J.Jacobs, 'Lateral migration radiography application to land mine detection confirmation and classification', Opt. Eng., Vol.39 No.9, pp2472-2479, 2000

[52] J.Sabatier, N.Xiang, 'An investigation of acoustic-to-seismic coupling to detect buried anti-tank landmines', IEEE Trans. Geosc.Rem.Sens., Vol.39 No.6, pp1146-1154, June 2001

[53] D.M.Donskoy, 'Non-linear seismo-acoustic technique for landmine detection and discrimination', , 2nd International Conference on the Detection of Abandoned Landmines, pp244-248, 1998

[54] M.Korman, J.Sabatier, 'Non-linear acoustic techniques for landmine detection: experiments and theory', Proc. Soc. Photo-Optical Instrumentation Engineers AeroSense Conference, 2002

[55] E.Rosen, K.Sherbondy, J.Sabatier, 'Performance assessment of a blind test using the University of Mississippi's acoustic/seismic laser Doppler vibrometer (LDV) mine detection apparatus at A.P.Hill', Soc. Photo-Optical Instrumentation Engineers, No.4038, pp656-666, 2000

[56] N.Andersson, C.P.D. Sousa, et al, 'Social cost of landmines in four countries: Afghanistan, Bosnia, Cambodia, and Mozambique', British Medical Journal, No.311, pp718-721, 16th Sep 1995

[57] F.Bloch, W.W.Hansen, M.Packard, 'Nuclear Induction',Phy.Rev., Vol.69,p127, 1946

[58] E.M.Purcell, H.C.Torrey, R.V.Pound, 'Resonance absorption by nuclear magnetic moments in a solid', Phys Rev., Vol.69, pp37-38. 1946

[59] Y.K.Lee, 'Spin-1 Nuclear Quadrupole Resonance theory with comparisons to Nuclear Magnetic Resonance', Concepts in Magnetic Resonance, No.14, pp155-171, 2002

[60] A.N.Garroway, et al., 'Remote sensing by Nuclear Quadrupole Resonance', IEEE Trans. Geos.Rem.Sens., Vol.39 No.6, pp1108-1118, June 2001

[61] D.J.Daniels, 'Surface Penetrating Radar', IEE, 1996

[62] P.M.Blagden, 'The changing scene of mine clearance', 2nd International conference on the detection of abandoned land mines, Edinburgh, UK, October 1998, pp19-22.

[63] A.H.Gunatilaka, B.A. Bertlein, 'Feature-Level and Decision-Level fusion on noncoincidently sampled sensors for land mine detection', IEEE Transactions on Pattern Analysis and Machine Intelligence, Vol. 23 No.6, pp557-589, 2001

[64] D.L.Hall, J.Llinas, 'An introduction to multisensor data fusion', Proc. IEEE, Vol.85 No.1, pp96-103, Jan 1997

3 Ground Penetrating Radar

This chapter considers the different transmission, reception and processing techniques commonly employed in Ground Penetrating Radar systems. A brief introduction to the RASOR scheme outlines the theoretical and operational concepts highlighting their advantages in comparison with the other ground penetrating radar techniques. Full analysis of the RASOR system is given in Chapter 4. GPR can be operated with the antennas in contact with the ground or in a non-contact mode. For the land-mine detection RASOR is non-contact and hence descriptions are mainly applied to non-contact GPR.

3.1 GPR Overview

After Electromagnetic Induction, GPR is probably the most mature sub-surface probing technology available. However, it is still at a reasonably early stage of development in land mine detection because only relatively recently has the problem environment been more fully understood [1]

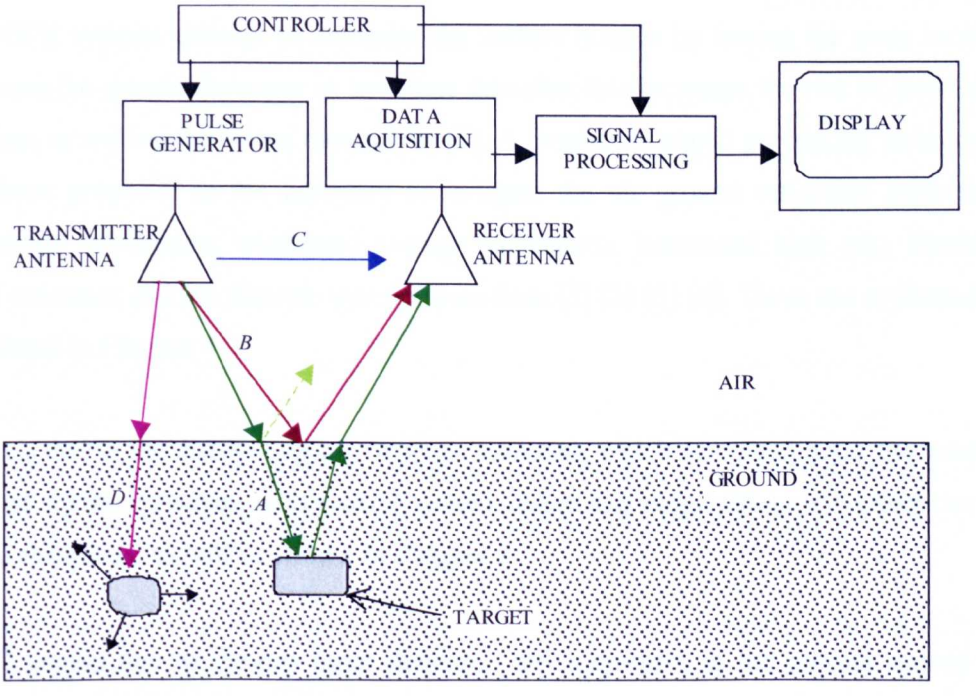

Figure 3-1 Generic Ground Penetrating Radar system

An example of a generic non-contact GPR System is shown in Figure 3-1. The antennas are positioned either close to or on the surface and an electromagnetic pulse or swept

frequency signal is transmitted. Provided the pulse has sufficient power, it will penetrate the ground, undergoing refraction at the air/soil interface and be reflected from the target back to the receiving antenna following path *A*. Assuming the losses that the pulse under goes during this propagation are small enough to preserve a detectable SNR, then the received signal will pass through a low noise amplifier stage, be digitised, processed and displayed. The various loss mechanisms will be elucidated later.

Difficulties in GPR arise from coupling and clutter, which can be summarised as being due to paths *B*, *C* and *D* in Figure 3-1. Path B shows the reflection at the ground - air interface due to the very large dielectric contrast that is typically between 2 to 4, but can be as large as 20 for certain soil conditions. This is often referred to *as surface clutter* and it represents one of the major difficulties with GPR particularly when reception of this signal overlaps with the signal reflected from a target, which is often the case for shallowly buried mines. Surface clutter also means that the dynamic range of the receiver must be sufficient to deal with the (very large) surface 'bounce', whilst still detecting the low-level signal scatterers in the ground.

Some GPR systems attempt to minimise the surface bounce by having the array located just above the ground, however in landmine detection this increases the risk of activating trip wires as well as the mines themselves [2]. A number of signal processing techniques have been proposed in the literature to mitigate the air ground reflection such as a background subtraction, windowed average subtraction, horizontal high pass filtering, model estimates and the discrete wavelet transform [3] [4] [5] [6]. These are evaluated in more detail in Chapter 4.

Path *C* is due to the direct coupling between antennas, which again can mask the wanted reflected signal. However, with careful system design and range gating this effect can be largely eliminated as will be shown in Chapter 5.

Path *D* occurs due to various other dielectric discontinuities in the ground caused by rocks, roots, voids and other inhomegenieties. This is often referred to as volume clutter and three notable difficulties arise as a consequence. Firstly, the clutter reflection can occur in the same range gate as the target reflection resulting in bearing ambiguity. This can be minimised by use of antenna arrays and signal processing focusing technique as

will be shown in Section 4.3.2. Secondly the clutter reflection could occur in path *A* causing the target to be shadowed or obscured. Again, use of an antenna array to illuminate the target in different directions can mitigate this effect. The third difficulty that volume clutter (and in fact surface clutter) poses is when the clutter point, ie. rock or root, has similar electrical or dimensional properties to that of a landmine. In effect this is a typical classification problem and an interesting challenge for GPR.

The following section looks at the typical choices available for each part of the generic system shown in Figure 3-1.

3.1.1 Antennas

GPR can operate monostatically, where the same antenna is used for transmission and reception. However, this represents difficulties because of the very short pulse propagation time. Consequently very fast switching between transmitting and receiver configuration is needed. Bistatic or multistatic operation is preferable where one or more antennas transmit and a separate antenna, or antenna array, receives.

The antennas require a large fractional bandwidth to achieve the required resolution and a linear phase response. Polarisation is normally fixed although circular and cross polarised antennas have been proposed to exploit the polarisation characteristics of certain targets [7]. The directivity of the aperture needs to be such that energy is radiated only in the required direction with minimum sidelobes and cross coupling, i.e. path *C* described above. Another important consideration is the robustness of the antenna particularly when the GPR is operated very close to the surface. Antenna horns are widely used in GPR applications because of their wide bandwidths and high directive gain [8] [9]. However their relative size and cost compared to other solutions mean they are not particularly suitable for large arrays. Other element designs that have been proposed for GPR are dipoles, bi-conical antennas and bow-tie antennas [10] [11] [12].

It is likely that arrays of antenna elements will become the favoured approach in GPR for landmine detection, particularly vehicle mounted systems, because of the greater spatial coverage and beamforming advantages that this gives. However, the use of wide bandwidth antenna arrays means that the simple phase shift beamforming, used for narrowband arrays, is no longer suitable and therefore more complex, and potentially

more costly, beam steering schemes are required. It will be shown how post-reception focusing can overcome this limitation, at least for the transmit path. Another consideration when using wideband arrays, as opposed to narrow band arrays, is the potential for increased interference noise over the bandwidth.

3.1.2 Pulse types.

For a particular GPR application, the signal processing method will determine the choice of pulse waveform to be used or vice versa. The two are strongly inter-dependent. Several pulse modulation techniques are available each with advantages and disadvantages.

3.1.2.1 Impulse

The impulse or baseband pulse is the favoured pulse in many GPR systems because of its relative simplicity and low cost [13]. Typically the pulse is between a few nano seconds down to a few hundred pico seconds in length usually with a peak amplitude of 20 to 200V. This corresponds to a frequency spectrum of several hundred MHz to 1-2GHz. The high frequency content provides good spatial resolution, for example at 2GHz the resolution achieved in soil with relative permittivity of 3 would be approximately 9cm. An important consideration with this method is the reliability and jitter[1] not only of the transmitter device but also for the receiver, which is generally a sampling device (see section 3.1.3).

3.1.2.2 Frequency Modulated Continuous Wave (FM–CW)

This method is used as an alternative to impulse radar as it allows better control of the spectral shape of the transmitted signal [14]. A basic block diagram of the scheme is shown in Figure 3-2. A continuously changing carrier frequency is linearly swept across the bandwidth. The received signal is mixed with the transmitted signal to produce a beat frequency, which yields directly the time delay of the reflected signal and hence the range, R, to the target using the equation:

$$R = 2vT\Delta f(f_2 - f_1) \qquad (3\text{-}1)$$

Where v is the speed of propagation

f_1 is the minimum frequency

f_2 is the maximum frequency

T is the period of the sweep from f_1 to f_2

and Δf is the difference frequency between transmitted and received signals

[1] Jitter is defined as the short-term deviation from the ideal timing of an event.

A discriminator is included to avoid negative difference frequencies when the sweep resets.

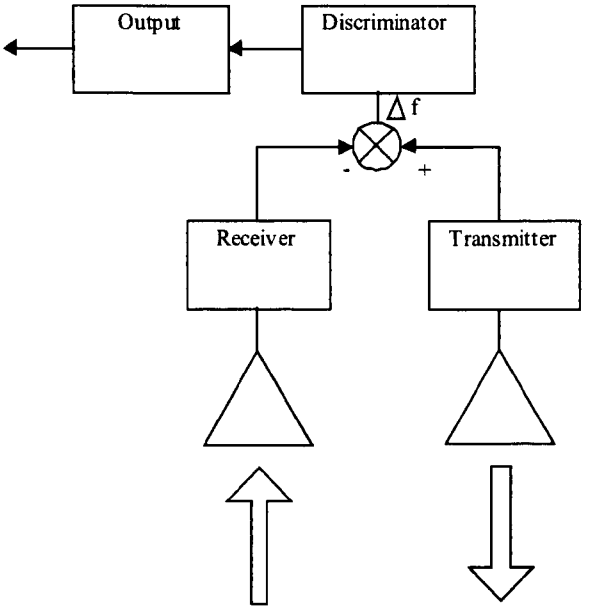

Figure 3-2 Basic block diagram of a FM-CW radar

The linearity of the sweep is a key factor in determining the system performance of a FM-CW system. As the non-linearity increases the effect is to broaden the width of the difference frequency spectrum and therefore reduce the achievable resolution.

3.1.2.3 Synthesised waveforms

This is a frequency domain technique similar to FM-CW. In effect an impulse waveform is synthesised by the transmission of a sequential series of frequencies. The frequency spacing synthesises the impulse repetition rate and the envelope synthesises the impulse shape. This method is very useful for matching the pulse to the antenna to avoid ringing and reduces the maximum pulse power by distributing the power across the frequency spectrum [15]. However, this method must maintain an accurate relative phase relation between spectral lines and this is difficult to achieve in real-time operation [13].

3.1.2.4 Single frequency techniques

This is used in some holography systems where the target is radiated at a single frequency from a number of antenna positions in order to construct an image from the response [16]. This technique has tended to be unsuccessful in GPR as the use of a single frequency tends to give low range resolution [17].

3.1.3 Data acquisition

In Impulse GPR, a sequential sampling receiver is typically used to capture the received signal. This technique, also known as equivalent time sampling, utilises a very fast sample and hold circuit that incrementally captures a sample of the waveform at each pulse repetition until the required waveform or *A-Scan* has been obtained. Normally a synchronising pulse from the transmitter triggers the sampling receiver. The sampling increment, t, must be selected to respect the Nyquist criteria,

$$t < 1/(2 \times Bandwidth) \qquad (3\text{-}2)$$

In practise the sample rate is normally selected to be well above the bandwidth [13] in order to reduce the required roll-off of the anti-aliasing filter. Thus the sampling increment needed to sample a 1GHz bandwidth at say five times the bandwidth would be

$$t = \frac{10^{-9}}{5} = 200ps \qquad (3\text{-}3)$$

Jitter should be no more than around 10% of the sampling interval to avoid excessive noise on the waveform. Even so high-speed sampling tends to give a low signal to noise ratio compared to other techniques and a low dynamic range. A series of sample A-scans from a number of transmissions can be averaged to improve the dynamic range, but this will reduce the scan rate.

This method in essence down converts the incoming RF signal to a data rate determined by the pulse repetition rate. A drawback with this sampling method is that the sequential sampling tends to increase overall scanning time and is also wasteful of transmitted RF power. For example, to capture a single A-scan containing 512 samples would require 512 transmissions which, at a pulse repetition rate of 100KHz, would take:

$$\text{scan time} = \frac{512}{100 \times 10^3} = 5.12ms \qquad (3\text{-}4)$$

An alternative to equivalent time sampling is to use a high-speed flash ADC converter to sample the RF signal in real time. Commercial off the shelf units have been used in RASOR that are capable of sampling at 8GSa/s with 8-bits of dynamic range and over 1.5GHz bandwidth are available [18] and further performance in the near future is anticipated [19]. Generally as sampling speeds increase the number of bits of dynamic

range decreases. The overall noise figure of these devices can be improved by employing a time varying gain prior to digitisation typically using a low noise amplifier with gain adjustment. A major difficulty with these devices in real time systems is data throughput, which can cause a bottleneck at the output of the sampling device, particularly for the short pulse repetition interval employed in GPR.

The FM-CW received pulse is acquired via an In-phase/Quadrature (I/Q) mixer pair to derive the beat or intermediate frequency (IF). This provides the amplitude and phase of the received signal for further signal processing. Provided that the sweep linearity is maintained and the output frequency is stable, then the FM-CW technique has greater dynamic range than for the impulse receiver. There are also other considerations for a good FM-CW receiver design, which are generally related to the component variation characteristics [20] [21]. However, these can be affected by environmental considerations such as antenna to surface separation.

Synthesised waveform pulse receivers employ a similar mixing receiver to that used for FM-CW pulses [15]. Again, a difference frequency is generated, usually via a network analyser, which is then inverse Fourier transformed into the time domain for post processing. This method utilises a relatively low bandwidth and so the receiver SNR is much greater than for impulse radars.

3.1.4 Signal processing

Signal processing, as defined here, encompasses the range of methods that are available for manipulating the received signals to achieve the ultimate aim - a detection decision with low probability of false alarm. GPR signal processing techniques can be separated by their application into three broad categories of data processing and presentation: A-scan processing, B-scan processing and C-scan processing.

An A-scan is a set of time samples collected from one position of an antenna or antenna pair. The co-ordinate system for an A-scan is shown in Figure 3-3 where the z direction is perpendicular to the antenna. Figure 3-4 shown a typical A-scan time series (taken from the RASOR system).

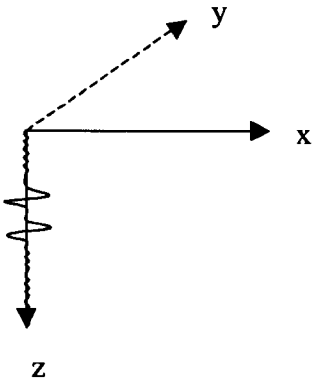

Figure 3-3 A-scan co-ordinate system

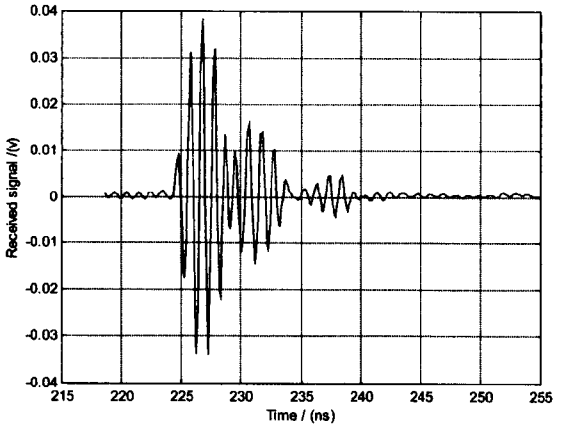

Figure 3-4 Typical A-scan waveform

A-scan processing is applied to individual time series signals normally to remove unwanted artefacts and enhance the wanted features prior to more sophisticated processing. Examples of A scan processing are:

- *Offset removal* to ensure that the mean value of the signal is zero over the time duration of the signal,
- *Averaging* of repeated A-scans data gathers to improve the signal to noise ratio of the time series,
- *Filtering* to remove undesirable frequency components from the time series,
- *Background subtraction* to remove the potentially troublesome surface bounce,
- *Deconvolution* or matched filtering to extract target 'spikes' from the data.

B-scans comprise of a series of A-scans that have been collected at spatially separated antenna positions in order to reveal information about a two dimensional space. The

horizontal axis normally denotes distance and the vertical access is expressed in time as shown in Figure 3-5. A representation of a B-scan is shown in Figure 3-6.

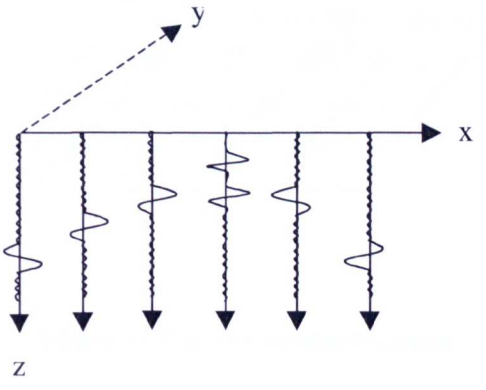

Figure 3-5 B-scan co-ordinate system

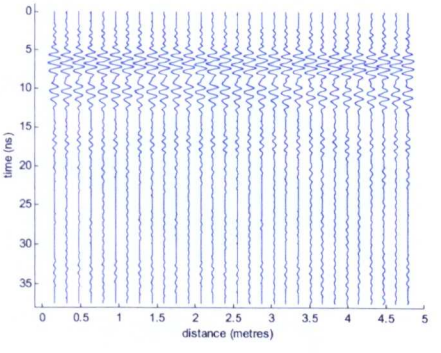

Figure 3-6 Representation of a B-scan plot

Processing methods are traditionally based around migration techniques originally developed in seismic surveying [22] [23] or synthetic aperture techniques [24] [25]. Image processing techniques such as hyperbola estimation and wavelet-based target feature detection can also be applied on B-scan data [26] [27].

A C-scan processing operates on a x-y plane at a specific depth, z, or a series of depths of z to provide a 3D image of a data set. The co-ordinate representation of a C-scan is shown in Figure 3-7. Many of the techniques applicable to B-scan processing are also applicable to C-scan processing. The RASOR spot focusing technique is in essence a C-scan processing method using electronic scanning to image a 3D space as shown in Figure 3-8.

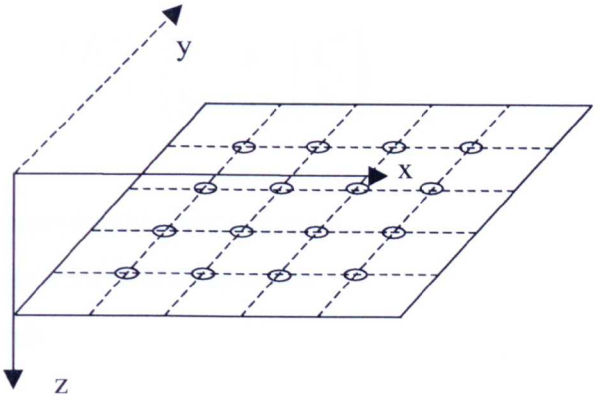

Figure 3-7 C-scan co-ordinate system

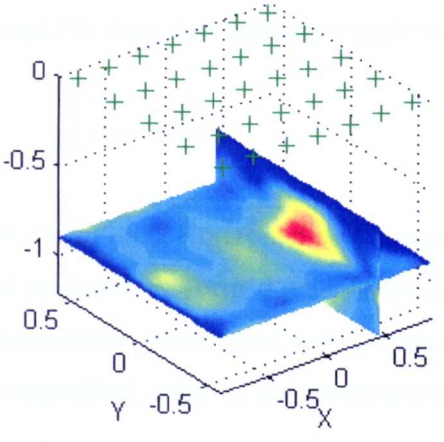

Figure 3-8 C-scan image (from RASOR)

3.2 System Designs for Target Detection

The previous section has shown that there are a variety of GPR design trade-offs that can be considered in order to achieve the design aim: detection and classification of landmines with a low Probability of False Alarm (PFA) and high Probability of Detection (PD). These design decisions will usually be dictated by the nature of the feature extraction or classification that is being attempted. This section looks at different approaches to classification and where appropriate highlights the type of system design that this mandates.

3.2.1 Polarisation Discrimination

The polarisation characteristics of man-made materials can enhance the discrimination between target and clutter. The formula for the scattering matrix is given by [28]

$$\begin{pmatrix} E_1^r \\ E_2^r \end{pmatrix} = \begin{pmatrix} S_{11} & S_{12} \\ S_{21} & S_{22} \end{pmatrix} \begin{pmatrix} E_1^t \\ E_2^t \end{pmatrix} \quad (3\text{-}5)$$

where

E_1^r and E_2^r are the received field components

E_1^t and E_1^t are the transmitted field components

S is the scattering matrix

The scattering matrix is the fundamental characteristic of the scattering object and determines how much of a certain type of polarisation is reflected. If a linear polarisation is employed at the antenna element it is assumed E_1^t will be horizontally polarised (H) and E_2^t is vertically polarised (V) then the scattering matrix will become

$$\begin{pmatrix} S_{HH} & S_{HV} \\ S_{VH} & S_{VV} \end{pmatrix} \quad (3\text{-}6)$$

Where

HH: horizontal polarisation transmitted, Horizontal polarisation received

HV: horizontal polarisation transmitted, Vertical polarisation received

VH: Vertical polarisation transmitted, Horizontal polarisation received

VV: Vertical polarisation transmitted, Vertical polarisation received

It has been shown that scattering from long linear objects such as plastic pipes produces a strong scattering with an orthogonal polarisation to the transmission [29]. For example, a horizontally polarised transmission results in the HV term dominating the scattering matrix. Thus by using cross dipole antennas it is possible to discriminate this type of target provided the antenna is polarised correctly with respect to the target orientation. It is possible that plastic landmines, being regularly shaped man-made objects, may be discriminated using this technique too and some success has been reported at detecting AP mines in a 'pseudo' mine-field using a circularly polarised spiral antenna [30].

Cross dipoles have been suggested as a suitable antenna for polarisation detection, although it has been suggested [31] that the search sweep would need to be repeated with the crossed dipole axially rotated in order to detect pipes at unknown origins. However, this seems unnecessary because the crossed dipole configuration can be electrically

rotated in any direction, at the expense of more sophisticated control hardware and processing software [32].

There are practical difficulties with this method. Variation in coupling between crossed dipoles due to variations in the ground impedance can be troublesome. Circular polarisation has been proposed as a method for electronically rotating the polarisation. However, this is generally associated with steady state CW transmissions and their response to impulse waveforms is complex. Normally several impulse transmissions would be required to establish a circular polarised state thus increasing search time [33].

3.2.2 Target Resonance

This method is based on the assumption that every object has a unique resonance [34,35]. The back scattered signals can be expanded using the singularity expansion technique in which each singularity corresponds to a resonance [36]. The waveform is represented as a summation of exponential terms

$$r(t) = \sum_{1}^{N} a_i e^{s_i t} \tag{3-7}$$

where,

$r(t)$ is the received waveform

s_i is the natural complex resonance

N is the number of resonances

a_i is a multiplying coefficient

In a lossy medium the high frequency information is low and so this method is very vulnerable in low SNR conditions. Furthermore knowledge of every targets characteristic is required *a priori* for the identification to be possible, because the natural resonance depends upon the dimensions and construction of the target [37]. Nonetheless this method could be viable as a complementary classification tool in a GPR imaging system such as RASOR, where a list of all known target resonance signatures are held in a look-up library.

3.2.3 Microwave Holography and Synthetic Aperture Techniques

Microwave holography makes use of a scanning antenna or an antenna array to provide three-dimensional imaging of concealed objects. Techniques have been proposed using single frequency holography by Anderson [38], however these tend to have poor range

resolution and the need to scan a single antenna to multiple positions severely reduces search speeds. Several researchers have proposed multi-frequency holography using swept frequency techniques [39][40][41] thus improving range and azimuth resolution, but search rate remains slow due to the sequential nature of the scanning and the techniques tend only to be applicable in the far field. In addition the highly directive antennas available at the time of the research were rather cumbersome.

Multi-frequency holography using impulses, rather than swept frequencies, have been proposed and developed by Osumi [42][43][44]. An experimental system has been constructed for the detection of buried pipes in soil. A pair of dipole antennas is scanned point by point over two dimensions, operating in-contact with the soil, with a pulse centre frequency of 450MHz and a 350MHz bandwidth. The image reconstruction principles are based on Kirchoff scalar diffraction theory to effectively estimate the complex amplitude reflectance $p(x)$ at focusing points in the ground from a transmitted pulse $u(t)$ and a set of recorded returns $\{s(x_r,t)\}$ where x_r is the mid point between the transmit position, x_T, and the receiver position x_R as shown in Figure 3-9.

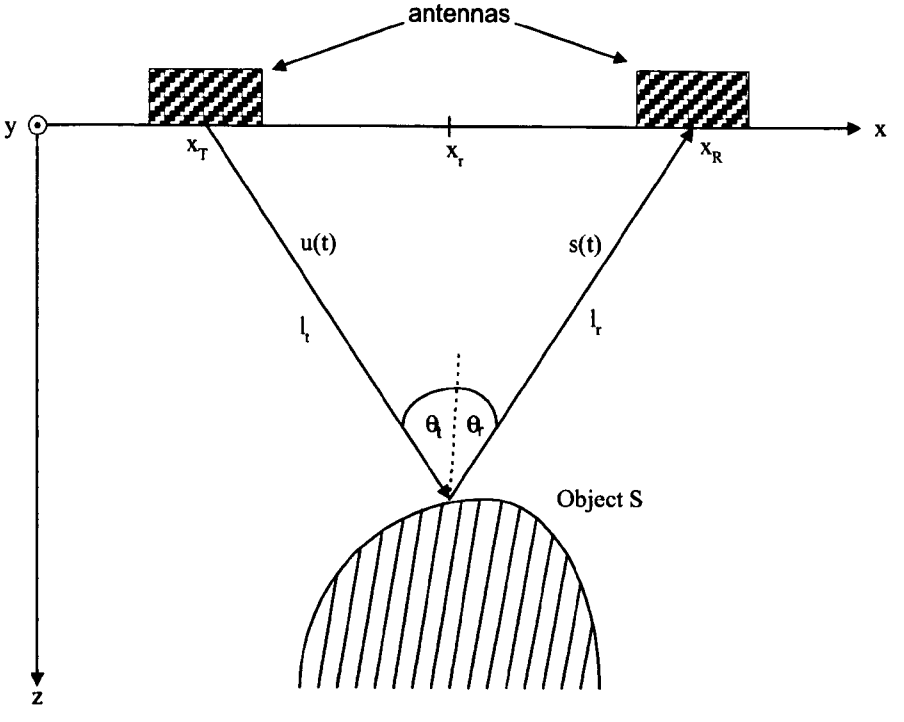

Figure 3-9 Holographic imaging geometry

From diffraction theory the formula for a given received signal is

$$s(x_r,t)=\frac{1}{2\pi v}\iint_S p(x)\frac{e^{-\alpha(l_t+l_r)}}{(l_t l_r)^2}\times u'\left(t-\frac{l_t-l_r}{v}\right)dxdy \tag{3-8}$$

Where

α is the soil attenuation

v is the propagation velocity

u' is the time derivative of the transmitted pulse

l_t and l_r are the lengths of the transmit and receive paths respectively

The image reconstruction then becomes a problem of finding a test function $h(x,t)$ that can be correlated with the set of received signals

$$b(x)=\iint\int_{-\infty}^{+\infty} s(x_r,t)h(x-x_r,t)\,dt\,dx_r\,dy_r \tag{3-9}$$

The test function is optimised such that the image function has a maximum value at the focusing point and is close to zero everywhere else [42]. $b(x)$ is known as the image function and is effectively a measure of the object reflectance.

The horizontal resolution has been shown empirically to be dependent on aperture length, permittivity and antenna directivity [44] with a horizontal resolution of approximately 0.2m being typical.

3.2.4 Spot Focusing

Near-field multi-static 2D spot focusing in subsurface radar was first proposed by Benjamin [45]. It uses similar synthetic aperture and holographic concepts to those described in the previous section, but with a two dimensional real aperture array that is synthetically organised via electrical switching (rather than the monostatic or bistatic approach with manual scanning). Figure 3-10 demonstrates the spot focusing method.

The transmitting elements launch an ultra-wideband pulse. Path delays are applied to either the transmitter or receiver (or both) such that the array acts as a lens to focus a small volume element or vortex in to the ground sometimes known as a resolution or focusing cell. A key aspect of this method is that the correct time delay needs to be calculated and introduced between each receiver so that the signals coming from the element add constructively.

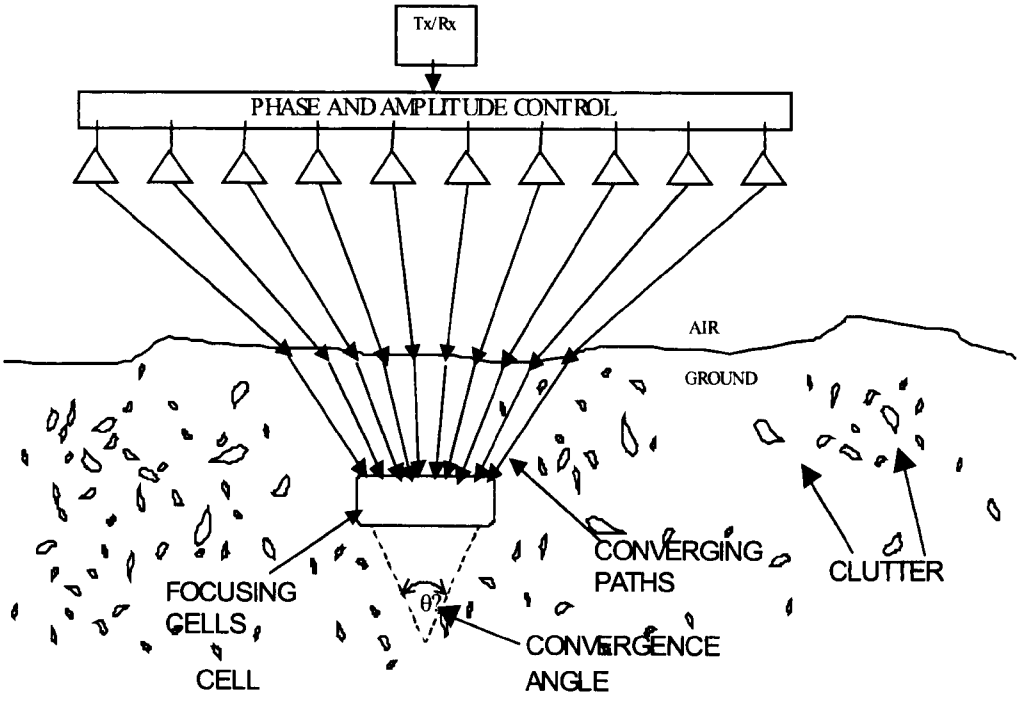

Figure 3-10 Spot Focusing

Conventional active phased array methods aim to scan a large volume with a small aperture by steering the transmitted beam [46]. Spot focusing differs from conventional phased arrays in two important respects. Firstly, unlike in conventional receive arrays, spot focusing occurs only on the receive data. The transmitter or transmitters launch the pulse perpendicularly to the array thus illuminating all volume elements within the antenna's field of view[1] in one go. The second important difference with conventional phased arrays is that the time delays applied to the antenna elements are not linearly increasing from one receiver to the next, but are directly proportional to the three dimensional position of the volume element and the round trip velocity of the pulse propagation.

3.3 Introducing RASOR

RASOR is a practical implementation of near field spot focusing. The following sections give an overview of RASOR and introduce its key theoretical performance and operational characteristics. These will be evaluated and validated in practice in subsequent chapters.

[1] Field of view could be regarded as the solid angle where signal is observed above the antenna's half-power beamwidths.

3.3.1 System Concept

RASOR concentrates on non-contact operation with a 2D planar in-air array. Non-contact operation is essential due to the operational hazards of the environment, principally mine detonation, but also trip wires, undulating ground and dense vegetation. Figure 3-11 shows the RASOR schematic in one dimension as a linear array, though it would generally be implemented as a planar array.

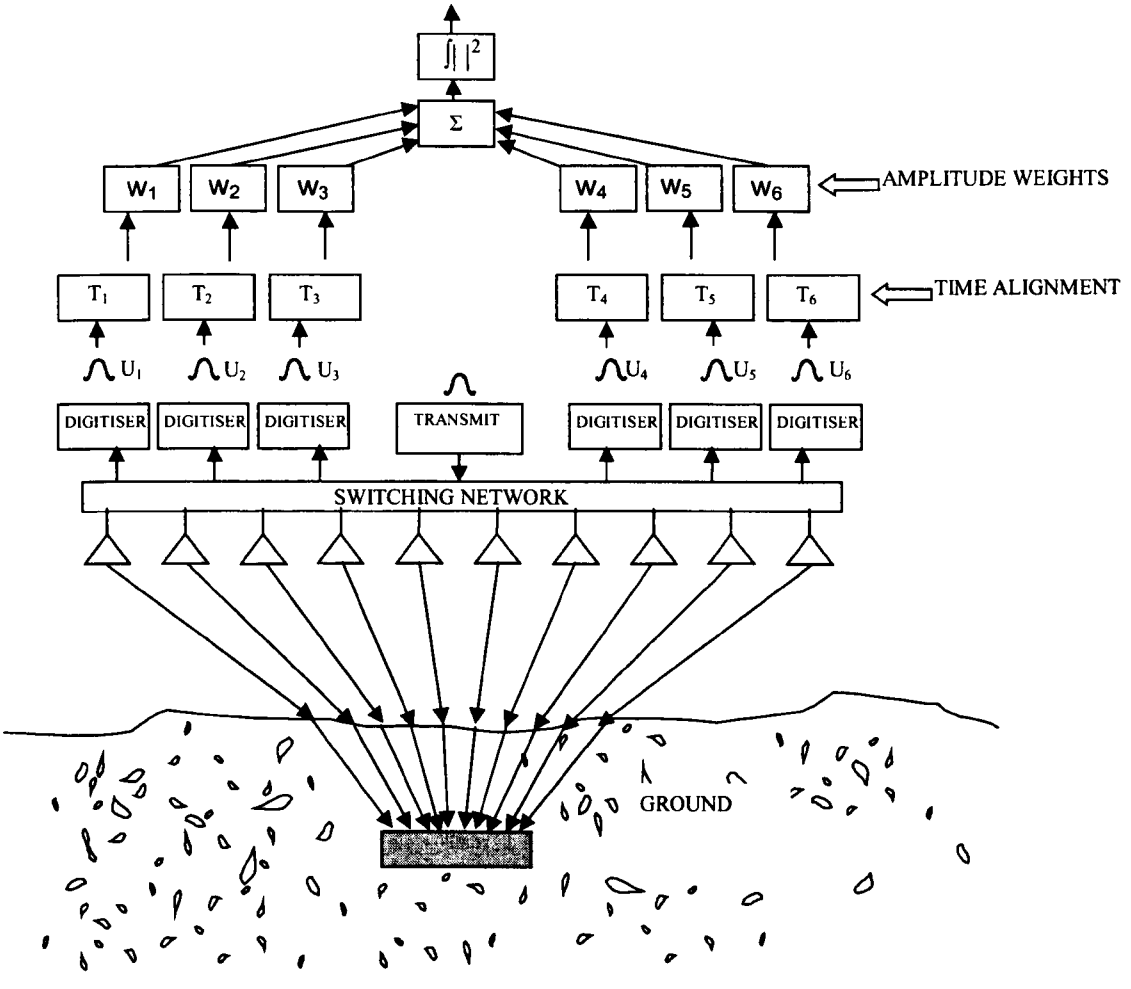

Figure 3-11 RASOR schematic in one dimension

All elements of the array transmit a wideband pulse in turn; all elements sharing any operationally relevant 3D field of view with the current transmit element then record the received signal. By predicting the path delay from the transmit antenna via any desired resolution cell to any receiving antenna, it is then possible to retrospectively extract and

time-align all the signals from the resolution cell. The return associated with this resolution cell is therefore:

$$V = \int_0^{\tau} \left(\sum_{i=1}^{N} w_i U_i(t - T_i) \right)^2 dt \qquad \textbf{(3-10)}$$

where $U_i(t)$ is the signal received from path i, N is the number of paths associated with the resolution cell, w_i is a weighting factor associated with the attenuation, spreading losses and susceptibility to clutter along path i, and T_i is the path delay associated with the trip to and from the resolution cell. Examples of practical weightings will be described in detail in Chapter 4. Knowledge of this path delay requires estimation of the in-ground propagation velocity and will of course ultimately fail if the ground is highly inhomogenous (this will also be explained more fully in Chapter 4). As shown above, the return associated with the resolution cell is computed by integrating the power in the sum of time-aligned and weighted signals, over a window corresponding to the transmit pulse width. This process is repeated for all resolution cells.

A rather exaggerated example of the alignment process is shown in Figure 3-12. Figure 3-12 (a) shows a set of three received A-scan signals obtained from three antenna positions. The scattering from a target will appear at different points in these A-scans due to the different propagation times. Figure 3-12 (b) shows the signals after they have been time aligned for a particular focusing cell corresponding to the target position. Figure 3-12 (c) shows the focused signal after the A-scans have been added together. The target signals have added constructively, i.e. are coherently combined whereas the noise will in general combine incoherently.

In practice of course the target signal will not be so obviously discernible in any particular A-scan. In practice only after the focusing process is complete will the signal be distinguishable from the background noise and clutter. The more received signals that are received then the greater the constructive effect of the process. In other words for any particular focusing point the *processing gain* of the system over background noise is directly proportional to the number of unique antenna measurements that have the resolution cell within its field of view. This will be explained further in Chapter 4.

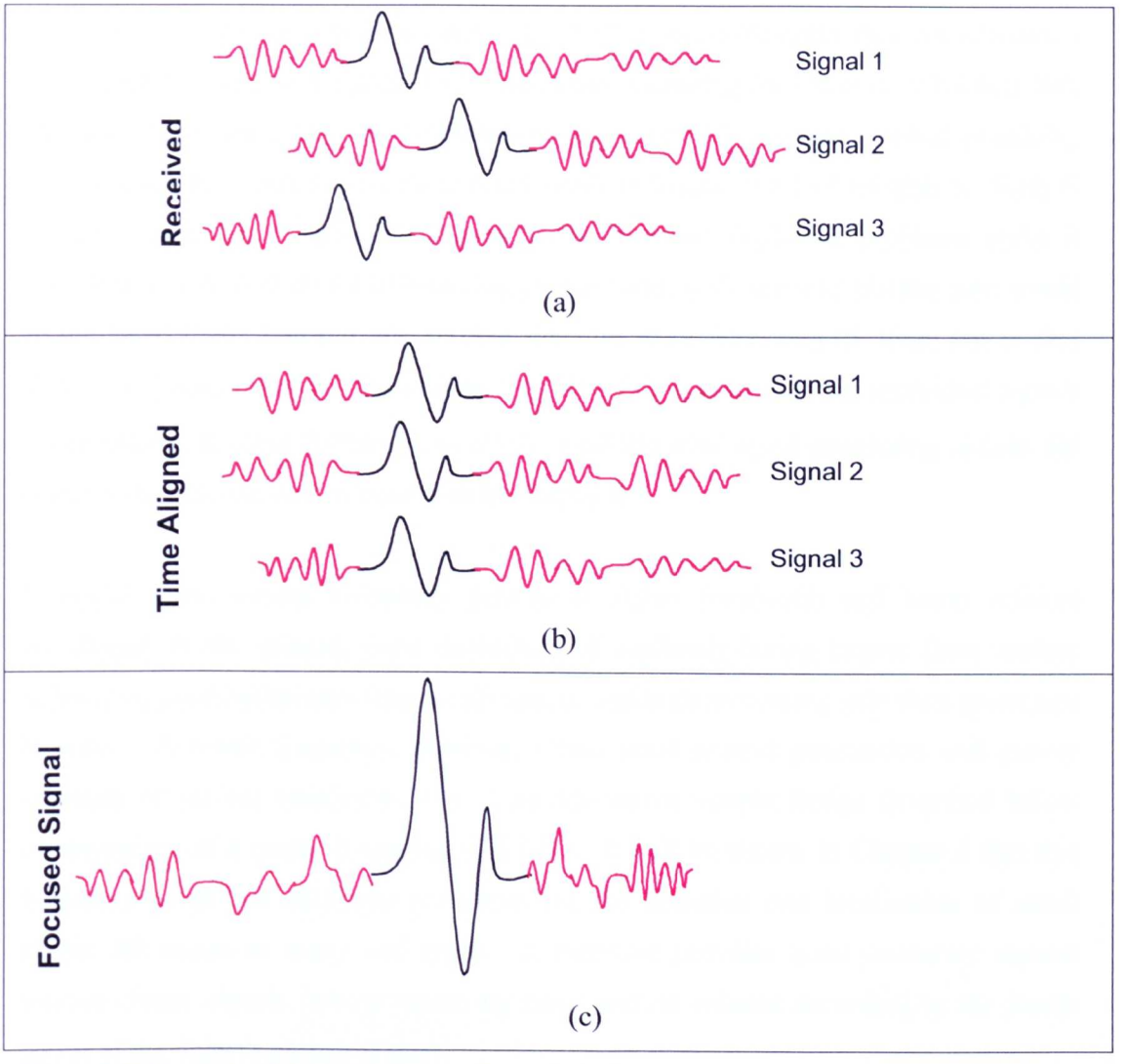

Figure 3-12 Example of time alignment and focusing (a) received signals, (b) time aligned signals, (c) focused signal

It is important to note that this is a fundamentally different mode of operation to Synthetic Aperture Radar (SAR) technique. RASOR generates distinct signals from all possible combinations of transmit and receive elements forming a fully-populated array (quite unlike [47], for example). In contrast, SAR usually relies upon vehicle movement[1] to generate a complete array aperture - this reduces the physical size of the array but consequentially loses valuable information from bistatic paths. The utilisation of information from the large number of independent bistatic paths gives RASOR greater immunity to clutter, since scattering angles and paths are diversified, at the cost of using a large, fully-populated antenna array.

[1] In practical systems a linear array would be attached to the front of a vehicle.

Figure 3-11 shows, in one dimension, the set of antenna elements that can observe a given resolution cell in the ground (in one plane), including the effect of refraction, but, for simplicity representing the antenna element pattern by a single uniform mainlobe, without sidelobes. This is covered in more detail in Section 5.1.1 of Chapter 5. With N elements, there are N^2 possible bistatic paths, however duplexing problems make it unattractive to receive on the transmitting element and, since the total bistatic path would be the same if the transmit and receive function were interchanged, there are in fact $N(N-1)/2$ unique paths per resolution cell. The ability to identify the individual signals corresponding to these distinct paths offers important new signal-processing options for clutter reduction that will be described in Chapter 4.

A higher pulse central frequency permits a higher bandwidth and lower relative wavelength in the ground, good distinction of shallowly-buried targets from surface reflections, good backscatter from small targets, and high processing gain for a given size of array. A lower frequency, however, offers good ground penetration and greater tolerance of surface roughness [48]. The illustrative sample design described below compromises on a centre frequency of 1 GHz. It will be shown in Chapter 4 that this frequency gives just sufficient resolution for the detection and localisation of small plastic AP mines in many soil types. It therefore provides good immunity against smaller clutter objects (whose scattering cross section reduces according to the fourth power of the object's electrical size).

3.3.2 Proposed Design

There are a number of system parameters that can be varied to alter the performance of this system. Optimisation is difficult without the ability to 'fix' some parameters initially, though these may be varied at a later stage. As a starting point for system analysis and based on practical design considerations a horizontal rectangular array at 0.75 λ_a spacing was suggested, where λ_a is the pulse's centre-frequency wavelength in air of 30cm. Selection of antenna element spacing is a trade-off. Large element spacing reduces mutual coupling between antenna elements. Too wide a spacing may not give sufficient overlapping paths for focusing and thus reduces processing gain. It also risks introducing grating lobes due to spatial under-sampling.

An array-to-ground spacing of $2\lambda_a$ and an element beam-width of ±45° implies an array width of $\pm 2\lambda_a$, merely to focus onto the surface centre-line. To cover the in-soil divergence of the beam, a further $\pm 2\lambda_a$ is provided, sufficient to maintain full gain and resolution for virtually any practical refractive index and burial depth, e.g. 66 cm at a refractive index of 5, with λ_a=30 cm. This requires an array width of 8 elements. To reduce mutual coupling further, these could be arranged in two interleaved sets of four coplanar elements, spaced at $1.5\lambda_a$ centre-to-centre, separated along the length of the array by $0.375\lambda_a$, maintaining an effective $0.75\lambda_a$ length-wise spacing as shown in Figure 3-13.

Naming each set of four elements a "column", 18 columns cover a sweep-width of 2 m. To focus with full gain onto the extremities of this sweep, a further seven columns are placed beyond each end, giving 32 columns and a size of approximately 3.5m by 1.75m (32 columns of 4 elements, 128 elements in total). Through application of the focussing process described above, the array generates a picture of a 2m wide vertical scan underneath its major axis. This can be considered to be a C-scan (see section 3.1.4), orientated in x-z plane. As the vehicle is swept forward additional vertical scans are obtained[1] every 10cm building up a 3D image of the soil.

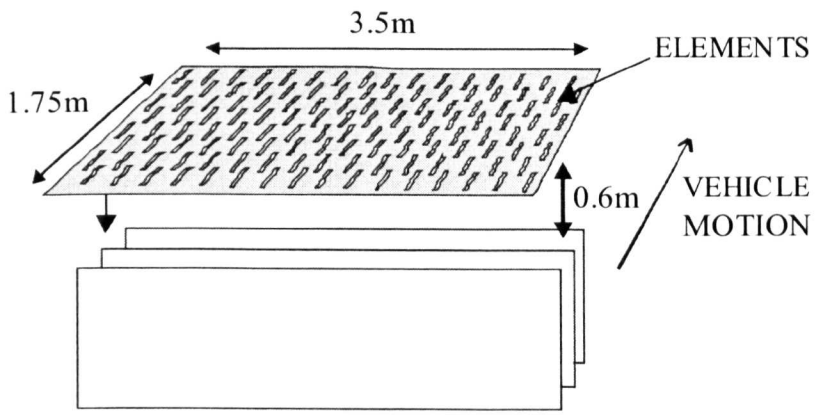

Figure 3-13: Array and stack of three scanned planes.

In the ground, the convergence angle θ (from Figure 3-10) is reduced by refraction, approximately as $1/\sqrt{\varepsilon}$ (where ε is the dielectric constant of the ground). It has been

[1] A set of 3 simple ultrasound or infra-red distance sensors can record the mean height and orientation of the array to the ground. Simple mechanical actuators would control the approximate position of the array and any departures from the ideal array position can be allowed for in processing.

postulated [49] that a lateral resolution of $\lambda_g / 2\theta$ would be achieved. The depth of focus, $2\lambda_g / \theta^2$ [49] increases (is degraded) as $\sqrt{\varepsilon}$, but only up to the point where it is limited by the pulse-length in the ground, $n\lambda_a/(2\sqrt{\varepsilon})$, where n is the number of cycles in the pulse length. This is dealt with in more detail in Section 0 of Chapter 4.

3.3.3 Operational Scenario

In deriving the RASOR system concepts thought has been given to the practicalities of an operational GPR system for landmine detection.

3.3.3.1 Search Rate

When advancing into an uncleared area, the array would be mounted on a boom ahead of the vehicle and a swathe 2m wide would be cleared as shown in Figure 3-14.

The vehicle might be built to be immune to anti-personnel mines. If anti-tank mines have to be faced, its speed would be limited by the need to stop before it is over a mine. A boom extension of 5m, and a braking rate of 0.25G, would permit an upper-limit speed of 18km/hr (assuming automatic warning and application of the brakes). A tracked vehicle with a 10m boom and a braking rate of 1G would permit a speed of 50 km/hr, and this speed could clearly also be used freely by a vehicle with a laterally projecting array, to extend the periphery of a cleared area.

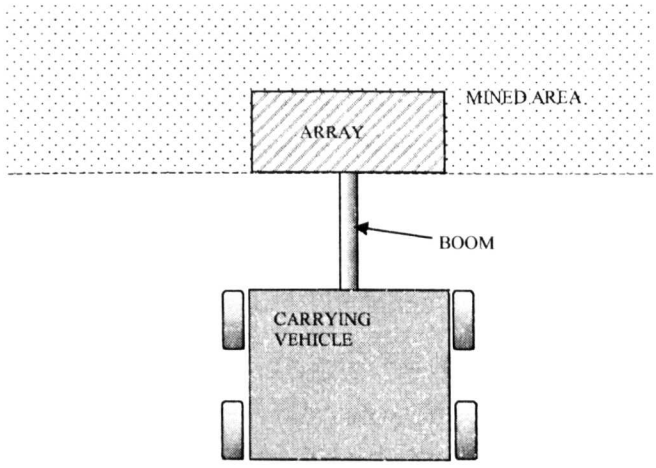

Figure 3-14 Vehicle mounted Array

The overall mine *clearance* rate is however likely to be determined by the time taken to respond to the putative mines discovered, be they real or false alarms. Hence a more modest speed v of 5 m/s (18 km/hr i.e. 11.2 mph) is assumed below.

3.3.3.2 The Effect of Vehicle Motion

A 30 cm advance of the vehicle, in the time taken to collect the data to generate a 30 cm thick stack of three 2m wide vertical scans, is equivalent to an 8.6° right-to-left skew of

these vertical scans. The data collection can be arranged so that it sweeps from left to right across the array, allowing for this tilt compensates for vehicle motion and so maintains data coherence. A vehicle speed of $v = 5$ m/s allows 60 ms to collect one such three-scan data "frame", in parallel with processing the data from the preceding frame. This represents a data collection and real time processing challenge and will be discussed further in subsequent chapters.

3.4 Conclusions

This chapter has described the hardware and processing that make up a generic GPR system. Alternative system designs have been considered with an evaluation of the their respective advantages and disadvantages.

An outline of the theoretical concepts of RASOR GPR has been given. Its advantages have been highlighted over other GPR in the field of landmine detection, with regards to search rate, resolution and performance against clutter, showing it to be worthy of further evaluation.

References

[1] A.Andrews, J.Ralston, M.Tuley, 'Research on Ground Penetrating Radar for detection of mines and unexploded ordinance: Current status and research strategy', Institute for Defense Analyses, D-2416, December 1999

[2] C.King, 'Demining: Enhancing the process', 2nd Intenational Conference on the Detection of Buried Land-Mines, Edinburgh, UK, pp1-9, October 1998

[3] M.Fritze, 'Detection of buried landmines using ground penetrating radar', Proc. SPIE, Vol. 2496, pp100-108, 1995.

[4] K.Gerlitz, M.Knoll, G.Cross, R.Luzitano, R.Knight, 'Processing ground penetrating radar data to improve resolution of near surface targets', Proc. SAGEEP, Geophysics, 1993, pp561-574

[5] T.B.Hansen, P.M.Johansen, 'Inversion scheme for ground penetrating radar that takes into account the planar air-soil interface', IEEE . Trans.Geosci. Remote Sens., Vol 38, No.1, pp496-506, 2000

[6] J.W.Brooks, L.van Kempen, H.Sahli, 'A primary study in adaptive clutter reduction and buried minelike target enhancement from GPR data', Proc. SPIE, vol 4038 (II), pp1183-1192, 2000

[7] L.C.Chan, L.Peters, D.L.Moffat, 'Improved Performance of a subsurface radar target identification system through antenna design', IEEE Trans. Ant. Prop., Vol. 29 No.2, pp307-311, 1981

[8] D.J.Daniels, 'Short pulse radar for stratified lossy dielectric layer measurements', Proc. IEE, Vol. 127. Part F, No.5, 1980

[9] L.Carin, N.Geng, M.McClure, J.Sichina, L.Nguyen, 'Ultrawideband synthetic aperture radar for mine field detection', IEEE Ant. Prop. Mag., Vol.41 No.1, pp18-33, 1999

[10] T.P.Montoya, G.S.Smith, 'Land mine detection using Ground-Penetrating Radar based on resistively loaded vee dipoles', IEE Trans. Ant. Prop., Vol 47. No.12, pp1795-1806, December 1999

[11] G.H.Brown, .M.Woodword Jr, 'Experimentally determined radiation characteristics of conical and triangular antennas', RCA Review, vol. 13, pp425-452, 1952

[12] R.Nilavalan, G.S.Hilton, R.Benjamin, 'Wideband printed bowtie antenna element development for post reception synthetic focusing surface penetrating radar', Electronics Letters, Vol.35 No.20, pp1771-2, 1999

[13] D.J.Daniels, 'Surface Penetrating Radar', IEE, 1996, Chapter 5.

[14] T.Moriyama, et al, 'Advanced polarimetric subsurface FM-CW Radar', IEEE Trans. Gesc. Rem. Sens., Vol. 36 No. 3, pp725-731, 1998

[15] L.A.Robinson, W.B.Weir, L.Young, 'Location and recognition of discontinuities in dielectric media using synthetic RF pulses', Proc. IEEE, Vol. 62, No. 1, pp36-44, 1974

[16] R.P.Dooley, 'X-band holography', Proc. IEEE, Vol. 53, pp1733-1736, 1965

[17] A.P.Anderson, R.D.Ohme, 'Multilevel computer-processed displays of small concealed objects remotely imaged by microwave holography', AEU, Vol. 31 No.4, pp150-156, 1977

[18] Infinium Service Guide, Agilent Technologies, Publication Number 54845-97008, February 2001

[19] R.H.Walden, 'Performance trands for Analog-to-Digital Converters', IEEE Communications Magazine, Feb 1999, pp96-101

[20] D.Adler, M.Jacobs, 'Application of a narrowband FM-CW system in the measurement of ice thickness', Proceedings of IEEE Measurement & Testing Society, International Microwave Symposium, Vol 2, pp809-812, 1993

[21] Y.Yamaguchi, et al., 'Human body detection in wet snowpack by an FM-CW radar', IEEE Trans. Geosci. Remote Sens., Vol 31, pp186-189, 1992

[22] O.Yilmaz, 'Seismic Data Processing', Society of Exploration Geophysicists, Tulsa, USA, 1987

[23] M.S.Zhdanov, P.Traynin, J.R.Booker, 'Underground imaging by frequency-domain electromagnetic migration', Geophysics, Vol.61 No.3, pp666-682, 1996

[24] N.Osumi, K.Ueno, 'Detection of buried plant', IEE Proc., Vol.135, Pt F, No. 4, Aug 1988

[25] E.M.Johansson, J.E.Mast, 'Three-dimensional ground penetrating radar imaging synthetic aperture time-domain focusing', Proc. SPIE, Vol.2275, pp205-214, Sep 1994

[26] T.Kaneko, 'Radar image processing for locating underground linear objects', IECIE Trans., Vol.74 No.10, pp3451-3459, 1991

[27] J.W.Brooks, 'The detection of buried non-metallic anti-personnel land mines', PhD dissertation, University of Alabama, 2000

[28] M.Scanlan, 'Modern Radar Techniques', Collins, 1997

[29] S.J.Radzevivius, J.J.Daniels, 'Ground penetrating radar polarization and scattering from cylinders', J. App. Geoph., Vol. 45, pp111-126, 2000

[30] J.Thaysen, K.B.Jakobsen, J.Appel-Hansen, 'Circular polarised stepped frequency ground penetrating radar for humanitarian demining', Proc. SPIE, Vol.4394 No.2, pp671-679, 2001

[31]D.J.Daniels, 'Surface Penetrating Radar', IEE, 1996, Chapter 4

[32] J.Van Der Kruk, 'Use of cross dipole antennas in 3D imaging of multicomponent GPR data', SEG Intl. Exp., San Antonio, Sep 2001

[33] H.Mott, 'Polarisation in Antennas and Radar', Wiley, New York, 1986

[34] S.R.Vechinski, T.H.Shumpert, 'Natural resonances of conducting bodies of revolution', IEEE Trans. Ant. Prop, Vol. 38, pp1133-1136, July 1990

[35] C.Chen, L.Peters,'Buried unexploded ordance identification via complex natural resonances',IEEE Trans. Ant. Prop., Vol. 45, No. 11, Nov 1997

[36] C.E.Baum, 'The singularity expansion method and its application to target identification', Proc IEEE, Vol. 79, pp 1481-1491, Oct 1991

[37] C.E.Baum, 'The discrimination of buried targets via the singularity expansion', Inverse Problems, Vol.13, pp557-570, 1997,

[38] A.P.Anderson, R.D.Ohme, 'Multilevel computer-processed displays of small concealed objects remotely imaged by microwave holography', Proc. IEE, Vol.133 No.1, pp22-23, 1975

[39] R.Karg, 'Multifrequency microwave holography', AEU, Vol.31 No.4, pp150-156, 1977

[40] J.Nakayame, H.Ogura, M.Fujiwara, 'Multifrequency hologram matrix and its application to two-dimensional imaging', Proc. IEEE, Vol.66 No.10, 1978

[41] N.Farhat, 'Computer simulation of frequency swept imaging', Proc. IEEE, Vol.64 No.9, pp1453-1454, 1976

[42] N.Osumi, K.Ueno, 'Microwave holographic imaging method with improved resolution', IEEE Trans. Ant. Prop, Vol.AP-32 No.10, pp1018-1026, Oct 1984

[43] N.Osumi, K.Ueno, "Microwave holographic of underground objects', IEEE Trans. Ant. Prop, Vol.AP-33 No.2, pp152-159, Feb 1985

[44] N.Osumi, K.Ueno, 'Detection of buried plant', Proc. IEE, Vol.135 Pt.F No.4, pp330-342, Aug 1988

[45] R.Benjamin, 'Near-field spot focused microwave sensing for the detection of buried landmines', Proceedings of the EUREL/IEE International Conference on the Detection of Abandoned Land Mines, IEE, Edinburgh, pp128-132, Oct 1996

[46] D.H.Johnson, 'Array Signal Processing: Concepts and Techniques', Prentice Hall, 1993

[47] E.S.Eide, J.F.HJELMSTAD, 'The development of an advanced mine detection system at the Norwegian University of Science and Technology', Proc. IEE/EUREL Conference on the detection of buried landmines, Edinburgh,1998, pp.101-104

[48] P.Beckmann, A.Spizzichino, 'The scattering of electromagnetic waves from rough surfaces', Artech House, 1987

[49] R.Benjamin, 'Synthetic-aperture antennas',Microwave Journal, 1995, Vol. 38, No. 9, pp68-81

4 Analysis of Real Aperture Synthetically Organised Radar

This chapter will develop the RASOR system concepts more rigorously using analytical modelling supported by early concept proving experiments conducted in a controlled environment. First the principles of electromagnetic propagation and the electrical properties of various soils are introduced. The various loss, de-correlation, and clutter mechanisms are then analysed and the novel solutions that RASOR offers to mitigate these effects are introduced.

4.1 Fundamentals

4.1.1 Principles of Electromagnetic Propagation

Radar is based on the propagation of electromagnetic waves, where energy is transmitted in the form of an electromagnetic field. An electromagnetic wave consists of an electric field intensity **E** and a magnetic field intensity **H** that vary normal to each other and transversely to the direction of propagation as predicted by Maxwell's equations [1]. Figure 4-1 shows a planar electromagnetic field that could be observed at some distance from the radiating antenna.

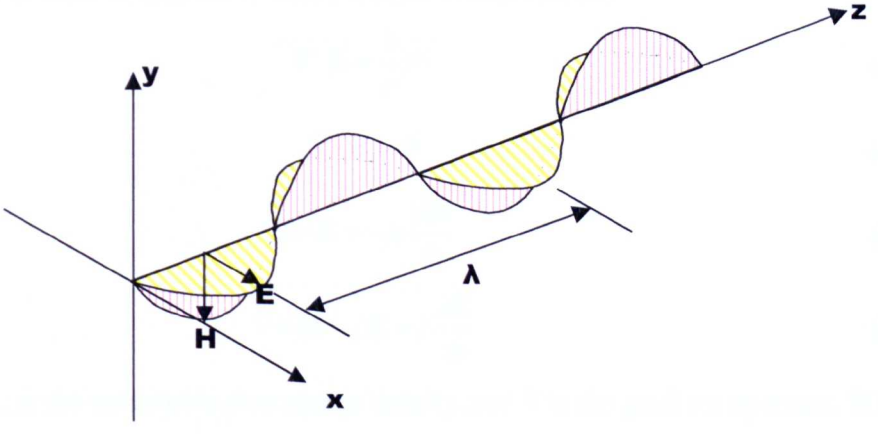

Figure 4-1 Plane wave propagation

The wavelength, λ, is the distance between repetitions of a wave peak. Frequency, f, is defined as the number of wave peaks to travel one wavelength per unit time. In radar, by convention, the wave is said to be polarised according to the direction of the **E** field

vector. In Figure 4-1, for example, the E field is pointing horizontally along the x-axis and so the wave is said to be horizontally polarised.

The electromagnetic properties of a medium are defined by three parameters **conductivity** σ, **permittivity** ε, and **permeability** μ. If the medium through which the wave is travelling is linear and isotropic then three constitutive equations can be written

$$\mathbf{J} = c\,\mathbf{E} \tag{4-1}$$

$$\mathbf{D} = \varepsilon\,\mathbf{E} \tag{4-2}$$

$$\mathbf{B} = \mu\,\mathbf{H} \tag{4-3}$$

Equation (4-1) relates the E field and the electrical conductivity of the medium to the current density vector, **J**. This is often referred to as Ohm's law. Equation (4-2) relates the **E** field and the dielectric permittivity of the medium to the electric flux density vector, **D**. Equation (4-3) relates the **H** field and the magnetic permeability of the medium to the magnetic induction, **B**.

Using these three constitutive equations it is possible to re-write Maxwell's equations in differential form to help show their physical interpretation:

$$\nabla \cdot \mathbf{E} = \frac{1}{\varepsilon}\rho_v \tag{4-4}$$

$$\nabla \cdot \mathbf{H} = 0 \tag{4-5}$$

$$\nabla \times \mathbf{E} = -\mu \frac{\mathrm{d}\mathbf{H}}{\mathrm{d}t} \tag{4-6}$$

$$\nabla \times \mathbf{H} = \sigma\mathbf{E} + \varepsilon \frac{\mathrm{d}\mathbf{E}}{\mathrm{d}t} \tag{4-7}$$

where ρ_v is the volumetric free charge density and ∇ is the gradient operator. When there is no free charge in the medium ρ_v=0 and it is said to be electrically neutral.

Manipulating and combining (4-6) and (4-7), the variation of electrical and magnetic field intensity in space and time can be described by

$$\nabla^2 \times \mathbf{E} = \mu\sigma \frac{\partial \mathbf{E}}{\partial t} + \mu\varepsilon \frac{\partial^2 \mathbf{E}}{\partial t^2} \tag{4-8}$$

$$\nabla^2 \times \mathbf{H} = \mu\sigma \frac{\partial \mathbf{H}}{\partial t} + \mu\varepsilon \frac{\partial^2 \mathbf{H}}{\partial t^2} \tag{4-9}$$

In free space and air - to a good approximation - the conductivity σ=0 and the plane wave in Figure 4-1 propagating in the z direction can be represented by

$$\frac{\partial^2 \mathbf{E}}{\partial z^2} = \frac{1}{v^2} \frac{\partial^2 \mathbf{E}}{\partial t^2} \tag{4-10}$$

where v is the propagation velocity (or phase velocity) in metres per second generally given by

$$c = \frac{1}{\sqrt{\mu_0 \varepsilon_0}} = \frac{1}{\sqrt{(4\pi \times 10^{-7})(8.854 \times 10^{-12})}} = 2.998 \times 10^8 \text{ m} \setminus \text{s} \tag{4-11}$$

where μ_0 and ε_0 are the free space permeability and permittivity constants, respectively. It should be noted that in the antenna near-field plane wave propagation can not be assumed and the electromagnetic wave front will look more like the example shown in Figure 4-2 for a balanced dipole.

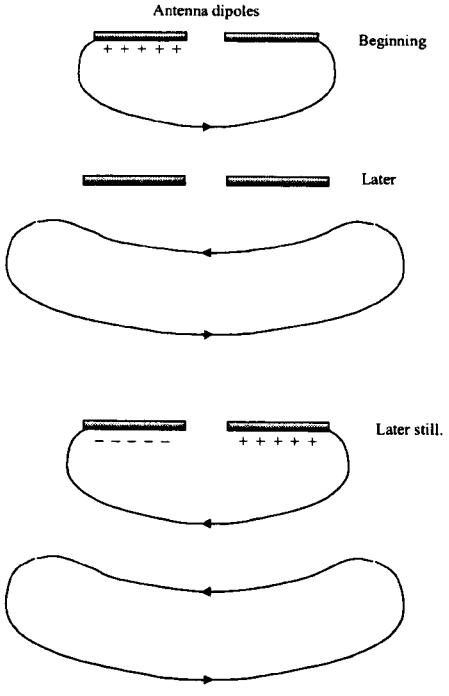

Figure 4-2 Near field wave propagation

4.1.2 Propagation in Dielectric Materials

In a material other than air the propagating electric and magnetic fields apply forces and torque on the material structure that cause the material to be polarised and magnetised [2]. The response of the material to these forces are out of phase with the excitation and is described by the absolute permittivity and permeability of the material by

$$\varepsilon = \varepsilon_0 \varepsilon_r \tag{4-12}$$

$$\mu = \mu_0 \mu_r \tag{4-13}$$

where μ_r and ε_r are generally complex quantities stated as

$$\varepsilon_r = \varepsilon' - j\varepsilon'' \tag{4-14}$$

$$\mu_r = \mu' - j\mu'' \tag{4-15}$$

For non-ferromagnetic materials μ_r=1 (as for free space) and therefore magnetisation effects are assumed to be of minor importance in GPR [3] .

The forces introduced by polarisation are opposed by thermodynamic molecular forces which implies an energy loss in addition to those due to conduction losses [4]. The losses associated with conductivity and polarisation are normally assumed to be in-phase to give an effective imaginary permittivity

$$\varepsilon''_{eff} = \varepsilon'' + \frac{\sigma}{\varepsilon_0 \omega} \tag{4-16}$$

where ω is the angular frequency of excitation in radians. It can be seen that as ω increases the effect of the conduction losses decrease. The ratio between the effective imaginary permittivity and the real permittivity is a measure of the loss of the material called the loss tangent

$$\tan\delta = \frac{\varepsilon''_{eff}}{\varepsilon'} \tag{4-17}$$

The loss of the material is therefore frequency dependent and generally determined by its polarisation and conductivity properties.

A solution to (4-8) for the sinusoidal variation in space and time shown earlier in Figure 4-1 can be described by the equation

$$E_x = E_0 e^{j\omega - \kappa z} \tag{4-18}$$

where ω is the angular frequency and κ is known as the propagation constant. Substituting (4-18) into (4-8) and solving for κ gives

$$\kappa = \sqrt{j\omega\sigma\mu - \omega^2\varepsilon\mu} \tag{4-19}$$

which can be rearranged using (4-11) and (4-14) to give

$$\kappa = \frac{\omega}{c}\sqrt{-\varepsilon'\mu + j\left(\varepsilon'' + \frac{\sigma}{\varepsilon_0\omega}\right)} = \frac{\omega\sqrt{\varepsilon'\mu}}{c}\sqrt{(-1 + j\tan\delta)} \tag{4-20}$$

(4-20) can be written in complex number form as

$$\kappa = \alpha + j\beta \tag{4-21}$$

where

$$\alpha = \frac{\omega}{c}\sqrt{\frac{\varepsilon'\mu}{2}\left(\sqrt{1+\tan^2\delta} - 1\right)} \tag{4-22}$$

and

$$\beta = \frac{\omega}{c}\sqrt{\frac{\varepsilon'\mu}{2}\left(\sqrt{1+\tan^2\delta} + 1\right)} \tag{4-23}$$

inserting (4-22) and (4-23), equation (4-18) can be rewritten

$$E_x = E_0 e^{-\alpha z} e^{j(\omega t - \beta z)} \tag{4-24}$$

where the first exponential containing α is effectively a measure of the attenuation of the electric field with distance z and β is the wave number.

α can be used to gain a useful insight into the propagation properties of the medium in the three cases $\tan\delta << 1$ (loss less medium), $\tan\delta \approx 1$ and $\tan\delta >> 1$ (lossy medium).

$$\tan\delta << 1 \qquad \alpha = \frac{\omega\sqrt{\varepsilon'}}{2c}\tan\delta \tag{4-25}$$

$$\tan\delta \approx 1 \qquad \alpha = 0.46\frac{\omega\sqrt{\varepsilon'}}{c} \tag{4-26}$$

$$\tan\delta >> 1 \qquad \alpha = \frac{\omega}{c}\sqrt{\frac{1}{2}\varepsilon''_{eff}} \tag{4-27}$$

Note: $\lim_{a\to 0}\left(\sqrt{1+a^2}\right) = 1 + \frac{a^2}{2}$

4.1.3 Dielectric Properties of Soil

The dielectric properties of earth materials depend on several factors such as texture and density of soil particles, volumetric water content and temperature [4]. Soil particles are generally categorised into one of three types: clay, silt and sand. A particular soil is a mixture of these types with the constituent quantities of the mix determining soil 'class'. For example, a soil with 20% clay, 50% sand and 30% silt belongs to the class of soils known as loam.

The mixture of soil particles determines the amount of free and bound water it contains where bound water refers to water molecules that are held together by the soil particles and free water refers to water molecule that are free to move. Bound water and free water tend to have different relaxation behaviour, i.e. their polarisation properties differ. The amount of water content also affects the conductivity properties of the soil. The water content is therefore a fundamental parameter in determining the soil dielectric properties [5].

The determination of the dielectric properties is largely experimental although some work has focused on devising theoretical and empirical models for different soils encountered in the field. Examples of these are [6] and [7] for frequencies ranging from 1.4 to 18GHz and [8] for frequencies from 0.3 to 1.3GHz.

An empirical estimation of the attenuation coefficient in dB/m can be obtained from [4]:

$$\alpha' = 8.686 d\alpha \quad \text{(dB/m)} \tag{4-28}$$

Where:

α is the attenuation coefficient from (4-22)

d is the total path length in soil in metres.

The variation of the dielectric properties of example soils with moisture content at a frequency of 1.5GHz is given by [15] and shown in Table 4-1

Soil Type	Moisture Content (%)	ε'	ε''	α (dB/m)
Sandy Loam	0.1	6	1	55.5
	0.3	17	3	98.9
	0.5	48	5	98.3
Loam	0.1	5.5	1	57.9
	0.3	17.5	3.2	103.9
	0.5	41	5.4	114.8
Silty Loam	0.1	5	1	60.7
	0.3	16	3.4	115.3
	0.4	37.5	6	133.3
Silty Clay	0.1	4	1	67.7
	0.3	18	4	127.9
	0.5	31	9	218.3

Table 4-1 Dielectric properties of example soil types at 1.5GHz

4.1.4 Dielectric Measurements

A new method of measuring the dielectric properties of sand was developed to measure the contents of the sandbox *in situ*. The complex dielectric constant of soil was measured using two ground probes. The ground probes were matched to the soil at 1 GHz to perform the measurements at the operating frequency of the proposed system. The ground probe configuration is shown in Figure 4-3.

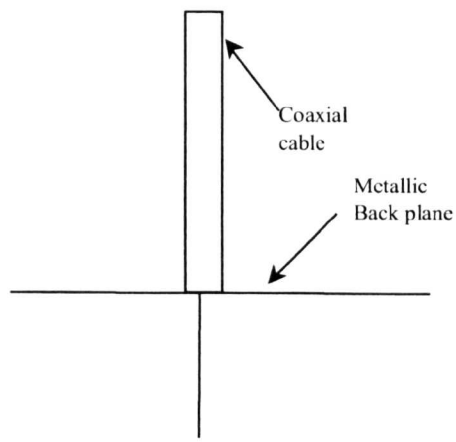

Figure 4-3 The ground probe

The ground probes were monopoles with metallic back plane measuring 5 cm. These ground probes were inserted in the ground with the metallic back plane on the soil-air interface. The back plane was kept large enough to ensure the measured dielectric properties do not significantly incorporate the free space characteristics. Great care was needed to ensure that no air gaps were present between the ground plane and earth.

A three-cycle pulse modulated at 1GHz was transmitted into the soil using a transmitting ground probe and observations were made at eight different receiving locations, as shown in Figure 4-4, using the second probe. The time delays associated with the displacements were measured and averaged to calculate the velocity of the transmitted energy in soil (yielding the real permittivity).

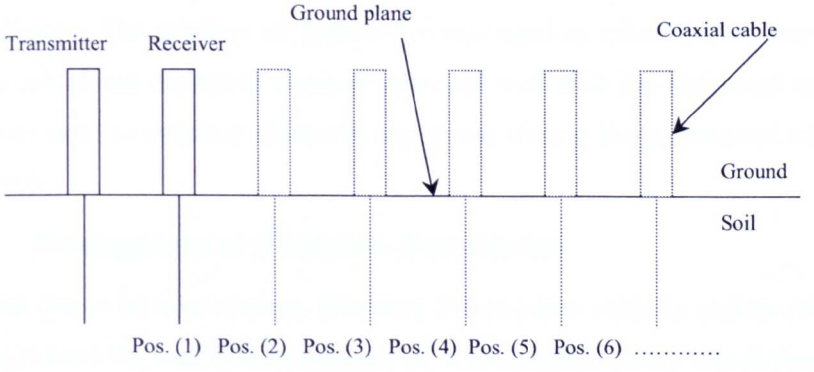

Figure 4-4 Dielectric measurement set-up

The received signal power was measured at 1GHz and plotted against displacement in Figure 4-5.

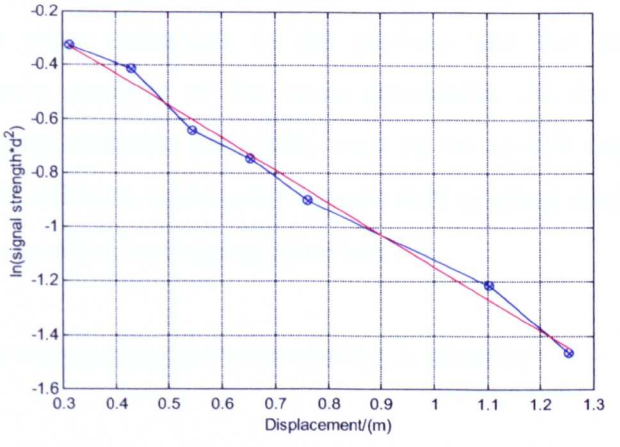

Figure 4-5 Variation of signal strength at 1GHz with displacement

Signal strength at the receiver location can be represented by,

$$\frac{P_r}{P_t}=\left[\frac{\lambda_{soil}}{4\pi d}\right]^2 \times e^{2\alpha} \times G \qquad \textbf{(4-29)}$$

Where

$$\alpha=2\pi df\sqrt{\frac{\mu_o\mu\varepsilon_o\varepsilon_r\left[\sqrt{\left(1+\tan^2\delta\right)}-1\right]}{2}} \qquad \textbf{(4-30)}$$

P_r and P_t are the received and the transmitted power

α is the soil attenuation

d is the distance between transmitter and receiver

G is the transmitter receiver gain

These theoretical predictions were matched with the observed results using appropriate axis selections. The gradient of Figure 4-5 was used to calculate the loss factor of the soil. The calculated dielectric constant matched well with the estimated values and this method was used to estimate dielectric properties during the subsequent trials described in Chapter 6.

4.1.5 Propagation at Dielectric Boundaries

The system has to be non-contact, therefore the antennas initially radiate into air, but the signal encounters the soil within a couple of wavelengths. Hence the dielectric boundary needs to be considered between air and soil. Furthermore boundaries between targets and the surrounding soil and other stratification, which constitute clutter for this system, will also give rise to reflections.

In general it can be stated that the real permittivity indicates the amount of velocity dispersion that the wave undergoes in the medium and the imaginary effective permittivity provides a measure of the wave attenuation. At the boundary of two materials with differing dielectric properties, such as the air-soil interface, part of the incident wave will be reflected, undergoing a phase shift or phase discontinuity, and part will pass through the material undergoing refraction [9].

The electromagnetic wave propagates with velocity, v, given by

$$v = \frac{\omega}{\beta} = \frac{c}{\sqrt{\frac{\varepsilon'\mu}{2}\left(\sqrt{1+\tan^2\delta}+1\right)}} \tag{4-31}$$

Where ω is the angular frequency and β is the imaginary component of the propagation constant defined in (4-32) which is also termed the refractive index of the medium, n. The velocity is therefore frequency dependent and it can be seen that for $\tan\delta << 1$ this becomes

$$n = \frac{c}{v} = \sqrt{\varepsilon'\mu} \tag{4-33}$$

The intrinsic impedance of the medium, η is given by

$$\eta = \sqrt{\frac{\mu}{(\varepsilon' - j\varepsilon'')}} \text{ ohms} \tag{4-34}$$

and the power reflected at the dielectric interface is given by the reflection coefficient, r, which is the ratio between the incident and reflected power

$$r = \frac{\eta_2 - \eta_1}{\eta_2 + \eta_1} \tag{4-35}$$

where the direction of propagation is from the medium with η_1 to that with η_2. However, in a non-conducting medium, and considering a single frequency only, this simplifies to

$$r = \frac{\left(\sqrt{\varepsilon'_2} - \sqrt{\varepsilon'_1}\right)^2}{\left(\sqrt{\varepsilon'_2} + \sqrt{\varepsilon'_1}\right)^2} \tag{4-36}$$

For example, using the values in Table 4-1 the reflection coefficient at the air/soil interface for dry sandy loam would be $r = \frac{\left(\sqrt{6}-1\right)^2}{\left(\sqrt{6}+1\right)^2} = 0.1766$ and in wet silty clay it would be $r = \frac{\left(\sqrt{31}-1\right)^2}{\left(\sqrt{31}+1\right)^2} = 0.4837$ showing how the amount of power that penetrates into the ground reduces as the permittivity increases.

4.2 Loss Mechanisms

Losses associated with propagation in the soil were described in Section 4.1.3. However, in RASOR, and indeed any GPR system, a number of other loss mechanisms exist, and it is necessary to analyse and quantify these losses in order to determine the pulse power

that is needed to achieve an optimum signal to noise ratio (SNR). The total losses associated with a GPR can be represented by [4]:

- Target scattering
- Soil attenuation
- Air/surface boundary losses (2 way)
- Antenna spreading (spacing)
- Antenna mismatch (feedline)
- Antenna efficiency (ohmic losses)
- Switching network and cable losses

Each of these will be considered in turn with regards to the RASOR system using some practical examples from Chapters five and six where appropriate.

4.2.1.1 Target Scattering Loss, L_{sc}

A radiated target reflects some energy back towards the receiver and the remainder is lost either through absorption or by being re-radiated in other directions. This target scattering loss is calculated in terms of the target's Radar Cross Section (RCS), which provides an indication of how well a given target reflects radar energy.

The RCS is defined as the projected area that would intercept the transmitted signal and reflect isotropically an amount that produces the return signal at the receiver [10]. It is measured in square metres and defined by:

$$\sigma = 4\pi \frac{P_s}{P_i} \tag{4-37}$$

where

P_i is the power density of a plane wave striking the target (W/m^2)

P_s is the power per unit solid angle reflected by the target in (W)

Since it can vary over a wide range it is often expressed in dBs referenced to $1m^2$:

$$\sigma^0 = \log\left(\frac{\sigma}{1m^2}\right) \tag{4-38}$$

RCS is a complex function determined by :

- Transmitter and receiver antenna position relative to the target
- Angular orientation of the target relative to the transmitter and receiver antennas.
- Target geometry and material composition
- Frequency

- Antenna polarisation (as explained in section 3.2.1 in Chapter 3)
- Dielectric properties of the surrounding soil

The operational wavelength, λ, relative to the target physical dimensions provides a rule of thumb measure of RCS. There are three cases to consider [11]:

- λ>>Target dimensions. In this case the target is said to be in the Rayleigh Region and the RCS tends to be smaller than the target's physical size.
- $\lambda \approx$ Target dimensions. The target in this case is said to be in the resonance region and the RCS varies significantly but tends to be larger than the physical size of the target size.
- λ<<Target dimensions. When this occurs the target is said to be in the optical region and the RCS is similar to its physical size.

The simplest target shape is a perfectly conducting sphere whose RCS can be determined exactly as $\sigma=\pi r^2$. The RCS estimations for simple target shapes such as flat squares, circular plates and cylinders have been derived using Geometrical Optics, Physical Optics and the Geometrical Theory of Diffraction [11,12]. Nilavalan [15] showed that these approximations compare well with FDTD simulated power measurements from a very simple RASOR. These FDTD simulations showed that the target scattering loss for mine like targets at these frequencies and at various look angles is on average around, L_{sc}=30dB.

4.2.1.2 Soil Attenuation, L_a

Taking the real part of the propagation constant α given by (4-22) a one way attenuation loss in dB per metre can be derived:

$$\text{attenuation loss} = 8.686\alpha d \text{ dB/m} \qquad (4\text{-}39)$$

where d is the depth of penetration in metres. Examples of the attenuation in dB per metre for the same example soil characteristics and frequency was shown in Table 4-1.

4.2.1.3 Air/Soil Interface Losses, L_i

It has already been highlighted that when the electromagnetic pulse reaches the air/soil interface part of the pulse will pass through the interface (under going refraction) and part will be reflected. The reflection constitutes a loss in detection power and occurs on both the transmit path, L_{it}, (air/soil interface) and the receive path, L_{ir}, (soil/air interface).

The reflected component in both these cases constitute losses to the wanted signal that can be written [15] [13] as

$$L_i = L_{it} + L_{ir} = 10\log\left(\left|1-\rho_1^2\right|\right) + 10\log\left(\left|1-\rho_2^2\right|\right) \quad \text{(4-40)}$$

where

$$\rho_1 = \frac{k_1\cos\theta_1 - \sqrt{1-j\tan\delta}\sqrt{1-k_1^2\sin^2\theta_1}}{k_1\cos\theta_1 + \sqrt{1-j\tan\delta}\sqrt{1-k_1^2\sin^2\theta_1}} \quad \text{(4-41)}$$

$$k_1 = \sqrt{\frac{1}{\varepsilon}} \quad \text{(4-42)}$$

θ_1 is the angle of incidence in air for the transmit path

$$\rho_2 = \frac{k_2\cos\theta_2\sqrt{1-j\tan\delta} - \sqrt{1-k_2^2\sin^2\theta_2}}{k_2\cos\theta_2\sqrt{1-j\tan\delta} + \sqrt{1-k_2^2\sin^2\theta_2}} \quad \text{(4-43)}$$

$$k_2 = \sqrt{\varepsilon} \quad \text{(4-44)}$$

θ_2 is the angle of incidence in soil for the return path

4.2.1.4 Antenna Spreading Loss, L_s

The spreading losses are dependent on the antenna radiation pattern. For a particular antenna element radiating over a planar surface as shown in Figure 4-6 the transmit path spreading loss, L_{st}, will be

$$L_{st} = 10\log\left(\frac{G(\theta)\beta}{4\pi}\right) \quad \text{(4-45)}$$

where,

θ is the angle of propagation relative to antenna nadir

$G(\theta)$ is the gain of the antenna at this angle

β is the solid angle (in air) which radiates the focusing cell after refraction.

RASOR transmits on one antenna and uses the received data from all antennas that have a particular resolution cell within their field of view, taken to be the 3dB beamwidth of the antenna as shown in Figure 4-7.

From Figure 4-7 α is the solid angle in the soil that reaches the field of view of these antennas after refraction thus the total spreading loss for all elements that see the target is

$$L_{sr} = 10\log\left(\frac{\alpha}{4\pi}\right) \text{ (dB)} \tag{4-46}$$

The solid angle that reaches area A_i for an individual antenna element is α_i thus the power density at this antenna element is

$$P_d = \frac{\alpha_i}{4\pi A_i} \tag{4-47}$$

And the return path spreading loss, L_{sr}, will be

$$L_{sr} = 10\log\left(\frac{\alpha_i A_{eff}}{4\pi A_i}\right) \text{ (dB)} \tag{4-48}$$

where,

A_i is the physical area for the antenna element i

A_{eff} is the effective aperture of element i given by $A_{eff} = \frac{4\pi G(\theta)}{\lambda^2}$

λ is the wavelength in air

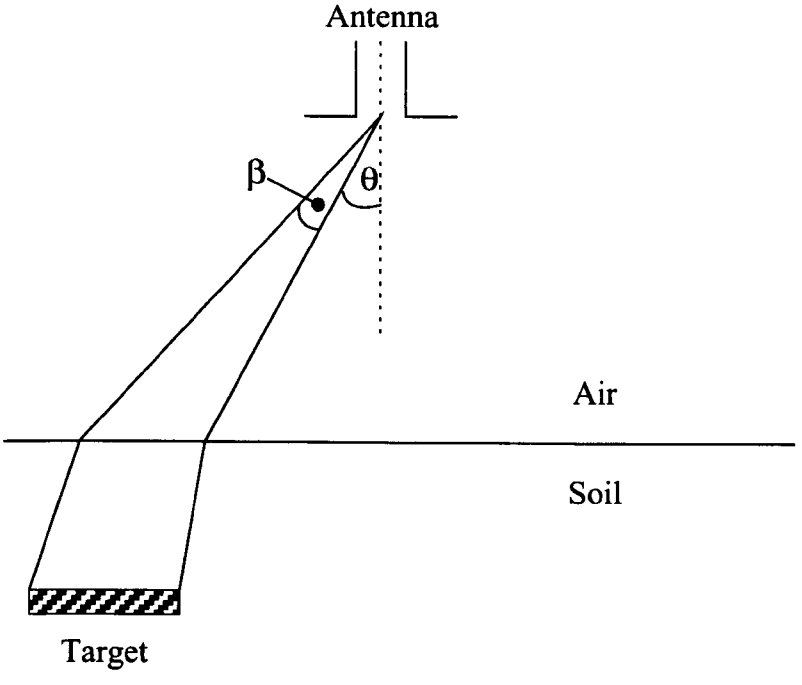

Figure 4-6 Transmit path spreading loss

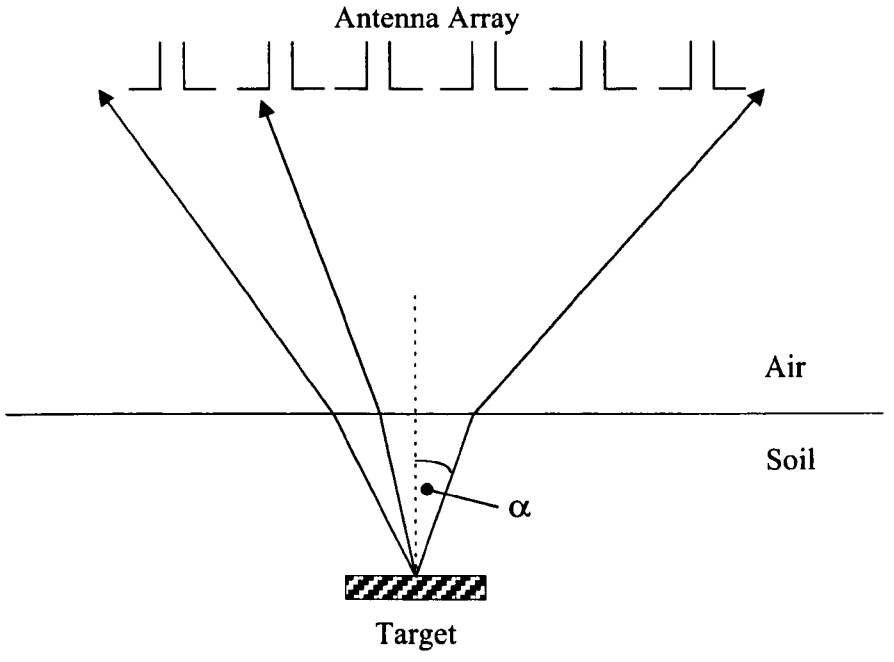

Figure 4-7 Received path spreading loss

4.2.1.5 Antenna Mismatch Loss, L_m

Antenna mismatch loss is determined by how well the antenna is matched to the switching network via the antenna feed. This loss can be minimised with careful impedance matching, for example for impedance of 70Ω and a transmission line of 50Ω there is a two way loss of L_m=1dB.

4.2.1.6 Antenna Loss, L_e

Antenna loss is due to power being dissipated in the antenna prior to radiation and relates directivity, *D*, to gain, *G*. Half wavelength dipoles can be designed with high efficiencies resulting in low losses of the order of 0.5 to 1dB [15]. However, temporally short transmitted pulses require antennas with larger fractional bandwidths than a dipole can offer [14]. A wideband bow-tie antenna with an absorbing backplane was developed for RASOR (see section 5.1.3 in Chapter 5), which has an increased loss of around L_e=3dB maximum for *both* transmit and receive since half the power is absorbed by the backplane.

4.2.1.7 Switching network and cable loss, L_c

RASOR requires a network of RF switches on both the transmitting and receiving paths in order to switch between each transmitting and receiving pair of the array. For the demonstrator system design described in Chapter 5, an insertion loss of around 1.2dB for each path was achieved. In addition, the cables connecting the switch network to the

antennas add a further small loss of around 0.3dB each way. The two way losses (transmit and receive) will therefore amount to around L_c=3dB.

4.3 RASOR Performance Analysis

4.3.1 Methods of Analysis

Analysis of the RASOR system using Finite Difference Time Domain (FDTD) modelling was conducted at University of Bristol [15] and described in several published papers [16] [17]. This study initially focused on developing a suitable balanced wideband antenna for RASOR and then progressed to analyse performance with a limited number of antennas in an array with very promising results. These antennas are used for practical purposes and are therefore described in more detail in section 5.1.1 of Chapter 5.

FDTD uses first order difference and second order accuracy approximations for the space and time derivatives of Maxwell's equations [18] [19]. The problem space is divided into a mesh of volume elements with each having a designated permittivity and permeability and the E and H field propagation can be recorded at each discrete time step over the analysis period. This method is useful for modelling the complex electromagnetic scenarios, such as those encountered in GPR, because the antenna array, soil, targets and clutter are in close proximity.

An example of a basic RASOR FDTD model is shown in Figure 4-8. This contains eight dipole antennas mounted on a metal ground plane and suspended over soil (the model is displayed upside down). One target is embedded in the soil material and the surface of the material is flat. The simulation was run eight times with a different antenna transmitting each time and with all other antennas receiving.

Figure 4-9 and Figure 4-10 show a comparison between measured data and FDTD investigations of the resolution achieved by an 8 element antenna and comparisons to the predicted resolution for this set-up (see section 4.3.3). The measured data was taken using a pair of antennas over a crude experimental sand-box where the antennas were manually scanned to all eight positions. The FDTD data was gathered from seven separate FDTD runs with a different antenna stimulated on each run and measurements taken on all the other antenna. These reults show that the two sets of data are in excellent

agreement and the resolution achieved from this small array is entirely in line with predictions.

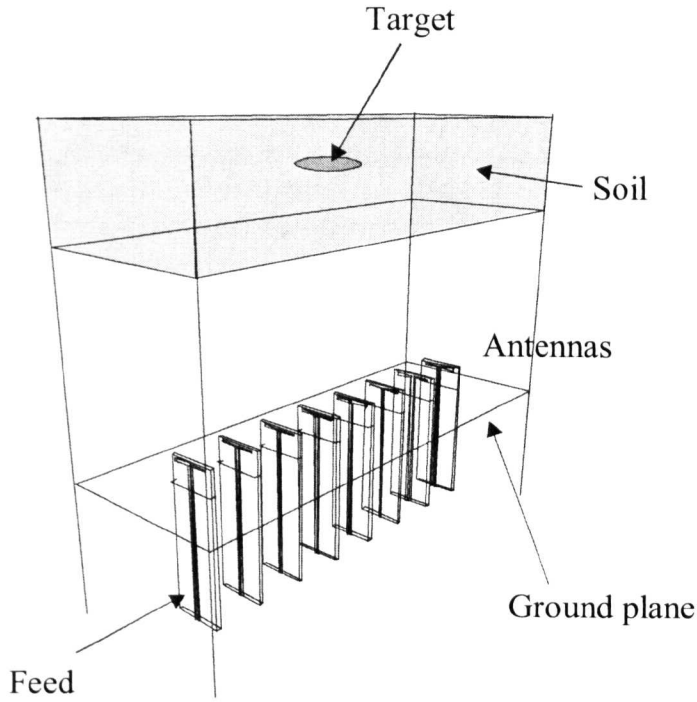

Figure 4-8 FDTD model of 8-element linear array

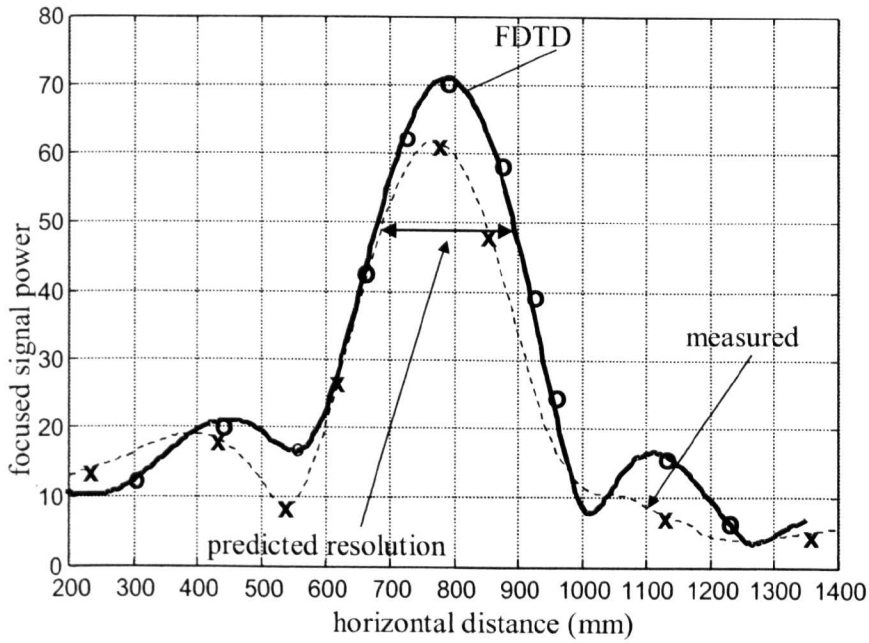

Figure 4-9 Lateral focusing through target location.

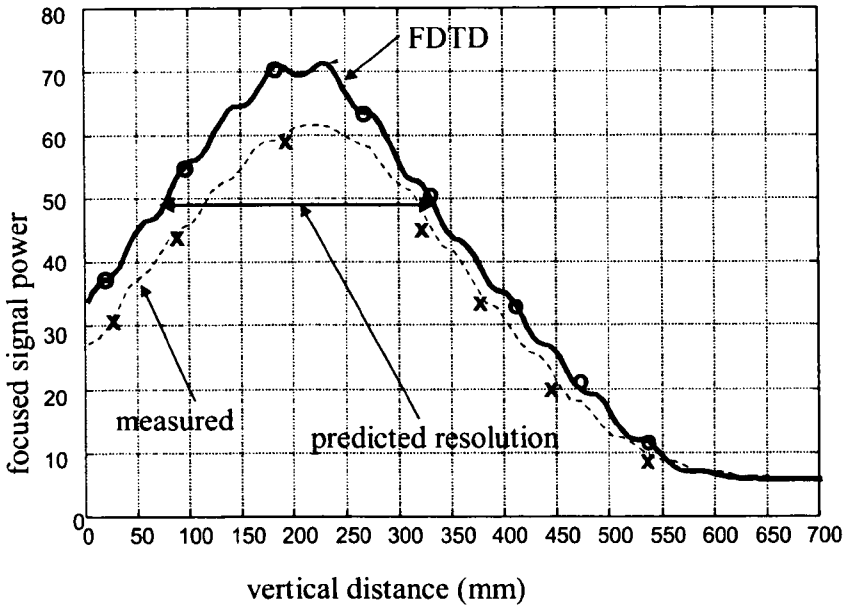

Figure 4-10 Vertical focusing through the target location.

FDTD remains computationally expensive both in terms of memory useage and run-time although improvements in the FDTD computation algorithm such as sub-gridding and parallelisation along with increasing computer processor power mean that run-times are gradually improving [20] [21]. Despite these advances it was not practical to model all the bistatic antenna pairs that are required in the RASOR system nor to model the wide range of soil and target types, clutter mechanisms and surface features that could be encountered by a real system. Assessment of cases such as these requires much simpler models using analytical analysis or simulation in order to calculate the system point spread function (PSF) or impulse response. However, the limitations of real equipment, such as sampling jitter and receiver noise figure, can not be easily modelled using FDTD or ray-tracing. To analyse these factors an experimental system is needed.

The terms PSF and impulse response are generally used in optics and radar respectively to describe the same system response; the PSF will generally be used here. The PSF of a system is a convenient way to express the combined effects of sensors and transmissions on an observed image. The "raw" image produced by the system is the true image convolved with the PSF, and thus the PSF is useful for measuring the errors and artefacts in the raw image.

As a simple example the PSF for a simplistic pulse might be expressed by the 2D sinc function given in

$$z = \left[\frac{\sin(x)\sin(y)}{xy}\right]^2 \tag{4-49}$$

where x and y are the spatial dimensions. This function is plotted in one and two dimensions in Figure 4-11 and Figure 4-12 respectively in linear and log amplitude scales.

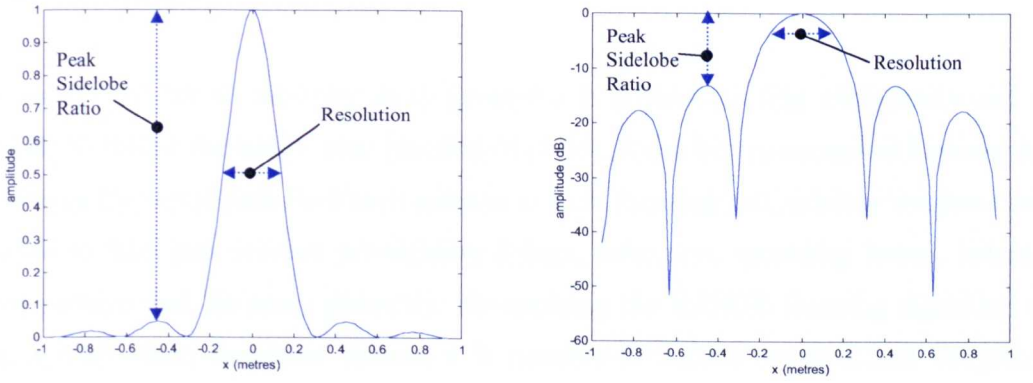

(a) (b)

Figure 4-11 Example point spread function in one dimension (a) linear amplitude (b) log amplitude

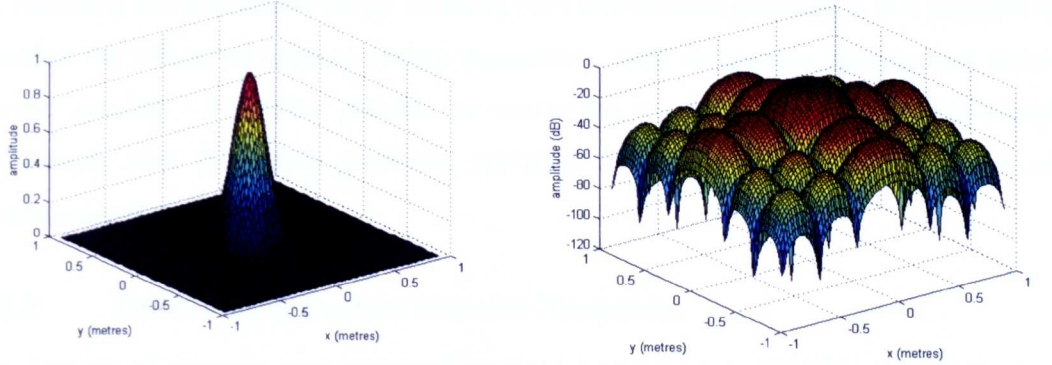

(a) (b)

Figure 4-12 Example point spread function in two dimensions (a) linear amplitude (b) log amplitude

The spatial resolution of the system, shown in Figure 4-11, is the width of the main lobe at half the maximum power and is the size of the minimum discernible detail of an image. This area is known as a resolution cell or voxel; in Figure 4-11 it is approximately 260mm^2. The peak sidelobe ratio (PSLR), also shown in Figure 4-11, is a measure of the maximum level of 'ghost' echoes caused by a target and indicates the

ability of a radar to detect weak targets in the presence of a strong target. It is defined here as the difference between the main lobe peak power a PSF to the highest sidelobe. In the Figure 4-11 example the PSLR is approximately -13dB. The integrated sidelobe ratio (ISLR) is defined here as the ratio of the integrated power contained in a rectangle of 10 by 10 resolution cells, but outside of a 2 by 2 resolution cell to the integrated power within the 2 by 2 resolution cell rectangle. PSLR and ISLR are convenient ways to measure the potential sidelobe clutter contributions and for developing algorithms to reduce their impact.

The exact PSF for an arbitrary array geometry is difficult to find analytically and is unlikely to follow the simple sinc function of (4.49). It can be approximated however by simulating the signal path from each antenna to each focusing cell, suitably weighted and delayed to take into account propagation delays, refraction, spreading losses, antenna beam patterns and the array geometry. By applying the RASOR focusing algorithm to this, and all other, simulated signals, it is possible to deduce the peak and integrated sidelobe ratios. The process of calculating the focusing weights will be described further in section 4.4.

By repeating this simulation for all focusing cells and various geometry's, it is possible to examine the effects of varying system parameters, such as antenna spacing and array-ground spacing. It is also possible to assess the impact of varying environmental parameters, such as surface gradients, curvature and ground dielectric properties, on resolution and processing gain.

4.3.2 Modelling of System Impulse Response

The concept of coarrays was proposed by Hoctor and Kassam [22][23] as a method of assessing the performance of active and passive imaging systems for Radar, Sonar and Ultrasound as well as in Seismic and Radio Astronomy applications. The sum coarray was originally proposed for narrowband, far-field active imaging and is represented by a set of vector sums of transmit and receive array element locations. This method was applied to wideband active imaging arrays in [24] in order to derive near and far field analysis of active arrays. It was shown that in this case the wide band operation could be seen as adding extra points at specific locations in the sum array.

This work is the starting point for the RASOR system modelling, which applies the coarray principles to a wideband, near-field 2D array with the additional complication of imaging in a stratified dielectric structure in front of the array due to non-contact operation with the soil. In fact the imaging process is the application of a convolution operation that relates the image to the true reflectivity distribution of the scene. The aim is to use coarray based design of array weightings or apodizations to optimise the sidelobe structure of the point spread function for resolution and performance against clutter.

The RASOR concept relies on an accurate estimation of the pulse propagation path from each transmit/receive pair to each focusing point in the search volume. This propagation path is the key component in determining the path delay for time aligning signals and for calculating path weightings to compensate for spreading losses, antenna gain and soil attenuation. The antenna array will not be in contact with the ground, so it is necessary to allow for the potentially significant reflection and refraction at the soil/air interface.

It is not possible to solve the inflection point position in closed form. However it can be approximated to a reasonable accuracy by considering the limiting cases of $\varepsilon_1=\varepsilon_2$ and $\varepsilon_2>>\varepsilon_1$ where ε_1 and ε_2 are the relative permittivity of the air and soil respectively as shown in Figure 4-13.

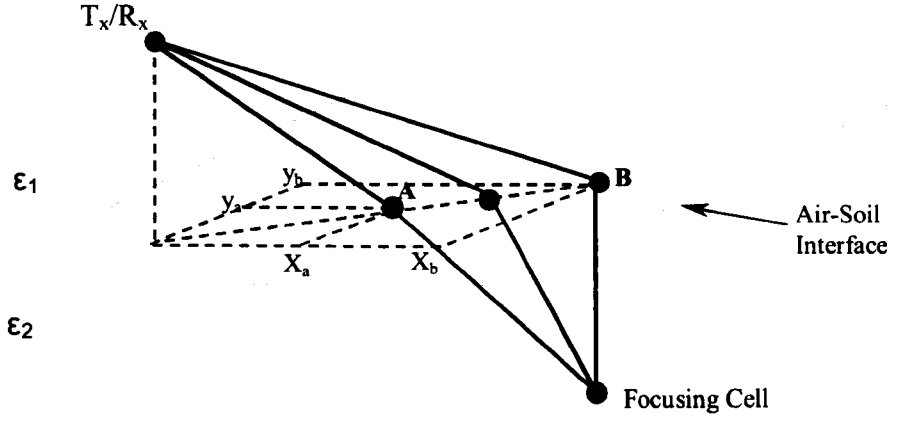

Figure 4-13 Inflection point between air and ground

When $\varepsilon_1=\varepsilon_2$ there is no inflection and the ray crosses the boundary at point A. When $\varepsilon_2>>\varepsilon_1$ the path is severely refracted so that, in the limit, the path direction in the ground

is normal to the interface, crossing it at B. The true inflection point lies between A and B and can be approximated by

$$x_i = x_a + \sqrt{\frac{\varepsilon_1}{\varepsilon_2}}(x_b - x_a) \quad \textbf{(4-50)}$$

$$y_i = y_a + \sqrt{\frac{\varepsilon_1}{\varepsilon_2}}(y_b - y_a) \quad \textbf{(4-51)}$$

Where x_a and x_b are the distances along the x dimension from the antenna to points A and B respectively and y_a and y_b are those along the y dimension. This ray path calculation can be repeated for all antenna elements to each focusing point as shown in Figure 4-14.

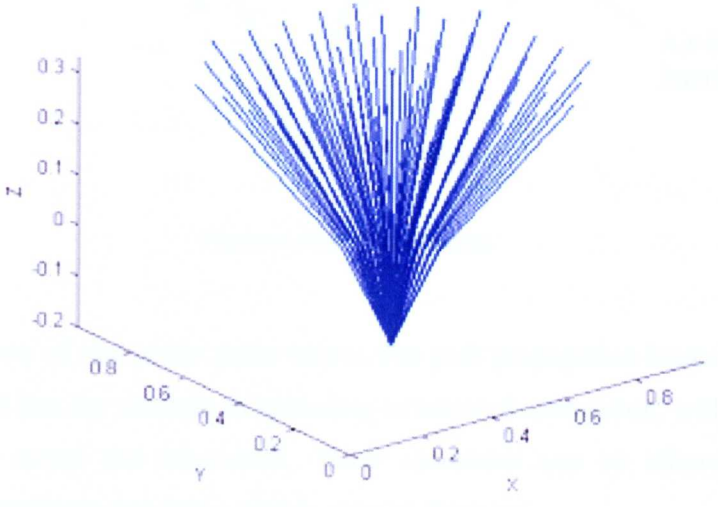

Figure 4-14 Propagation paths from an array to a focusing cell after refraction at the air-soil interface

For each transmitter and receiver pair the total path delay to any focusing point as shown in Figure 4-15 can be calculated from

$$d = c\left(p_1 + \left(\frac{p_2 + p_3}{\sqrt{\varepsilon_2}}\right) + p_4\right) \quad \textbf{(4-52)}$$

where c is the speed of light in air and p_1, p_2, p_3 and p_4 are the ray vectors from transmitter to focus cell to receiver and ε_2 is the permittivity in the ground.

The region of interest or search area in front of the two dimensional array is therefore divided into a set of focusing cells with range R, azimuth θ and elevation φ. For each of the N transmitting antenna positions a set of M receiving antennas exist which will have

a particular focusing cell within its field of view. The signal corresponding to the image of the k-th focusing cell located at p_k is obtained by applying to each of the received signals a time delay d_k from (4-52) and a weighting value w_k, which will be derived later.

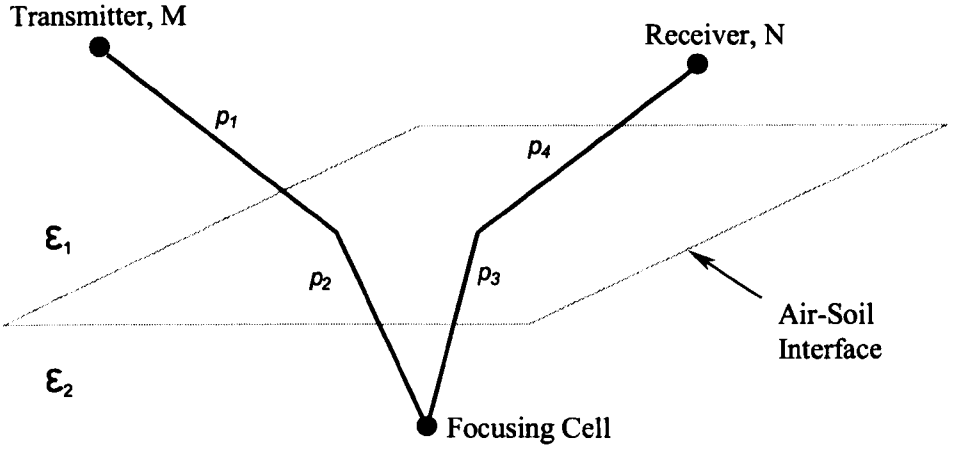

Figure 4-15 Inflected paths

In RASOR the use of multistatic paths means that path propagation losses from antenna to resolution cell due, for example to spreading or material attenuation, will vary between paths and also across the bandwidth. These variations can be allowed for in the processing by amplitude weighting signals prior to focusing.

Spreading loss weighting, A_s, can be modelled as being proportional to the square of the inflected path length from antenna to resolution cell thus the weighting for transmitter to resolution cell to receiver is the product of each path length squared

$$A_s = (p_1 + p_2)^2 (p_3 + p_4)^2 \qquad \textbf{(4-53)}$$

Attenuation loss weighting, A_a, can be calculated, as we have seen, (4-39). Writing this in linear form the weighting is

$$A_a = 10^{8.686\alpha L} \qquad \textbf{(4-54)}$$

where

$$L = p_2 + p_3 \qquad \textbf{(4-55)}$$

The antenna beam patterns weighting, A_b, can be modelled by assuming a modified cosine pattern (based upon a printed bow-tie antenna design described in the chapter 5)

$$A_b = \cos^{2.1}(\theta_t)\cos^{2.1}(\theta_r) \quad (4\text{-}56)$$

where θ_t and θ_r are the angle of propagation for the transmit and receive path respectively. The power of 2.1 in both cosine terms are empirically derived based on analysis of the antenna radiation patterns taken from FDTD models of the bow-tie antenna in an array [15].

Using these estimates, it was possible to model the RASOR performance and obtain the impulse response for a variety of scenarios. These models will be used in subsequent sections to analyse the RASOR lateral and vertical resolution, processing gain and performance against macroscale surface features.

4.3.3 Lateral Resolution

A predicted lateral resolution for RASOR of $\lambda_g/2\theta$ was given by Benjamin [25] where λ_g is the wavelength in the ground and θ is the in ground convergence angle. In the ground, the convergence angle θ (from Figure 3-10) is reduced by refraction, approximately as $1/\sqrt{\varepsilon}$ (where ε is the dielectric constant of the ground). However, since the wavelength λ_g is similarly reduced, the actual lateral resolution would be unchanged for a given wavelength.

Using analysis described in section 4.3.2 the point spread functions of point scatter at a depth of 300mm were generated for soil relative permittivity, ε_r, of 3, 10 and 40 respectively. The plots for this are shown in Figure 4-16. The plots are normalised to the maximum value in the focused data set. Blue indicates low signal strength and red/brown indicates high strength. The profiles at the bottom and on the left-hand side of each main plot show normalised signal amplitude profiles along the x and y dimension respectively at points indicated by the cross hairs on the main plot.

A 7 by 4 element array is modelled with 0.75λ spacing between elements. The half power vertical resolution is shown to be constant at around $2\lambda/3$ for a 2ns pulse modulated at 1GHz. Note that for ε_r=40, the PSF shown in Figure 4-16 (c) has an increased peak sidelobe level of -10dB which is at 4 resolution cells from the scatterer (±0.8m on the x-axis).

Values for horizontal resolution are approximately 190mm, in excellent agreement with the postulated λ/θ for horizontal resolution.

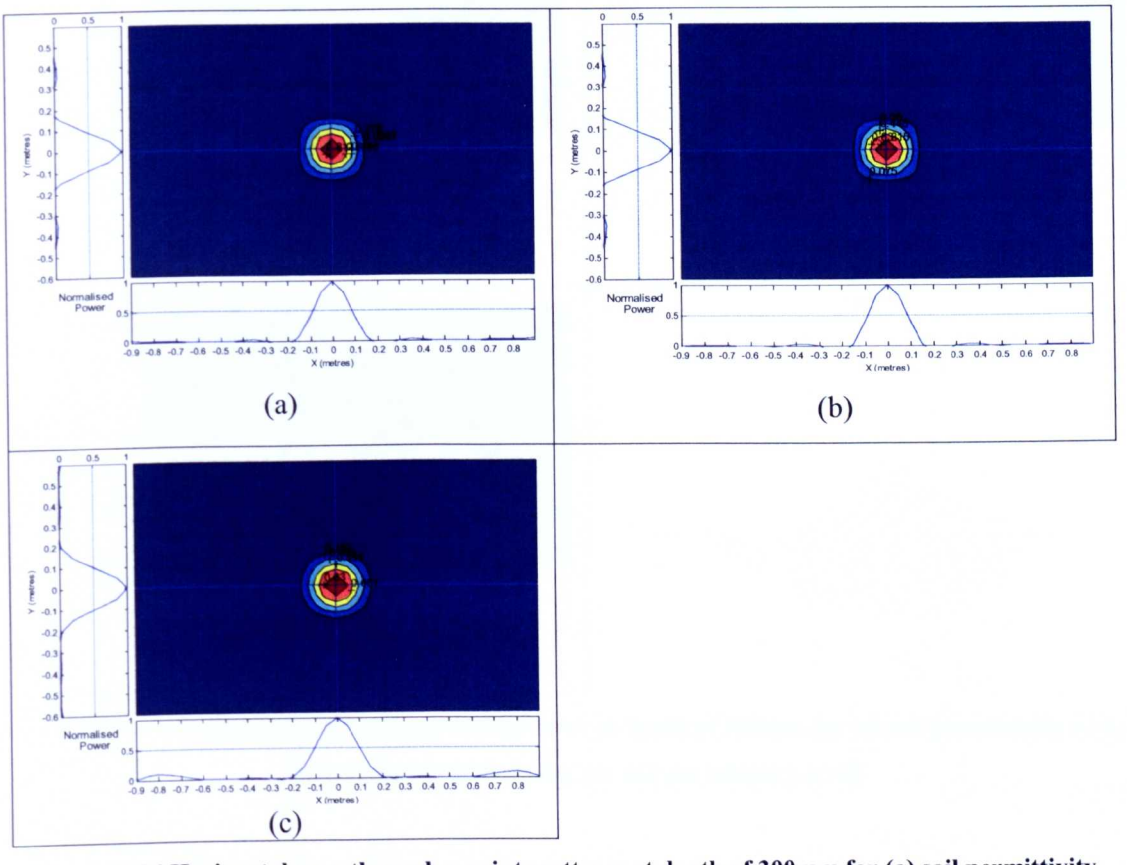

Figure 4-16 Horizontal scan through a point scatterer at depth of 300mm for (a) soil permittivity ε_r=3, (b) soil permittivity ε_r=10, (c) soil permittivity ε_r=40

4.3.4 Vertical Resolution

The depth of focus, $2\lambda_g/\theta^2$ [49] increases (is degraded) as $\sqrt{\varepsilon}$, but only up to the point where it is limited by the pulse-length in the ground, $n\lambda_a/(2\sqrt{\varepsilon})$, where n is the number of cycles (see section 5.1.5) in the pulse length. This is shown in the plots of Figure 4-17 where the vertical resolution is improved with increasing permittivity.

Figure 4-17 shows a vertical slice through the target through the x dimension at x=0. The target is buried at x=0,y=0 and depth 300m. Figure 4-17 (a), Figure 4-17 (b) and Figure 4-17 (c) shows the resolution with soil permittivities of ε_r=3, ε_r=10 and ε_r=40 respectively. Values for vertical resolution are approximately 240mm, in excellent agreement with the earlier postulated $2\lambda/\theta^2$ for vertical resolution.

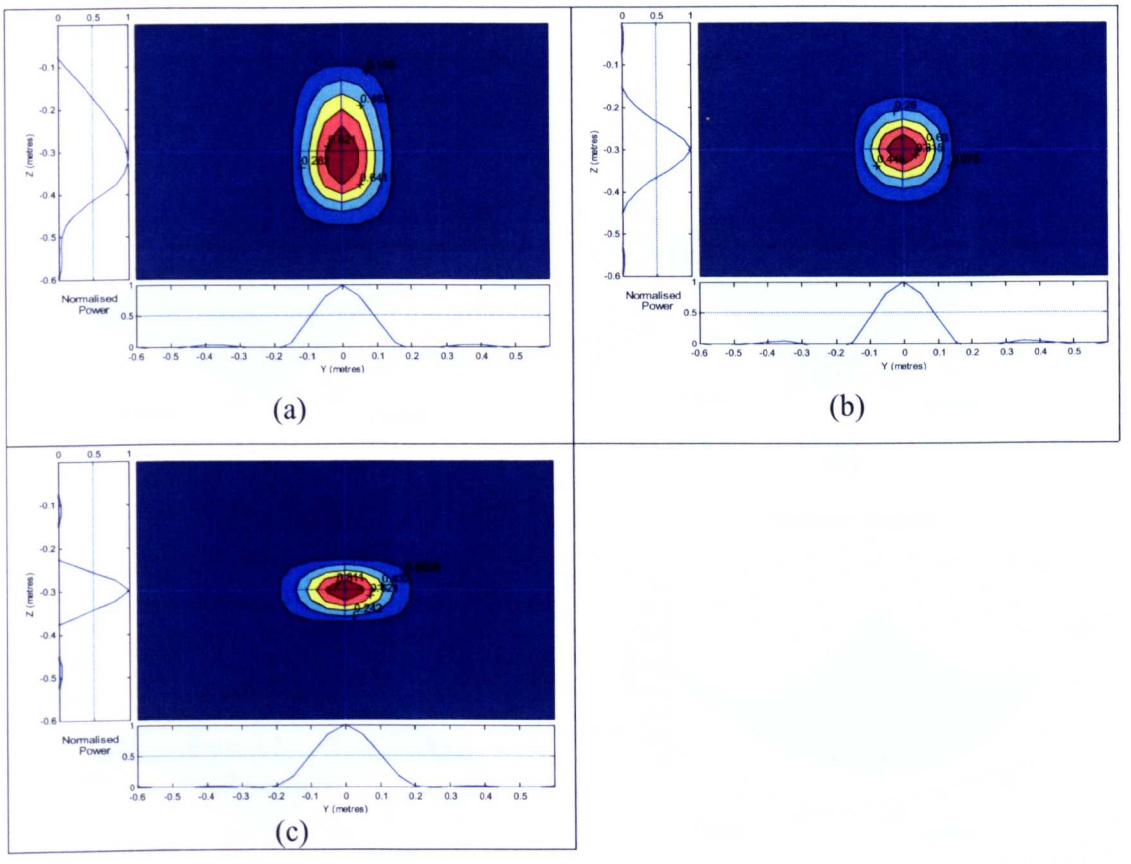

Figure 4-17 Vertical scan through a point scatterer at depth of 300mm for (a) soil permittivity ε_r=3, (b) soil permittivity ε_r=10, (c) soil permittivity ε_r=40

4.3.5 Surface Macroscale Features

Macro-scale variations in the surface profile, that is, variations that are large compared to the operational wavelength, are also suitable for analysis with the impulse response modelling ('microscopic' random variations in soil profile are considered in section 4.4.1). Examples of macroscale variations are:

- 2D gradients in otherwise level ground
- concave or convex surface curvature
- undulating surfaces
- a combination of the above.

Initially the system response was estimated for various 'worst case' surface types, with a target buried at 300mm below the surface of the sand. An estimate was obtained for the degradation in performance by comparison with the response obtained for a perfectly flat surface. Figure 4-18 shows the 7x4 element array (indicated as crosses) along with the

six modelled surfaces. The x and y dimensions correspond to the size of the experimental sandbox (see section 6.3.1).

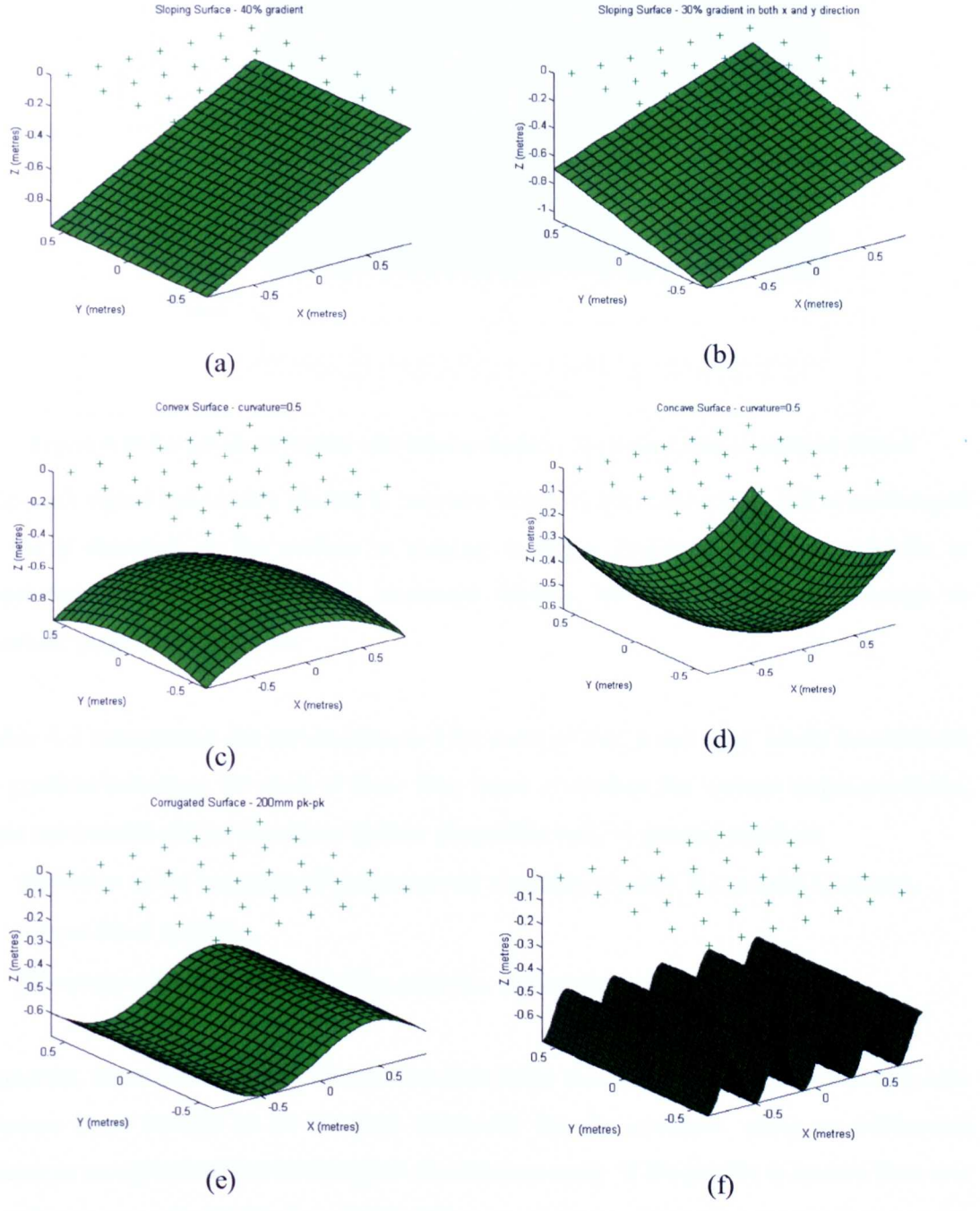

Figure 4-18 Six modelled surfaces (a) sloping surface in x direction, (b) sloping surface in x and y direction, (c) convex surface, (d) concave surface, (e) lightly undulated, (f) heavily undulated

Figure 4-19 shows a horizontal slice through the target of the focused results from the ray-tracing algorithm when the surface is sloping with a 40% gradient. The target location and slice depth is exactly the same as for the flat surface results.

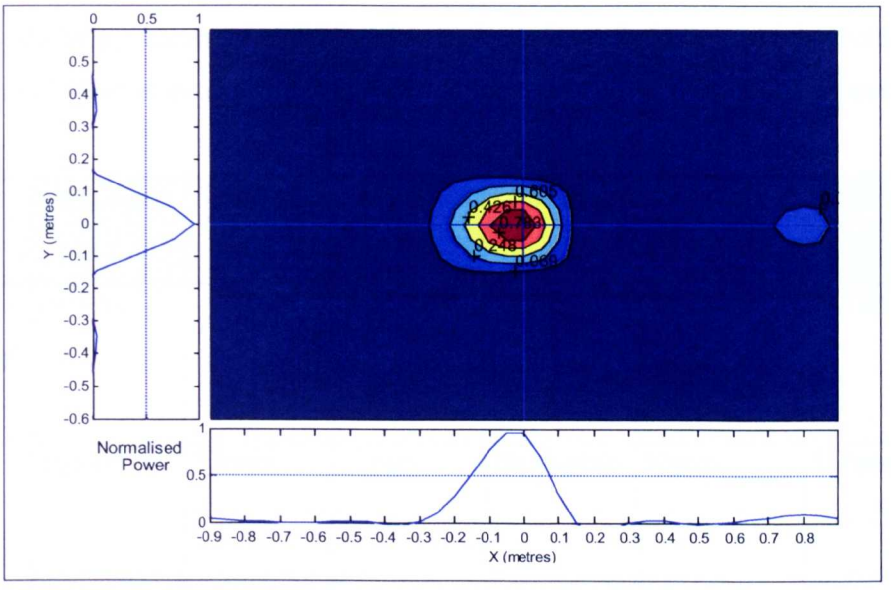

Figure 4-19 Target identification with sloping surface - horizontal slice at depth of 300mm

The peak signal has clearly shifted by around 50mm in the x direction, but is unchanged in the y direction as the surface is sloping in the x direction only. A sidelobe at approximately x=0.8m,y=0m has increased slightly, but not significantly enough to preclude target identification.

Table 4-2 summarises the results obtained for some of the 'worst case' likely occurrences of gradient/curvature for each of these four types of surface for various target positions. This assessment shows that these surface properties will, in general result in:

- distortion in the mapping of reconstructed locations vs. true 3D ground locations,
- loss of focal quality
- 3D spatial variation in processing gain (i.e. in focusing gain).

However, when these surface features become large enough to cause a problem they also become large enough to be detected on-the-fly by, for example, using an ultrasound sensor or an optical sensor mounted on the antenna array. If the profile is known then it is possible to compensate for the altered delays by changing the surface profile used in the RASOR time delay calculation model.

Finally, it should be noted that these macro-scale ground features could introduce significant specular-reflection surface clutter, where it would not otherwise arise. This is

however unlikely, except for fairly "strong" surface features, which would also significantly impair or even prevent the normal focusing and reconstruction process.

Surface Type	Slope in x	Slope in x and y	Convex	Concave	Lightly Undulating	Heavily Undulating
Change in Processing Gain	-4.3dB	-4.1dB	+.002dB	-0.7dB	-10.1db	-5.1db
Target location error	50mm	20mm	25mm	Negligible	20mm	150mm
Horizontal resolution degradation	60mm	30mm	Negligible	20mm	20mm	Negligible
Vertical resolution degradation	40mm	30mm	Negligible	50mm	20mm	Negligible

Table 4-2 Summary of system degradation for different surface types

4.4 RASOR Focusing Optimisation and Weighting

The concept of array weighting or apodization was introduced in section 4.3.2 to optimise the sidelobe stucture of the array point spread function. This section will describe methods for estimating these weightings with the aim of optimising either signal to clutter performance or signal to noise performance of RASOR. In general either one or the other of these will limit RASOR performance. It can be seen from Table 4-1 and the discussion of system losses in section 4.2 that except in the case of very wet soils it is likely that RASOR is not likely to be noise limited, and that clutter will be the limiting factor on performance. This conclusion is in agreement with almost all current literature on GPR for landmine detection [26][27][28][29].

Clutter is defined as any signal components that are not directly correlated with the primary scattering from the target objects. Examples of clutter sources are external radio interference (RFI), surface scattering, inhomogeneities in the soil and multiple

reflections. The first and last of these are unlikely to be troublesome for RASOR. RFI should not be an issue because the antenna array will be facing directly down towards the ground and will be in reasonably close proximity to it. The antennas will therefore be largely shielded from external interference by the antenna conducting backplane. Multiple reflections between ground and array can be greatly reduced by the use of an absorbing material in-front of the antenna array backplane. This is described in more detail in section 5.1.3. This leaves surface scattering and soil inhomogeneities and each of these will be analysed in turn.

4.4.1 Surface Scattering

Surface clutter due to the large air soil reflection has already been mentioned in chapter 3 as a key and potentially troublesome factor in GPR. This section looks at the clutter mechanism and examines the alternatives for dealing with it.

4.4.1.1 Surface Roughness

Macroscopic surface variations which are relatively large compared to the wavelength were analysed in section 4.3.5 and shown to have a potential decorrelating effect on focusing performance and resolution, but, since these variations can in general be sensed and allowed for, this was not considered serious.

Surface roughness however, is considering microscopic random variations in the surface profile. Techniques have been described [30] for estimating and classifying random surface scattering for microwaves, but with particular emphasis on far-field applications such as Synthetic Aperture Radar (SAR). A number of studies have been described [31] on low-grazing angle backscatter from rough surfaces and some of the techniques used are relevant to RASOR. Useful statistics on radar scattering from terrain have been published [32] and wave scattering from rough surfaces has been addressed [33] [34] [35]. However, the key phenomenon, for RASOR, is bistatic backscatter in the near field, and this is less explicitly covered in the literature.

Common methods of surface classification given in the literature are surface height variation and surface correlation length. Surface height variation, or rms. height, is used to find the standard deviation of a point on the surface from either a mean value or a periodic pattern. The value can be expressed in terms of wavelength and it is relatively

straightforward to digitise the technique for signal processing purposes. Surface correlation length is a measure of the similarity between two points on the surface.

It is certain that backscattering from the surface will be greater than returns from a deeply buried mine. However, since the half power beamwidths of any element pair should only overlap on the surface for element pairs that are close together, the RASOR focusing technique should almost certainly be able to reduce this type of interference. This analysis is valid as long as the surface roughness, curvature and gradient are negligible. Under certain circumstances the reflections will become significantly directionally dependent and for very rough surfaces, relative to the wavelength, the transmitted signal will consist entirely of a diffuse component that will prevent coherent processing altogether.

If the surface height variation, χ, is considered to be the governing parameter for surface roughness, then the lower limit of interest for RASOR is the value below which the surface can be considered specular and the upper limit is the value above which the surface can be regarded as very rough.

Fraunhofer criteria for surface roughness [30] is a proposed method for determining the value of χ below which the surface behaves specularly. It is given by:

$$\chi < \frac{\lambda}{32 \cos \theta} \tag{4-57}$$

where λ is the wavelength and θ is the angle of incidence. For a 1GHz signal λ=30cm and assuming an angle of incidence normal to the surface, i.e. the worst case, there is a limit for a specular surface, χ<1cm.

At the other extreme a very rough surface, also known as a Lambertian surface, is proposed to be given by $k\chi<1.0$, where k is the wave number hence:

$$\chi > \frac{1.0 \times \lambda}{2\pi} \approx 5\,cm \tag{4-58}$$

A preliminary conclusion, based exclusively on the study of rms height, is that for surfaces with a rms height greater than around 5cm, coherent focusing will begin to be

degraded. It is also associated with quite strong specula scattering and only a low diffuse backscatter coefficient. By contrast, surface roughness that is large compared to the wavelength is not very likely to arise, at wavelengths of 15 - 30 cm in air, but where it does occur, it gives rise to mainly diffuse scattering with very little specula reflections. This could potentially destroy the phase coherence of the signals penetrating into the ground, and so would preclude the RASOR coherent processing.

4.4.2 Surface Clutter Processing Options

4.4.2.1 Surface Racetrack Weighting

Surface clutter would theoretically compete with the wanted target from a given 2-way path only within the surface area shown in Figure 4-20 and defined by the coincidence of:

- The "race-track" locus whose outer perimeter corresponds to a path delay equal to that from the transmit element via the centre of the given resolution cell to the receive element plus half the pulse length, and whose inner perimeter corresponds to this path delay minus half the pulse length.
- The (in air) 3dB beam widths of both the transmit and receive elements.

For a practical ground gradient, any specular reflection from the transmit path might point well away from the receive element, and so any clutter can only arise from diffuse scattering.

In practice, deeply buried objects might produce no significant overlap between the "race-track" and the common fields of view and the two elements may not suffer from surface clutter, Figure 4-20.

For very shallowly buried objects, the inner perimeter of the "race-track" locus shrinks to a very small area and since there is little further divergence of the beams after ground-entry, there is very substantial overlap between the beams, especially for closely-spaced elements. Furthermore, with the right moderate ground gradient, some element pairs can experience localised specular reflection. This is not good from an operational viewpoint.

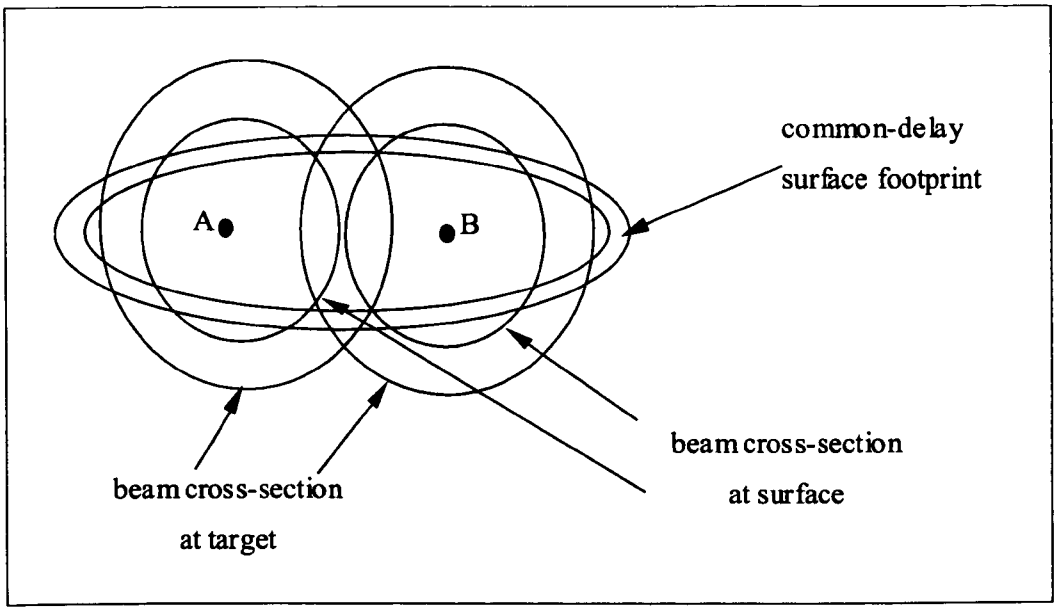

Figure 4-20 Two Elements with no common main beam surface clutter

With regards to intermediate depths of burial, any surface clutter that is significant for this depth range can only arise in element pairs with a substantial common-delay area A_c, i.e. in elements close to each other, and only where the surface texture give rises to substantial diffuse-scattering. In this case a weighting function of the form $1/(\sigma A_c+1)$ can be applied, where σ is a surface roughness factor such that:

$\sigma = 0$ when the surface is smooth compared to the wavelength

$\sigma = 1$ when the surface is comparable to the wavelength.

This is the basis of a weighting algorithm to remove surface clutter that was analysed with real test data (see section 6.3.2). Unfortunately the algorithm did not mitigate the surface clutter to an acceptable operational level for the following reasons:

- Scattering from the surface area - even diffuse scattering - is still at a significantly high level to interfere with targets down to a depth of 300mm and can thus not be neglected. It was validated that beyond a depth of around 300mm surface clutter there is little or no overlap between the surface racetrack and the antenna beam pattern and consequently surface clutter poses few problems at this depth. However, operationally an area of whiteout from the surface to 300mm would not be acceptable - almost all APM and many ATM are buried in this corridor.
- In practice the coupling between the array and ground is complex and means that the above analysis based on simple solid angle geometrical optics does not hold.

Thus although the above algorithm provides a limited performance improvement against surface clutter, it was necessary to explore alternative algorithms and perhaps combine them with the above.

4.4.2.2 Average Background Subtraction

This is probably the most widely used method of eliminating the air ground interface. Typically a mean or median average A-scan is calculated over the whole B scan and then subtracted from each A scan. In fact this only removes horizontal background clutter and, since noise, surface and dielectric variations will almost always be present, this estimate is not very accurate in anything other than a tightly controlled environment.

An alternative that worked well in laboratory experiments is to obtain the background ground truth for all A-scans prior to burying the target, or after its removal, and subtract these from all target A-scans. In practical scenarios where a perfect ground truth is unavailable, this method is not of course available.

4.4.2.3 A Scan Clutter Modelling

Some research has concentrated on modelling the clutter signal using system identification methods [36] [37] [38] in order to subtract this from the received signal A-scans. This method consists of estimating the parameters of the system transfer function by finding the composite parameter vector using a recursive least squares algorithm such as a Kalman Filter.

Good results were reported in off-line processing of experimental data [39]. However, this method tends to be relatively computationally intensive, which may preclude it from a viable real-time processing system.

4.4.2.4 Discrete Wavelet Transform

The theory of this cancellation method [40] is that the horizontal energy in a B-scan will appear in the coefficients of the lowest octaves of a wavelet transform. If these coefficients are set to zero and then an inverse transform is applied, the air - ground bounce should be removed.

4.4.2.5 Improved Average Background Subtraction

The RASOR approach offers several alternatives or extensions to the average A scan subtraction. Firstly, RASOR collects multiple versions of the same A scan pair as the array is swept forward. Taking the long term median average of these would provide one

subtraction method and also the energy in this signal would provide a measure of the average surface variation. Secondly, a windowed average subtraction is available where the average A scan only around the vicinity of an A-scan is subtracted so that reflections from slight local surface variations can be removed. A third approach is to recognise that RASOR comprises of a number of identically spaced bistatic pairs of antennas which can provide another useful median average for subtraction because these can be expected to contain similar antenna to ground coupling characteristics.

4.4.2.6 Post Focusing Background Removal

An additional form of background removal is available at the level of the C-Scan. A focused data set can be obtained from, for example, a calibration area of similar soil types known not to contain any objects. This becomes the system point spread function each voxel of which can be deducted from a newly acquired search C-scan.

The drawback with this approach is an empty calibration area is difficult to find in practice and even if it were the method assumes an identical (and homogenous) soil profile between the calibration and search area, which will not generally be the case.

4.4.2.7 Adaptive focusing window

RASOR offers another technique to enhance the focusing onto targets close to the surface. This method uses a variable focusing gate when focusing onto depths that are within the specular surface reflection range, i.e. from the surface to less than 300mm depth. The gate acts to remove all but the late time portion of the transmitted pulse at the surface and gradually increases until the full pulse gate is used at 300mm.

The gate can be easily achieved by setting the early time focusing weights for the surface voxels to zero.

4.4.3 Soil Inhomogeneities

Soil inhomegeneities or local variations in the dielectric profile of the soil give rise to unwanted returns sometimes termed volume clutter. Almost anything under the surface of the ground could give rise to clutter return signals. The RASOR technique offers a number of possibilities for adaptively reducing the importance of these unwanting reflections.

4.4.3.1 Locus of common delay

The echoes of pebbles or other objects scattered in the volume of the ground will compete with the wanted target only when they are located within a locus of common

delay. This locus is unique to each specific 2-way path delay from transmitter to resolution cell to receiver. It is in fact a 'shell' defined by two concentric ellipsoids of revolution drastically compressed in the ground due to refraction as shown plan and side elevation in Figure 4-21 and in 3D in Figure 4-22. The transmitter and receiver form the loci and the pulse length in the ground determines the shell thickness.

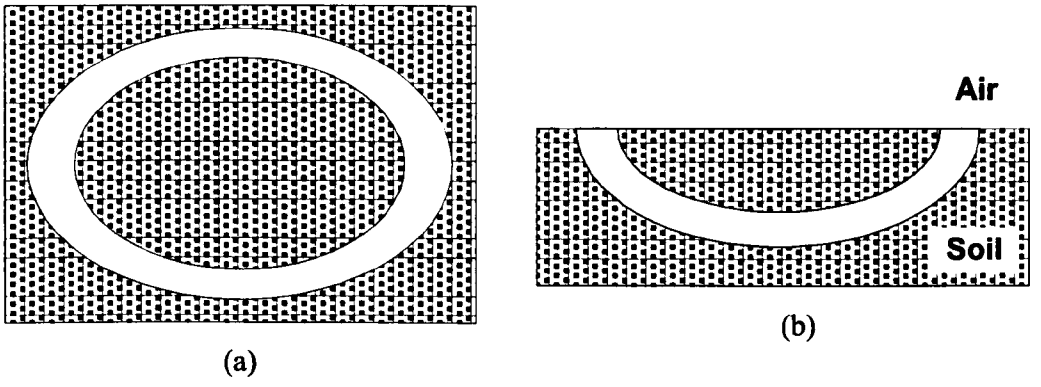

Figure 4-21 Shell of common delay (a) plan view, (b) side elevation

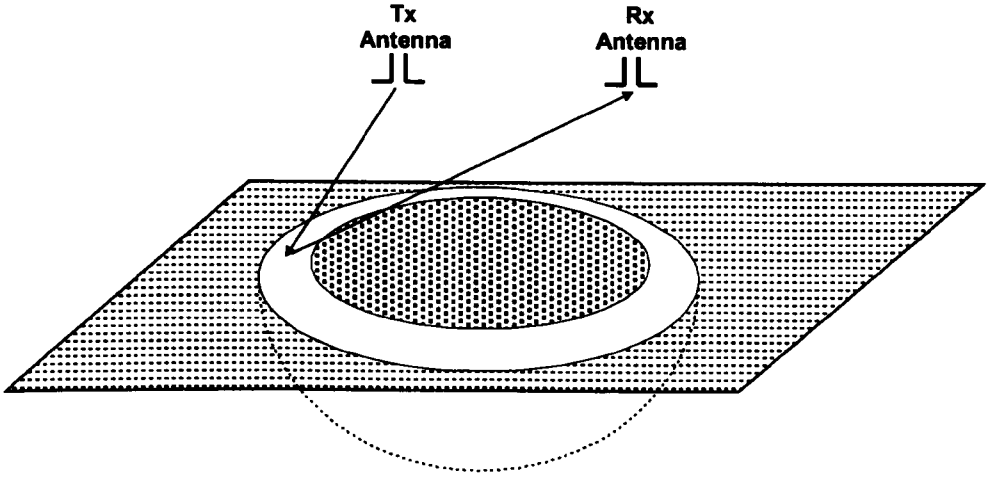

Figure 4-22 3D view of shell of common delay

4.4.3.2 Common Delay Volume Clutter

The combination of the common-delay locus surface and the two beam cross sections forms a (petal-shaped) common-delay clutter *area* A_c, as shown in Figure 4-23. This is unique to each specific 2-way path, and is defined by the coincidence of:

- The locus-surface of path delay equal to that from the transmit element via the centre of the given resolution cell to the receive element.
- A thickness, orthogonal to that surface, equivalent to that delay varying by ± half the pulse length. (This thickness is thus inversely proportional to the refractive index of the soil.)

- The beam cross section of the transmit element (as reduced in the soil by refraction).
- The beam cross section of the receive element (similarly reduced by refraction).

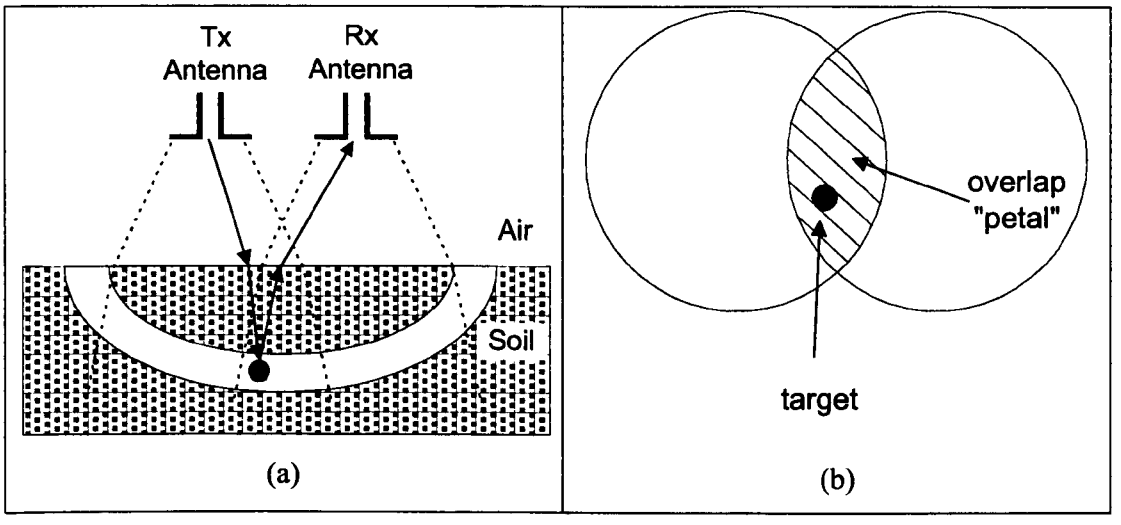

Figure 4-23 Common Delay Clutter Locus: (a) side elevation, (b) plan view

Through system modelling it can be shown that, *for any given 2-way path*, the soil-attenuation loss to any part of the locus of common delay varies only slightly for the chosen resolution cell. This is demonstrated by the plots in Figure 4-24, which show the attenuation variation over a clutter shell at three depths of focus for roughly the minimum and maximum RASOR antenna spacings.

These results show that the variation of path attenuation over the common delay shell is relatively low. Even for deeply buried and widely spaced antenna elements this amounts to only around ±1dB in the worst case and hence paths to the overlapping petal area can be assumed to have a near constant attenuation for all antenna pair spacings.

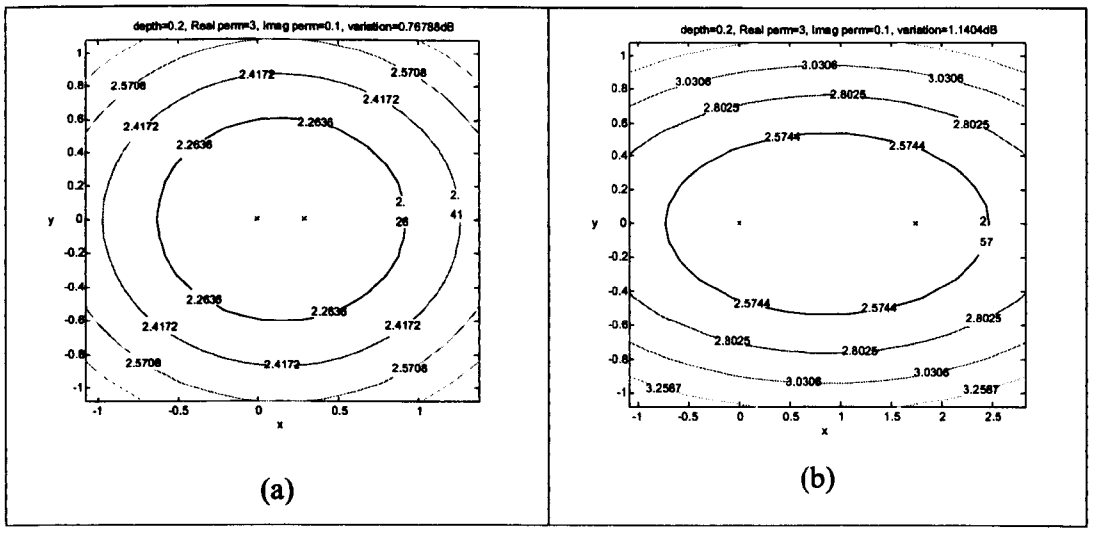

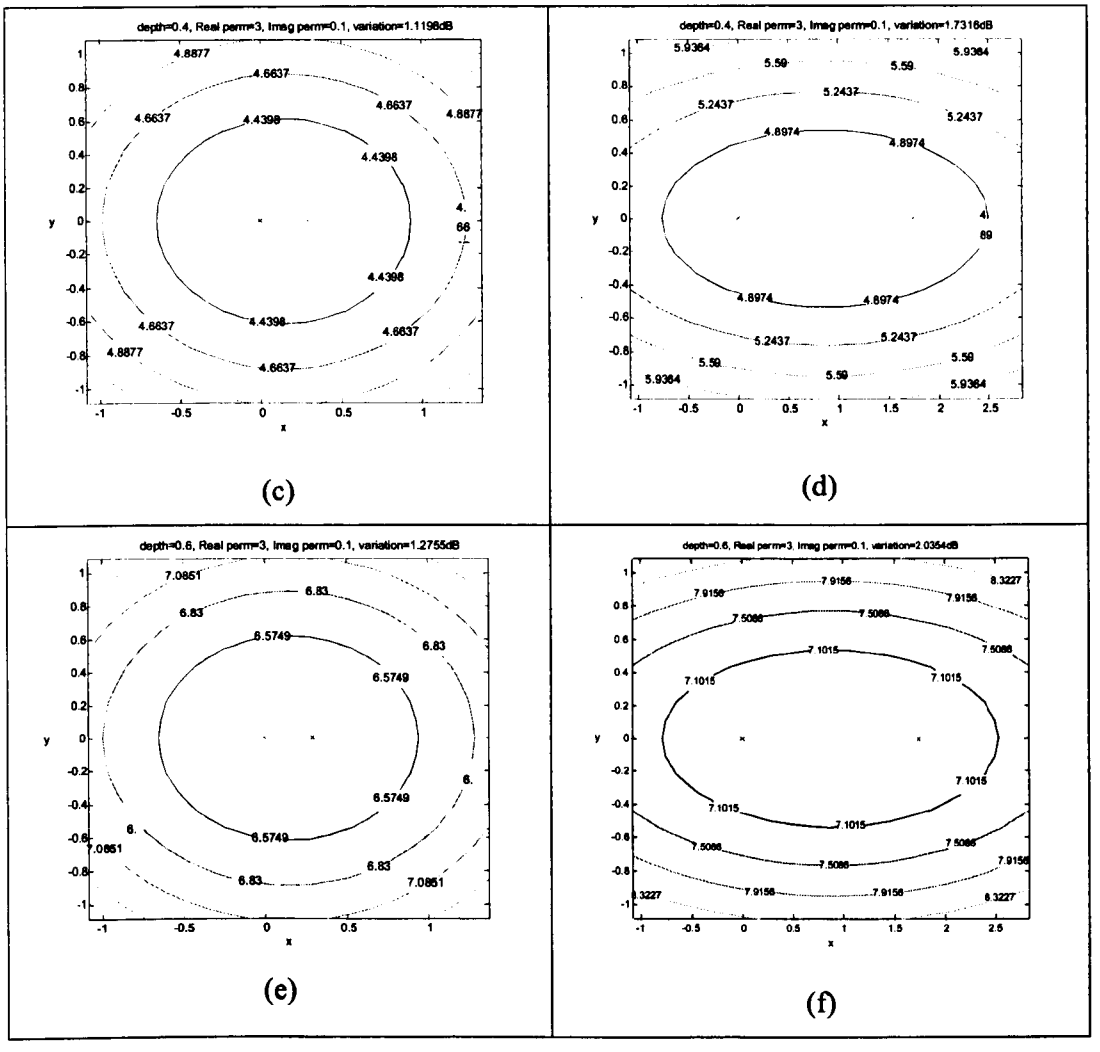

Figure 4-24 Common delay attenuation variation with varying antenna spacing and ε'=3, ε''=0.1 at depths of (a) 0.2m and λ spacing, (b) 0.2m and 6λ spacing, (c) 0.4m and λ spacing, (d) 0.2m and 6λ spacing, (e) 0.6m and λ spacing, (f) 0.2m and 6λ spacing,

Assuming the clutter is quasi-uniformly distributed over the relevant volume, the signal/clutter ratio is inversely proportional to the common-delay shell volume, and hence to the (petal-shaped) common-delay clutter *area* A_c, defined by the combination of the common-delay locus surface and the two beam cross sections as shown in Figure 4-25.

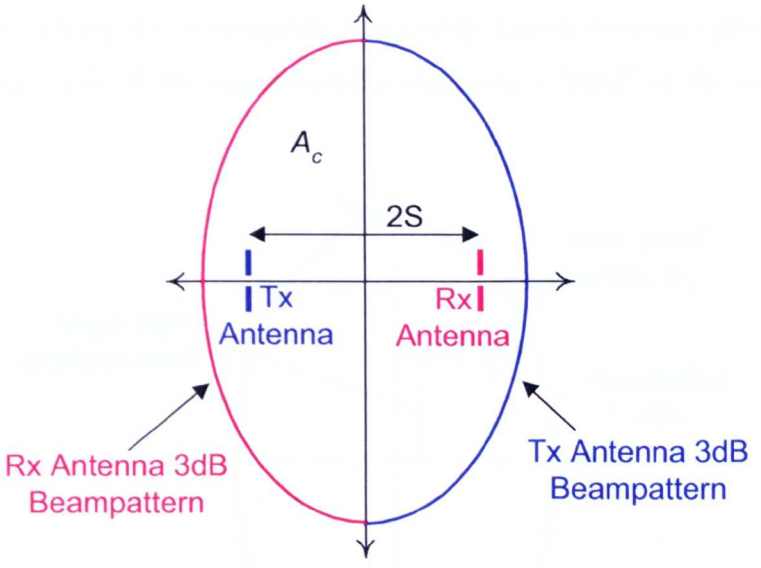

Figure 4-25 Common delay petal shaped clutter area and antennas

In order to minimise the effect of such non-coherent volume clutter on the reconstructed image, each path can be weighted inversely to this common-delay clutter area, A_c. This weighting is particularly important when a few paths are associated with much stronger clutter than the remainder.

If the beam radius[1] at the target depth is R, and the separation of the two antenna elements is 2S, then half the minor axis of the petal area, A_c is

$$L_{min} = (R-S) \tag{4-59}$$

and half its major axis is

$$L_{maj} = \sqrt{(R^2-S^2)} \tag{4-60}$$

and A_c is approximately proportional to

$$A_c \approx L_{min} \times L_{maj} = w_1 \tag{4-61}$$

For a given eccentricity of the clutter area, relative to the resolution cell, a larger clutter area also implies a poorer focal quality. Hence this weighting will also yield some improvement in the focal quality.

[1] Beam radius means here the radius at the antenna radiation pattern half power beamwidth

An additional weighting for focal quality is available. This is measured primarily by the reciprocal of the width of the common-delay clutter area "petal" *at the resolution-cell location*, F.

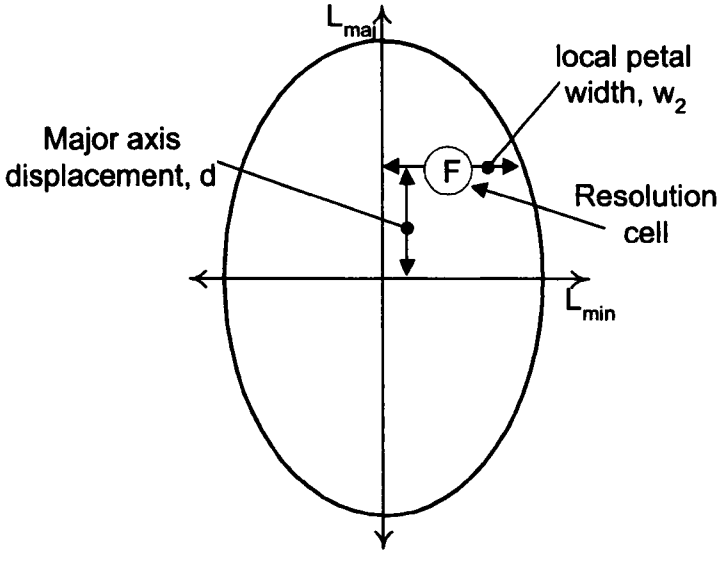

Figure 4-26 Focal quality weighting function

When the resolution cell is underneath the straight line joining the transmit and receive antenna elements, it lies on the minor axis of the common-delay clutter area. Indeed, when the focal cell is midway between the antenna elements, it lies at the intersection of the minor and major axes of A_c. In general, however, the resolution cell is eccentric, being asymmetrically displaced along one or both of these axes as shown in Figure 4-26. Asymmetry along the minor axis is of little significance, but w_2, the local width of the "petal", varies from L_{min} when d (the major-axis displacement from the centre) is zero, to 0 when $d = L_{maj}$.

This variation is approximately parabolic, according to the formula:

$$\frac{(L_{maj} - d)}{L_{maj}} = \left(w_2 / L_{min}\right)^2 \qquad \textbf{(4-62)}$$

$$\therefore w_2 = L_{min}\left\{\frac{(L_{maj} - d)}{L_{maj}}\right\}^{1/2} \qquad \textbf{(4-63)}$$

Another aspect of focal quality is the magnitude of the gradient of the common-delay surface at the focal cell. This gradient increases with increasing eccentricity of the clutter

area, relative to the focal cell. Hence, for a given "petal" area A_c, it increases with decreasing width w, thus reinforcing the value of this weighting parameter but not sufficiently to warrant weighting by a higher power of (1/m).

Combining (4-61) and (4-61) gives a total volume clutter weighting function, W, of:

$$W = \frac{1}{w_1 \times w_2} = \frac{1}{L_{\min}^{\,2}\left[L_{\mathrm{mix}}(L_{\mathrm{mix}} - d)\right]^{1/2}} \tag{4-64}$$

4.4.3.3 Obscuration

In addition to clutter in the common-delay volume, the effect of clutter within the "go" and "return" segments of all relevant 2-way paths must be considered. Figure 4-27 illustrates this blockage process. When the clutter objects are small compared to the wavelength, the signal is diffracted round these objects with negligible absorption, scattering or phase dispersion. It is also predicted that the effect of any clutter objects that are large compared to the wavelength would be equivalent to a blockage of that proportion of the solid angle between the focal cell and the relevant part of the array that is obstructed by these large clutter objects.

Since the fractional blockage, *b*, is equally likely to affect transmit and receive paths, it reduces the processing gain by the factor $(1\text{-}b)^2$.

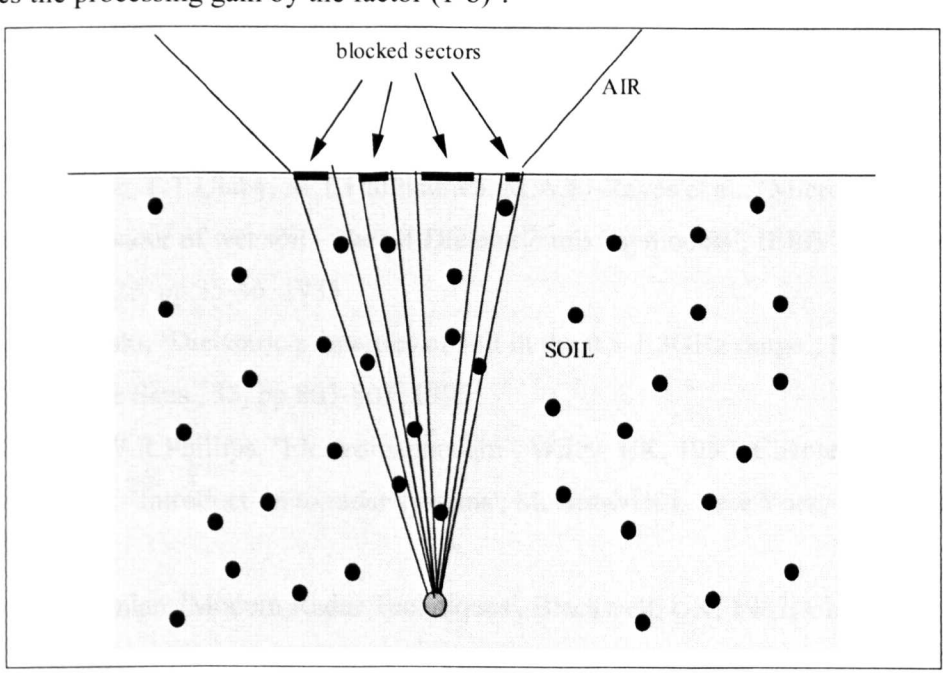

Figure 4-27 Pebbles blocking part of coverage solid angle

However, when large clutter or target objects cast shadows, RASOR's post-reception focusing offers a means of dealing with it. When a large object is detected in the 3D focused image its position can be used to identify the time samples of the original signals that gave rise to it. Zeroing out these portions (by zero weighting for example) and refocusing will reveal any previously hidden targets.

4.5 Conclusions

The RASOR system concepts have been developed using analytical modelling, FDTD results and early concept proving experiments in a controlled environment. Novel algorithmic solutions have been introduced to reduce clutter, arguably the most challenging aspect of ground penetrating radar.

References

[1] I.S.Grant, W.R.Phillips, 'Electromagnetism', Wiley, UK, 1990, Chapter 10

[2] I.S.Grant, W.R.Phillips, 'Electromagnetism', Wiley, UK, 1990, Chapter 2

[3] W.M.Telford, L.P.Geldart, R.E.Sheriff, D.A.Keys, 'Applied Geophysics: Cambridge', Cambridge University Press, 1976

[4] D.J.Daniels, 'Surface Penetrating Radar', IEE London 1996, Chapter 3

[5] T.W.Miller, et al., 'Effects of soil physical properties on GPR for landmine detection', 5th International Symposium Technology and the Mine Problem, April 2002

[6] M.T.Hallikainen, F.T.Ulaby, M.C.Dobson, M.A.El-Rayes, 'Microwave dielectric behaviour of wet soil – Part I: Empirical models and experimental observations', IEEE Trans. Geosci. Remote Sens., 23, pp 25-34, 1985

[7] M.C.Dobson, F.T.Ulaby, M.T.Hallikainen, M.A.El-Rayes et al., 'Microwave dielectric behaviour of wet soil – Part II:Dielectric mixing models', IEEE Trans. Geosci. Remote Sens., 23, pp 35-46, 1985

[8] N.R.Peplinski, 'Dielectric properties of soil in the 0.3-1.3GHz range', IEEE Trans. Geosci. Remote Sens., 33, pp 803-807, 1995

[9] I.S.Grant, W.R.Phillips, 'Electromagnetism', Wiley, UK, 1990, Chapter 11

[10] M.Skolnik, 'Introduction to radar systems', McGraw-Hill, New York, 3rd edition, 2001

[11] M.J.B.Scanlan, 'Modern Radar Techniques', Blackwell, UK, 1987, Chapter 3

[12] S.Kingsley, S.Quagan, 'Understanding Radar Systems', McGraw Hill, 1989, Chapter 2

[13] D.J.Daniels, 'Short pulse radar for stratified lossy dielectric layer measurements', Proc. IEEE, Vol.27, Part F, No.5, pp384-388, 1980

[14] T.P.Montoya, G.S.Smith, 'A study of pulse radiation from several broad-band loaded monopoles', IEE Trans. Ant. Prop., Vol.44, pp1172-1182, Aug 1996

[15] R.Nilavalan, 'FDTD modelling, measurements and analyses of Post Reception Synthetic Focusing Techniques in Ground Penetrating Radar', University of Bristol PhD Thesis, 2000

[16] R.Nilavalan, G.Hilton, R.Benjamin, 'Wideband printed bowtie antenna element development for post reception synthetic focusing surface penetrating radar', Electronics Letters, Vol.35, No.20,pp1771-2, IEE, UK, 1999

[17] R.Nilavalan, G.S.Hilton, R.Benjamin, I.Craddock, 'FDTD Analysis of a post-reception synthetic focusing surface penetrating radar performance in various ground conditions', Proceedings of the Millenium Conference on Antennas and Propagation, Davos, Switzerland, 2000

[18] K.S.Yee, 'Numerical solution of initial boundary value problems involving Maxwell's equations in isotropic media', IEEE Trans. Ant. Prop., Vol AP-14, pp302-307, 1966

[19] A.Taflove, 'Computational Electrodynamics: The Finite Difference Time Domain Method', Artech House, USA, 1995

[20] P.Monk, 'Sub-gridding FDTD schemes', Applied Computational Electromagnetic Society Journal, Vol.11 No.1, pp37-46, Jan 1996

[21] R.P.Rodohan, S.R.Saunders, R.J.Glover, 'A distribution implementation of the finite difference time-domain (FDTD) method', Int. J. Num. Mod., Vol.8 No.3-4, pp283-91, May-Aug 1995

[22] R.T.Hoctor, S.A.Kassam, 'The unifying role of the coarray in aperture synthesis for coherent and incoherent imaging', Proc. IEEE , Vol.78 No.4, April 1990, 735-752

[23] R.T.Hoctor, 'Array redundancy for active line arrays', IEEE Trans. Image Proc., Vol.5 No.7, July 1996, pp1179-1183

[24] F.Ahmad, S.A.Kassam, 'Coarray amalysis of the wide-band point spread function for active array imaging', Sig. Proc., Vol.81, 2001, pp99-115

[25] R.Benjamin, 'Synthetic-aperture antennas',Microwave Journal, 1995, Vol. 38, No. 9, pp68-81

[26] H.Brunzell, 'Clutter reduction and object detection in surface penetrating radar', Proc. IEE Radar 97, Issue 449, 1997, pp688-691

[27] J.W.Brooks, L.Van Kempen, H.Sahli, 'Primary study in adaptive clutter reduction and buried minelike target enhancement from GPR data', Proc SPIE AeroSense 2000: Setection and Remote Technology for Mines and Minelike Targets V, Vol.4038, 2000, pp1183-1192

[28] A.Van der Merwe, I.J.Gupta, 'A novel signal processing technique for clutter reduction in GPR measurements of small, shallow land mines', IEEE Trans Geosc. & Rem. Sens., Vol. 38 No.6, Nov 2000, pp2627-2637

[29] T.B.Hansen, P.M.Johansen, 'Inversion scheme for Ground Penetrating Radar that takes into account the planar air-soil interface', IEEE Trans. Geosc. & Rem. Sens., Vol.38 No.1, Jan 2000, pp496-506

[30] F.T. Ulaby, R.K. Moore, A.K. Fung 'Microwave Remote Sensing: Active and Passive Volume II', Addison-Wesley, 1982.

[31] IEE Trans. Ant. Prop., vol. 46 no. 1, Jan 98

[32] M.A.Narwood, 'Handbook of Radar Scattering Statistics for Terrain', Artech 1989.

[33] A.G. Voronovich, 'Wave Scattering from Rough Surfaces', Springer-Verlag, 1994.

[34] J.A.Ogilvy, 'Theory of wave scattering from random rough surfaces', Adam Hilger, Bristol, 1991

[35] P.Beckmann, A.Spizzichino, 'The scattering of electromagnetic waves from rough surfaces', Artech House, 1987

[36] L.Ljung, 'System Indentification: Theory for the User', Prentice-Hall, 1987

[37] J.W. Brooks, M.W.Maier, S.R.Vechinski, 'Applying system identification and neural networks to the efficient discrimination of unexploded ordinance', Proc. IEEE Aerospace 97 Conference, pp449-467, Oct 1997

[38] D.Carevic, 'Kalman filter-based approach to target detection and target-background separation in ground-penetrating radar data', SPIE Conf. Detection Remediation Technol. Mines, Minelike Targets IV, pp1284-1288, 1999

[39] A.M.Zoubir, 'Signal processing techniques for landmine detection using impulse ground penetrating radar', IEEE Sensors Journal, Vol. 2, No. 1, Feb 2002

[40] M.Fritze, 'Detection of buried landmines using ground penetrating radar', SPIE Proc, Vol 2496, pp 100-108,1995

5 Demonstrator System Design

This chapter describes how the system and environment characteristics described in Chapter 4 were applied in the construction of a demonstrator system. The development was incremental in terms of complexity reflecting, on the one hand, the need for early validation of certain key system concepts such as resolution, clutter reduction and loss mechanisms, and, on the other hand, the need to prove key design components, such as the antenna array, prior to moving on to more ambitious implementations.

Results from the early stages of the system development have already been introduced in Chapter 4. Inevitably there is an element of iteration between the analytical and experimental investigations described there and the demonstrator system design. By which it is meant that some of the practical constraints imposed by designing and building the demonstrator placed constraints on the scope of the analysis that could be feasibly validated by the experiment. For example, analysis of target scattering and indeed some published papers [1] shows that an operating frequency of 2-4GHz would be an important frequency for mine detection and discrimination, but availability of reasonably priced high speed digitisation equipment[1] mandated an upper operational bandwidth of 1.5GHz for the demonstrator.

These design trade-offs mandated by practical constraints of cost, time and resources are an important aspect in evaluating whether the *proposed* system could be realised in *practice* at a reasonable cost. It is also useful for highlighting any areas where the technique may need equipment that is at or beyond the current state of the art. Such trade-offs and limitations are highlighted as necessary and may give ideas for the focus of future research.

The chapter is divided into three broad sections covering hardware development, algorithmic development and real time implementation. The hardware development description covers the antenna array design, pulse generation, digitisation and data acquisition. The algorithm development description also takes in the software controller and considers in particular computational and real-time aspects. The real time

[1] In all experiment work an Agilent Infinium 4-channel real-time digitising oscilloscope (HP54845A) was employed. .

implementation section describes the steps needed to convert the final demonstrator system into a real time processing and detection system capable of attaining the postulated search speeds.

5.1 Hardware Development

A block diagram of the prototype hardware design is shown in Figure 5-1. The key elements will be considered in turn and comprise of an array of bow-tie antenna, an RF and digital switching network, a wideband pulse generator, a real time digitiser, a PC based processor and display.

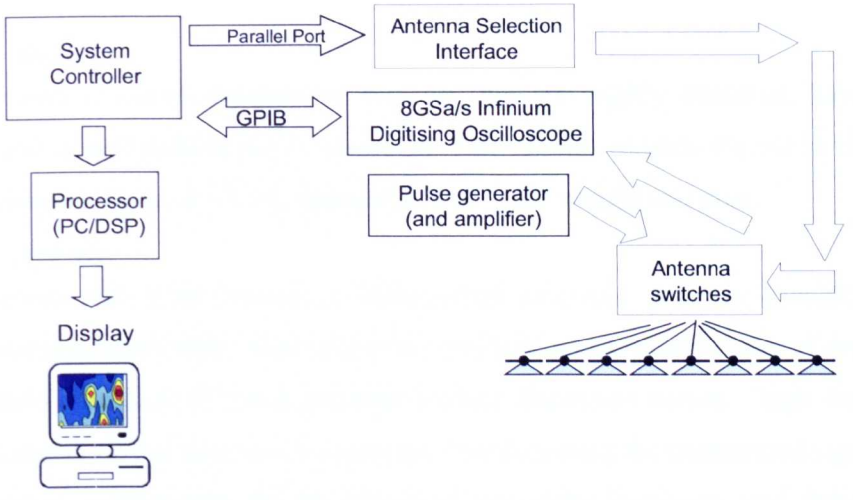

Figure 5-1 The automated experimental system

5.1.1 Antenna Design Alternatives

It is challenging to design antenna elements for GPR applications. For in-contact operation the antennas have to be matched to the soil and must therefore be capable of operating in a wide range of soil types. RASOR is non-contact, which means the antenna must be matched to the air, but nonetheless its properties will be modified by the soil structure that is in close proximity.

For RASOR an array of antenna elements will be mounted on a moving vehicle. Each antenna design needs a wideband frequency response to transmit and receive an impulse with directivity such that only the focusing area is illuminated. In addition it needs to possess the desired physical properties for such operation: low weight, low profile and simple, low cost construction.

A number of antenna designs have been considered for GPR [2] and will be briefly discussed.

5.1.1.1 Travelling Wave Transmission Lines

Travelling wave antennas are designed with V shaped transmission lines where the impedance varies from the feed impedance to free space impedance enabling good wide band matching [3]. The ends are typically terminated with resistive loads in practice to avoid resonance problems and reduce the antenna length [4]. These antennas typically have a directivity of around ±25° [5], which is too narrow to cover the RASOR search volume.

5.1.1.2 Horns

Horns are used in many applications because they are highly directive, have simple excitation and wide bandwidths [3]. However, they are not suitable for use in the tightly packed antenna array for RASOR, because of their size, weight and cost.

5.1.1.3 Spirals

Spiral antennas and other frequency independent antennas, such as Vivaldi and log periodic antennas, have wide band properties and half power beamwidths of around 75° [6]. The main drawback of these antennas is their dispersive nature - high frequencies leave the antenna earlier than low frequencies thus distorting the transmitted signal. They are also rather cumbersome for the proposed operating frequency and therefore not suitable for antenna arrays.

5.1.1.4 Dipoles

Various dipole arrangements can be used in GPR antenna array, such as crossed dipoles and cylindrical dipoles. They are simple to design and suitable for implementation in antenna arrays on substrate materials. Although they are characterised by linear polarisation and low directivity, they generally have limited bandwidths compared to other antennas [3], making them not as useful for passing wide band pulses.

5.1.1.5 Bi-conical

Bi-conical antennas are formed by placing two cones together to act as a guide for spherical waves [7]. The input impedance depends on cone angle and is broadly independent of its physical length therefore it exhibits broadband characteristics. Solid bi-conical structures are very large and they are therefore impractical in antenna arrays.

5.1.1.6 Bow-ties

Bow-tie antennas are a simplification of the bi-conical antenna and are in essence a flat triangular dipole. The properties of bow-ties, such as input and radiation characteristics,

were first analysed by Brown [8]. This design has relatively wide bandwith, suitable directivity, can be easily etched on substrate and suitable for inclusion in an array. It is also comparatively cheap and lightweight.

5.1.2 Bowtie Antenna Design

A bow-tie antenna element was designed specifically for the project study [9][10] and the details of the design are included here to show the input of the design in the operation of the system. The bow-tie is in essence a flat triangle dipole and a simplification of the bi-conical antenna. It offers reasonably good bandwidth and linear phase response at a relatively low cost compared with horn antennas, for example.

A diagram of the Bowtie antenna lay out is shown in Figure 5-2. The antenna was designed to operate at a centre frequency of 1GHz and achieved a fractional bandwidth of≈ 80% between 0.8GHz and 1.8GHz with a half power beamwidth of $\approx \pm 50°$. Ihas an antenna length of 220mm, a total width (both flares) of 215mm and is printed on RT/Duroid 5880 PTFE substrate [11] which has a dielectric constant of 2.2 and thickness of 1.57mm.

Printed bow-tie dipoles need to be fed by a balanced feed because unbalanced current distributions tend to disturb the radiation patterns. However, the antenna feed from the transmission and reception distribution network is unbalanced, typically coaxial. An unbalanced transmission line has conductors with unequal currents with respect to ground whereas balanced lines have the same, but opposite, currents. To convert between *bal*anced and *un*balanced transmission lines a device known as a balun is used which usually short circuits the unbalanced currents and permits only the balanced currents to flow into the balanced sections. The coplanar microstrip feed on the substrate has a microstrip L-shaped balun on the board reverse side that achieves this. It is based on a design by Edward and Rees [12].

The feed lines are based on the 50Ω impedance of conventional RF coaxial cables. The slight taper in the stripline feed provides an impedance match to the bowtie flares and reduces unwanted radiation from the stripline itself.

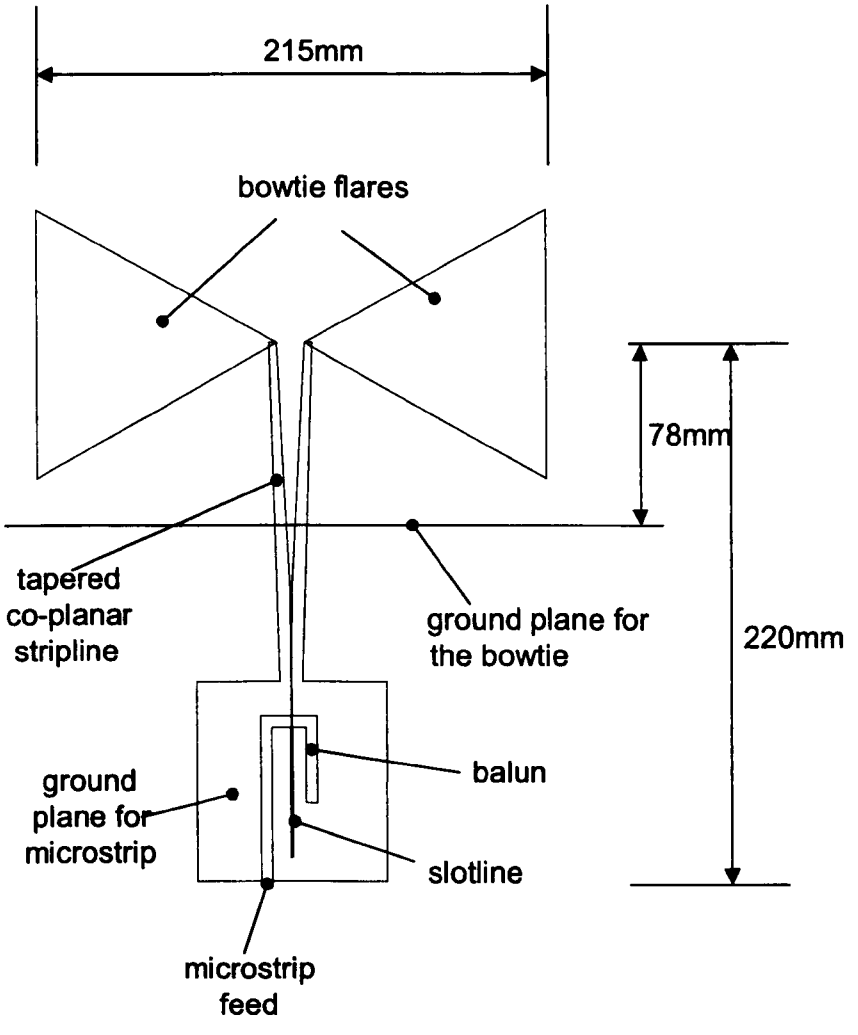

Figure 5-2 Bowtie element with microstrip feed

The radiation pattern of the antenna element was measured in the H plane and the E plane using a log periodic antenna. The observed radiation patterns at 0.8GHz and 1.2GHz are shown in Figure 5-3 and Figure 5-4 respectively.

These results demonstrate that a suitable unbalanced to balanced transition is achieved and the dipole is radiating with a half power beamwidth of $\pm 45^{\circ}$. It can be seen that a null develops around 0 degree in the upper frequency limits. Similar observations were made in the FDTD simulation results. This effect is a result of the element ground plane separation , which is $\lambda/4$ corresponding to 1 GHz.

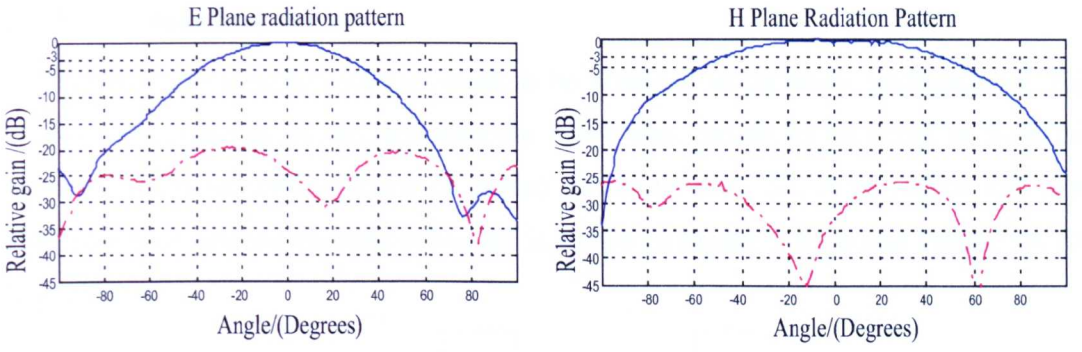

(a) (b)

Figure 5-3 Radiation pattern of the bowtie element at 0.800 GHz co-polar=solid blue, cross-polar=dashed red (a) E Plane (b) H Plane

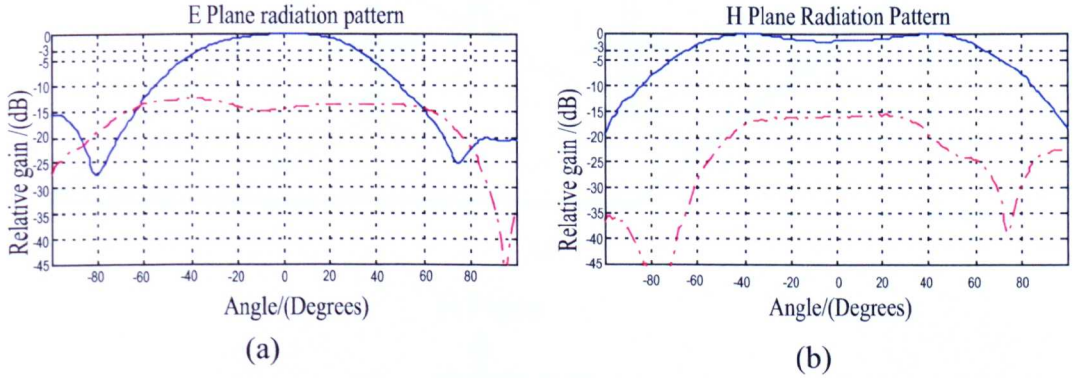

(a) (b)

Figure 5-4 Radiation pattern of the bowtie element at 1.2GHz co-polar=solid blue, cross-polar=dashed red (a) E Plane (b) H Plane, blue indicates co-polar, red dash indicates cross-polar

The frequency response of this design was measured and the return loss for the antenna element is shown in Figure 5-5, which shows a good antenna-feed match from 0.8 - 1.7 GHz.

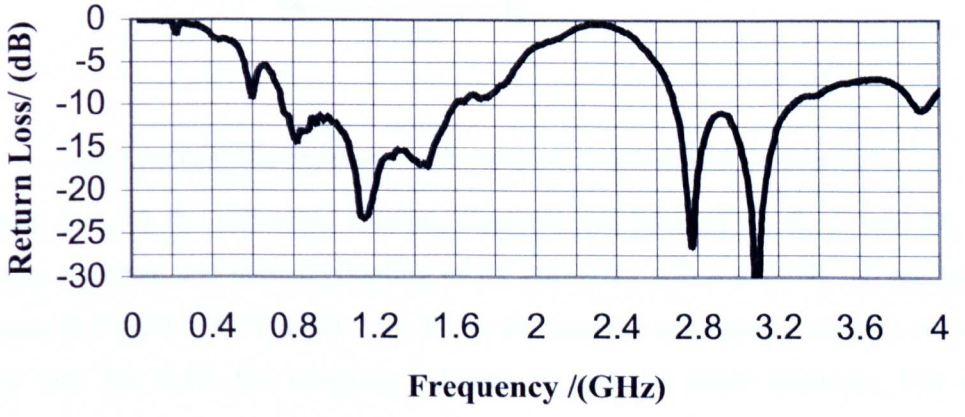

Figure 5-5 Input response of bow-tie element

5.1.3 Antenna Array

For RASOR the bow-tie antennas need to be arranged in an array configuration. The inter-element spacing of the demonstrator array was chosen to be equal in both the boresight (H plane) and collinear (E plane) directions at 0.75λ. A projection and plan view of a four-antenna element sub-array is shown in Figure 5-6 (a) and Figure 5-6 (b) respectively.

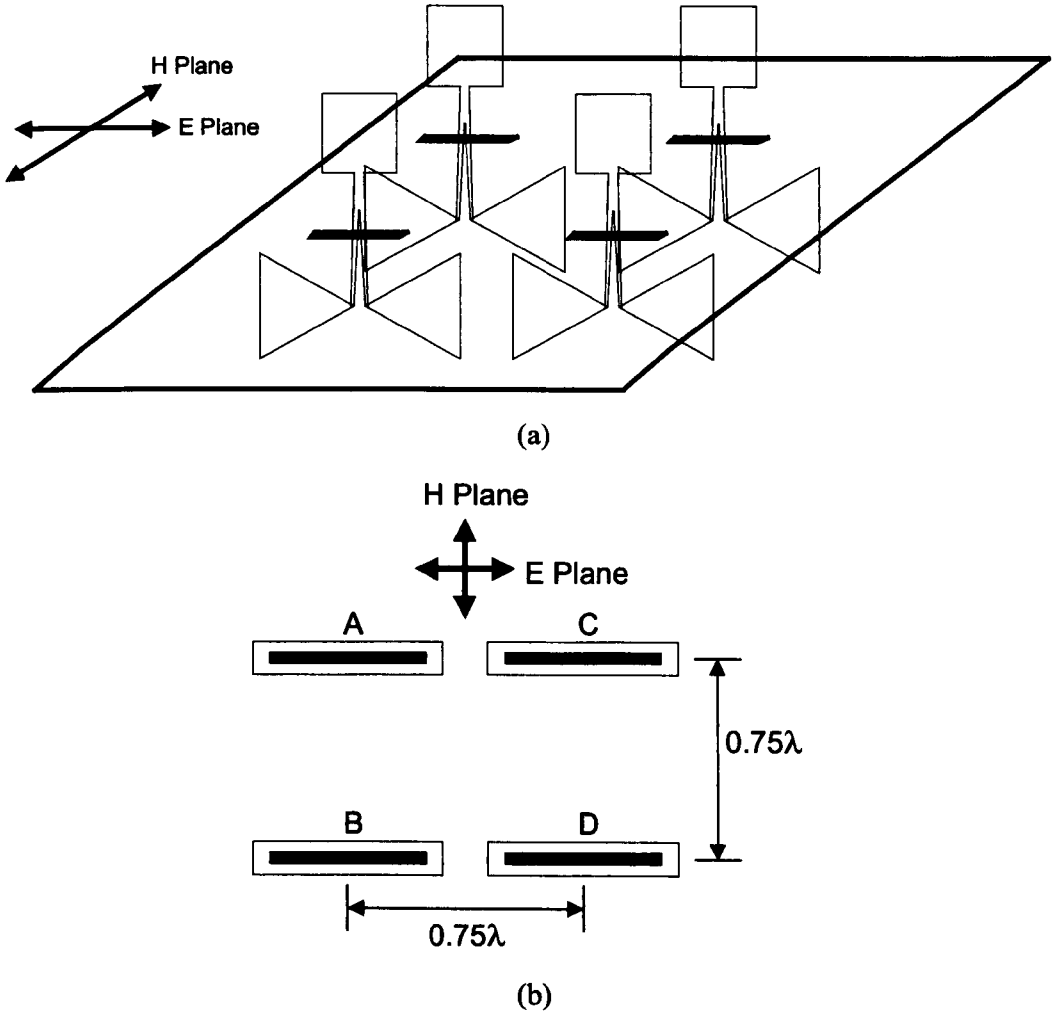

Figure 5-6 Four element antenna sub-array (a) projection view (b) plan view

In Figure 5-6 (b) the sub-array antenna elements are labelled A, B, C and D. The frequency response and mutual coupling of the sub-array was measured and the results are shown in Figure 5-7. Figure 5-7 (a) shows the impulse response of element A, while (b), (c) and (d) show the coupling between A and the other elements. For each measurement the antennas not in use are terminated in a 50Ω matched load in order to reduce unwanted ringing from these antennas.

The impulse response for B, C and D element was similar to that for A. For the couplings, the dominant coupling is with the boresight and collinear nearest neighbours and is in the order of −18dB over the frequency range of interest. A dominant mutual coupling frequency component can be seen at around 200MHz, however it will be shown later that this can be filtered out in the digital signal processing.

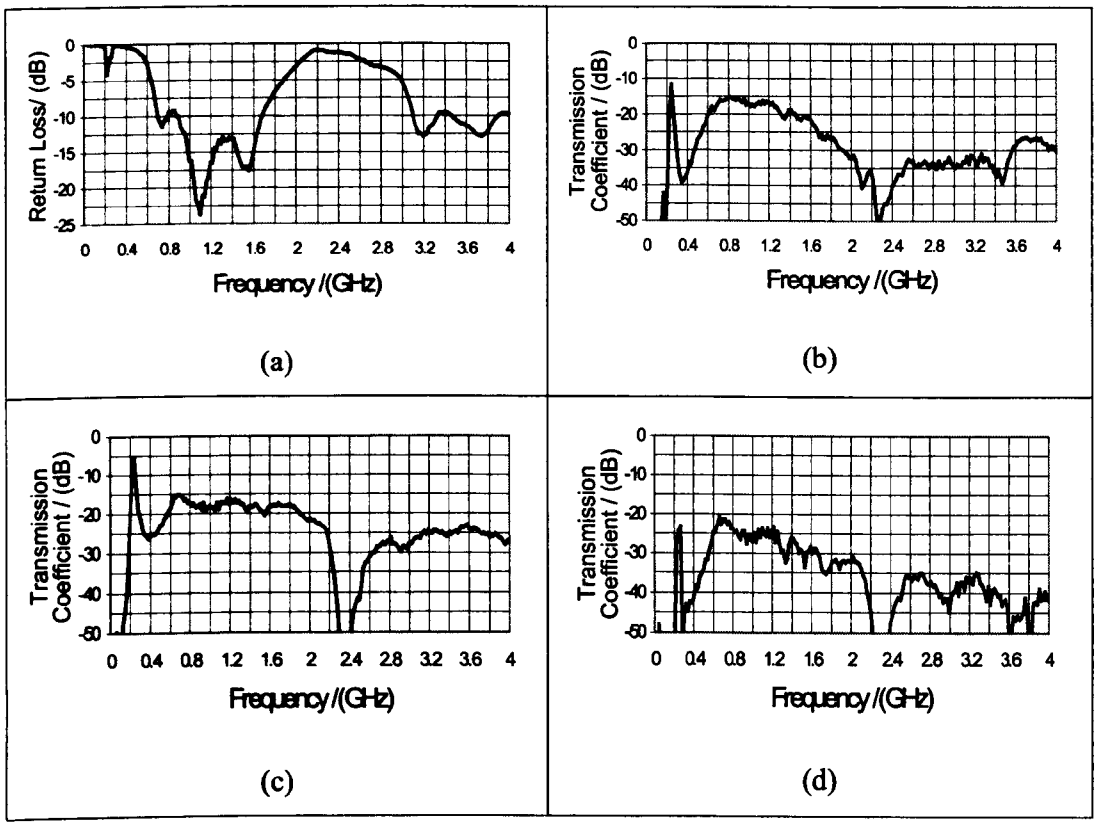

Figure 5-7 Frequency response and mutual couping of four element subarray, (a) return loss of the transmit element, (b) mutual coupling between A and B, (c) mutual coupling between A and C, (d) mutual coupling between A and D

The radiation patterns for the elements in the sub-array in the principal planes are shown in Figure 5-8 for element B at 1 GHz. The squinting observed in these patterns was due to both the non-symmetrical ground plane and the inter-element interactions in the sub-array although this is considered acceptable, because no nulls are formed within the ±45° range. In the full size array, it is the edge element patterns that would undergo more distortions while the inner element patterns are almost the same as the isolated antenna element patterns.

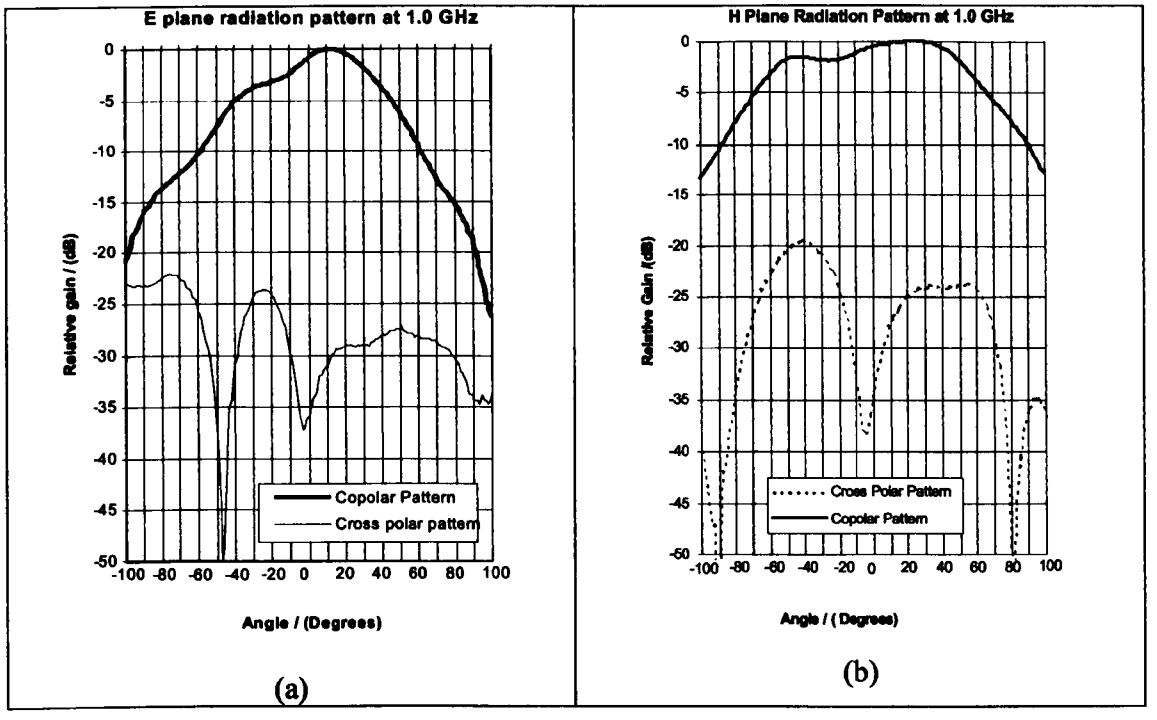

Figure 5-8 Radiation pattern of element B in the 2x2 array (a) E plane radiation pattern, (b) H plane radiation pattern.

The full array consists of 28 bowtie elements with seven elements in the boresight direction and four in the collinear direction as shown in Figure 5-9. This gives sufficient coverage of the ground to evaluate the key aspects of the RASOR performance. Vehicle motion will sweep the array forward in the collinear direction, i.e. in the horizontal direction as shown in Figure 5-9.

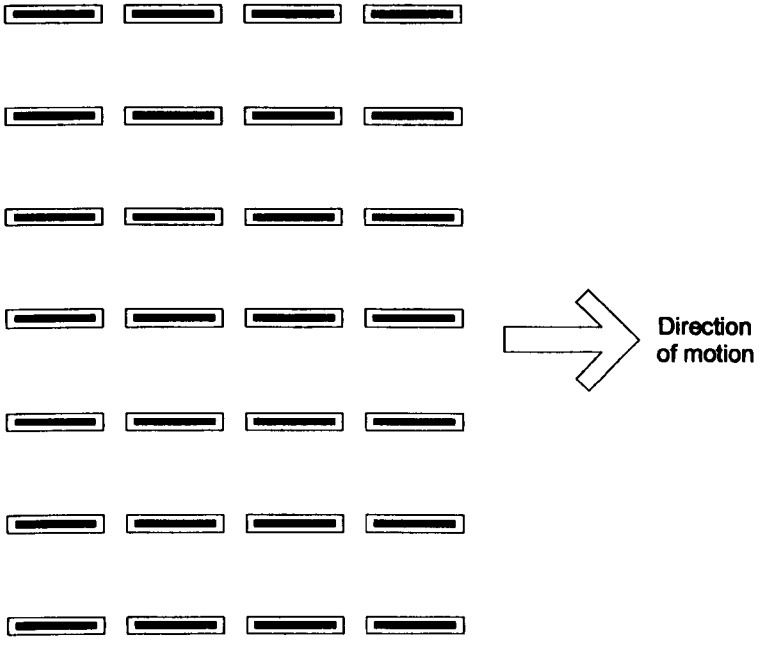

Figure 5-9 Plan view of full RASOR demonstrator array containing twenty-eight bow-tie elements

The array backplane was constructed from wooden panels supporting a sheet aluminium ground plane covered with a 40mm layer of Radar Absorbent Material (RAM). It was found on initial measurements when a reflecting ground plane was employed that multiple reflections between the surface and ground plane generated additional delayed signals [13]. The RAM reduced this multiple reverberation interference. The RAM does reduce the antenna efficiency of the elements since the ground plane is no longer focusing signals towards the soil, but does have the beneficial side-effect of increasing the antenna -10dB bandwidth since the antenna now has a lower Q-factor (due to increased losses).

A photograph of part of the demonstrator antenna array is shown in Figure 5-10. The squares of black absorbing material are clearly visible covering the metal ground plane.

Figure 5-10: Part of the RASOR demonstrator bow-tie antenna array

5.1.4 Switching Network

A digitally controlled RF switching network was mounted on the other side of the antenna backplane, which is shown in the picture in Figure 5-11.

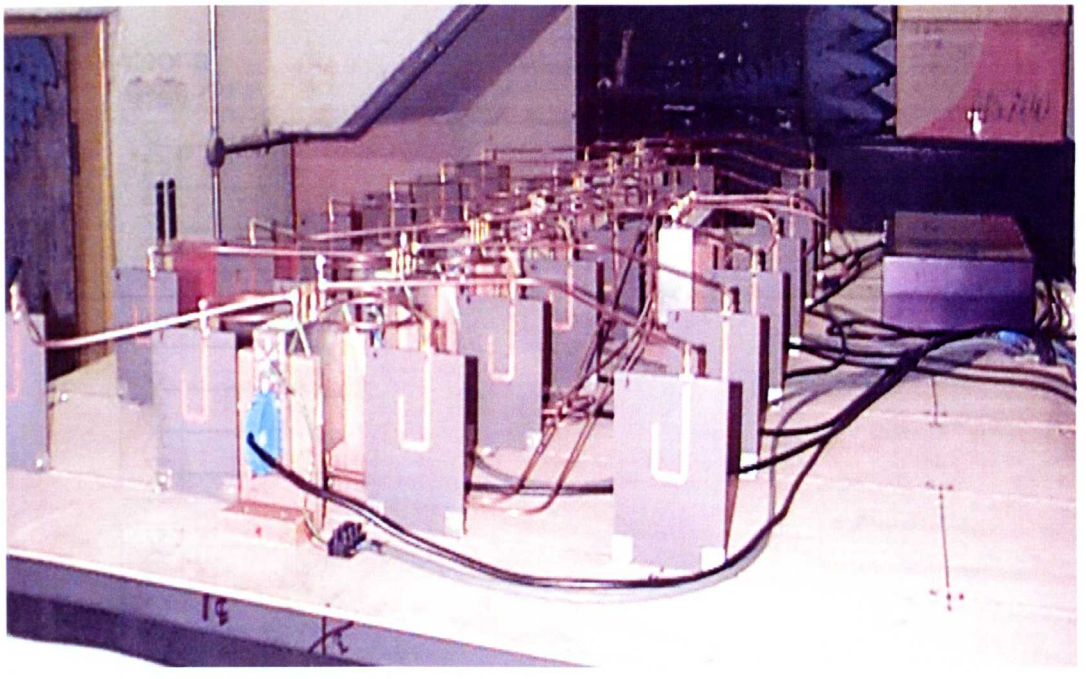

Figure 5-11 Array backplane showing the switching network

The purpose of this network is to allow each antenna element in the array to be switched into one of three states:

- *Transmitting*: the antenna is switched to the pulse generator and power amplifiers RF circuit and will radiate a wideband pulse.
- *Receiving*: the antenna is switched to the receiver low noise amplifier and digitisation circuit and will receive the pulse reflections from the soil
- *Off*: the antenna is switched to a matched load of 50Ω, so that it neither transmits, receives, nor re-radiates any cross-coupled signals from the direct propagation path.

For the RASOR technique only one antenna can be transmitting at any time and, for the purposes of the demonstrator, only one antenna can be receiving. All the others are switched to the matched load. An example of the selection of one particular transmit and receive antenna pair from a twenty-eight antenna array is shown schematically in Figure 5-12.

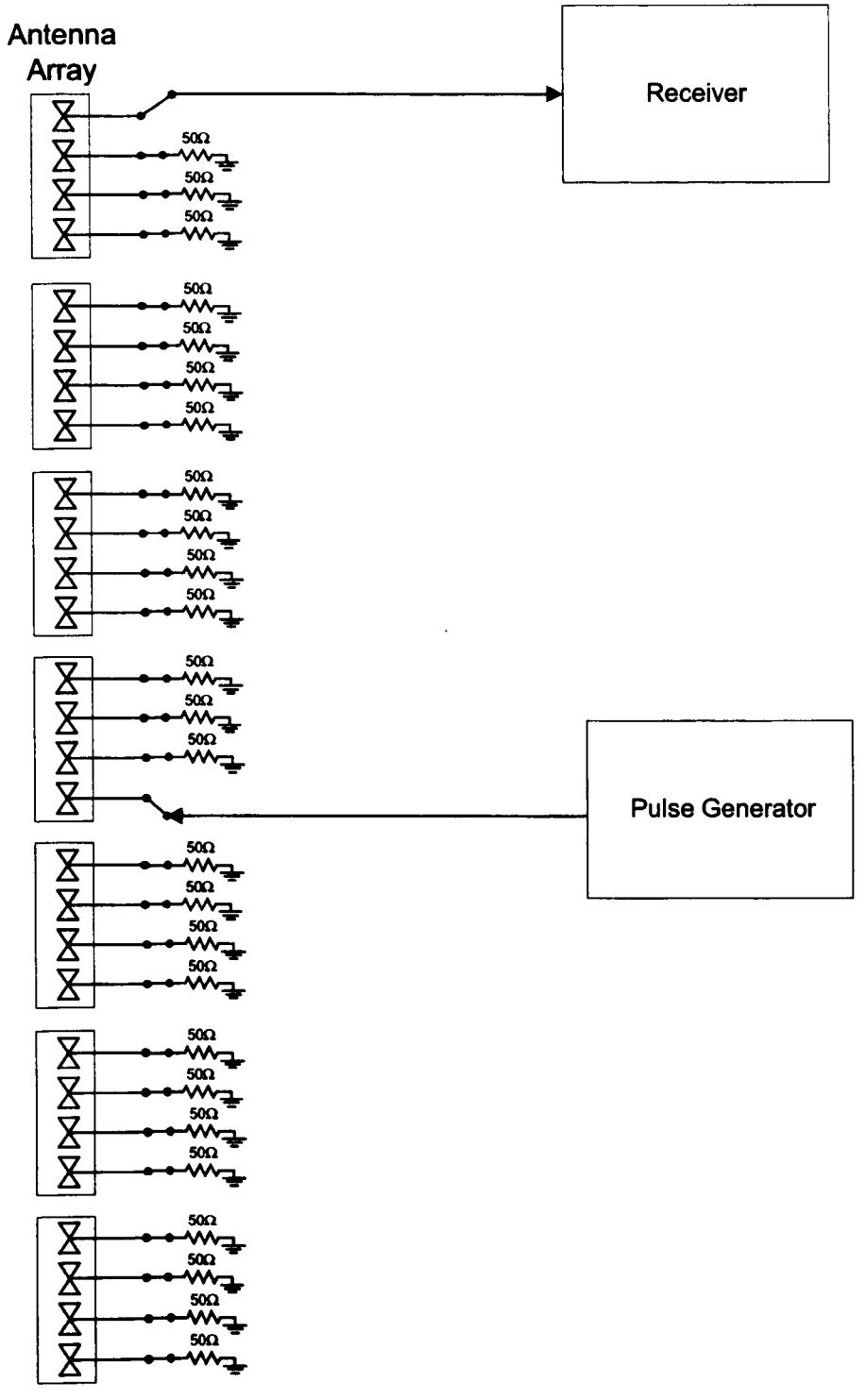

Figure 5-12 Example switching schematic for a twenty eight element array

The twenty-eight antenna elements that comprise the RASOR array are logically grouped in to seven rows of four columns, where each column represents the set of four collinear

elements. One seven-way RF switch box and seven four-way RF switches were designed to connect each of the twenty-eight elements in turn. A block diagram of the RASOR switching network is shown in Figure 5-13.

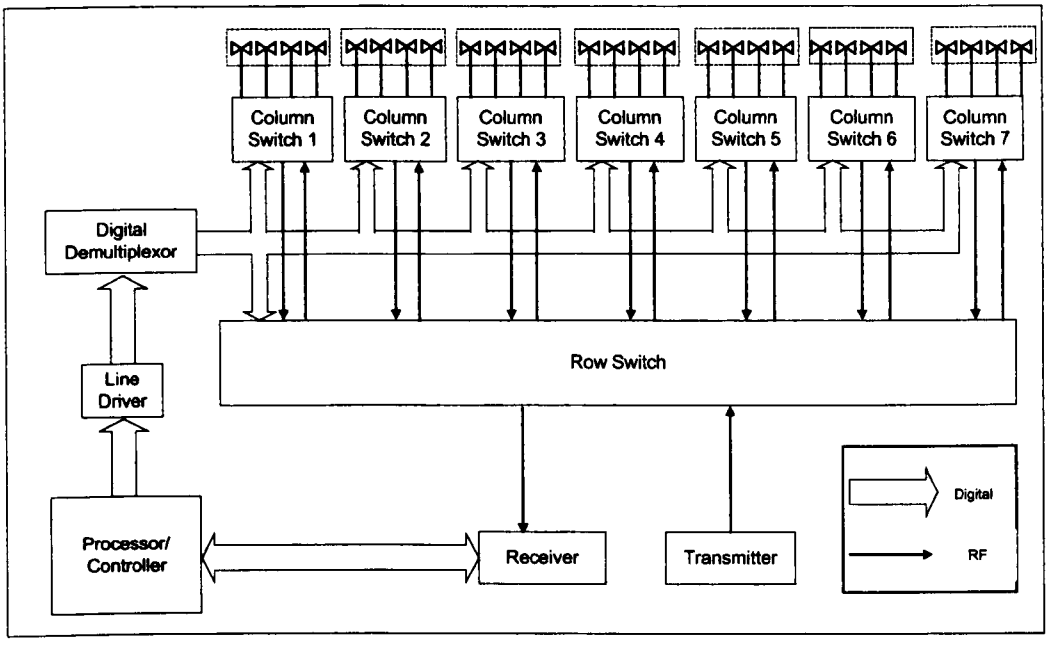

Figure 5-13 RF switching block diagram

Figure 5-14 and Figure 5-15 show the column switch circuits schematic and circuit diagram respectively which utilise three types of analogue switches [14][15][16].

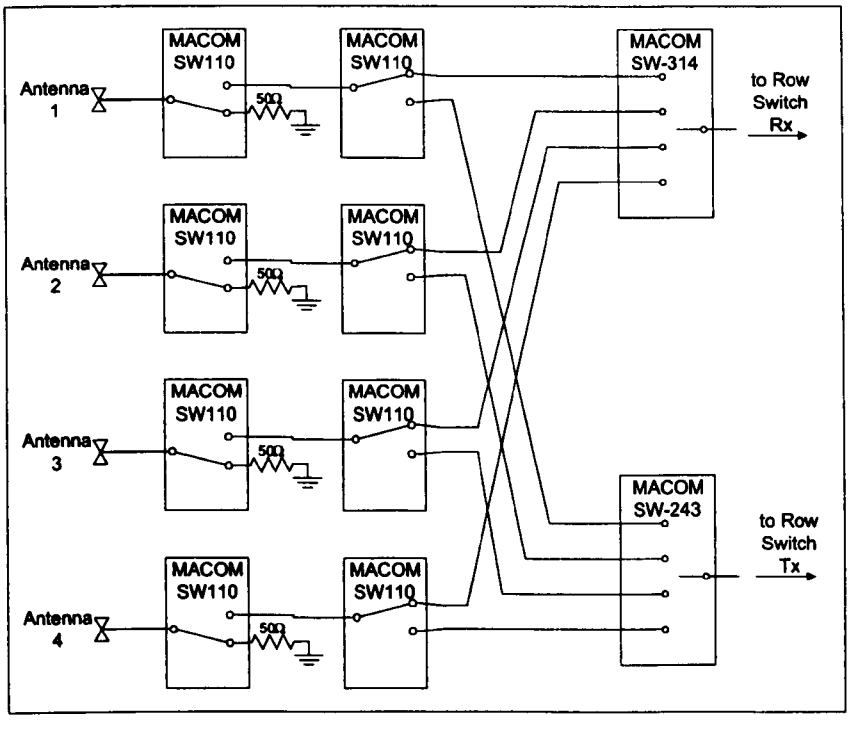

Figure 5-14 Column switch schematic

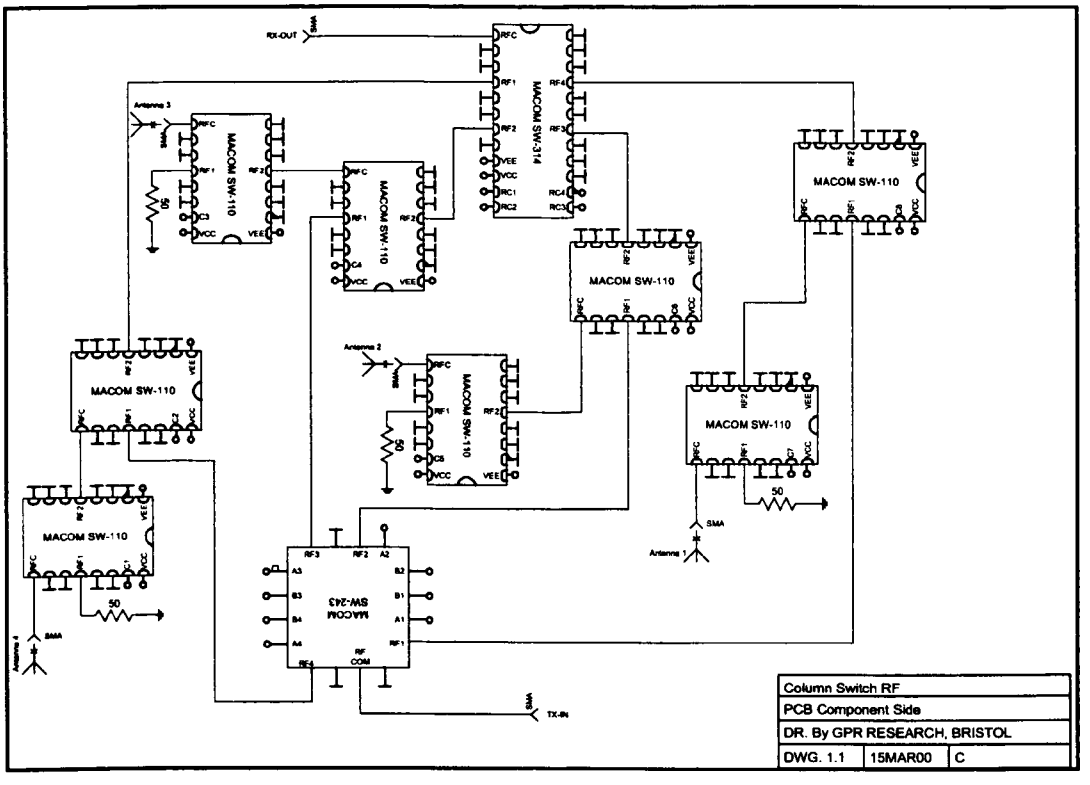

Figure 5-15 Column switch circuit diagram layout

Figure 5-16 and Figure 5-17 show the row switch circuits schematic and circuit diagram which also utilise the same three MACOM analogue switches as for the column switch in different arrangement.

The circuits are shown in situ in Figure 5-18. Both circuits were constructed on RT/Duroid 6010 PTFE [17] which has dielectric constant of 10.2 and thickness of 0.635mm utilising microstrip tracks. These switches were selected to provide high isolation of >30dB per switch to minimise cross talk between circuits. Typical insertion loss was measured to be around 3dB in total for each transmit and receive paths.

Differences between boards were designed to be minimal so that relative path losses and delays are equalised. SMA connectors and cables interconnect the switch boxes, antennas, pulse generator and receiver digitiser. These cables were of equal length hence the links to antennas close to the switch box had to be looped as can be seen in Figure 5-18.

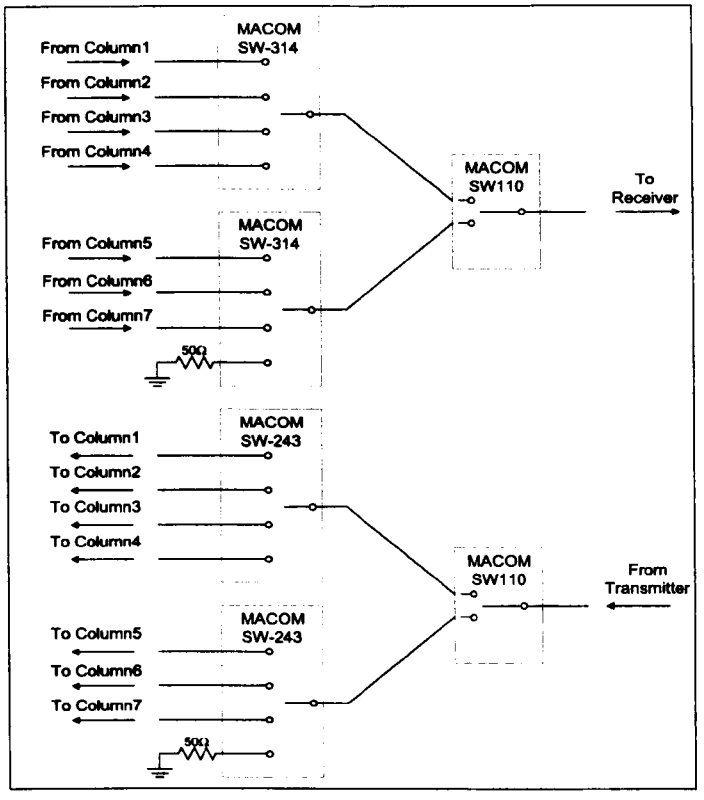

Figure 5-16 Row switch schematic

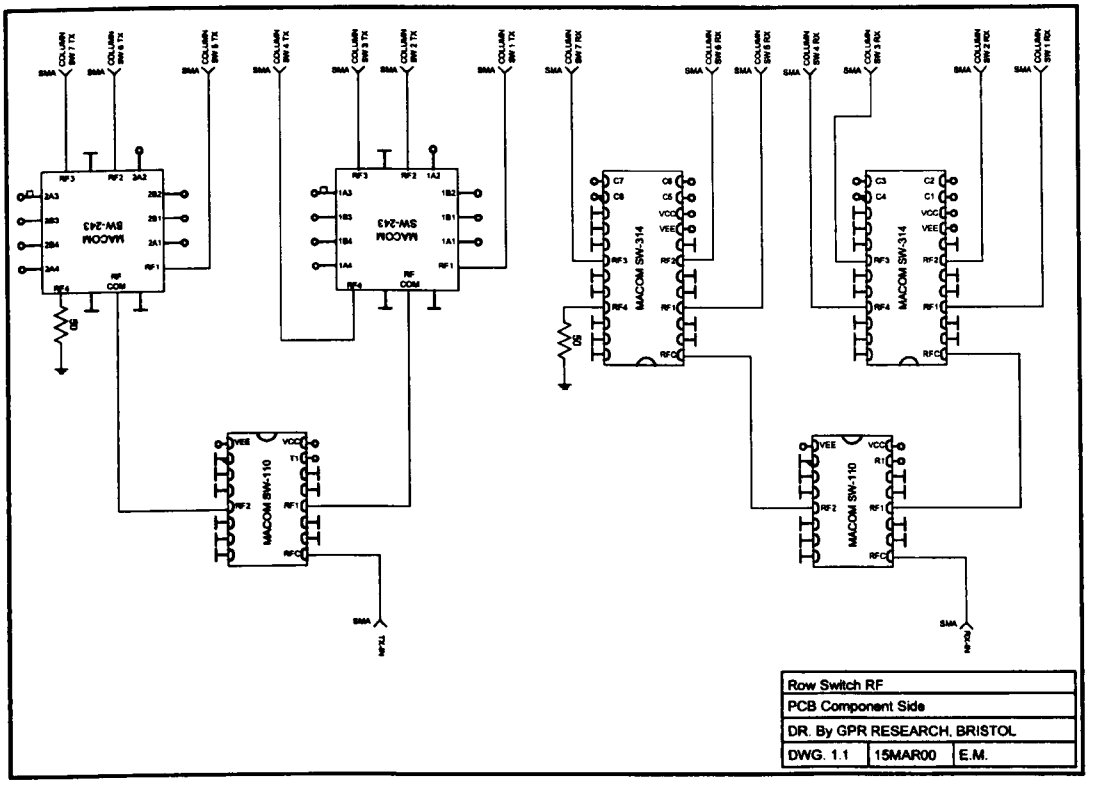

Figure 5-17 Row switch circuit diagram layout

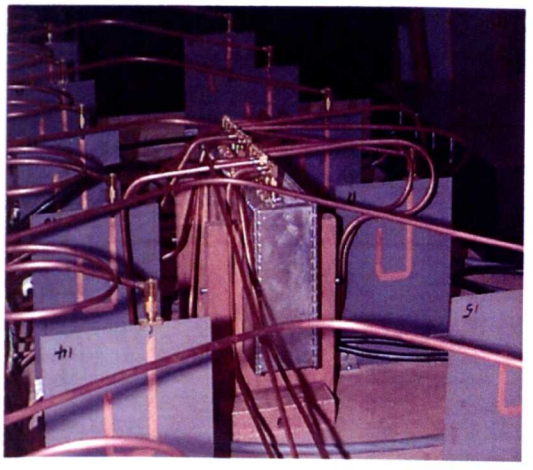

(a)

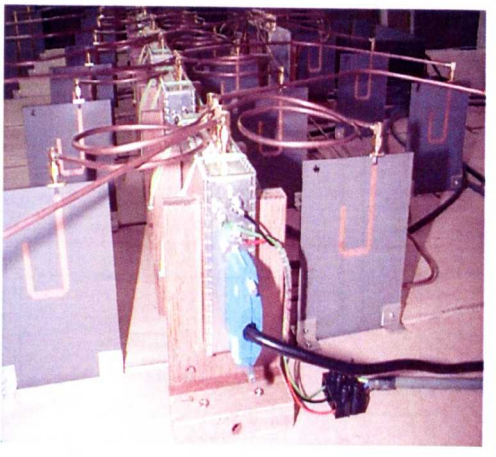

(b)

Figure 5-18 RF switch boxes (a) seven way row switch (b) four way column switches

The semi-rigid SMA cables were also constructed to close tolerances to minimise phase and loss differences between paths. Nonetheless slight relative differences are inevitable and a calibration process was devised to compensate for this. In Figure 5-10 small white rectangles can be seen on the bottom of the bowtie flares. These are actually velcro strips which were used to secure a measurement antenna (another bowtie) temporarily onto each antenna element in the array in turn. By transmitting a pulse through this circuit with the array antenna switched to transmit and then receive the relative path length of RF path to each antenna could be measured and the small differences in the circuit path calibrated out in the focusing algorithm.

A centralised digital switching and driver unit was designed to generate the required logic levels to drive each of the RF switches. The switching unit was also mounted on the array backplane and is shown schematically and pictorially in Figure 5-19 and Figure 5-20 respectively. The digital control signals are fed to the row and column switch boxes via screened multicore cable and D type connectors visible on Figure 5-18 (b). The circuit logic is held on two Complex Programmable Logic Devices (CPLD) [18] with an additional three line drivers [19] required for driving the analogue switches.

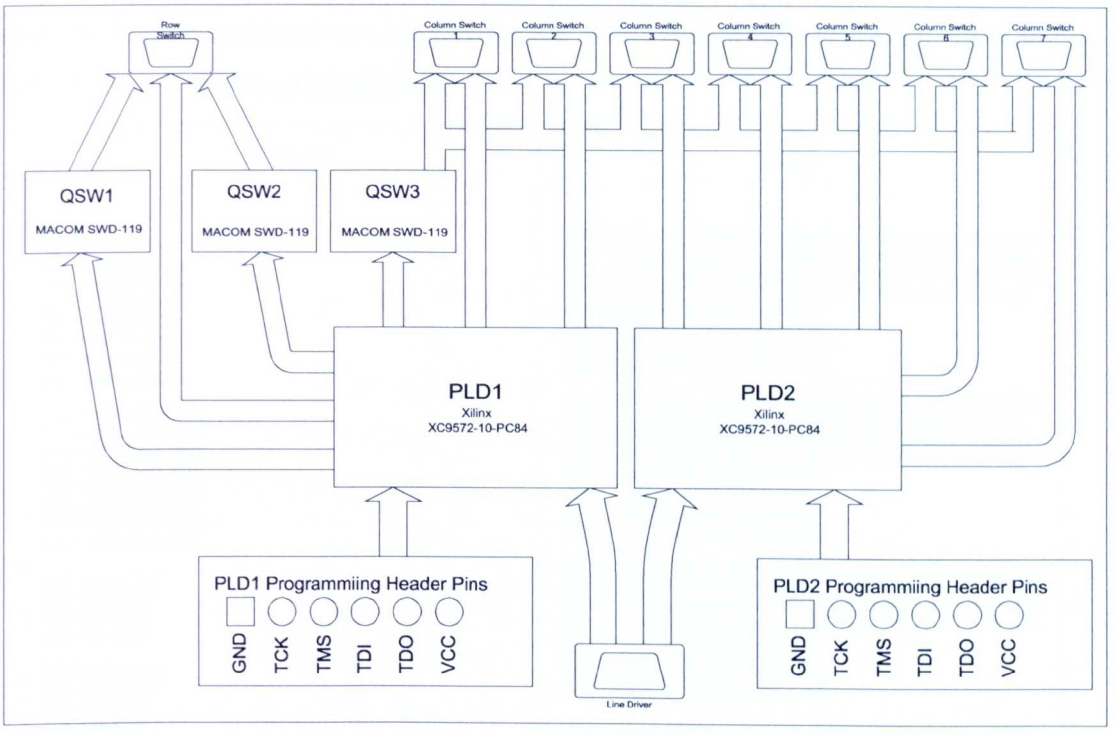

Figure 5-19 Array digital switching control box circuit

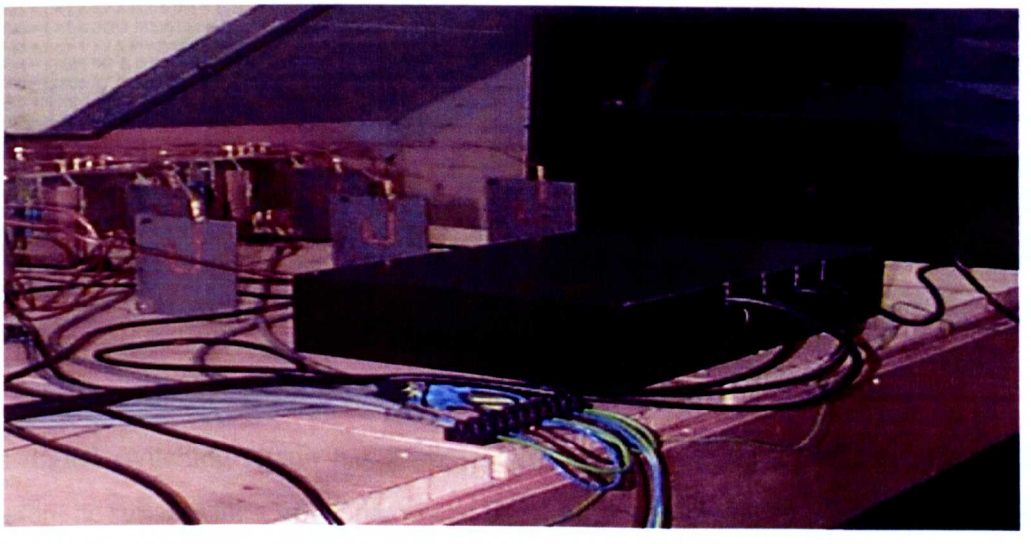

Figure 5-20 Array digital switching control box in situ (with associated cabling)

Header pins are incorporated into the PCB layout so that the chips can be programmed *in situ* using the Joint Test Action Group (JTAG) standard protocol via a PC serial port (the chips can also be programmed separately if required). The CPLD devices can therefore be easily reprogrammed later if, for example, a different switching scheme were required. The required Boolean expressions - 10 inputs and 85 outputs - were minimised by hand

and then implemented and simulated using the Xilinx design suite [20] [21]. An example control logic is shown in Figure 5-21.

PLD1

```
F1 = !X3;
F2 = !X8;
F3 = !X3 & !X4 & !X5;
F4 = !X3 & !X4 & X5;
F5 = !X3 & X4 & !X5;
F6 = !X3 & X4 & X5;
F7 = X3 & !X4 & !X5;
F8 = X3 & !X4 & X5;
F9 = X3 & X4 & !X5;

F10 = !X8 & !X9 & !X10;
F11 = !X8 & !X9 & X10;
F12 = !X8 & X9 & !X10;
F13 = !X8 & X9 & X10;
F14 = X8 & !X9 & !X10;
F15 = X8 & !X9 & X10;
F16 = X8 & X9 & !X10;
F17 = X8 & X9 & X10;

F18 = !X6 & !X7;
F19 = !X6 & X7;
F20 = X6 & !X7;
F21 = X6 & X7;

F22 = !X6 & !X7;
F23 = !X6 & X7;
F24 = X6 & !X7;
F25 = X6 & X7;

F26 = !X1 & !X2;
F27 = !X1 & X2;
F28 = X1 & !X2;
F29 = X1 & X2;

F30 = (!X1 & !X2 & !X3 & !X4 & !X5) # (!X6 & !X7 & !X8 & !X9 & !X10);
F31 = (!X1 & X2 & !X3 & !X4 & !X5) # (!X6 & X7 & !X8 & !X9 & !X10);
F32 = ( X1 & !X2 & !X3 & !X4 & !X5) # ( X6 & !X7 & !X8 & !X9 & !X10);
F33 = ( X1 & X2 & !X3 & !X4 & !X5) # ( X6 & X7 & !X8 & !X9 & !X10);
F34 = !(!X6& !X7 & !X8 & !X9 & !X10);
F35 = !(!X6& X7 & !X8 & !X9 & !X10);
F36 = !( X6 & !X7 & !X8 & !X9 & !X10);
F37 = !( X6 & X7 & !X8 & !X9 & !X10);

F38 = (!X1 & !X2 & !X3 & !X4 & X5) # (!X6 & !X7 & !X8 & !X9 & X10);
F39 = (!X1 & X2 & !X3 & !X4 & X5) # (!X6 & X7 & !X8 & !X9 & X10);
F40 = ( X1 & !X2 & !X3 & !X4 & X5) # ( X6 & !X7 & !X8 & !X9 & X10);
F41 = ( X1 & X2 & !X3 & !X4 & X5) # ( X6 & X7 & !X8 & !X9 & X10);
F42 = !(!X6& !X7 & !X8 & !X9 & X10);
F43 = !(!X6& X7 & !X8 & !X9 & X10);
F44 = !( X6 & !X7 & !X8 & !X9 & X10);
F45 = !( X6 & X7 & !X8 & !X9 & X10);
```

PLD2

```
F46 = (!X1 & !X2 & !X3 & X4 & !X5) # (!X6 & !X7 & !X8 & X9 & !X10);
F47 = (!X1 & X2 & !X3 & X4 & !X5) # (!X6 & X7 & !X8 & X9 & !X10);
F48 = ( X1 & !X2 & !X3 & X4 & !X5) # ( X6 & !X7 & !X8 & X9 & !X10);
F49 = ( X1 & X2 & !X3 & X4 & !X5) # ( X6 & X7 & !X8 & X9 & !X10);
F50 = !(!X6& !X7 & !X8 & X9 & !X10);
F51 = !(!X6& X7 & !X8 & X9 & !X10);
F52 = !( X6 & !X7 & !X8 & X9 & !X10);
F53 = !( X6 & X7 & !X8 & X9 & !X10);

F54 = (!X1 & !X2 & !X3 & X4 & X5) # (!X6 & !X7 & !X8 & X9 & X10);
F55 = (!X1 & X2 & !X3 & X4 & X5) # (!X6 & X7 & !X8 & X9 & X10);
F56 = ( X1 & !X2 & !X3 & X4 & X5) # ( X6 & !X7 & !X8 & X9 & X10);
F57 = ( X1 & X2 & !X3 & X4 & X5) # ( X6 & X7 & !X8 & X9 & X10);
F58 = !(!X6& !X7 & !X8 & X9 & X10);
F59 = !(!X6& X7 & !X8 & X9 & X10);
F60 = !( X6 & !X7 & !X8 & X9 & X10);
F61 = !( X6 & X7 & !X8 & X9 & X10);

F62 = (!X1 & !X2 & X3 & !X4 & !X5) # (!X6 & !X7 & X8 & !X9 & !X10);
F63 = (!X1 & X2 & X3 & !X4 & !X5) # (!X6 & X7 & X8 & !X9 & !X10);
F64 = ( X1 & !X2 & X3 & !X4 & !X5) # ( X6 & !X7 & X8 & !X9 & !X10);
F65 = ( X1 & X2 & X3 & !X4 & !X5) # ( X6 & X7 & X8 & !X9 & !X10);
F66 = !(!X6& !X7 & X8 & !X9 & !X10);
F67 = !(!X6& X7 & X8 & !X9 & !X10);
F68 = !( X6 & !X7 & X8 & !X9 & !X10);
F69 = !( X6 & X7 & X8 & !X9 & !X10);

F70 = (!X1 & !X2 & X3 & !X4 & X5) # (!X6 & !X7 & X8 & !X9 & X10);
F71 = (!X1 & X2 & X3 & !X4 & X5) # (!X6 & X7 & X8 & !X9 & X10);
F72 = ( X1 & !X2 & X3 & !X4 & X5) # ( X6 & !X7 & X8 & !X9 & X10);
F73 = ( X1 & X2 & X3 & !X4 & X5) # ( X6 & X7 & X8 & !X9 & X10);
F74 = !(!X6& !X7 & X8 & !X9 & X10);
F75 = !(!X6& X7 & X8 & !X9 & X10);
F76 = !( X6 & !X7 & X8 & !X9 & X10);
F77 = !( X6 & X7 & X8 & !X9 & X10);

F78 = (!X1 & !X2 & X3 & X4 & !X5) # (!X6 & !X7 & X8 & X9 & !X10);
F79 = (!X1 & X2 & X3 & X4 & !X5) # (!X6 & X7 & X8 & X9 & !X10);
F80 = ( X1 & !X2 & X3 & X4 & !X5) # ( X6 & !X7 & X8 & X9 & !X10);
F81 = ( X1 & X2 & X3 & X4 & !X5) # ( X6 & X7 & X8 & X9 & !X10);
F82 = !(!X6& !X7 & X8 & X9 & !X10);
F83 = !(!X6& X7 & X8 & X9 & !X10);
F84 = !( X6 & !X7 & X8 & X9 & !X10);
F85 = !( X6 & X7 & X8 & X9 & !X10);
```

Figure 5-21 Example CPLD digital control logic

This digital switching circuit has a propagation/settling time of only ≈ 7ns and would therefore be suitable for a fully operational high-speed system as will be shown in section 5.3. In the demonstrator system it is controlled via a standard PC parallel port via an additional line driver and buffer.

5.1.4.1 Switching Sequence

For each focusing sweep each unique transmitter and receiver pair needs to be exercised and antenna reciprocity means that in a *N* element array there are *N(N-1)/2* unique antenna pairs, i.e. there is no need to exercise bistatic pairs both ways. The antenna pairs can be switched in any order and in the majority of experiments the switching scheme

depicted in Figure 5-22 was used. For a given transmitting antenna, the receiving antennas are switched sequentially sweeping column-wise and then row-wise in a raster sweep. The next transmitting antenna is then selected in a similar raster and the remaining antennas switched sequentially again. This gives a total number of paths for the demonstrator system of

$$P = \frac{28 \times 27}{2} - 7 \times 3! = 336 \qquad \textbf{(5-1)}$$

giving a theoretical processing gain over conventional bi-static GPR of 25dB where the slight deduction in the theoretical gain of 7 x 3! is as a consequence of not using the transmit/receive pairs within a column.

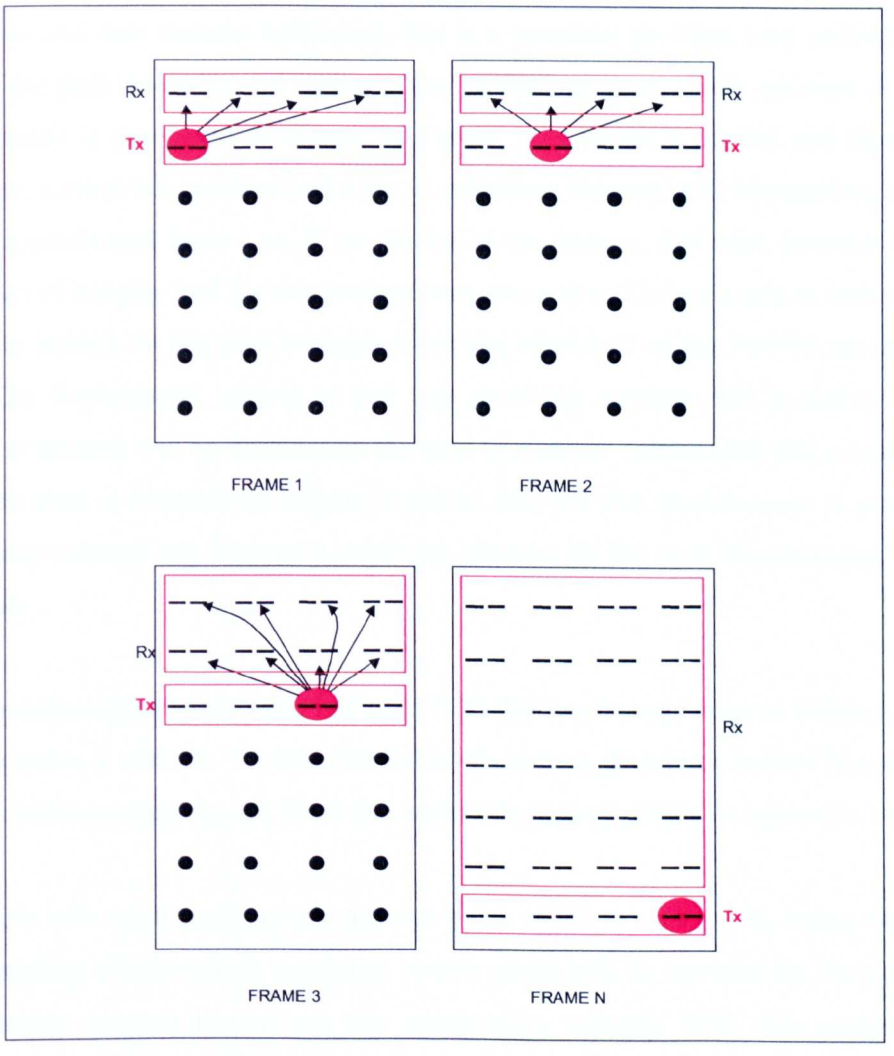

Figure 5-22 RASOR Switching scheme

In addition to this reduction in the maximum theoretical processing gain this scheme does in fact have a further drawback. Firstly it takes no advantage of bistatic redundancy to help with digitisation bottlenecks - which is a potential problem for real time RASOR

as will be shown in section 5.3.1. Secondly it tends to overemphasis the contribution of the last column of transmitters with two consequences.

1. Obscuraction blockages in the paths become more significant due to the reduction in Tx/Rx path diversity.
2. A failure of the last row of transmitters has increased impact on overall performance. For example, if the second column of transmitters is lost, then only 16 paths are unavailable. However if the last column of transmitters is lost, then 96 paths are unavailable.

An alternative switching scheme was devised, but not implemented, to reduce the digitisation and data transfer bottleneck that is a potential problem (see section 5.3.1), reinstate the path diversity and increase the processing gain. Each antenna in the 28 element array is numbered as shown in Figure 5-23 where a circled red dipole is a transmitter, a cross is a receiver and a dot is a dormant antenna. The transmitting antenna index is incremented from 1 to 28 as shown in the frames. For each transmit event a reduced set of roughly half the receive antennas are active (13 for an odd tx index, 14 for an even tx index). At the next transmit event the other half of the receive antennas are active. The fundamental criteria is that any receiving antenna that is active for one transmitter antenna will be dormant on the next transmitter antenna thereby ensuring that double the time is available to acquire digitised data for that antenna pair. A previously transmitting antenna can become a receiving antenna on the next transmission, but not vice-versa.

Using the indexing notation given in Figure 5-23 this can be expressed as follows:
When Tx index is odd: Rx = { Odd (Rx index>Tx index) , Even (Rx index<Tx index) }
When Tx index is even: Rx = { Even (Rx index>Tx index) , Odd (Rx index<Tx index) }

Clearly this will result in all unique antenna pairs, (13+14) x 14 = 378, being exercised. Cross coupling effects within a column switch could still be avoided by excluding the *single* receive antenna present on any transmitting column. With this exclusion the switching scheme is compatible with the existing rf switching design at the expense of only 28 paths in total (rather than 42 for the other scheme).

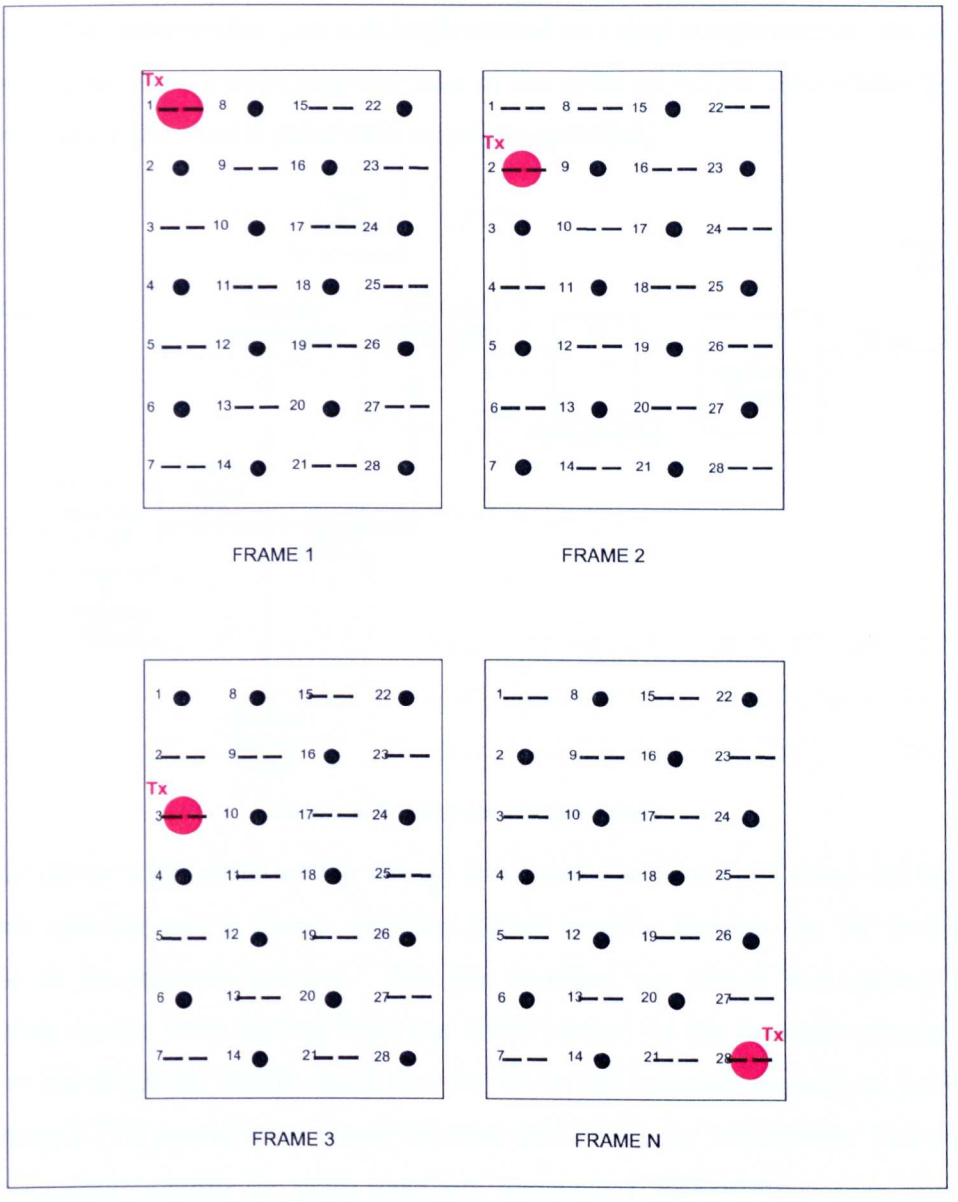

Figure 5-23 Alternative RASOR Switching Scheme

5.1.5 Pulse Generator

An RF pulse generator was developed to produce a 3ns pulse modulated by a 1GHz sinusoid using widely available off-the-shelf circuits and test equipment as shown in Figure 5-24. The mean transmitted pulse power, without any amplification, was around 10dBm. This was increased to around 30dBm by using an available wideband amplifier to combat path losses.

The pulse-train transmission gate was implemented as a dual complementary cascade of GaAs switches. With a switching rise time of the order of 1.5 ns, this method proved quite suitable for the 3-cycle pulse-train originally specified.

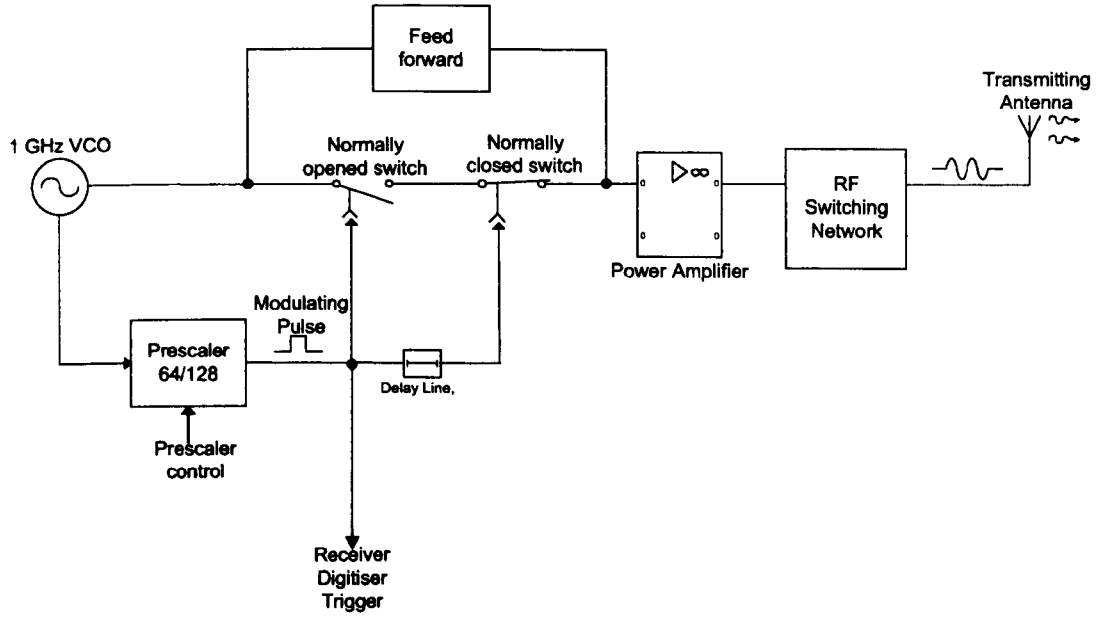

Figure 5-24 Pulse generation circuit

A 1GHz carrier is generated by the voltage controlled oscillator (VCO) and fed through two line switches and a power amplifier before passing through the RF switching network to the transmit antenna. The line switches are closed and opened by a modulating square wave derived from the 1GHz carrier via the prescaler circuit. This prescaler can divide the 1 GHz signal by either 64 or 128 (selected manually as a switch) thus giving a TTL square wave output of either 15.625MHz or 7.8125MHz. This square wave effectively controls the pulse repetition frequency (PRF) of the system. For real-time RASOR the PRF would potentially need to increase by 2 to provide a total pulse repetition interval (PRI) of 32ns as will be shown in section 5.3.1.

The line switches are complementary SPDT GaAs switches and effectively time gate the incoming 1GHz carrier to produce impulse. The length of the impulse is controlled by the delay line, τ and is tuneable to one, two or three 1GHz cycles. The feedforward circuit is suitably scaled and phase shifted in order to cancel out any carrier signal that bleeds through the switches.

An example transmit pulse is shown in Figure 5-25.

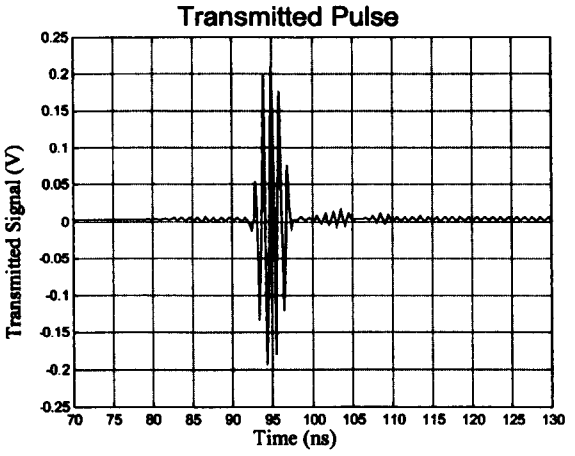

Figure 5-25 Example transmit pulse

5.1.6 Digitisation

An off-the-shelf laboratory digital sampling oscilloscope samples the received signal [22]. This offers up to 8GHz real-time sampling with 8 bits resolution using flash ADC technology. An input anti-aliasing filter limits the sampling bandwidth to 1.5 GHz.

The oscilloscope was edge triggered by the transmitter gating signal and operated at the maximum sampling rate of 8GSa/s. The oscilloscope offers the facility to average A-scans to reduce sampling noise and increase dynamic range to around 12 bits (depending on the number of averages taken), with, of course, a penalty in data collection time. For the demonstrator a sampling window of 400 samples was taken covering a time window of 50ns. This covers a much larger range (nominally 1 to 4m in the ground) than would be needed for land-mine detection, but since the PRI allowed this it was thought prudent to test full capabilities of the system.

The sampling oscilloscope was the single most expensive item purchased for the development project and at the time of purchase was the best commercial device available. It was highlighted in Chapter 4 that a device with a wider input bandwidth allows an enhanced detection and classification ability against AP mines. However, even if a wider bandwidth were available there are other data acquisition difficulties that must be overcome if a practical RASOR is to be brought to fruition.

The main real-time difficulty is the bottleneck in downloading data from the digitiser into the signal processing cards. Consider the lowest pulse repetition frequency of

7.8125MHz (from the transmit circuit) and for each pulse a time sampling window of 400 bytes is gathered gives a total data rate of 25Gbits/second. This data rate is significantly above the limit for the oscilloscope's GPIB buses or Ethernet. For the RASOR demonstrator the data was transferred over GPIB to the signal processing co-processors, thus only 1 in every 1000 transmissions at this PRF was collectable.

5.2 Algorithmic implementation

A block diagram representation of the algorithm implementation is shown in Figure 5-26. The signal processing proceeds from left to right in the diagram in terms of data throughput and, in general, algorithm complexity. The incoming data indicated as Antenna Pair 1 to Antenna pair *N* are A-scan time samples from each transmit/receive pair. Averaging (or stacking) and filtering are applied before an average background (see section 4.4.2) is deducted prior to passing the data on to the focusing algorithm. The 3D focused image is passed on for further image processing and display. Each of these building blocks will be described in more detail.

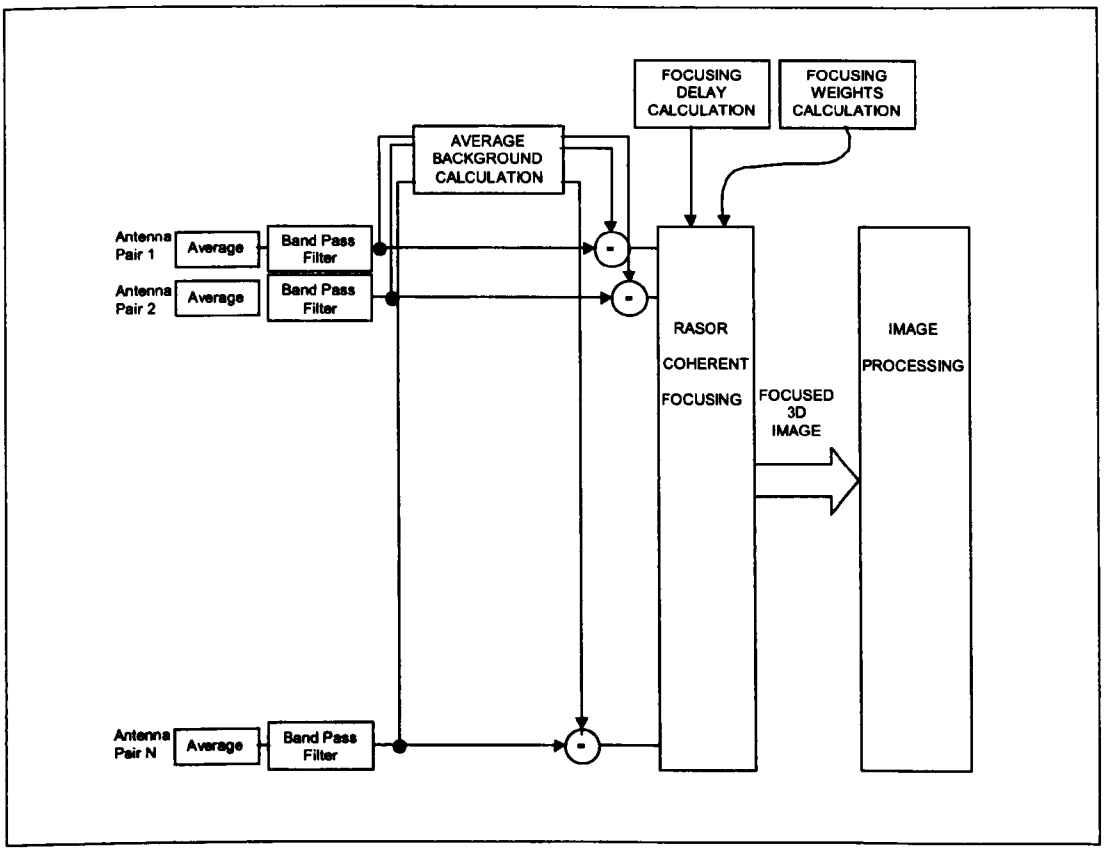

Figure 5-26 Algorithmic Implementation

5.2.1 A-Scan Signal Processing

5.2.1.1 Ensemble average

Taking a series of A scan measurements and averaging improves the SNR of captured signal at the expense of data collection time. The sampling oscilloscope provided the capability to average up to 65356 A-scans and, since for the demonstrator system data throughput rather than data collection was the bottle neck, an average of eight A scans was normally used. Figure 5-27 shows an example A scan and identifies the area of the A scan that is likely to be due to target plus clutter effects.

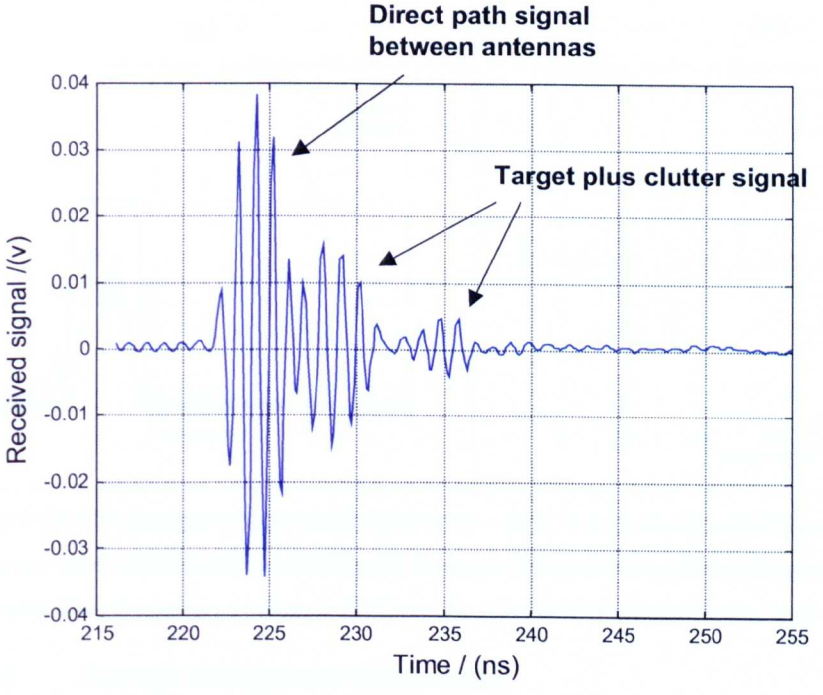

Figure 5-27 Example A scan plot

5.2.1.2 Band-pass filtering

After transfer to the processing core a band pass filter was applied to each A-scan in order to remove interference signals that lie outside the useful bandwidth of the antenna. Any frequency components outside the antenna bandwidth is likely to be due to noise or other unwanted effects. A 200 point windowed-sinc FIR filter with blackman shading was designed for this with a pass-band from 640MHz to 1.36MHz and stop band attenuation <-70dB [23] [24]. Figure 5-28 shows the filter characteristics and example input and output signals.

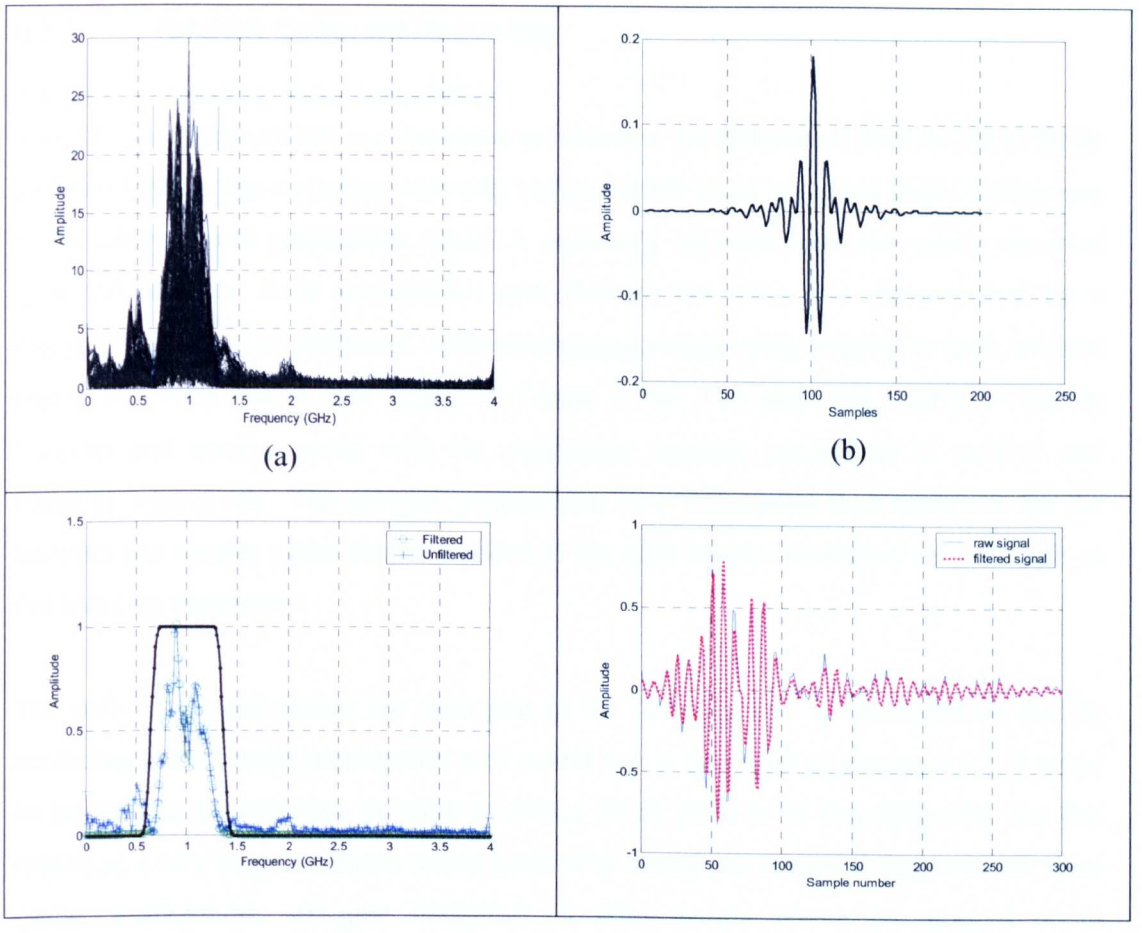

Figure 5-28 FIR bandpass filter (a) Unfiltered averaged A scan signals, (b) Filter kernel - 200 point windowed-sinc with blackman shading, (c) Example filtered and unfiltered signal frequencies along with filter frequency response, (d) Example time domain signal before and after filtering

5.2.1.3 Average Background Calculation

The effects of surface clutter or ground bounce was introduced in Chapter three and described more fully in Chapter four. It is a one of the major problems in GPR and a number of algorithms were considered for its removal, some of which are unique to the RASOR method.

The average background calculation is generated for each of the background averages described in Section 4.4.2.5 and allows any (or none) of them to be applied to the A scan data to allow comparison of their suitability. The results from the comparison of these techniques will be presented in the next chapter.

5.2.2 RASOR Coherent Focusing

5.2.2.1 Focusing delay calculation

The RF switching network was designed to minimise the differential path delays as far as possible through the switching network, but inevitably there remained slight differences in the network path propagation times. A once only calibration process easily removed these differentials. Each propagation path through the array was characterised by a measurement using an additional calibration antenna temporarily coupled to each antenna (using the white velcro tabs visible in Figure 5-10). The path was then exercised in transmit and receive mode with the calibration antenna configured to receive and transmit respectively. The network propagation time differential thus measured for the transmit and receive paths was then added to the path length calculation for each pair in the focusing algorithm.

The path length calculation for each pair to the focusing cell is calculated on the fly according to the simple propagation path model that is described in section 4.3.2. It could be possible to pre-calculate an array of delays for all pairs to all focusing cells, but this results in a very large array that would need to be stored and retrieved from a lower level cache. Furthermore real-time variations in array height above the ground or in permittivity could not be dealt with.

The best real time implementation is for the n+1 focusing point to be calculated and held in a register or level 1 cache in parallel with the focusing of point n. Where there is perhaps scope for further efficiency is in deriving the functions to generate sets of focus delay curves for a range of soil dielectrics, perhaps around 80 functions. The appropriate function can then be loaded for the measured dielectric properties and the path length calculation is, thus, no longer necessary.

5.2.2.2 Focusing Weights Calculation

The focusing window has a width equal to the pulse length. The ability to derive and apply weights to the focused window is one of the key strengths of the RASOR algorithms. The various weighting schemes derived in section 4.4.2 are applied through this mechanism

1. Volume clutter and focal quality weighting
2. Surface racetrack weighting

3. Antenna pattern weighting
4. Spreading loss
5. Path loss
6. Pair exclusion - all zero
7. Adaptive focusing windowing - zero early time

5.2.2.3 Focusing algorithm

The focusing algorithm is shown schematically in Figure 5-29. A running total, held in level 1 cache, is kept for each focus point in the 3-D space. When each A scan becomes available the appropriate portion is selected, weighted and added to focus point running total.

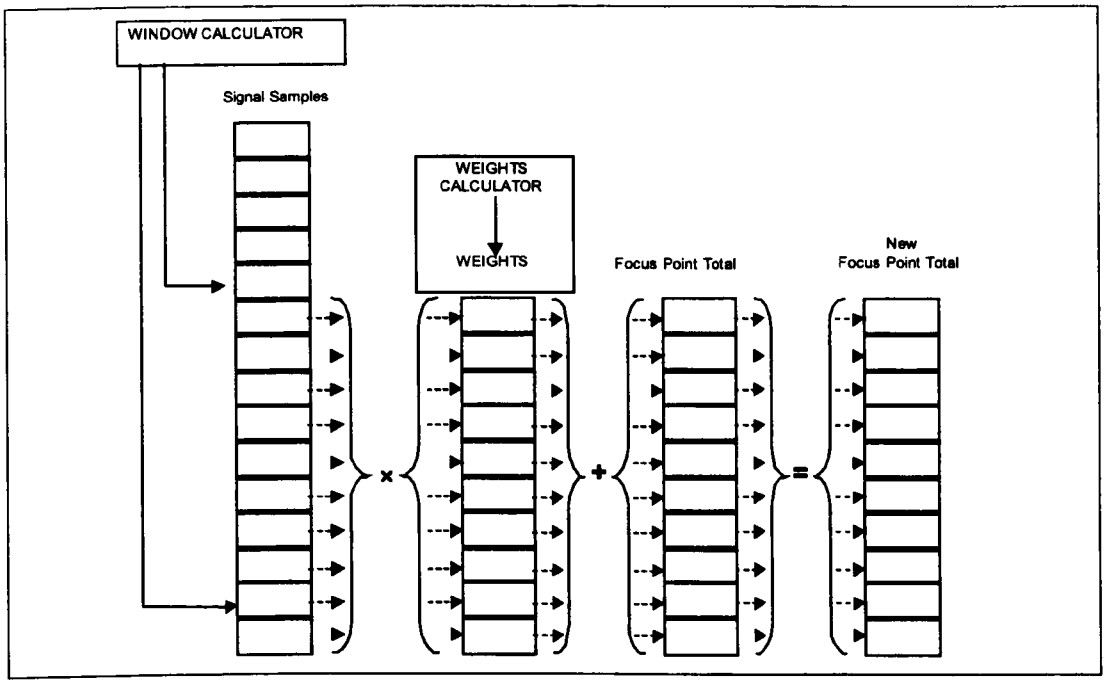

Figure 5-29 Focusing schematic

When all A scans have been processed the focused window is integrated to give the total energy for that resolution cell - in essence the reflectivity of that volume in the ground has been measured.

5.2.2.4 C-scan Processing

The output from the RASOR focusing algorithms is a 3D image that can potentially contain target detections at different depths. When only one data set is captured and analysed off-line it is possible to examine each horizontal (or plan or C-scan) slice or a vertical (or cross-sectional) slice through the data at a depth of interest. This is the approach taken for analysing the early trials data given in Chapter 6.

However, when a large number of data sets have been captured, as the array traverses a trial lane for example, this approach is not efficient. A method is therefore required for stacking up the horizontal slices of data into a 2D dimensional image whilst preserving all the 3D information.

5.3 Real Time RASOR

This section discusses the practical issues of designing a real time RASOR system using the operating parameters identified in the preceeding sections. The array dimensions postulated in Chapter 3 are assumed and a time sampling rate of 8GSa/s.

5.3.1 Data Collection

The data collection and real time processing constraints were introduced in Chapter three (Section 3.3.3.2). A vehicle speed, v, of 5m/s and a 3 scan focusing frame of 30cm, see Figure 5-30, would give a time budget for each data collection frame, t_f, of 60ms. In this time each transmit/receive path must be sequentially exercised, the received data must be digitised and, in real-time operation, the data must be processed and a detection decision produced.

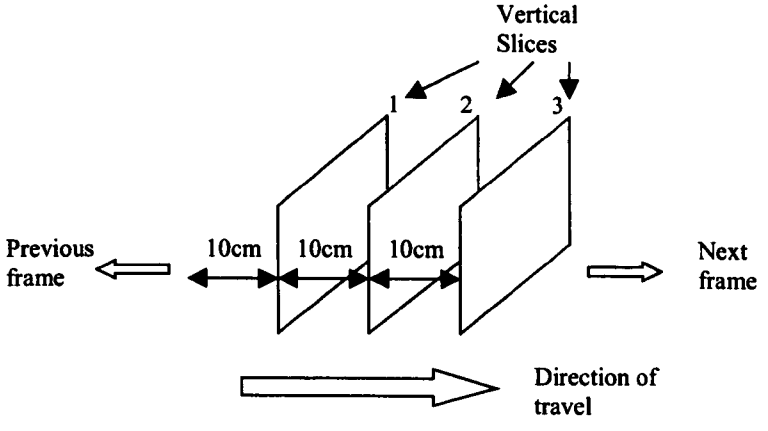

Figure 5-30 Three scan focusing frame

Figure 5-31 shows a timing diagram for all the time budgets that can be allocated within a data collection frame.

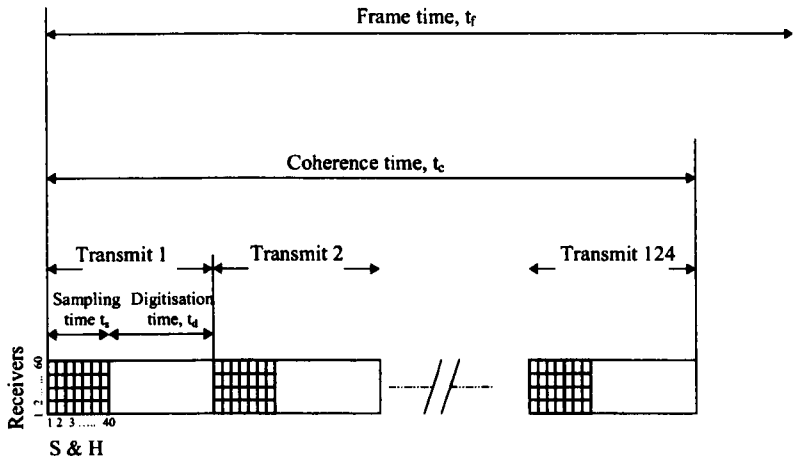

Figure 5-31 Data collection timing diagram

A worst case soil permittivity of ε_r=40 would give a propagation velocity in soil, v_p=47x10^{6}m/s. For a maximum depth of interest of 0.5m a worst case round trip propagation time, t_p, could be assumed to be equivalent to 12λ which, at an operating frequency of 1GHz gives.

$$t_p = \frac{12}{f} = 12\text{ns} \qquad \textbf{(5-2)}$$

Choosing a sampling frequency of 3.3GHz, in order to respect the Nyquist sampling criteria across the 05.GHz to 1.5GHz bandwidth, then each receiving antenna would need to collect around 40 samples for each transmission.

Based on the ray-tracing analysis described in Chapter 4 it is postulated that the effect of the vehicle motion on the focusing coherence can be discounted provided the vehicle does not move more than approximately 0.1λ during array collection period. This gives a coherence time budget, t_c, considering the upper operating frequency of 1.5GHz, of

$$t_c = \frac{0.1\lambda}{v} = 4ms \qquad \textbf{(5-3)}$$

For the postulated array there would be 124 transmit events in each coherence time window. For each transmit event a set of parallel sample and hold circuits capture the received signals giving a sample and hold period, t_p and a time period for digitasation and analgoue switching, t_d, given by

$$t_d = \frac{t_c}{124} - t_p = 31.988\mu s \quad (5\text{-}4)$$

For each transmission around 60 receiving antennas would share a resolution cells field of view. In Figure 5-31, it is assumed that these 60 antennas receive concurrently and that a bank of parallel sample and hold devices act concurrently on each receive path. This scheme is the most efficient in terms of rf power transmitted and offers the maximum time for digitiation and analogue switching. The digitisation period for any one receiver antenna can in fact be almost doubled by implementing the alternative switching scheme described in Section 5.1.4, which ensures that no receiving antenna is used on consectutive sweeps.

Alternatvely, the time budget for each transmit period, $t_c/124$, is large enough to allow sequential transmit and receive from each antenna pair. A single bank of sample and holds and digitiser can then be used to capture each of the 60 received signals and is therefore a much cheaper solution. This is the method chosen for the (non-real time) demonstrator system design decribed in Section 5.1.6. The drawback with this approach is the potential for bottlenecks arising at the output of the digitiser and also the analogue switching time becomes much more critical.

A further alternative would be to use an equivalent time sampling method where one sample and hold device is used on each of the 60 receive paths. The transmission is repeated 40 times with a small delay added to the sample and hold trigger each time. This method uses transmitted power inefficiently and would be more prone to sampling jitter.

5.4 Conclusions

The RASOR system design and design trade-offs have been described including a description of the antenna and antenna array design, the RF switching network, pulse generator and sampling scheme. The algorithmic implementation has also been described. Design considerations for real time RASOR have been described showing that with sufficient resources real time operation can be achieved.

References

[1] T.P.Montaya, et al., 'Land Mine detection using GPR based on resistively loaded V dipoles', IEEE AP47, pp1795-1806

[2] D.J.Daniels, 'Surface Penetrating Radar', , IEE London 1996, Chapter 4

[3] C.Balanis, 'Antenna theory analysis and design', John Wiley, New York, 1982

[4] T.P.Montoya, G.S.Smith, 'Land mine detection using a ground-penetrating radar based on resistively loaded Vee dipoles', IEEE Trans.Ant. & Prop., Vol.47 No.12, Dec 1999, pp1795-1806

[5] D.J.Caniels, D.J.Gunton, H.F.Scott, 'Introduction to subsurface Radar', Proc IEE Pt H, Vol.128 No.5, 1988, pp278-302

[6] T.E.Morgan, 'Spiral antennas for ESM', Proc IEE, Pt F, Vol.132 No.4, 1985, pp245-251

[7] J.D.Kraus, 'Antennas', McGraw-Hill, London, 1950

[8] G.H.Brown, O.M.Woodward, 'Experimentally determined radiation characteristics of conical and triangular antennas', RCA Review, Vol.13, 1952, pp425-452

[9] R.Nilavalan, G.Hilton, R.Benjamin, 'Wideband printed bowtie antenna element development for post reception synthetic focusing surface penetrating radar', Electronics Letters, Vol.35, No.20,pp1771-2, IEE, UK, 1999

[10] R.Nilavalan, G.S.Hilton, R.Benjamin, 'A FDTD model for the post-reception synthetic focusing surface penetrating radar with mine detecting applications', Proc. IEE Conf. on Ant. & Prop., York, UK, 1999, pp69-72

[11] RT/duroid 5880, Rogers Corporation Microwave Materials Division, www.rogers-corp.com

[12] B.Edwards,D.Rees, 'A Broadband Printed Dipole with Integrated Balun', Microwave Journal, May 1987, pp 339-344,

[13] R.Nilavalan, 'FDTD modelling, measurements and analyses of Post Reception Synthetic Focusing Techniques in Ground Penetrating Radar', University of Bristol PhD Thesis, 2000

[14] SW-110 GaAs SPDT Reflective SwitchDC-3GHz with TTL/CMOS Control Input, M/A-COM Inc,

[15] SW-243 Matched GaAs SP4T Switch DC-4GHz, M/A-COM Inc

[16] SW-314 GaAs SPST Absorptive Switch DC-3GHz, M/A-COM Inc

[17] RT/duroid 6010, Rogers Corporation Microwave Materials Division, www.rogers-corp.com

[18] XC9572-10-PC84 In-System Programmable CPLD, Data Sheet, 4th Dec 1998, Xilinx Corp.

[19] SWD-119, Quad drivers for GaAs FET Switches and Attenuators, M/A-COM Inc,

[20] 'Using ABEL with Xilinx CPLDs', Application Note XAPP075 January 1997 (Version 1.0), Jan 1997

[21] 'Xilinx Programmer Qualification Specification XC9500 Family', Application Note, Rev. 3.1, March 1999

[22] 'Agilent Model 54835A/45A/46A Oscilloscopes Service Guide', Publication Number 54845-97008, February 2001

[23] S.W.Smith, 'The Scientist and Engineers Guide to Digital Signal Processing', 2nd Edition, California Technical Publishing, San Diego, 1999

[24] F.J.Harris, 'On the use of windows for harmonic analysis with the discrete Fourier transform', Proc. IEEE, Vol. 66, No. 1, pp51-83, Jan 1978

6 Experimental Results

This chapter describes results obtained from the RASOR system in indoor and outdoor experiments. The system was developed incrementally and the series of results presented in this chapter reflects the gradual increase in complexity of the design and challenge of the environment. Initially data was gathered in a sandbox by manually moving a pair of antennas to synthesise an array. Later results obtained at various test sites were obtained with the automatic RASOR demonstrator utilising a 2D planar array and switching network.

After each design increment some of the previous experiments were repeated, at the same test site where practical, in order to revalidate the new equipment and characterise/compare its behaviour. The ambition of the experiments progressed from design proving of the detection process in various conditions to more advanced statistical analysis of RASOR performance in terms of False Alarm Rate (FAR) and Probability of Detection (Pd) from data gathered in specially constructed trial sites.

6.1 Summary of Test Sites

Experiments were conducted using the following test sites (arranged chronologically):

1. University of Bristol Laboratory
2. Quarry Site, Wells, Somerset
3. Long Ashton, South Bristol, Somerset
4. DERA Chertsey, Chertsey, Hampshire
5. ERA, Leatherhead, Surrey

The University of Bristol, Quarry and Long Ashton trial sites were specifically constructed for the RASOR project. The DERA Chertsey site was built to support their land-mine detector sensor programs [1] and consists of four plots containing different soil types.

The site at ERA was specially built to allow ERA to demonstrate their GPR technology for a potential government contract and the RASOR demonstrator was also invited to take part on this trial in a 'blind' trial. It consisted of six plots of different soil types each

containing a range of targets, but with the exact positions of the targets only known to ERA.

In the following sections more specific details on the test sites are given along with the measurement results that were obtained at each one.

6.2 Summary of Test Targets

The test targets that were used in these experiments 1) to 4) above are shown in Figure 6-1. Details of the TM-57, TMA-4, VS-50, BLU-61/A/B and PMA-3 have been given in Chapter 2 although obviously items have been modified to be safe. To give an idea of the scale of Figure 6-1 TM-57 diameter is 300mm and the VS-50 diameter is 90mm. The APM replica is entirely plastic with a small air gap below the central 'detonator' button. The APM CK replica is a mine surrogate supplied by Colin King Associates [2] and designed to replicate the signature of a PMN mine.

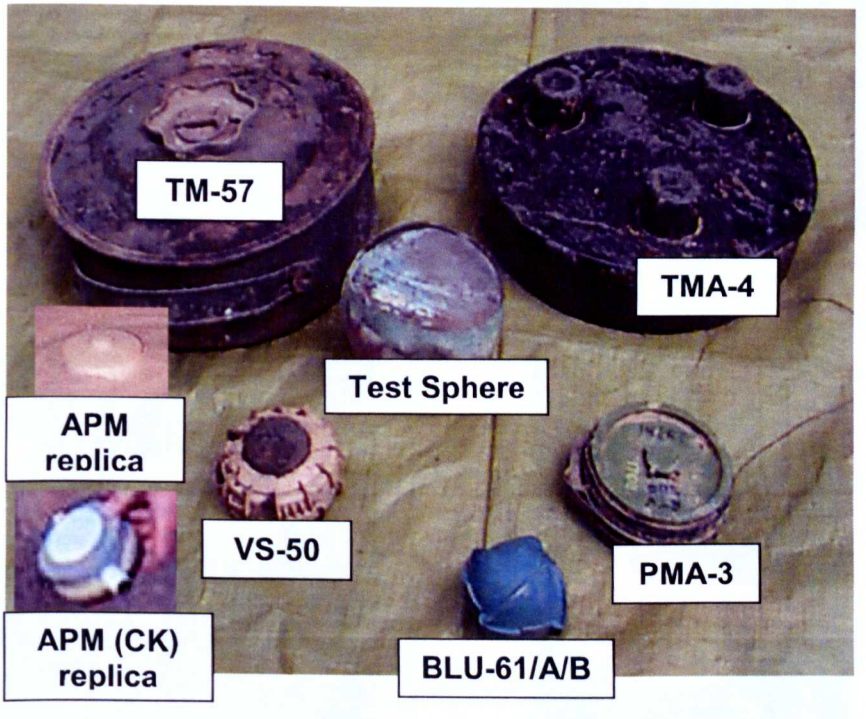

Figure 6-1 Targets used in experiments

The specific targets deployed at the ERA test site are generally unknown, other than that both APM and ATM were present along with clutter objects.

6.3 Indoor Sandbox Experiments

6.3.1 Experimental Facility

A measurement facility, including an indoor sandbox, was constructed to enable early testing of the system's viability and validation of theoretical modelling. The main advantages of using a sandbox for these early system measurements is that the climate is fixed, unlike outdoor field measurements where the measuring workspace is subject to the prevailing weather conditions. This means that important factors, such as humidity, temperature, ground moisture content and permittivity, can be tightly controlled making results repeatable.

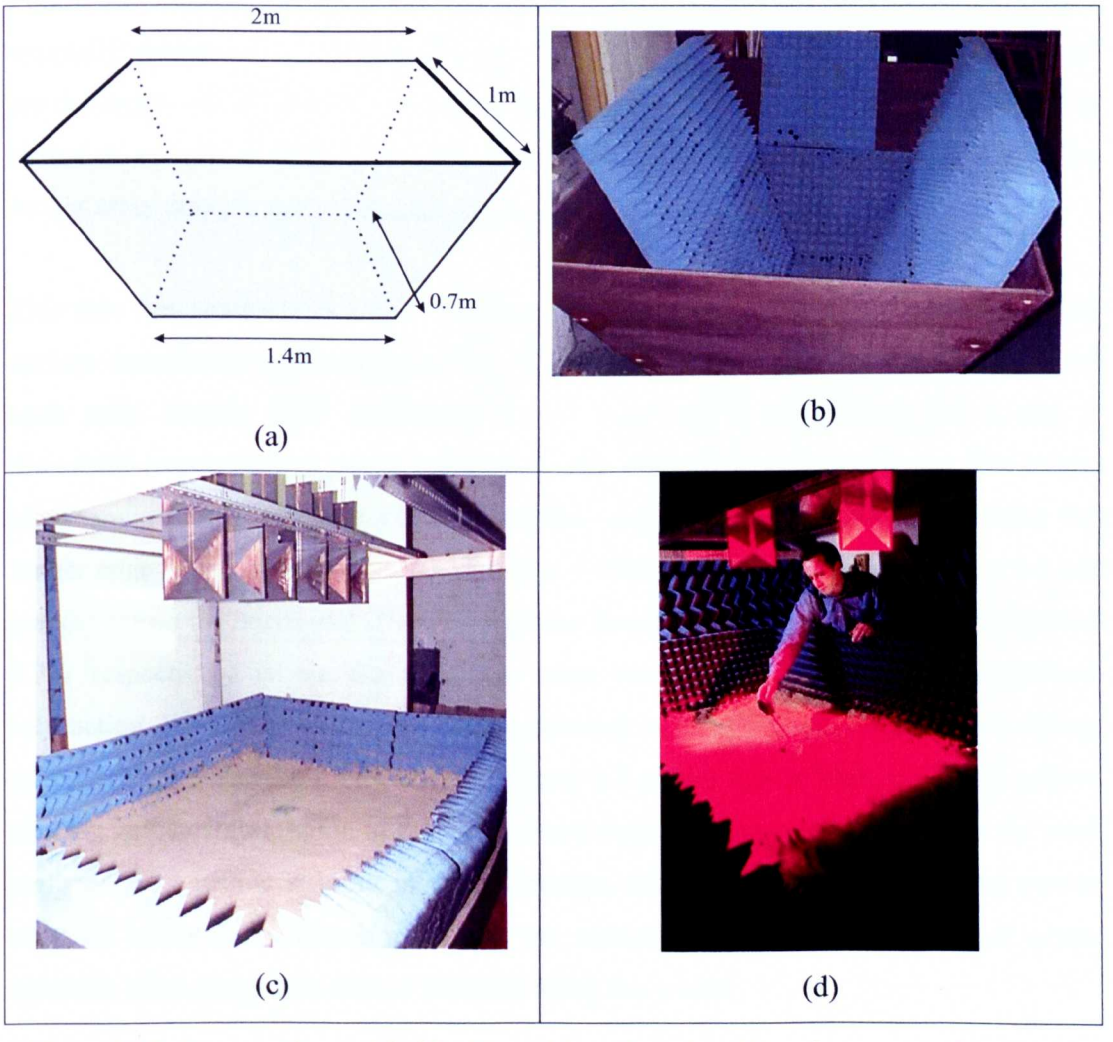

Figure 6-2 Indoor experimental facility (a) sand-box dimensions (b) under construction, (c) early antenna array (d) data collection

The sandbox dimensions were specified as 2 metres x 1.4 metres x 1 metre deep following analysis of the system noise limits and filled with around 1 ton of builders sand. Figure 6-2 shows the dimensions and pictures of the sandbox construction. The box sides were made from plywood and were held together using doweling and glue to avoid introducing backscatter from metal screws or nails. Radar absorbent material (RAM) was used to line the sides and base so that reflections from the boundary of the workspace were reduced. The sides were sloped so that the residual reflections from the RAM are directed away from the relevant antenna element.

6.3.2 Test Results

6.3.2.1 Metal Plates

Figure 6-3 shows one of the first practical experiments conducted in the sand-box using a manually synthesised 7 x 4 element array. Two square metal plates of dimension $10cm^2$ are deployed; one is located on the sand surface at x=0.3m and y=0.3m and the second is buried at a depth of 0.3m and below the centre of the array at x=0.8m, y=0.5m. The longer array dimension is along the x axis.

This data was processed in several different ways to analyse the different weighting and surface cancellation methodologies. The plots at the bottom and on the left-hand side of each main display show normalised signal amplitude profiles along the x and y dimension respectively at points indicated by the cross hairs on the main plot. The origin of the main plot is by convention the sandbox corner[1] with the x dimension being the longer edge of the 2d array, i.e. the one with 7 elements. dimensions are Figure 6-3 (a) and (b) shows the horizontal slices through the focused data at the surface and a depth of 0.3m respectively where the data has been focused without average background subtraction. Both metal plates are clearly detected as would be expected for two strong reflectors. On the surface plot shown (Figure 6-3 a) the lighter blue, cyan and yellow shading in the central region of the plot indicate strong specular reflections from the sand surface. The yellow striping in the y-direction indicates the greater resolving power obtained along the x direction due to the rectangular array configuration of seven antennas wide along the x-axis, 4 antennas along the y-axis.

[1] In later field experiments the origin is moved to either be at centre of the 2D array or at the corner of the test plot that is being searched depending on the size of the data set being displayed.

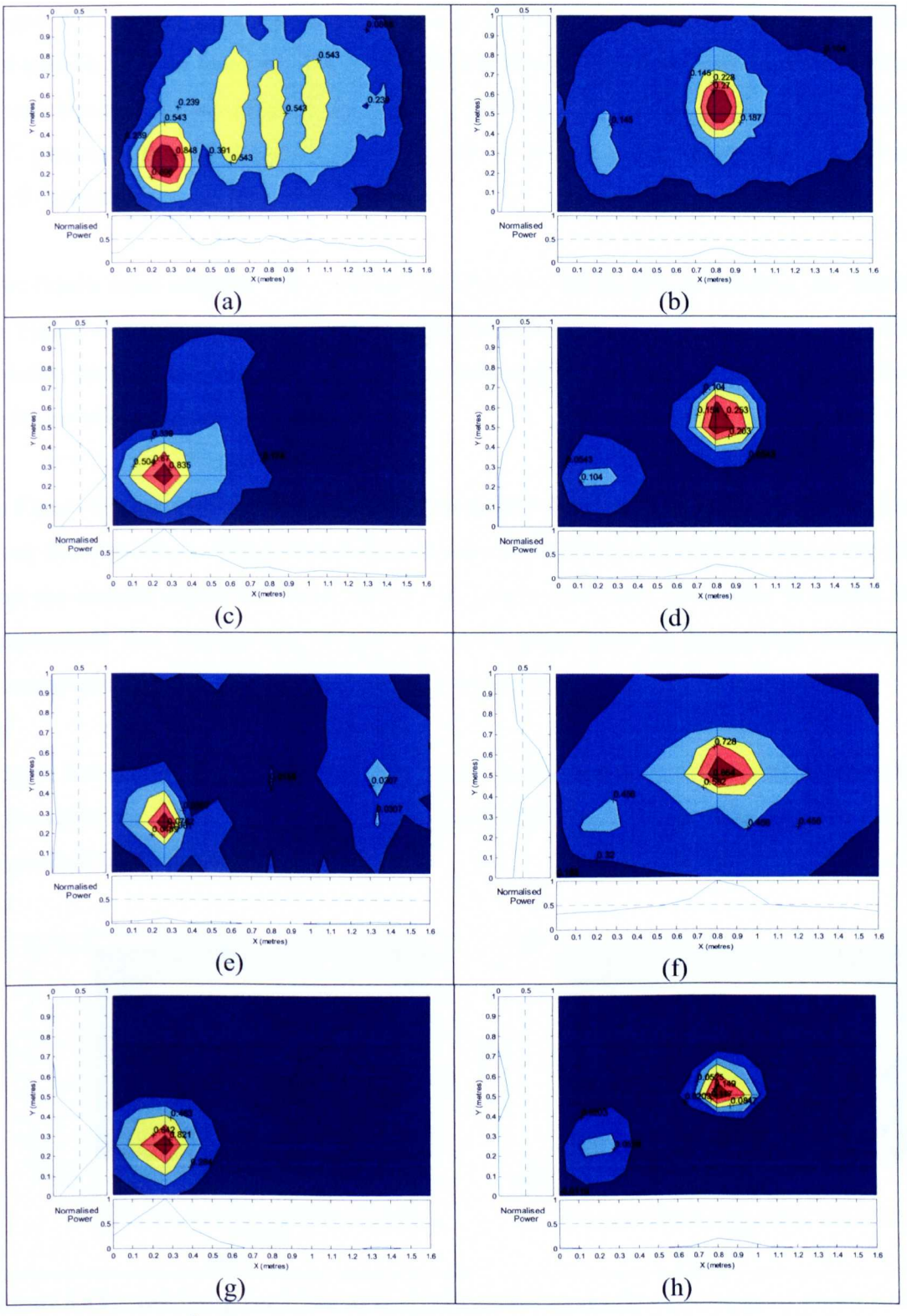

Figure 6-3 Two 10cm^2 metal plates positioned on surface at x=0.3m, y=0.3m and at depth of 0.3m at x=0.8m,y=0.5m with different surface cancellation methods, (a), (c), (e), (g) are horizontal slices at the surface, (b), (d), (f), (g) are horizontal slices at 0.3m depth, (a) and (b) with no average background subtraction, (c) and (d) with median average background subtraction, (e) and (f) with adaptive windowing, (g) and (h) with post processed background subtraction

Figure 6-3 (c) and (d) shows the horizontal slices with a median average background subtraction prior to focusing. The PSLR and ISLR have been improved and the surface clutter has been greatly reduced. In Figure 6-3 (d) some residual from the surface plate is still present at this depth (this is noticeable also on Figure 6-3 b, but the shape is not as well defined).

The results from adaptive focus windowing, with no background subtraction, are shown in Figure 6-3 (e) and (f). The surface reflections have been removed, but so has the relative strength of the surface plate. The buried plate now appears as the dominant reflector in the data set.

In Figure 6-3 (g) and (h) a post processing background subtraction has been applied. The Peak Side-lobe Ratio (PSLR) has been markedly improved over that in (a), (b),(c) and (d) and the surface clutter has been almost completely removed. However, it should be emphasised that this method is unlikely to be practicable in operational situations because of difficulty of obtaining a good background set.

Figure 6-4 shows the background focused data set or ground truth that was used in the subtraction for Figure 6-3 (g) and (h). This was taken over the sandbox after the metal plates had been removed.

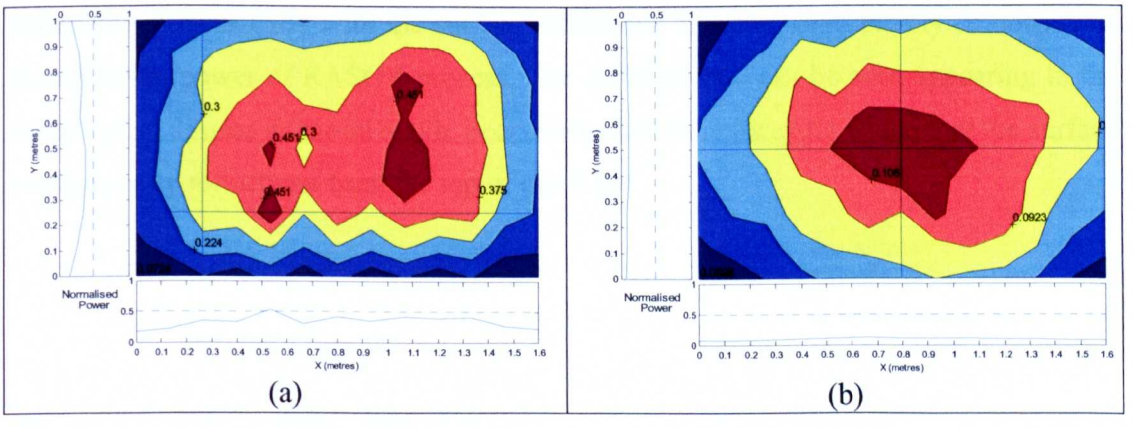

Figure 6-4 Focused background data set used in Figure 6-3 (g) and (h) where (a) shows a horizontal scan at the surface and (b) shows a scan at a depth of 0.3m

Clearly the surface reflection dominates in this data set. Whenever practicable the background data set was always captured along with or before the measurement data set to aid algorithm comparison and analysis.

6.3.2.2 Land mines

Figure 6-5 shows the plots from an experiment containing three targets:

- An APM simulant located below the centre of the array x=0.8m, y=0.5m and buried such that its top is flush with the sand surface.
- A calibration sphere located at x=0.2m, y=0.2m buried just below the surface.
- An TM-57 ATM with centre located at x=1.4m, y=0.8m buried with its top 0.15m below the surface.

A median background subtraction has been applied. All three figures show the same horizontal plot at the surface, but with different 1D profiles displayed on the left and bottom sides of the plot. The data selection for the 1D profiles are indicated by the blue cross hairs drawn over the 2D plot. Figure 6-5 (a) shows the 1D profile through the metal sphere, Figure 6-5 (b) is through the APM and Figure 6-5 (c) is through the ATM.

As would be expected the metal sphere dominates return, but the APM is also clearly visible at the centre of the plot. This APM position is considered to be the most challenging of all because the reflections from the top of the mine are received completely concurrently with the surface reflections and this result clearly demonstrates the resolving power of RASOR process. The ATM outline can be seen appearing in the surface plot, despite its burial depth, because the late time focusing window at the surface contains early reflections from the top of the ATM .

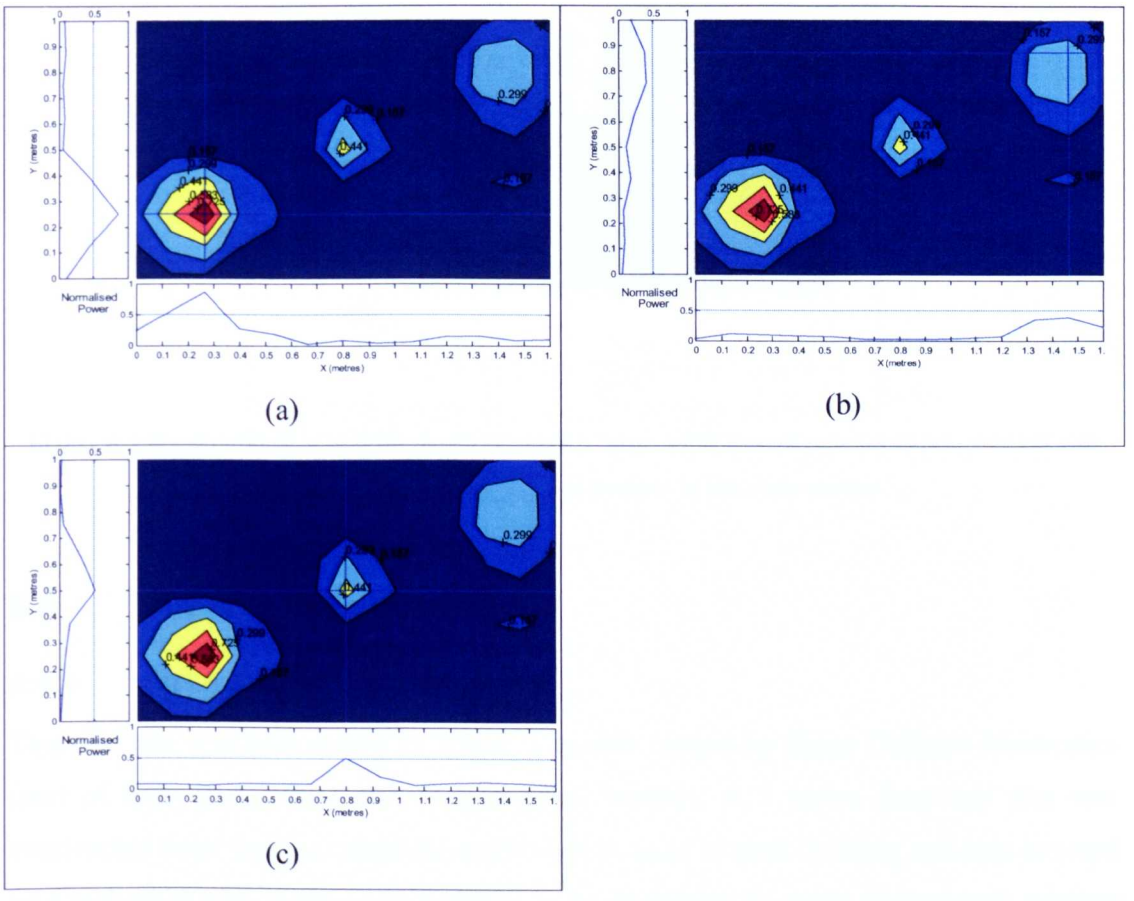

Figure 6-5 Horizontal plot at surface with median background subtraction showing APM and metal sphere flush buried at x=0.8m, y=0.5m and x=0.2m, y=0.2m respectively and metal sphere buried at x=1.4m, y=0.8m (a) amplitude profile through metal sphere, (b) amplitude profile through APM, (c) amplitude profile through ATM

6.3.2.3 Clutter

The plot shown in Figure 6-6 shows an APM detected in a cluttered environment. The plot is a horizontal slice at a depth of 100mm through a Large APM simulant positioned at x=1.1m, y=0.6m and buried such that its top is at 100mm. The clutter consists of 128 small pebbles scattered randomly throughout the volume at a density of 520 per m^3.

It can be seen that the mine is detected, but with an increase in strong spurious signals such as at x=0.7m,y=0.7m. The clutter returns could be removed by a basic threshold detector if and only if they remain lower than the mine target, but this is by no means guaranteed. Additional image processing techniques would be required to distinguish mine like shapes.

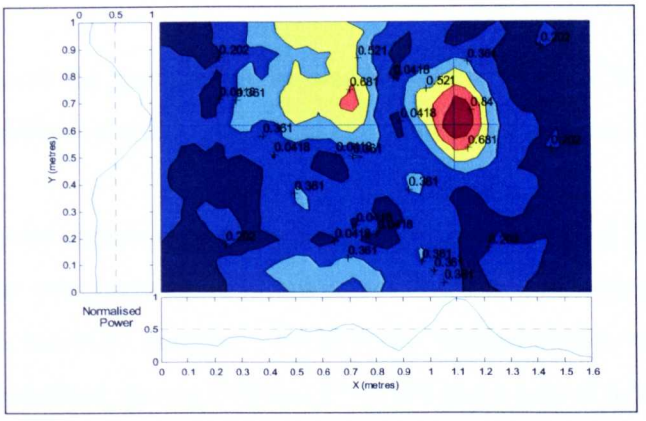

Figure 6-6 Horizontal slice at 0.3m depth through a large APM buried at 0.3m depth, x=1.1m and y=0.6m. 128 pebble objects are present to simulate clutter

6.4 Quarry experiments

6.4.1 Trial Site

This trial site was in a quarry in Wells, Somerset owned by Racal Defence Electronics (part of their Radar Signature Measurement facility). A 1 metre deep test plot was constructed from finely crushed dolomite rock as used in road building and was covered by a makeshift tent, as shown in Figure 6-7, for protection from the (inclement!) weather to try to control the ground conditions, but also to protect the experimental equipment.

Two experimental campaigns were carried out at this site. The first utilised a manual scanning system where two antennas were moved to each position to synthesise a fully populated 28-element array as shown in Figure 6-8 and Figure 6-9. The first trial represented a significant step, as all previous measurements had been taken indoors in dry sand. The transfer to a more representative outdoor environment with a significant change in attenuation, dielectric constant, surface roughness and ground inhomogenity all constituted a considerable challenge.

The second campaign was carried out with a fully populated twenty-eight antenna array with automatic switching. The main aim of the second campaign was to revalidate RASOR detection performance in this environment before moving on to more diverse experimental sites. Of course on the second campaign the experiment run times were much reduced improving from 30 minutes to approximately 30 seconds (although nonetheless this was still some way from the postulated real-time speed).

The targets used were the predominately plastic "Colin King" (CK) APM simulant, a TMA-4 ATM, a calibration metal sphere and calibration metal plates.

The test area measured approximately 4m x 4m x 3m and contained 20 tons of limestone rock. The limestone was made up of 40mm stones down to dust with a 30% dust content and relatively low moisture content. Permittivity measurements were made on-site, using a probe array method, giving $\varepsilon'=9$ and $\varepsilon''=0.189$ and a loss of 6.5dB/m.

Figure 6-7 Protective awning showing raised area of crushed rock

Figure 6-8 Inside awning, showing the array backplane, supports, processing/control PC and Infinium sampling oscilloscope

Figure 6-9 Close-up of PC showing current set of processed data.

6.4.2 Quarry Trial Results (1st Campaign)

For the first experimental campaign a simple background subtraction method was used to remove surface reflections. A data set was gathered with no targets present and this was used as the ground truth.

Figure 6-10 shows a vertical scan under the centre of the array with a metal plate buried at a depth of 0.2m and a second plate lying on the surface at a lateral displacement of 0.4m from the array centre. This shows that the background subtraction method can clearly eliminate the surface reflection in other environments than dry sand. Note the slightly higher signal levels denoted by the light blue and green in the plot. This area was disturbed during the burial of the plate and consequently has a slightly different dielectric contrast to the undisturbed rock.

The region of maximum processing gain is below the centre of the array where the maximum number of elements have the focusing cell within their field of view. Scattering from the metal plate positioned on the surface, but located to the right of the array aperture, has a lower focused strength than the buried metal plate at the centre even

though the scattering from the latter will have undergone attenuation in the ground at the air-surface interface.

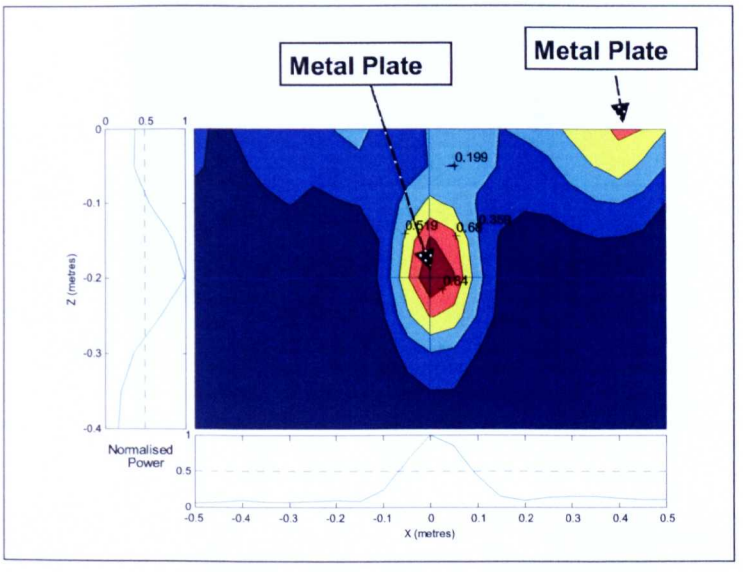

Figure 6-10 Vertical scan through a 100mm^2 metal plate buried below the centre of the array at a depth of 0.2m and another 100mm^2 metal plate located on the surface.

Figure 6-11 (a) and (b) shows another experiment that contains a metal sphere offset 0.4m from the array centre and an APM below the centre of the array both buried at a depth of 0.1m. The metal sphere is clearly visible, however, the APM is less distinct and the reflections due to the ground disturbance during burial tend to mask the APM returns.

The ground disturbance effect was examined further by leaving this experimental set-up to settle for a period of thirteen days. The data shown in Figure 6-12 is exactly the same vertical scan as that shown in Figure 6-11 (b) captured after the period has elapsed. The dielectric discontinuity due to the ground disturbance has clearly decreased leaving only the dielectric contrast from the mine and sphere. As would be expected the increased processing gain at the centre of the array means that the mine has greater strength than the sphere. The slight difference in target location between Figure 6-11 and Figure 6-12 is due to small equipment positional differences between experiments.

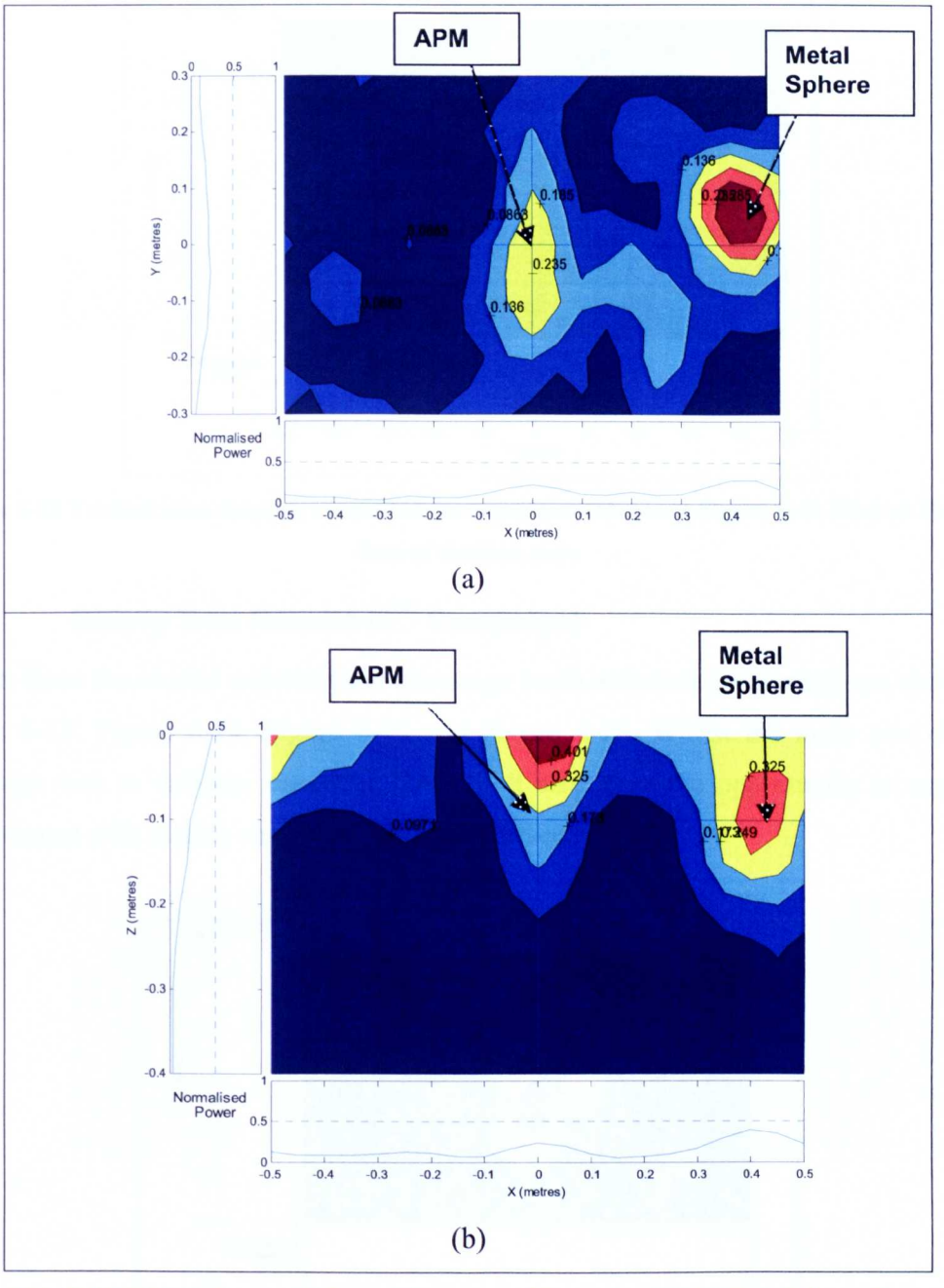

Figure 6-11 CK APM simulant buried near the centre of the array at a depth of 0.1m and a metal sphere buried at a depth of 0.1m towards the edge of the array (a) horizontal scan at 0.1m (b) vertical scan under the centre of array.

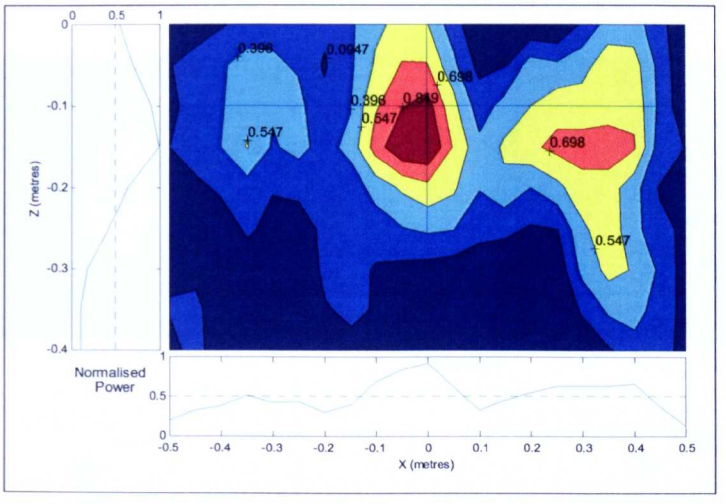

Figure 6-12 Vertical scan showing a repeat of the experiment shown in Figure 6-11 after an elapsed time of thirteen days

6.4.3 Quarry Trial Results (2nd Campaign)

Results from the second experimental campaign (with automated scanning) are shown in Figure 6-13, Figure 6-14, Figure 6-15 and Figure 6-16. Whilst the main aim of this campaign was to validate automatic RASOR it also gave the opportunity to examine performance with targets on or flush with the surface.

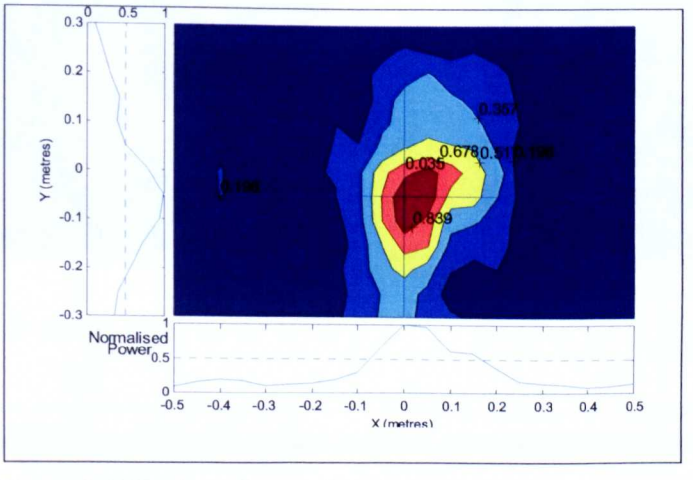

Figure 6-13 Horizontal scan: Metal sphere on surface at centre

Figure 6-13 and Figure 6-14 give the results from the first design proving scans with the automatically scanned demonstrator system. Figure 6-13 shows a calibration metal sphere lying on the surface of the ground below the centre of the array. Figure 6-14 is a similar experiment, but this time with the CK APM simulant.

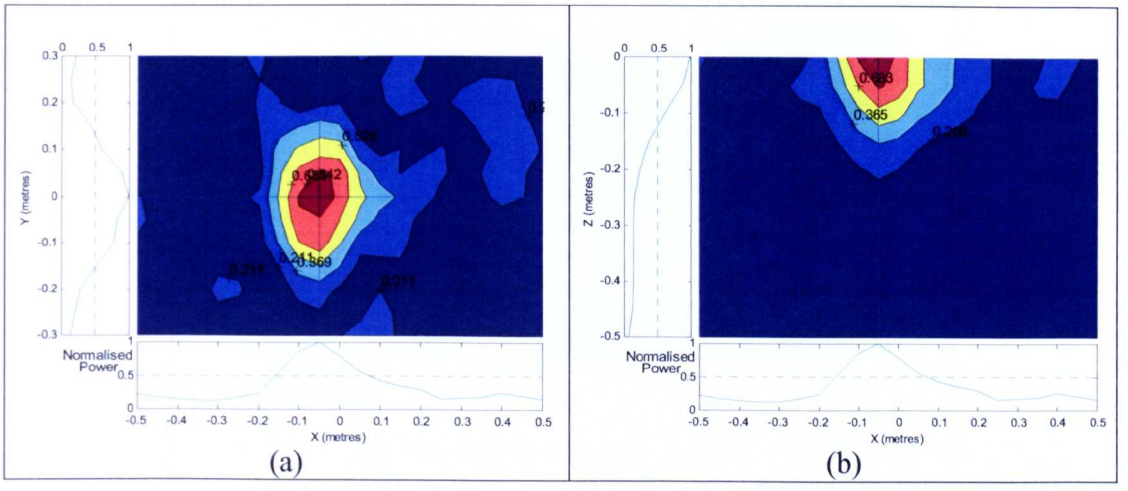

Figure 6-14 Large Colin King APM simulant on surface below centre of array (a) horizontal scan (b) vertical scan

Figure 6-15 is subtly different and considerably more challenging than the earlier two. Here the CK APM is buried with the top of the mine flush with the surface. Reflections from the ground and APM top are difficult to discriminate nonetheless the target is clearly detected.

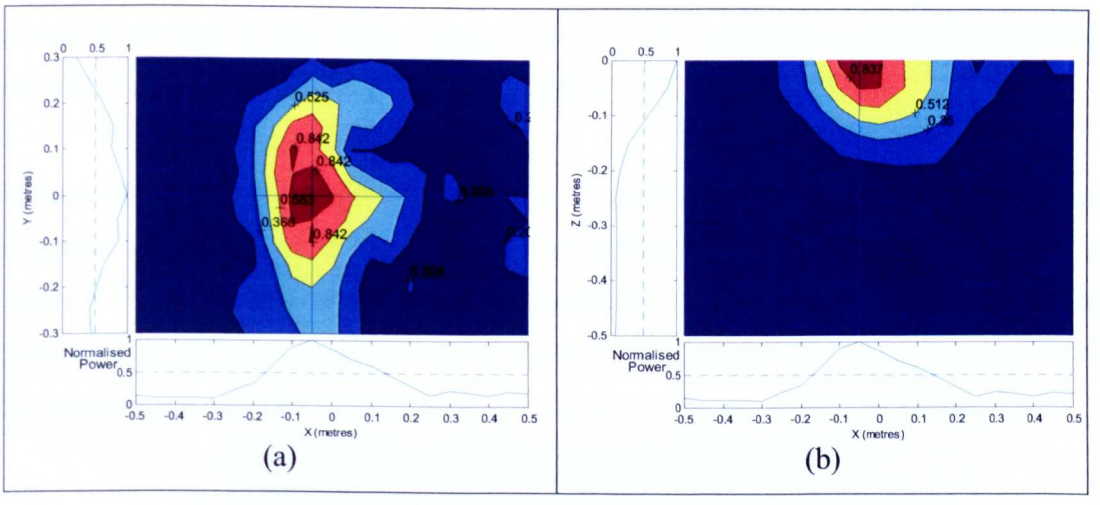

Figure 6-15 Large Colin King flush with surface at centre array (a) horizontal scan (b) vertical scan

Figure 6-16 shows the predominately plastic TMA-4 ATM clearly detected at a depth of 0.5m. This is probably around the maximum depth that an ATM would be buried operationally. The signal attenuation at this depth of burial is such that the strength of the target return relative to the surface reflection is lowered. This is the reason why the surface reflection, due to the disturbance of the material during burial, is clearly distinguishable on this plot down to a depth of around 0.1m.

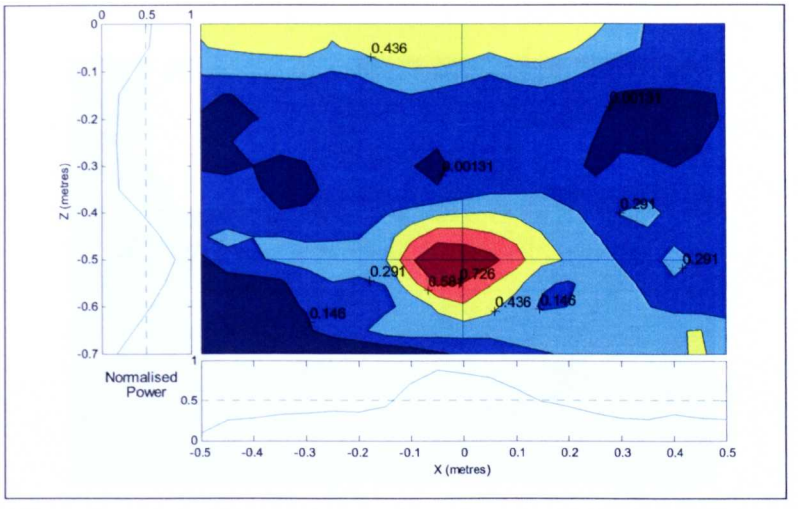

Figure 6-16 Vertical slice through a TMA-4 buried at a depth of 0.5m.

6.5 Long Ashton

6.5.1 Trial Site

This trial site was a section of loamy soil covered with turf on the land of the University of Bristol Agricultural Research Department. The aim of the trial was to test RASOR in realistic 'off-road' conditions and in particular to measure the performance when the ground is covered in vegetation. This scenario is very common in practical de-mining activities because mined land has often lain fallow for months and years.

Pictures of the test site are shown in Figure 6-17 and Figure 6-18. The tent was provided to protect the equipment in wet weather, but in fact the weather was very hot and, as Figure 6-18 shows, fans were required to reduce the risk of the equipment overheating. Between this trial and the earlier ones at Racal improvements were made the stability of the transmission pulse by increasing the regulation of the transmitter power supplies.

Figure 6-17 Long Ashton experimental set-up

Figure 6-18 Inside the tent at Long Ashton

6.5.2 Trial Results

The experiments conducted at this site concentrated upon targets buried just below the interfering turf using the fully automated system. A calibration measurement is shown in Figure 6-19 with the metal sphere buried just below the surface. The 3dB lateral and vertical resolution can be seen to be in good correspondence with theoretical modelling (as discussed in sections 4.3.3 and 4.3.4) and the effect of the turf has had negligible defocusing effect.

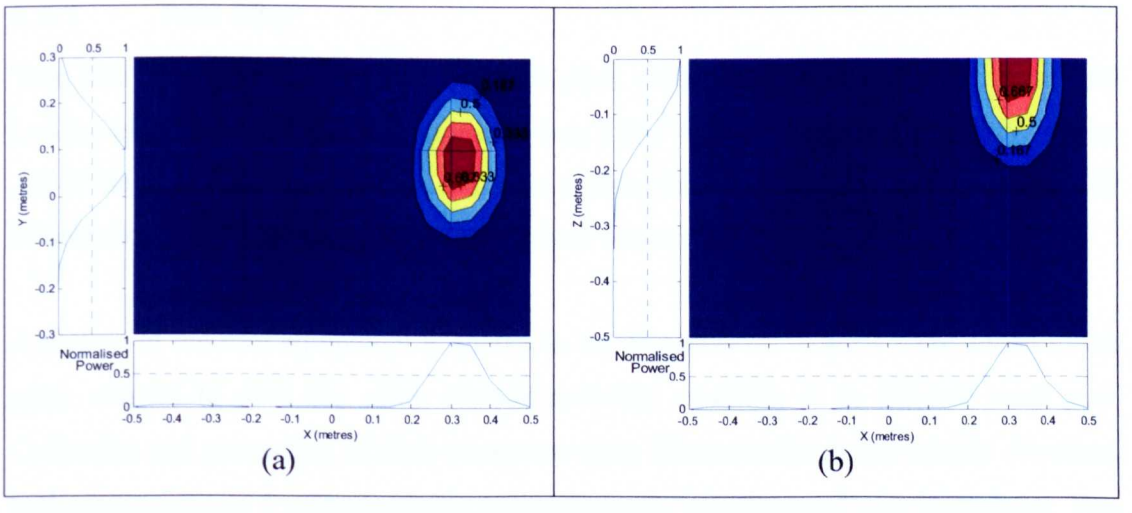

Figure 6-19 Metal sphere buried close to the surface at x=0.3 y=0.1 (a) horizontal scan at surface (b) vertical scan through 0.1m

Figure 6-20 shows the results with the Large CK buried about 1cm below the surface of the soil. An additional layer of vegetation around 3 to 4 cm thick lies on top of this. On the experiment shown the target is offset from the centre of the array in the y dimension to test performance away from the centre line. The target is strongly detected and the surface clutter has been well cancelled.

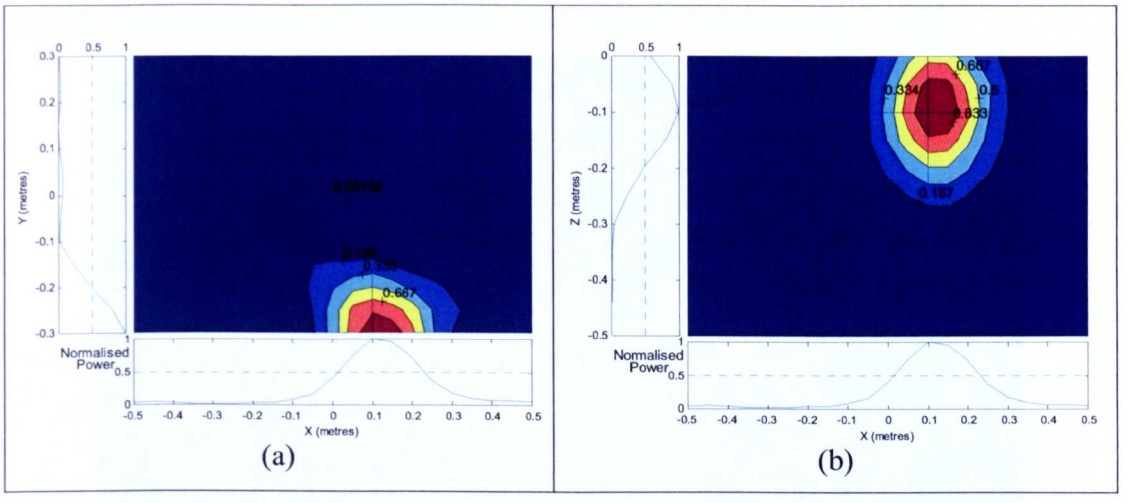

Figure 6-20 Large Colin King APM at depth of 0.1mm x=0.1 y=-0.3 (a) horizontal scan at depth of 0.1m (b) vertical scan at y=-0.3

6.6 DERA Chertsey

6.6.1 Trial Site

This trial site consisted of four separate plots containing loam, dolomite, sand and London clay. Each plot covered approximately a $6m^2$ and had built up a vegetative cover. All of the targets shown in Figure 6-1 were utilised in order to gather data on probability of detection and False Alarm Rate for different targets.

A picture of the trial equipment is shown in the Figure 6-21. Wheels were added to the array corners to give the array limited mobility, enabling it to traverse each plot. Collection and processing of each sweep covering 30cm swathe in the vehicle direction, took approximately 3 seconds giving an approximate vehicle speed of 0.36km/hour. This is still far below the postulated vehicle speed, but quite encouraging considering the majority of processing at this time was done on a standard PC.

Sand, dolomite and loam had already been encountered at the trials sites in the research lab, quarry site and Long Ashton site. However, clay represented a new challenge and is an extremely challenging soil type for any electromagnetic sensor. The clay particle structure means that it is able to hold a large amount of bound water (see section 4.1.3), thus its loss tangent is very high and signal attenuation and refraction is severe. The permittivity was measured using the probing method described in 4.1.4 giving a real permittivity measurement of 30-35 and a loss estimate of 50-60dB per metre.

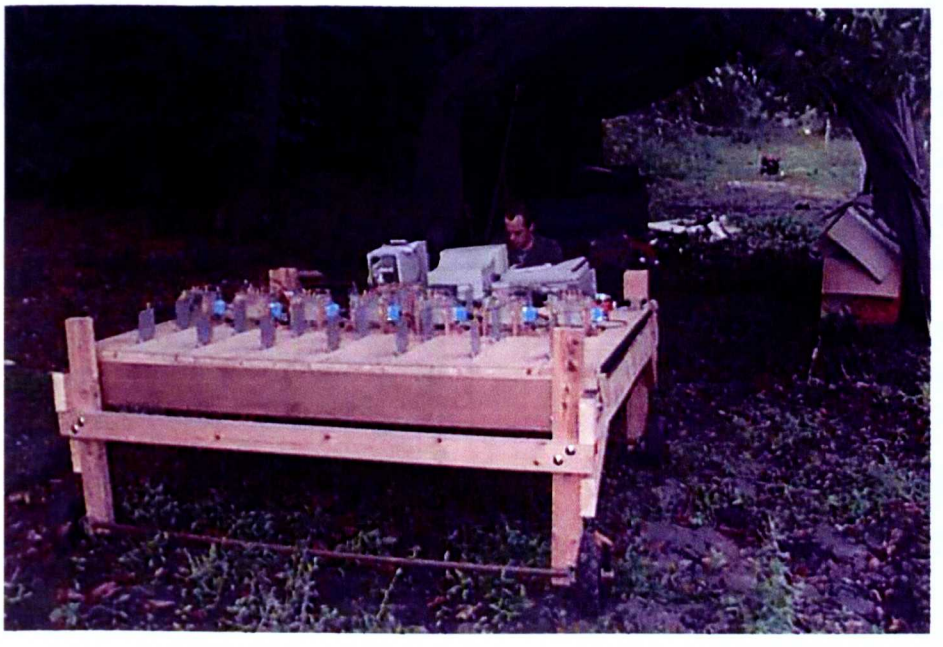

Figure 6-21 Experimental set-up at DERA Chertsey

6.6.2 Trial Results

Figure 6-22 shows the results for an experiment in London clay containing the predominately plastic PMA-3 APM and the metal cased BLU-61 bomblet buried. The PMA-3 is surface buried and the BLU-61 is very shallowly buried.

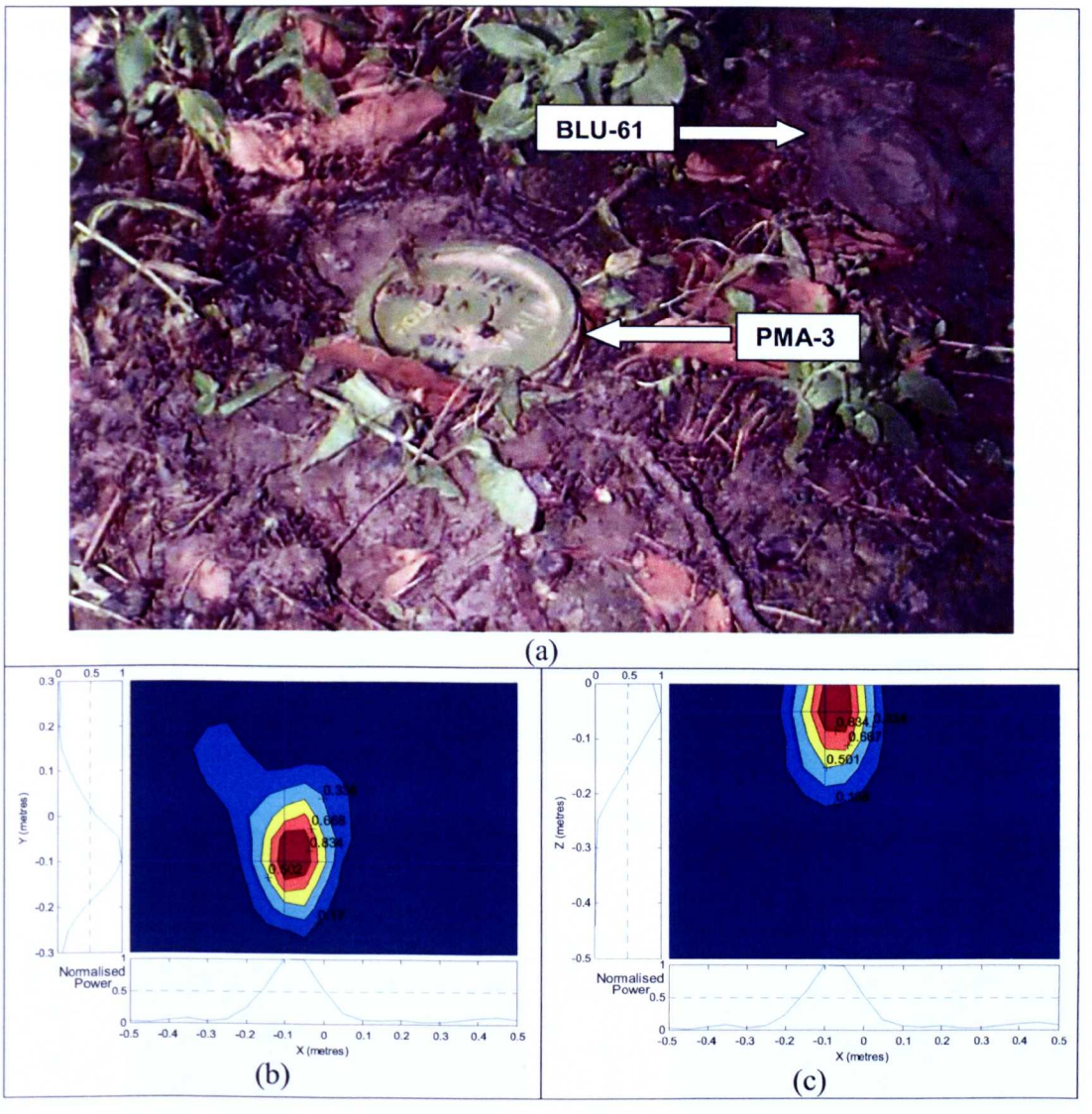

Figure 6-22 BLU-61/A/B bomblet (x=-0.3, y=0.2) and PMA-3 (x=-0.1, y=-0.1) buried in London Clay with vegetation with top flush with surface (a) picture of flush buried targets, (b) horizontal scan at -0.05m depth (c) vertical scan through y=-0.15m

The PMA-3 is located towards the centre of the array at x=-0.m1,y-0.1m and the BLU-61 is off centre at x=-0.3m, y=0.2m. The PMA-3 is strongly detected whilst only a faint trace of the BLU-3 is picked up. Two important conclusions for detection in London Clay can be drawn from this result.

Firstly, when a plastic or metal target is buried with its top flush with or higher than the surface in London Clay the high dielectric contrast between the target and clay enhances the detection performance compared to detection in to other soil types. Secondly, the

attenuation of London clay is such that even shallowly buried metal targets may not be detected by RASOR.

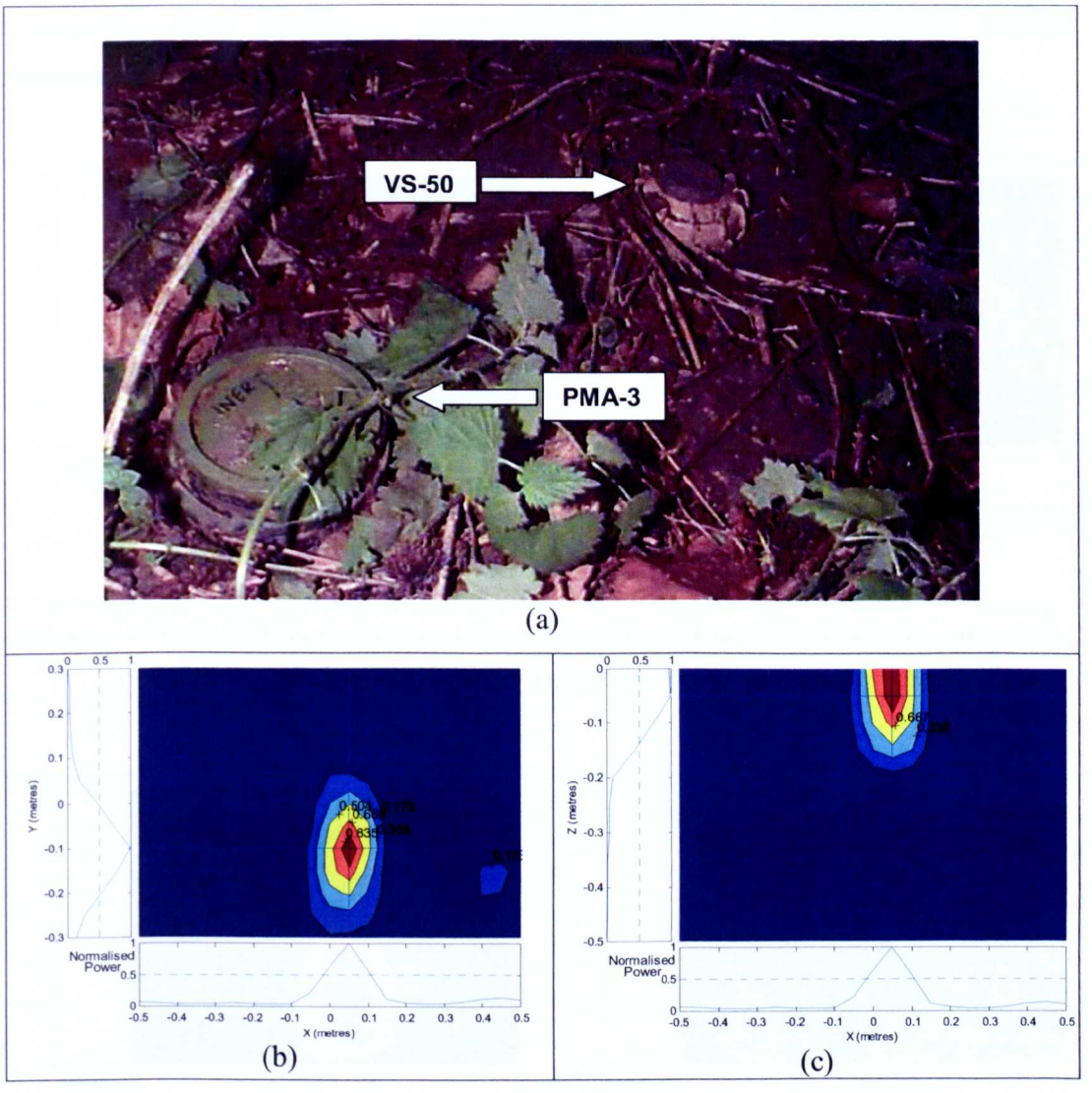

Figure 6-23 PMA-3 APM (x=0.05m, y=-0.1m) and VS-50 APM (x=0.4m, y=-0.15m) on surface of loam with vegetation at (a) picture showing target locations (b) horizontal scan at -0.05m depth (c) vertical scan through y=-0.1m

Figure 6-23 shows a similar experiment set-up to the previous one, but taken in loam plot and with a VS-50 APM replacing the BLU-61. Here the VS-50 is located under the opposite side of the array at x=0.4m, y=-0.15m and buried with its top flush. The PMA-3 is at x=0.05m, y=-0.1m and also buried flush[1]. The PMA-3 is detected strongly again,

[1] Notice that the PMA-3 is mistakenly buried upside down, i.e. with its detonator pointing downwards into the ground. This is not thought to be significant for its RCS (for the bandwidth of interest).

but at reduced strength compared to the detection in London Clay, probably due to the reduced dielectric contrast. The VS-50 is detected, but not at the same strength. This is due to the VS-50 actually being located at the extreme of the sensitivity of the demonstrator array resulting in much reduced processing. An operational RASOR, consisting of a larger antenna array, would cover a wider swathe.

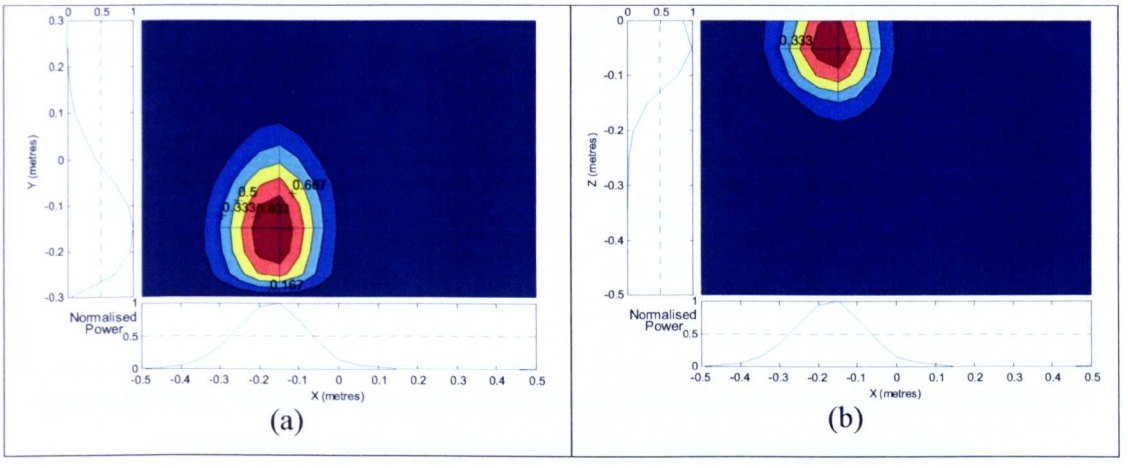

Figure 6-24 TM-57 ATM buried in loam with no vegetation with top flush with surface at x=-0.2m, y=-0.2m (a) horizontal scan at -0.05m depth (b) vertical scan through y=-0.15m

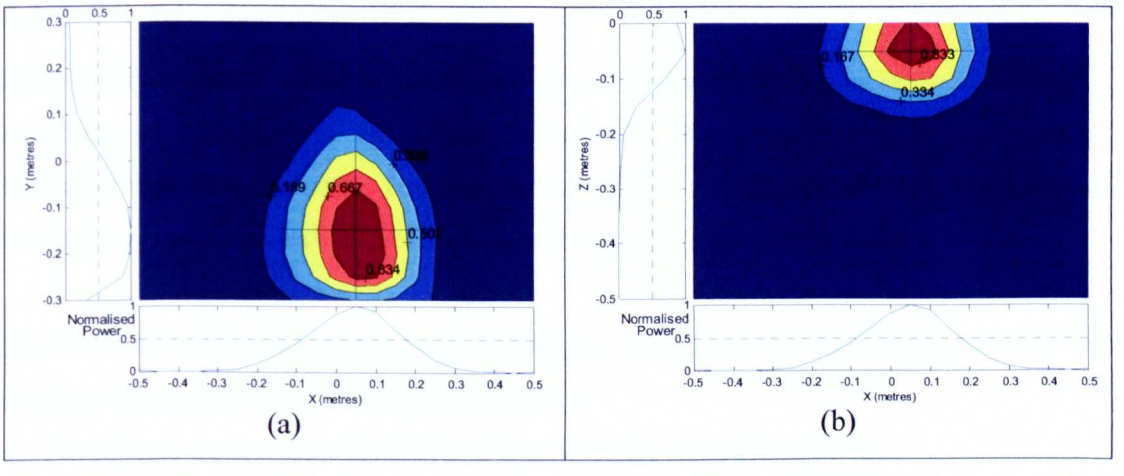

Figure 6-25 TMA-4 ATM buried in loam with no vegetation with top flush with surface at x=0.05m, y=-0.2m (a) horizontal scan at -0.05m depth (b) vertical scan through y=-0.15m

In addition the alternative array switching scheme described in section 5.1.4 should allow improved performance across the array by distributing transmit paths more evenly - the 'raster' switching scheme implemented on these trials tends to skew processing gain towards the negative x quadrants.

Figure 6-24 and Figure 6-25 show the TM-57 and TMA-4 ATMs buried in Loam. Both are clearly detected.

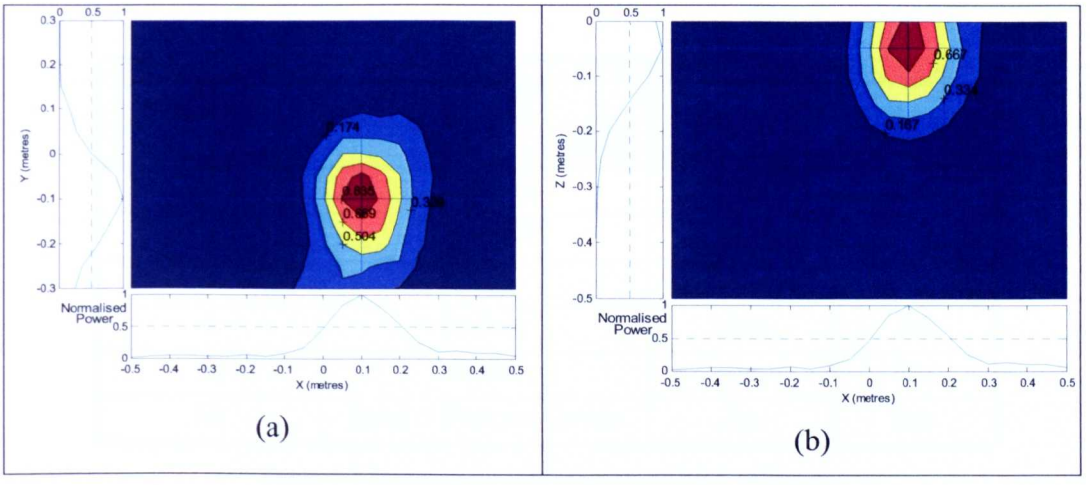

Figure 6-26 PMA-3 buried in vegetation covered loam with top flush with surface at x=0.05m, y=-0.1m (a) horizontal scan at -0.05m depth (b) vertical scan through y=-0.1m

6.7 ERA

6.7.1 Trial Site

ERA Technology Ltd constructed this test site at Leatherhead, Surrey in order to test the suitability of a number of GPR sensors, including their own, for a vehicle mounted landmine detection contract. The test site comprised of six different plots of soil of varying sizes summarised in Table 6-1 and photographed in Figure 6-27.

The location and number of targets and clutter objects in the plots was generally not disclosed except for the following information:

- No objects were within the first and last metre (in the y dimension).
- No targets were within 0.5 metres of the sides (in the x dimension).
- Eight APMs of various types were disclosed for calibration purposes. These were positioned along a straight line in the y-axis starting at 2.9m and ending at 8.9m with a regular 1m spacing. Each mine was located 0.6m from the side wall of the plot as indicated in Figure 6-27.

Eight ATMs of various types were disclosed for calibration purposes. These were positioned along a straight line in the y-axis starting at 2.5m and ending at 8.5m with a regular 1m spacing. Each mine was located 1m from the side wall of the plot as indicated in Figure 6-27.

Plot Zone Number	Soil Type	Length (y axis)	Width (x axis)
1	Top Soil	10m	5m
2	DTP-MOT	10m	5m
3	Clay	10m	5m
4	Ballast	10m	5m
5a	Sand	8m	5m
5b	Sand + Ferrous Oxide	2m	5m

Table 6-1 Dimensions and contents of ERA soil plots

Figure 6-27 Picture of ERA Trial plots

Conditions had been very wet immediately prior to commencement of the trial and, because the plots were bounded by concrete and membrane linings, the drainage was clearly rather poor, hence most of the plots were quite saturated and some were in fact covered in surface water. In these conditions mine detection with any GPR system is difficult[1]. It was not possible to measure the permittivity and loss tangent of the soil since

[1] In these conditions an acoustic sensor is likely to perform better and this is an example of where sensor fusion could be of great benefit.

this would disturb the soil, however, it was concluded that the high level of soil saturation would severely hamper detection at any depth due to the increased losses that this implies.

The drainage through the Ballast and DTP-MOT plots was obviously better than through the clay, soil and sand plots. This is not unexpected since ballast and DTP materials are essentially crushed rock and therefore do not retain bound water to the same extent as clay, for example.

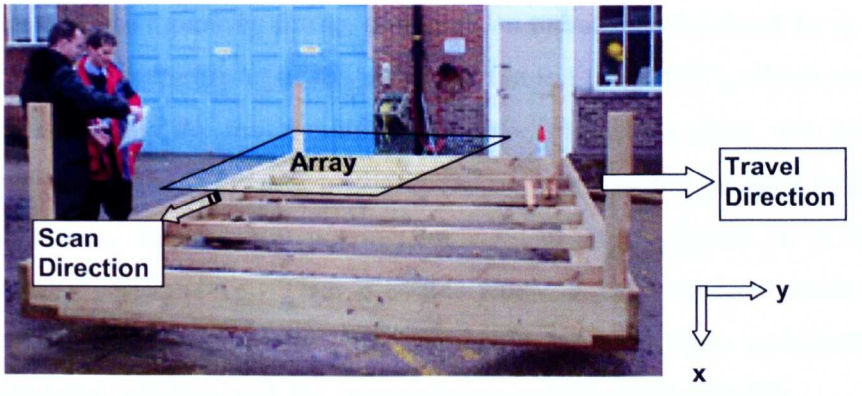

Figure 6-28 Mounting frame

It was required that the soil surface should not be touched in order that subsequent equipment experiments were not put at a disadvantage. The wheeled mounting frame that was used in earlier trials was therefore not suitable because, being only the width of the array, its wheels would foul the soil surface. A new mounting frame was constructed as shown in Figure 6-28 that traversed the shorter, x-dimension of the plot. Wheels were placed at the four corners of the frame so that it could be pushed forward in the y direction over the plots. After each full sweep the array was moved over by 0.5m steps in the x direction and another full sweep conducted, thus eight sweeps were conducted to cover 0.5m to 4.5m inclusive in the x direction.

The mounting arrangement caused two difficulties. Firstly, it was rather cumbersome making it difficult to control and steer. There were no runners along the sides of the plots to keep the mounting straight, therefore it tended to stray off line as it traversed down the plots. In order to correctly detect, localise and pinpoint targets against a prearranged grid and also to correctly join together the datasets, the sensor needs to have an accurate estimate of its position at all times during the data collection with regards to a

clear reference point. In the practical system RASOR would be fitted with GPS sensors to pinpoint the exact reference system as well as position sensors and actuators to maintain array to ground spacing. The vehicle would also probably have a marking system (similar to road marking) to mark possible targets. The demonstrator system was not sufficiently sophisticated to have any of this functionality and therefore inevitably positioning errors were introduced during the data collection. The array was swept forward in 30cm steps and lined up with marker pegs driven into the ground along the full 50m length of the lane on both sides.

The second problem with the mounting frame, or at least an unknown introduced by it, is the inclusion of wooden beams in front of the array (visible in Figure 6-27), which were necessary to provide rigidity to the mounting structure. Although these are non-conducting and relatively short compared to the operating wavelengths (at least in the bore-sight of the antenna), they were at no time included in any analytical or FDTD simulations of the array performance. Their presence would at the very least result in additional losses being introduced to the path, but could also introduce undesirable multiple reverberation and interfere with the antenna beam-pattern and bandwidth.

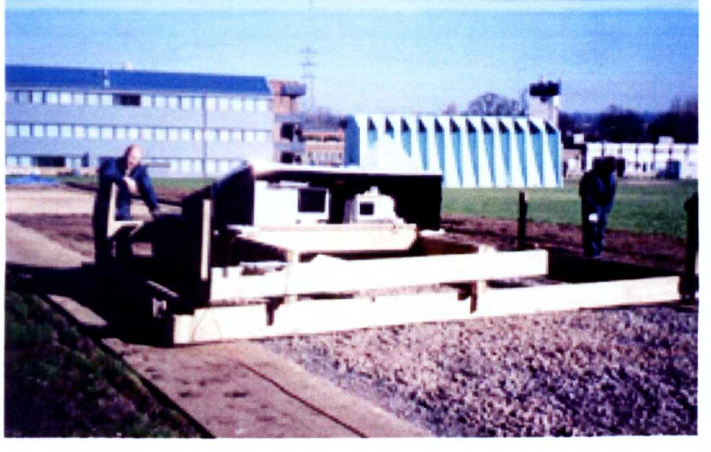

Figure 6-29 ERA trial Set-up

A strict time limit of 3 days was imposed for all data collection over all 5 zones. In fact this time was easily met including setting up, clear down and some post trial analysis.

6.7.2 Trial Results

The calibration AP and AT provided mines were used to determine the zones within which detection is possible with the current state of the system.

The 3D data set was combined into a 2D slice or C-scan using the stacking algorithm described in Section 5.2.2.4. A simple detection threshold was employed based on an analysis of the ROC curves developed from previous trials. With the processing performed, there is good reason to suppose that the data from Zones 2 (DTP-MOT) and 4 (Ballast) is reliable.

6.7.2.1 Zone 2 Results: DTP-MOT

This Zone consisted of a material denoted DTP-MOT; a road building material.

From Figure 6-30 (plan view) it is possible to see the majority of the calibration ATM mines along the x=4m line. The AP mines are not as clear. It seems likely that there are also mines present at the 8 positions identified by red dots.

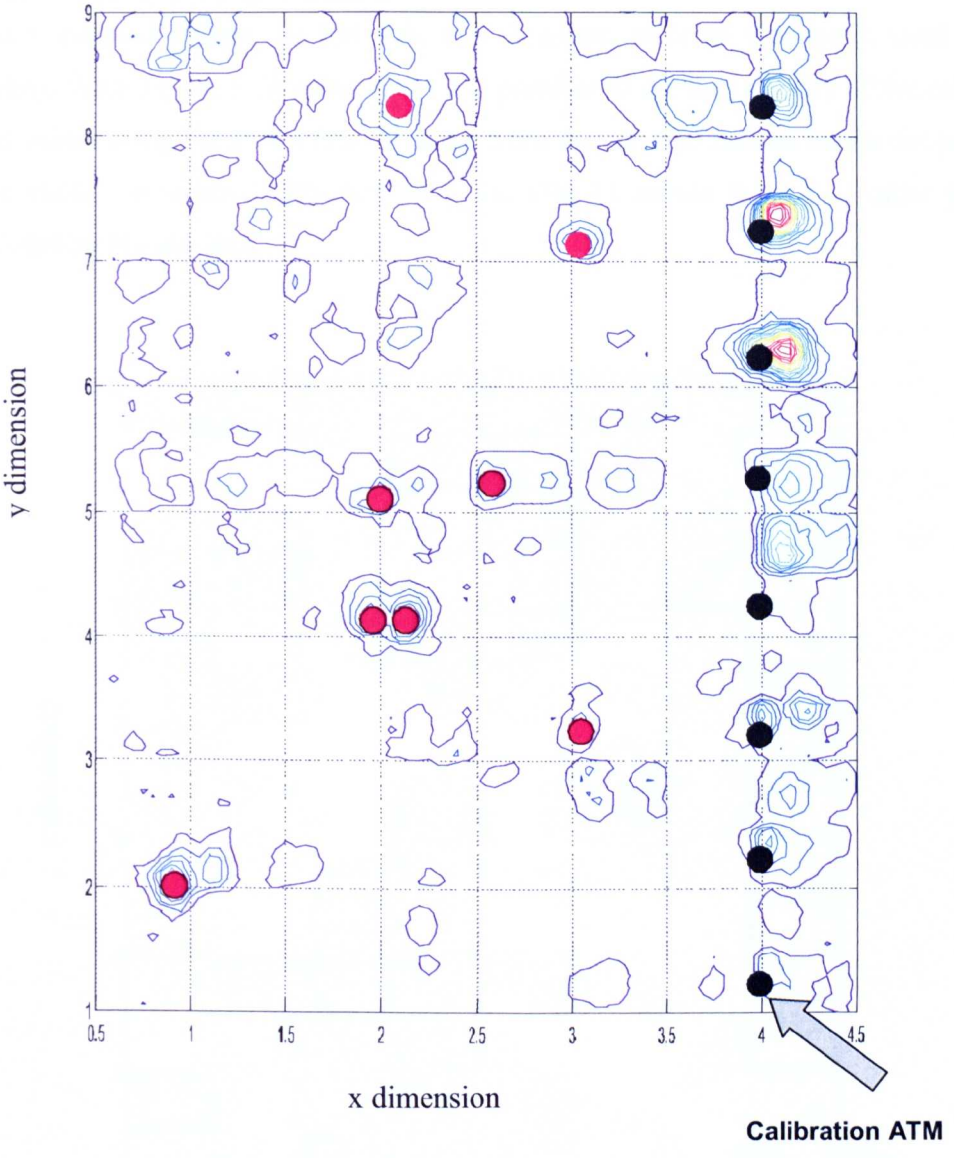

Figure 6-30 Zone 2 map - DTP-MOT

6.7.2.2 Zone 4 Results: Ballast

Zone 4 denoted ballast; in fact this is a dolomite material frequently used in road building. From Figure 6-31 (plan view) it is possible to see the majority of the calibration ATM mines along the x=4m line. Returns from the AP calibrations mines are present in some cases. It seems likely that there are also 11 mines present at other positions indicated by the red dots.

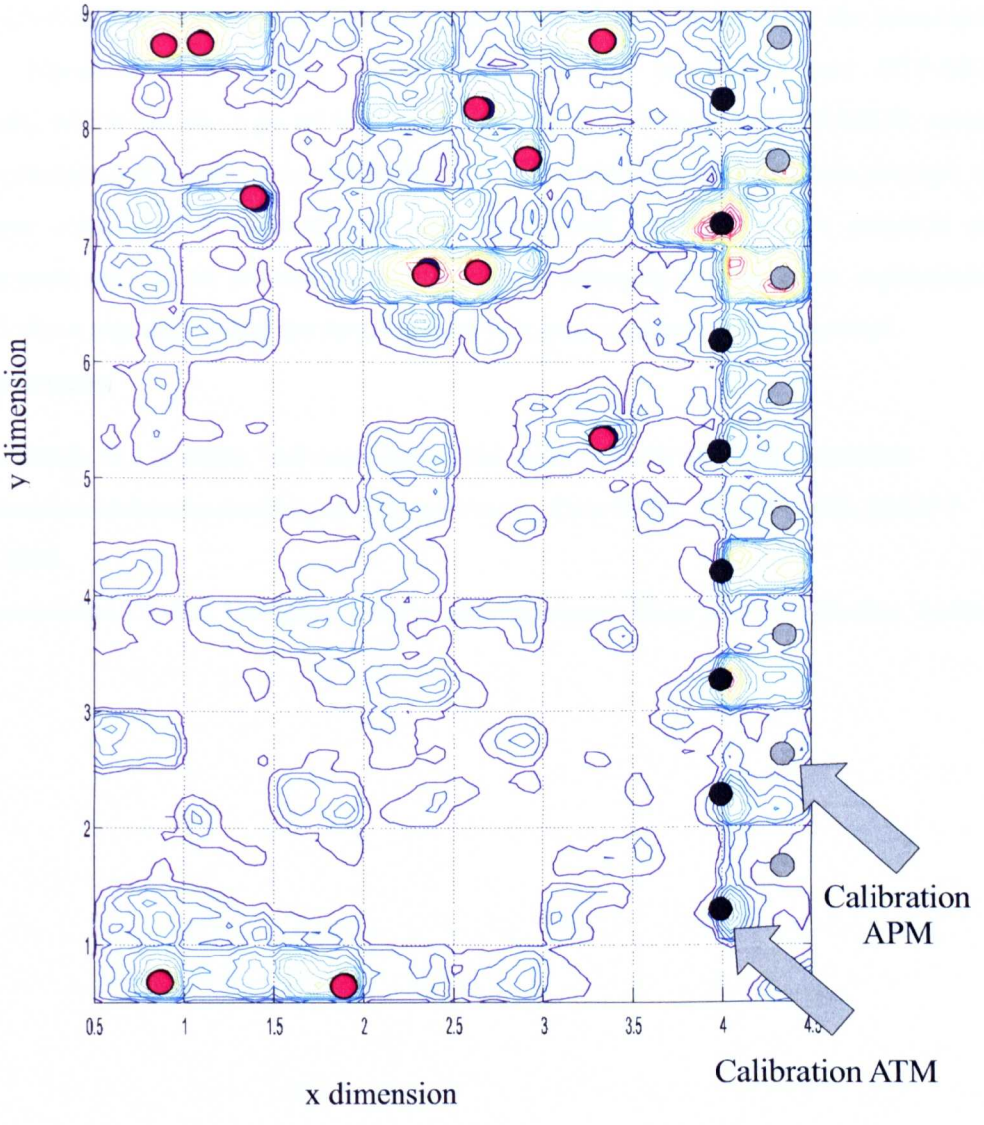

Figure 6-31 Zone 4 results - Ballast

6.8 Conclusions

Trial results obtained from six different trial sites have been presented. Results in the sandbox, Quarry site, Long Ashton field and DERA Chertsey were very promising showing good performance in a range of soil types and difficult clutter environments.

The 'blind' test trials at ERA represented a considerable challenge for the RASOR demonstrator, due to the heavy saturation of the ground, the mounting arrangement and the positioning inaccuracies; the first two factors considerably attenuating the transmitted power. Nonetheless, promising results were obtained on Ballast and DTP-MOT materials, which are the type of road materials that a vehicle-mounted RASOR system might commonly traverse. As a demonstration of the potential of the system concept, the trial was considered a success, and also highlighted areas for future research and development such as an improved mounting and positioning system, more sophisticated classification algorithms and the development of a multi-sensor fusion approach.

References

[1] I.A.Burch, D.J.Allsopp, 'Advance hand held mine detector and mine detection neutralisation and route marking system overview', Proc SPIE, Vol.4038 (II), pp1237-1248, 2000.

[2] Promotional Leaflet, Colin King Associates Surrogate Mine Systems, Horley, Surrey

7 Conclusions, Other Applications and Future Work

The broad objective of this research was to develop a fully functional ground penetrating radar (GPR) demonstrator system capable of detecting buried anti-personnel and anti-tank landmines when installed on a moving vehicle. The demonstrator system implements a novel Real Aperture Synthetically Organised Radar (RASOR) technique, which uses a two dimensional antenna array and post-reception synthetically-focusing to image a three dimensional space under the array.

It has been shown that state-of-the-art GPR systems for landmine detection are limited by resolution, operation in highly cluttered environments, classification performance, penetration depth and operating speed.

7.1 Specific contribution of this Dissertation

This thesis has described the author's specific contribution in the following areas:

- Analysis and modelling of the RASOR system concepts including an assessment of the operating environment such as soil types, target types, clutter limits, noise limits and de-correlating effects in order to postulate and analyse suitable array configurations, mounting arrangements and processing algorithms.
- Derivation, implementation and experimentation with new algorithms to deal with the problem of surface reflections, volume clutter reduction and classification.
- Definition of system parameters such as operating frequency, power and array size and configuration in order to deal with the operational environment based on modelling and early experimentation.
- System design including the design of RF and digital circuits and control software and the implementation of processing algorithms for a real time system.

Using the developed demonstrator system, real measured data was obtained on real targets under various soil conditions and at a variety of test sites. Results have been presented and discussed which show RASORs ability to detect mines in challenging cluttered

environments. However, it has also been shown that the RASOR demonstrator system on its own does not provide sufficient classification and detection accuracy for APM detection. Possible improvements and enhancements to the demonstrator system are suggested in the next section along with other ideas for further research.

7.2 Suggestions for further research

The operating frequency chosen for the RASOR demonstrator was the highest possible using off-the-shelf high-speed sampling equipment at a reasonable cost. Subsequent developments of real time sampling devices mean that a higher operating frequency and larger bandwidth could now be utilised, thus providing an improvement in overall resolution and classification capability without sacrificing real-time operating speed.

More advanced classification algorithms should be examined such as the use of promising wavelet-based algorithms [1] and recursive least squares methods [2] in order to improve classification performance. This should also consider the possibility of fusing data from another sensor system, such as nuclear quadrupole resonance or acoustic sensor. These would need to be deployed closer to the ground than RASOR, but in the case of NQR, could be called into action when a possible target detected by RASOR needs to be positively classified.

Real time RASOR will be mounted on a boom ahead of the vehicle. Examination of system performance including array to ground spacing compensation, actuator stabilisation and real-time algorithm adaptation is required. At the same time real time implementation of the RASOR system should be considered on, for example, VME based processing rack(s) with the additional capability for bulk storage and operator analysis.

7.3 Other applications

RASOR is by no means limited to the field of landmine detection and a number of other applications are suitable for realisation. The author in conjunction with the above research has conducted some preliminary investigations and other areas are the subjects of active on-going research.

7.3.1 Archaeology

GPR are quite well established in archaeological applications for detection of large scale features such as walls and foundations [3]. The improved resolution and real-time search rates of RASOR have the potential to enhance the capability for archaeologists to detect small items such as bones and pottery.

7.3.2 Security

The capability of using RASOR to detect the presence of people through walls has been examined. In this case the array is mounted vertically. Promising results have been obtained through plasterboard, cavity walls and breeze block.

7.3.3 Manufacturing

It may be possible to use RASOR for screening batch manufacturing processes. For example it could be possible to scan for foreign bodies present in jars of food. This would require an increase in operating frequency to detect small objects. In this application it would be possible to consider using two or more spatially separated arrays around a conveyor belt and utilising forward, rather than backward, scattering paths.

7.3.4 Medical

It has been postulated that the microwave imaging techniques, such as RASOR, could be suitable for medical screening in order to detect, for example, breast tumours. Again this would require an increase in frequency, although real time operation may not be necessary. This is the subject of active current research [4][5][6][7].

Reference

[1] J.W.Brooks, 'The detection of buried non-metallic anti-personnel land mines', PhD dissertation, University of Alabama, 2000

[2] A.M.Zoubir, et al., 'Signal processing techniques for land mine detection using impulse ground penetrating radar', IEEE Sensors Journal, Vol.2 No.1, pp41-51, Feb 2002

[3] D.J.Daniels, 'Surface Penetrating Radar', IEE, 1996, Chapter 7

[4] E.C.Fear, X.Li, S.C.Hagness, M.A.Stuchly, 'Confocal microwave imaging for breast cancer detection: localization of tumours in three dimensions', IEEE Trans. Biomed.Eng., Vol.49 No.8, pp812-822, August 2002

[5] X.Li, S.C.Hagness, 'A confocal microwave imaging algorithm for breast cancer detection', IEEE Microwave & Wireless Components Letters, Vol.11 No.3, pp130-132, March 2001

[6] E.J.Bond, X.Li, S.C.Hagness, B.D.Van Veen, 'Microwave imaging via space-time beamforming for early detection of breast cancer', IEEE Trans.Ant. & Prop., Vol.51 No.8, pp1690-1705, August 2003

[7] R.Nilavalan, et al., 'Numerical investigation of breast tumour detection using multi-static radar', Elec. Lett., Vol.39 No.25, 11th December 2003